Theory of ultrafast waveguided parametric down-conversion: From fundamentals to applications

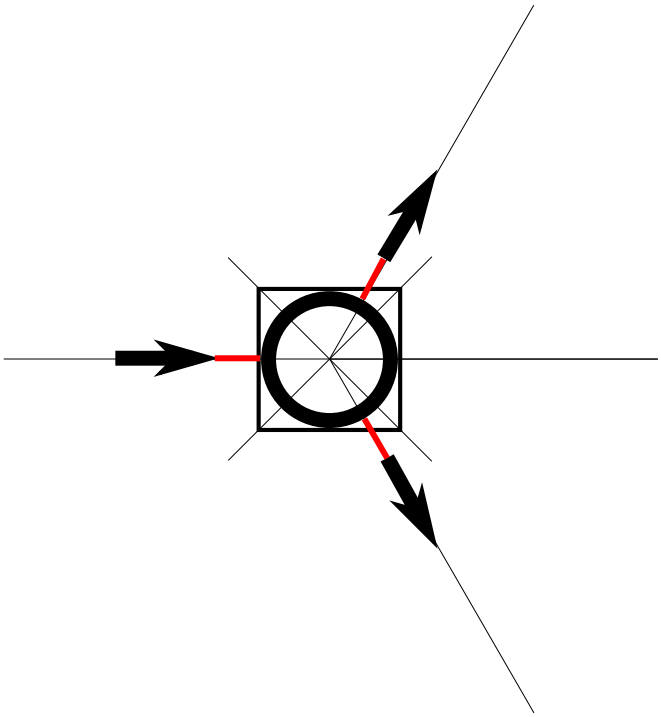

Der Naturwissenschaftlichen Fakultät
der Universität Paderborn
zur
Erlangung des Doktorgrades Dr. rer. nat.

vorgelegt von
Andreas Christ

Contents

Uns ist in alten mæren wunders vil geseit
von helden lobebæren, von grôzer arebeit,

(Nibelungenlied)

1. Summary

In experimental implementations of photonic quantum systems parametric down-conversion (PDC) is omnipresent, yet despite its widespread deployment the theoretical treatment of PDC remains challenging.

In this thesis we address this problem and develop a theoretical model of ultrafast waveguided PDC extending the current perturbation approaches to include the spatial and spectral degree of freedom [1, 2]. We further investigate PDC beyond the perturbation approximation and put forward a rigorous theoretical description as well as a simplified analytical model [3], which also enables the theoretical treatment of frequency conversion processes.

This theoretical framework of PDC enables us to research future applications for PDC in quantum enhanced applications: We explore the limits of PDC to serve as a source of single photons [4], present a new approach to engineer the spectral properties of PDC sources independently of the dispersion properties of the applied nonlinear crystal [5] and put forward a new method to characterize PDC sources in the lab, which is robust, simple and most importantly loss independent [6]. Finally, we develop a new multiplexed quantum communication protocol which, based on the multi-mode nature of PDC, enables exponentially higher quantum communication rates than the standard single-mode coding [7].

2. Zusammenfassung

In der Quantenoptik gib es kaum einen Prozess der öfter eingesetzt wird als die Parametrische Fluoreszenz (PDC). Doch trotz der weiten Verbreitung bereitet die theoretische Beschreibung der PDC noch immer Schwierigkeiten.

In dieser Dissertation beschäftigen wir uns mit diesem Problem und erweitern die gegenwärtige störungstheoretische Beschreibung von "ultrafast" PDC in Wellenleitern um sowohl den räumlichen als auch den spektralen Freiheitsgrad [1, 2]. Weiterhin gehen wir über diese störungstheoretischen Betrachtungen hinaus und entwickeln eine numerische und eine vereinfachte analytisches rigorose theoretische Modellierung der PDC, die sich überdies zur Beschreibung von Frequenzkonversion eignet [3].

Dieses tiefgreifende Verständnis der PDC ermöglicht es uns zukünftige Anwendungen der PDC im Bereich der Quanteninformation zu erforschen: Wir untersuchen wie gut PDC eine deterministische Einphotonenquelle annähern kann [5], präsentieren eine neue Methode die spektralen Eigenschaften der PDC unabhängig von der Dispersion im Kristall zu verändern [5] und entwickeln einen neuen Ansatz um PDC, robust, einfach und, vor allem, verlustunabhängig zu charakterisieren [6]. Schließlich stellen wir ein gemultiplextes Quantenkommunikationsprotokoll vor welches, basierend auf den multimodigen Eigenschaften der PDC, exponentiell höhere Datenraten, als vergleichbare einmodige Protokolle ermöglicht [7].

Everything starts somewhere, although many physicists disagree.

(Terry Pratchett)

3. Introduction

The history of quantum mechanics dates back to the very beginning of the 20th century when, in the year 1900, Max Planck postulated that the energy of light is emitted and absorbed in discrete quanta, to explain the spectrum of black body radiation [8]. Planck however insisted that his quantization of light was merely a mathematical construct which has no connection to physical reality whatsoever. In 1905, however, Einstein interpreted his idea realistically and used Planck's model of quantized light to describe the photoelectric effect. This sparked the development of quantum theory by Max Planck, Niels Bohr, Werner Heisenberg, Louis de Broglie, Arthur Compton, Albert Einstein, Erwin Schrödinger, Max Born, John von Neumann, Paul Dirac, Wolfgang Pauli, David Hilbert, Wilhelm Wien, Satyendra Nath Bose, Arnold Sommerfeld and others during the first half of the 20th century [9], but it was not until 1977 that Kimble et. al. performed the first experimental observation of the quantized nature of light [10].

The term "photon", to describe the quantized nature of light, coined by G.N. Lewis, dates back to the year 1926, where it should be noted that Lewis explicitly denied any connection of his "photons" to the concepts of Planck and Einstein. Still the word "photon" caught on and is now universally used to describe the quantized nature of light [11].

Since the advent of quantum mechanics these "photons" are one of the main tools to experimentally investigate quantum mechanics, they offer insights into the quantum nature of light, while also serving as a fundamental building block for quantum enhanced applications.

To date the most prominent method to create photonic quantum states is parametric down-conversion (PDC). The history of PDC dates back to the year 1961 when it was first predicted by Lousiell et. al. [12], and subsequently investigated by others [13, 14, 15, 16, 17, 18]. In 1969 Zeldovich and Klyshko proposed an experiment to observe the created photon-pairs during PDC and suggested its use as a source of non-classical states of light [19]. In 1970 Burnham and Weinberg performed the first observation of pair production from PDC [20]. The usage of PDC in the framework of quantum information theory was sparked in 1987 by Hong, Ou and Mandel [21]. Their experiment, now known as "Hong-Ou-Mandel Dip", forms one of *the* basic building blocks of optical quantum information processing [22].

Since then quantum optics developed into a flourishing field with PDC serving as one of the major sources of quantum states of light. From the year 1987 onward the amount of papers published on the subject of PDC is growing at a staggering rate. The process is not only omnipresent as a source of single quanta of light [21, 23, 24, 25, 26, 27], but its quantum nature further enables the creation of other fundamental quantum states of light: Bell-states in the form of entangled photon-pairs [28, 29, 30], squeezers

[31, 32] featuring quantum fluctuation below the standard Heisenberg limit and the omnipresent EPR-states [33, 6] introduced by Einstein, Podolsky and Rosen in 1935 [34]. However, despite its widespread applications, the theoretical treatment of PDC still remains challenging.

In this thesis we address this problem and present a rigorous theoretical description of ultrafast waveguided PDC, taking into account the spatial, spectral and photon-number degree of freedom. This detailed theoretical description of PDC enables us to build, develop and propose enhanced sources for quantum information processing: We explore the limits of PDC as a source of single-photon Fock states, put forward a scheme to create single-mode PDC states independent of the applied material, develop a loss *independent* method to effectively probe PDC states in the laboratory and present a multiplexed quantum communication protocol featuring an exponentially enhanced quantum communication rate in comparison to the standard single-mode coding.

This cumulative dissertation is structured as follows: After a general introduction into the theory of PDC in Chap. 4 the following chapters give short summaries of the individual works, each followed by the corresponding publication(s):

Chap. 4 reviews a basic model of PDC, based on the widespread first-order perturbation theory treatment. Despite its simplicity it already features all important process properties required for working with PDC sources and enables us to introduce all necessary concepts and formulas.

Chap. 5 starts the summaries of the individual publications and extends Chap. 4 to PDC in waveguides. Taking into account the spatial degree of freedom our theoretical model enables us to evaluate the impacts of waveguiding structures on the PDC process [1]. We unveil an intricate interplay between the spatial and spectral properties of the generated PDC states, which facilitates the creation of hyperentangled quantum states [2]. This model was not only successfully tested in the laboratory [1, 2], but has also already been extended to describe two-photon quantum walks in waveguide arrays [35].

However, when first-order perturbation theory is not sufficient any more, the theoretical description of PDC becomes challenging. Especially the multi-photon components, as well as the explicit time-dependence of the involved Hamiltonians hamper an efficient theoretical description of PDC. In Chap. 6 we investigate these effects and build two models which enable a of full description of ultrafast PDC in the high gain regime. Firstly we present a rigorous numerical model, which relies on the solution of coupled integro-differential equations and covers the complete dynamics of the process. Secondly we put forward a simplified model that, at the expense of neglecting time-ordering effects, enables an analytic solution [3].

Furthermore we show that our developed theoretical framework is not restricted to PDC processes, but can also be applied to describe frequency conversion (FC), which enables us to benchmark the performance of FC as a quantum pulse gate.

This concludes our theoretical investigation of the PDC process. The developed theoretical framework of ultrafast waveguided PDC enables us to research future applications for PDC in for quantum information processing applications:

In Chap. 7 we discuss the heralding of single-photons from PDC sources. We benchmark the purity of the heralded signal photons and the achievable rates, for the first

time, taking into account the spectral *and* the photon number degree of freedom. This enables us to determine the limits of PDC sources for *pure* single-photon generation. Our calculations unveil that, using perfect photon-number resolving detectors and an optimal source, PDC is able to supply single-photon Fock states with a heralding probability of 25%. Consequently an array of 17 switched PDC sources is required to approximate a *pure* deterministic single-photon source ($> 99\%$ emission probability) [5].

In Chap. 8 we turn to the problem of source engineering. As discussed in Chap. 7, very specific PDC states are required to herald *pure* single-photon states. Unfortunately only very few nonlinear crystals feature the required dispersion properties. Here we present a new method to engineer the PDC process, not relying on specific dispersion curves, but instead by creating the signal and idler waves in opposite directions. This enables the use of nonlinear materials which previously where deemed unsuitable for this task [5].

Chap. 9 elaborates on the issue of characterizing ultrafast PDC states in the laboratory. For this purpose, we put forward a new characterization procedure based on measuring broadband time-integrated correlation functions [6]. This approach enables the fast, robust, straightforward, and, most importantly, *loss independent* probing of PDC sources and has already established itself as a standard tool in our laboratory [36].

Finally, in Chap. 10, we investigate continuous-variable (CV) quantum communication. Hereby the major challenge resides in the transmission of quantum information with high rates over long distances in the presence of loss. We explore the possibility to multiplex CV quantum communication by encoding the information on multiple optical pulse modes simultaneously. Our research reveals that our multi-mode PDC states are optimally suited for this multiplexing which leads to an enhanced energy efficiency achieving an *exponential* increase in the quantum communication rate in comparison to the standard single-mode coding.

Chap. 11 summarizes our findings and discusses the prospects of ultrafast waveguided parametric down-conversion in the framework of quantum information applications. Appendix A contains additional calculations. Appendix B collects additional publications sorted by date.

Part I.

PDC theory

It's a magical world Hobbes, ol' buddy
. . . let's go exploring.

(Calvin and Hobbes)

4. Theory of PDC in the two-photon picture

4.1. Introduction

The first theoretical description of PDC dates back to the year 1961 [12]. The model, introduced by Lousiell et. al., sparked many other early contributions to the theory of PDC in the sixties and seventies [13, 14, 15, 16, 17, 18] and the first observation of PDC by Burnham and Weinberg in 1970 [20]. Since then the theoretical framework of PDC has been continuously expanded to span a variety of different theoretical approaches which focus on a multitude of topics: different nonlinear materials, various types of PDC processes, quasi-phase-matching, and the spatial, spectral and photon number degrees of freedom. Each model features different advantages and disadvantages depending on its intended application.

In this chapter we start off with an investigation of PDC using first-order perturbation theory [37, 38, 39]. Due to its simplicity this model forms the basis of almost all modern theoretical investigation and enables us to introduce all the necessary concepts and formulas.

4.2. The PDC Hamiltonian

Fig. 4.1 sketches the basic principle of PDC: A photon of an incident pump field spontaneously decays, inside a crystal exhibiting a $\chi^{(2)}$-nonlinearity, into two photons, for historical reasons, labelled signal and idler.[1]

On an atomic level the pump photons, in the medium, are continuously absorbed and re-emitted by the atoms in the material, or to be more precise, they interact with the individual atoms in the crystal lattice. This matter-wave interaction leads to optical

[1] The concept of the photon is a difficult one indeed. A photon is *neither* a particle *nor* a wave, but a quantum field amplitude that exhibits a quantized nature upon detection. A historical overview of the evolution of the term photon, its original meaning and common misunderstandings is given in the paper "Anti-photon" by W.E. Lamb, Jr. [11]. In fact photons do not spontaneously decay into photon pairs at some point inside a nonlinear crystal. PDC is a fully deterministic unitary process where two quantum field amplitudes signal and idler are created. Their amplitudes give the probabilities to detect two quanta of light after the nonlinear interaction. This, quite involved, explanation of PDC is usually abbreviated to "A pump photon spontaneously decays into a photon-pair inside the nonlinear crystal", which has the advantage of being accessible and giving an intuition of the process. One should however keep in mind its limitations.

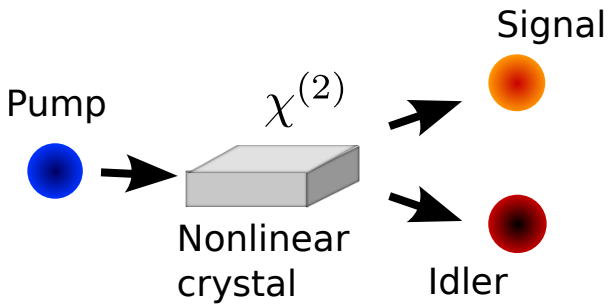

Figure 4.1.: In the process of PDC a pump photon spontaneously decays, inside a medium exhibiting a $\chi^{(2)}$-nonlinearity, into two photons, for historical reasons, labelled signal and idler.

effects such as refraction, absorption, and, as we will see, PDC. It is however very difficult to describe PDC on an atomic level due to the sheer number of atoms and photons involved. Consequently the process of PDC is usually modelled neglecting the quantum mechanical properties of the atoms.

In this simplified picture we approximate the atoms in the material as an array of dipoles. The incoming pump wave excites these dipoles and drives them to emit electromagnetic radiation. The frequency and direction of the emitted light are determined by the constraint that all dipoles have to constructively interfere to build up a significant amount of electromagnetic radiation. Mathematically this interaction is described by a time-varying dipole moment $\vec{P}(t)$ induced in the material via the incoming pump wave.

If we assume that the atoms or dipoles act as perfect harmonic oscillators the energy transfer from the pump field to the dipoles and the following emission merely leads to a delay of the pump light which gives rise to the well known process of refraction. At high pump intensities, however, they show a nonlinear response. In this case it is not sufficient to describe the atoms in the medium by harmonic oscillators, but the nonlinear response represented by anharmonic oscillations has to be considered as well.

For this purpose it is useful to write down the dipole moment $\vec{P}$ per unit volume as a power series [40]:

$$\begin{aligned} P_i(t) &= \epsilon_0 \left[\sum_j \chi_j^{(1)} E_j(t) + \sum_{jk} \chi_{ijk}^{(2)} E_j(t) E_k(t) + \sum_{jkl} \chi_{ijkl}^{(3)} E_j(t) E_k(t) E_l(t) + \dots \right] \\ &= P_i^{(1)} + P_i^{(2)} + P_i^{(3)} + \dots \\ &= P_i^{(1)} + P_i^{\mathrm{NL}} \end{aligned} \tag{4.1}$$

The term $P_i^{(1)}$ describes the harmonic response which leads to the process of refraction, whereas the time-varying nonlinear polarization terms P_i^{NL} act as a source of new components of the electromagnetic field. This is evident from the wave equation in a

nonlinear optical medium [40]

$$\nabla^2 \vec{E} - \frac{n^2}{c^2}\frac{\partial^2 \vec{E}}{\partial t^2} = \frac{1}{\epsilon_0 c^2}\frac{\partial^2 \vec{P}^{\mathrm{NL}}}{\partial t^2}, \tag{4.2}$$

where n is the index of refraction and c the speed of light. This expression can be regarded as a dipole emitting light $\vec{E}$ driven by the nonlinear polarization $\vec{P}^{\mathrm{NL}}$ induced by the pump wave in the medium.

The PDC emission stems from the $\chi^{(2)}$-nonlinearity. It features the advantage to be much stronger than the higher-order nonlinear terms and enables an efficient nonlinear interaction.[2] Note that $\chi^{(2)}$-nonlinearities are only present in crystal materials featuring noncentrosymmetric crystal structures [40].[3] The most commonly used crystals for PDC generation are BBO, LiNbO3, and KTP.

In order to develop a quantum mechanical description of PDC we first have to derive the Hamiltonian of the process, given by the energy inside the material. According to Poynting's theorem the energy of an electric field inside a medium is given as [44]:

$$\mathcal{E} = \frac{1}{2}\int_V \mathrm{d}^3 r \, \left(\vec{E}\vec{D} + \vec{B}\vec{H}\right) \tag{4.3}$$

In our case we are not interested in the contribution by the magnetic component, since the PDC interaction stems from the electric displacement field $\vec{D}$. We obtain [40]

$$\begin{aligned}
\mathcal{E} &= \frac{1}{2}\int_V \mathrm{d}^3 r \, \vec{E}^{(p)}\vec{D} \\
&= \int_V \mathrm{d}^3 r \, \left(\frac{\epsilon_0}{2}\chi^{(1)}\vec{E}^{(p)}\vec{E} + \frac{\epsilon_0}{3}\chi^{(2)}\vec{E}^{(p)}\vec{E}\vec{E}\right) \\
&= \int_V \mathrm{d}^3 r \, \left(\frac{\epsilon_0}{2}\sum_{ij}\chi^{(1)}_{ij}E^{(p)*}_i E_j + \frac{\epsilon_0}{3}\sum_{ijk}\chi^{(2)}_{ijk}E^{(p)*}_i E_j E_k\right),
\end{aligned} \tag{4.4}$$

where we explicitly labelled the incoming wave $\vec{E}^{(p)}$ and the ijk subscripts describe the polarization of the individual beams.[4]

The corresponding Hamiltonian is directly obtained from Eq. (4.4) by quantising the involved electric fields. Here we restrict ourselves to an interaction in one dimension, i.e. we assume a fully collinear propagation of the electric fields through the medium in a single spatial mode.[5] We first separate the quantized electric field into its positive and negative frequency parts:

$$\hat{E}(z,t) = \hat{E}^{(+)}(z,t) + \hat{E}^{(-)}(z,t) \tag{4.5}$$

[2] The $\chi^{(3)}$-nonlinearity enables four-wave-mixing. While it is not as strong as the $\chi^{(2)}$-nonlinearity has the advantage of being present in optical fibers [41, 42]. $\chi^{(4)}$ and even higher-order nonlinearities are, to our knowledge, currently not investigated.

[3] Out of the 32 different crystal classes 21 are noncentrosymmetric [43].

[4] More information on the polarization $\tilde{P}(t)$ and nonlinear optics in the classical regime is given in the book "Nonlinear Optics" by Robert W. Boyd [40].

[5] A three dimensional treatment of PDC in waveguides is given in Chap. 5.

Inside a nonlinear medium they are of the form [45]

$$\begin{aligned}\hat{E}^{(+)}(z,t) &= \hat{E}^{(-)\dagger}(z,t) \\ &= \imath \left(\frac{\hbar}{4\pi\epsilon_0 c\, A\, n(\omega_0)}\right)^{\frac{1}{2}} \int \mathrm{d}\omega\, \sqrt{\omega} \exp\left[\imath(k(\omega)z - \omega t)\right] \hat{a}(\omega), \end{aligned} \tag{4.6}$$

where A labels the transverse quantization area in the material [46]. Here we use the slowly varying envelope approximation, i.e. the bandwidth $\Delta\omega$ of the considered electric fields is small compared to their central frequency ω_0 ($\Delta\omega \ll \omega_0$) and hence move the dispersion term in front of the integral and treat it as a constant $n(\omega_0)$. This approximation is justified, since we only consider electric fields not too broad in frequency and take into account the rather flat dispersion in nonlinear crystals. Finally $\hat{a}(\omega)$ is the photon annihilation operator which destroys one photon at frequency ω and obeys:

$$\left[\hat{a}(\omega), \hat{a}(\omega')^\dagger\right] = \delta(\omega - \omega') \qquad [\hat{a}(\omega), \hat{a}(\omega')] = 0 \tag{4.7}$$

In our case we are not interested in the effects of free propagation and only regard the Hamiltonian of the nonlinear interaction inside the crystal.[6] It is given by the energy inside the material created by the pump, signal and idler fields interacting through the $\chi^{(2)}$-nonlinearity of the crystal [47, 40, 48]. According to Eq. (4.4) it reads[7]

$$\hat{H}(t) = \frac{\epsilon_0}{3} \sum_{ijk} \chi^{(2)}_{ijk} \int_{-\frac{L}{2}}^{\frac{L}{2}} \mathrm{d}z\, \hat{E}^{(p)}_i(z,t) \hat{E}_j(z,t) \hat{E}_k(z,t), \tag{4.8}$$

where we assume a crystal of length L extending from $-\frac{L}{2}$ to $\frac{L}{2}$. The $\chi^{(2)}_{ijk}$-tensor enables a multitude of nonlinear interactions in the medium. In the scope of this thesis we assume a propagation of all electric fields along one crystal axis. Depending on the applied crystal and its corresponding $\chi^{(2)}_{ijk}$-tensor, this leads to a variety of different polarizations interacting with each other. In quantum optics two distinct PDC processes are usually considered: in type-I PDC the signal and idler photons are emitted in the same polarization, whereas during type-II PDC the photon-pairs are generated into orthogonal polarizations and hence different optical modes.[8] In the scope of this thesis we restrict ourselves to a discussion of type-II PDC.[9] For type-II interactions the Hamiltonian reads

$$\hat{H}(t) = \frac{\epsilon_0}{3} \chi^{(2)} \int_{-\frac{L}{2}}^{\frac{L}{2}} \mathrm{d}z\, \hat{E}_p(z,t) \hat{E}_s(z,t) \hat{E}_i(z,t), \tag{4.9}$$

[6] Effectively this means that we move into the interaction picture (see Chap. 6).

[7] It is possible to have different constants in front of the Hamiltonian, $\epsilon_0/3$ in our case, depending on the exact definition of the electric fields and the energy density inside a nonlinear medium. In the scope of this thesis we use the conventions from "Nonlinear Optics" by Robert W. Boyd [40]

[8] In classical optics there also exists the notion of a type-0 process: In this special case the pump exhibits the same polarisation as signal and idler, whereas type-I describes a process where the pump polarization is orthogonal to the signal and idler polarization. This distinction, however, got lost during the transition of PDC into the quantum domain, where all process where signal and idler share the same polarizations are labelled as type-I processes, independently of the pump polarization.

[9] All the presented calculations in this thesis can be straightforwardly extended to type-I PDC. In most cases it is in fact easier to work with type-I PDC processes.

where the fact that the two created fields are of orthogonal polarization is highlighted by the two subscripts s and i for signal and idler fields. The term $\chi^{(2)}$ in this equation labels the corresponding nonlinearity. Finally we expand the electric fields into their positive and negative frequency parts, according to Eq. (4.5) and Eq. (4.6):

$$\begin{aligned}\hat{H}(t) = \frac{\epsilon_0}{3}\chi^{(2)} \int_{-\frac{L}{2}}^{\frac{L}{2}} \mathrm{d}z \, \left(\hat{E}_p^{(+)}(z,t) + \hat{E}_p^{(+)}(z,t)\right) \\ \times \left(\hat{E}_s^{(-)}(z,t) + \hat{E}_s^{(-)}(z,t)\right) \left(\hat{E}_i^{(-)}(z,t) + \hat{E}_i^{(-)}(z,t)\right)\end{aligned} \tag{4.10}$$

The $\hat{E}^{(+)}(z,t)$ terms include photon annihilation operators, whereas the $\hat{E}^{(-)}(z,t)$ terms involve photon creation operators. The eight resulting terms lead to a variety of different nonlinear processes. PDC stems from the operator combination describing the destruction of a pump photon and the creation of a signal and an idler photon and the reverse process where signal and idler photon fuse into a pump photon.[10] We obtain the PDC Hamiltonian:

$$\hat{H}_{PDC}(t) = \frac{\epsilon_0}{3}\chi^{(2)} \int_{-\frac{L}{2}}^{\frac{L}{2}} \mathrm{d}z \, \hat{E}_p^{(+)}(z,t)\hat{E}_s^{(-)}(z,t)\hat{E}_i^{(-)}(z,t) + h.c. \tag{4.11}$$

The remaining terms lead to processes such as frequency conversion [3, 49]. In the scope of this thesis, however, we use the rotating wave approximation [33], i.e. we assume that due to a properly adjusted pump only the PDC process is excited whereas the other nonlinear optical processes oscillate so fast that their net impact on the output state is zero.[11] This enables us to solely regard the parametric down-conversion terms of the nonlinear interaction neglecting the other nonlinear optical processes.

4.3. Modelling PDC using first-oder perturbation theory

In this chapter we treat the parametric down-conversion process using first-order perturbation theory. Firstly parametric down-conversion is a very inefficient process, depending on the $\chi^{(2)}$ nonlinearity and length of the crystal, only every 10^6 to 10^{11} pump photon decays into a photon-pair. Hence, in order to achieve a significant number of down-conversion events the incoming pump field has to be a bright wave. We consequently treat it as a classical field:

$$E_p^{(+)}(z,t) = E_p^{(-)*}(z,t) = A_p \int \mathrm{d}k \, \alpha\left[\omega(k)\right] \exp\left[\imath(kz - \omega(k)t)\right] \tag{4.12}$$

[10] The reverse process has to be included in order to form a hermitian Hamiltonian.

[11] The easiest way to see this is to perform the calculations from Sec. 4.3 with one of the three remaining Hamiltonians. The time-integration over the frequency mismatch between the three waves, must be zero to give an efficient interaction. When this is the case for the PDC Hamiltonian the frequency mismatch is far from zero for the other Hamiltonians. Performing the time-integration over these terms will consequently result in an integration over a fast oscillation, which yields zero. This fact enables us to only regard the PDC interactions, while neglecting the other processes.

Here A_p labels the pump amplitude and $\alpha\left[\omega(k)\right]$ its spectral distribution ranging from $\delta(\omega-\omega_c)$ for cw-laser sources up to more complicated forms in the case of ultrafast pulsed laser systems, which are in the main focus of this thesis. We also assume that the pump field is not depleted during propagation through the crystal, since only a minor part of the strong pump beam is lost during the PDC process. We obtain the unitary transformation

$$\hat{U}_{PDC} = \mathcal{T} \exp\left[-\frac{\imath}{\hbar}\int_{-\infty}^{\infty} \mathrm{d}t\, \hat{H}_{PDC}(t)\right], \tag{4.13}$$

where $\mathcal{T}$ is the time-ordering operator since the electric fields in the PDC Hamiltonian do not commute in time [50, 51]. We further extended the time-integration to plus and minus infinity, which is justified since we regard the state long after the nonlinear interaction in the medium.

In the Schrödinger picture the generated PDC state is given by the formula

$$|\psi\rangle_{PDC} = \hat{U}_{PDC}\,|0\rangle = \mathcal{T} \exp\left[-\frac{\imath}{\hbar}\int_{-\infty}^{\infty} \mathrm{d}t\, \hat{H}_{PDC}(t)\right]|0\rangle\,. \tag{4.14}$$

In most cases the nonlinear interaction during the process of PDC is not very strong and it is hence sufficient to perform a first-order expansion of Eq. (4.14)

$$|\psi\rangle_{PDC} \approx |0\rangle - \frac{\imath}{\hbar}\int_{-\infty}^{\infty} \mathrm{d}t\, \hat{H}_{PDC}(t)\,|0\rangle\,, \tag{4.15}$$

which gives us the emitted, but *not* normalized two-photon PDC state.[12] Following the presentation in [37, 38, 39] and combining Eq. (4.6), (4.11), (4.12) and (4.15), we arrive at

$$\begin{aligned}\int_{-\infty}^{\infty} \mathrm{d}t\, \hat{H}_{PDC}(t) = B\int_{-\infty}^{\infty}\mathrm{d}t \int_{-\frac{L}{2}}^{\frac{L}{2}}\mathrm{d}z \iiint \mathrm{d}\omega_p \mathrm{d}\omega_s \mathrm{d}\omega_i\, \alpha(\omega_p) \exp\left[-\imath\left(\omega_p-\omega_s-\omega_i\right)t\right] \\ \times \exp\left[\imath\left(k_p(\omega_p)-k_s(\omega_s)-k_i(\omega_i)\right)z\right] \hat{a}^\dagger(\omega_s)\hat{b}^\dagger(\omega_i) + h.c.\,,\end{aligned} \tag{4.16}$$

where we merged all constants into an overall factor B and mark the signal and idler creation operators $\hat{a}^\dagger(\omega_s)$ and $\hat{b}^\dagger(\omega_i)$ respectively.[13] Performing the z-integration we obtain:

$$\begin{aligned}\int_{-\infty}^{\infty} \mathrm{d}t\, \hat{H}_{PDC}(t) = B\int_{-\infty}^{\infty}\mathrm{d}t \iiint \mathrm{d}\omega_p \mathrm{d}\omega_s \mathrm{d}\omega_i\, \alpha(\omega_p) \exp\left[-\imath\left(\omega_p-\omega_s-\omega_i\right)t\right] \\ \times L\,\mathrm{sinc}\left[\left(k_p(\omega_p)-k_s(\omega_s)-k_i(\omega_i)\right)\frac{L}{2}\right] \hat{a}^\dagger(\omega_s)\hat{b}^\dagger(\omega_i) + h.c.\end{aligned} \tag{4.17}$$

[12] Higher order expansion terms are discussed in Chap. 6.

[13] Sometimes signal and idler are operators are labelled $\hat{a}_s^\dagger(\omega_s)$ and $\hat{a}_i^\dagger(\omega_i)$ as well. For the sake of consistency, however, we choose the $\hat{a}^\dagger(\omega_s)$ and $\hat{b}^\dagger(\omega_i)$ convention.

The integration over the time-dependence t results in a delta function $2\pi\delta(\omega_p - \omega_s - \omega_i)$ and we subsequently perform the integral over the pump frequencies ω_p:

$$\int_{-\infty}^{\infty} \mathrm{d}t\, \hat{H}_{PDC}(t) = B' \iint \mathrm{d}\omega_s\, \mathrm{d}\omega_i\, \alpha(\omega_s + \omega_i) \times L\, \mathrm{sinc}\left[\Delta k(\omega_s, \omega_i)\frac{L}{2}\right] \hat{a}^\dagger(\omega_s)\hat{b}^\dagger(\omega_i) + h.c. \tag{4.18}$$

Here we have introduced the shorthand relation $\Delta k(\omega_s, \omega_i) = k_p(\omega_s+\omega_i) - k_s(\omega_s) - k_i(\omega_i)$ and $B' = 2\pi B$. Using Eq. (4.15) and Eq. (4.18), we are able to write down the *not* normalized PDC state as:

$$\begin{aligned} |\psi\rangle_{PDC} &= |0\rangle + B' \iint \mathrm{d}\omega_s \mathrm{d}\omega_i\, \alpha(\omega_s + \omega_i) \underbrace{\mathrm{sinc}\left[\Delta k\,(\omega_s, \omega_i)\,\frac{L}{2}\right]}_{\Phi(\omega_s,\omega_i)} \hat{a}^\dagger(\omega_s)\hat{b}^\dagger(\omega_i)\,|0\rangle \\ &= |0\rangle + B' \iint \mathrm{d}\omega_s \mathrm{d}\omega_i\, \alpha(\omega_s + \omega_i)\Phi(\omega_s, \omega_i)\hat{a}^\dagger(\omega_s)\hat{b}^\dagger(\omega_i)\,|0\rangle \\ &= |0\rangle + B' \iint \mathrm{d}\omega_s \mathrm{d}\omega_i\, f(\omega_s, \omega_i)\hat{a}^\dagger(\omega_s)\hat{b}^\dagger(\omega_i)\,|0\rangle \end{aligned} \tag{4.19}$$

The overall efficiency of the down-conversion process is given by the constant $B' \propto A_p L$, which depends linearly on the crystal length L and the field amplitude A_p of the pump field.

The created photon-pairs feature an intricate spectral structure dependent on the joint-spectral-amplitude (JSA) $f(\omega_s, \omega_i)$ consisting of two terms: the pump distribution $\alpha(\omega_s+\omega_i)$ and the phase-matching function $\Phi(\omega_s, \omega_i)$. The pump distribution represents the energy conservation condition $\omega_p = \omega_s + \omega_i$ and is defined by the incoming pump wave. The phase-matching function results from momentum conservation $k_p(\omega_p) = k_s(\omega_s) + k_i(\omega_i)$ and is dependent on the dispersion properties of the applied material and the length of the crystal (see Fig. 4.2).

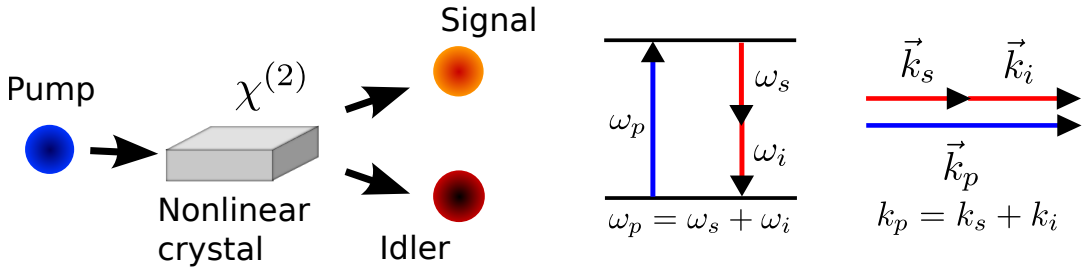

Figure 4.2.: In the PDC process the spectral properties of the generated photon-pair are constrained by momentum and energy conservation between the three interacting photons, which yield the joint spectral distribution $f(\omega_s, \omega_i)$ of the signal and idler photon-pair.

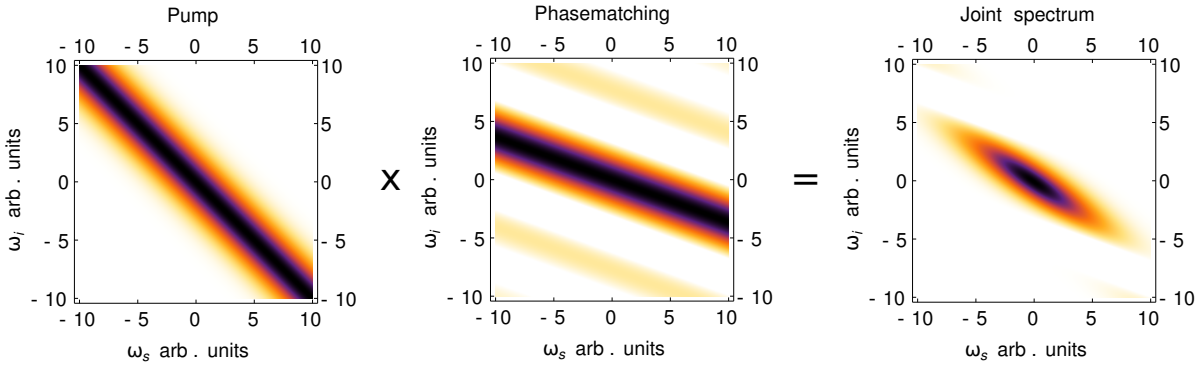

Figure 4.3.: Exemplary pump spectrum $\alpha(\omega_s + \omega_i)$, phase-matching function $\Phi(\omega_s, \omega_i)$ and joint-spectral amplitude distribution $f(\omega_s, \omega_i)$ of a generic PDC state.

In Fig. 4.3 we plotted the three functions for a generic PDC process. Due to the energy conservation condition the pump distribution $\alpha(\omega_s + \omega_i)$ is always aligned along the $-45°$ axis, where the width of the function gives the width of the applied pump laser. In the case of a continuous-wave (cw) laser source it is a line which gets broader when pulsed laser systems are applied. The slope of the phase-matching function $\Phi(\omega_s, \omega_i)$ is dependent on the group velocities of the three interacting waves — pump, signal and idler — in the medium and can, in principle, feature any angle [52]. Its width is given by the length of the nonlinear crystal. The longer the crystal the narrower the phase-matching function. Together they form the joint-spectral distribution function $f(\omega_s, \omega_i)$ describing the spectral properties of the generated photon pairs.

In order to simplify further calculations with the two-photon PDC state the sinc structure of the phase-matching function $\Phi(\omega_s, \omega_i)$ is often approximated by a Gaussian distribution of the form [52]

$$\operatorname{sinc}(x) \approx \exp\left(-\gamma x^2\right) \qquad \gamma \approx 0.193. \tag{4.20}$$

Eq. (4.20) enables us to rewrite the PDC output state in Eq. (4.19) as:

$$|\psi\rangle_{PDC} = |0\rangle + B' \iint \mathrm{d}\omega_s \mathrm{d}\omega_i \, \alpha(\omega_s + \omega_i) \underbrace{\exp\left[-\gamma \left(\Delta k\left(\omega_s, \omega_i\right) \frac{L}{2}\right)^2\right]}_{\Phi(\omega_s, \omega_i)} \hat{a}^\dagger(\omega_s) \hat{b}^\dagger(\omega_i) \, |0\rangle \tag{4.21}$$

For Gaussian pump pulses, as created by our ultrafast laser systems, this approximation of the sinc function recasts the joint-spectral-amplitude distribution $f(\omega_s, \omega_i)$ into a two-dimensional Gaussian distribution, which is mathematically much easier to handle [53, 52].

4.3.1. Normalizing PDC states

One major drawback of the PDC state in Eq. (4.19) is the fact that the state is *not* normalized, since we truncated the perturbation expansion after the first order. Furthermore the vacuum term of the zero-oder perturbation expansion does not give any insights into the process properties. It is hence very common to renormalise the quantum state from Eq. (4.19) by post-selecting on a successful detection of a photon pair. This enables us to drop the vacuum component and renormalise the quantum state by adding a normalization constant in front of the two-photon term. We obtain

$$|\psi\rangle_{PDC} = \frac{1}{\sqrt{N}} \iint \mathrm{d}\omega_s \mathrm{d}\omega_i \, f(\omega_s, \omega_i) \hat{a}^\dagger(\omega_s) \hat{b}^\dagger(\omega_i) \, |0\rangle \,, \tag{4.22}$$

with N being the normalization factor defined as:

$$N = \iint \mathrm{d}\omega_s \, \mathrm{d}\omega_i \; |f(\omega_s, \omega_i)|^2 \tag{4.23}$$

4.4. Ultrafast PDC in the broadband mode picture

In the scope of this thesis we consider ultrafast PDC, i.e. PDC processes pumped by ultrafast lasers systems. The created spectral distribution function $f(\omega_s, \omega_i)$ of the ultrafast PDC state in Eq. (4.22) conceals an intricate mode structure, caused by the spectral correlations between signal and idler. In order to reveal it we have to perform a Schmidt or singular-value decomposition [54] (see App. A) of the joint-spectral-amplitude $\frac{1}{\sqrt{N}} f(\omega_s, \omega_i)$ and rewrite PDC in the so-called broadband mode picture [55, 37, 52, 56]:

$$\frac{1}{\sqrt{N}} f(\omega_s, \omega_i) = \sum_k \lambda_k \psi_k(\omega_s) \phi_k(\omega_i) \tag{4.24}$$

Here $\{\psi_k(\omega_s)\}$ and $\{\phi_k(\omega_i)\}$ each form a complete and orthonormal basis set whereas the λ_k are real positive values ($\lambda_k \in \mathbb{R}_0^+$) . Since $\frac{1}{\sqrt{N}} f(\omega_s, \omega_i)$ is a normalized distribution the λ_k values satisfy $\sum_k \lambda_k^2 = 1$.

Using Eq. (4.22) and Eq. (4.24) we rewrite the PDC state as

$$\begin{aligned}
|\psi\rangle_{PDC} &= \iint \mathrm{d}\omega_s \mathrm{d}\omega_i \sum_k \lambda_k \psi_k(\omega_s) \phi_k(\omega_i) \hat{a}^\dagger(\omega_s) \hat{b}^\dagger(\omega_i) \, |0\rangle \\
&= \sum_k \lambda_k \underbrace{\int \mathrm{d}\omega_s \psi_k(\omega_s) \hat{a}^\dagger(\omega_s)}_{\hat{A}_k} \underbrace{\int \mathrm{d}\omega_i \phi_k(\omega_i) \hat{b}^\dagger(\omega_i)}_{\hat{B}_k} \, |0\rangle \\
&= \sum_k \lambda_k \hat{A}_k^\dagger \hat{B}_k^\dagger \, |0\rangle \,,
\end{aligned} \tag{4.25}$$

where we defined the new broadband mode operators [37, 52, 56]:

$$\hat{A}_k^\dagger = \int \mathrm{d}\omega_s \, \psi_k(\omega_s) \hat{a}^\dagger(\omega_s) \qquad \hat{B}_k^\dagger = \int \mathrm{d}\omega_i \, \phi_k(\omega_i) \hat{b}^\dagger(\omega_i) \tag{4.26}$$

These broadband photon creation operators $\hat{A}_k^\dagger$ and $\hat{B}_k^\dagger$, behave exactly as the standard monochromatic operators $\hat{a}^\dagger(\omega)$ and $\hat{b}^\dagger(\omega)$:

$$\left[\hat{a}(\omega), \hat{a}^\dagger(\omega')\right] = \delta_{\omega\omega'} \qquad \left[\hat{A}_k, \hat{A}_l^\dagger\right] = \delta_{kl} \tag{4.27}$$

The only difference is that $\hat{a}(\omega)$ creates a photon at the specific frequency ω whereas $\hat{A}_k$ creates a single photon into the broadband mode $\psi_k(\omega_s)$. The switch between the two representations is identical to a basis transformation from an operator basis using monochromatic frequencies to a set of broadband modes spanning the frequency range.

Rewriting the PDC state using broadband mode operators reveals its internal structure. According to Eq. (4.25) PDC emits two photons into a superposition of ultrafast pulse modes $\hat{A}_k$ and $\hat{B}_k$. This ultrafast multi-mode structure of PDC is sketched in Fig. 4.4.

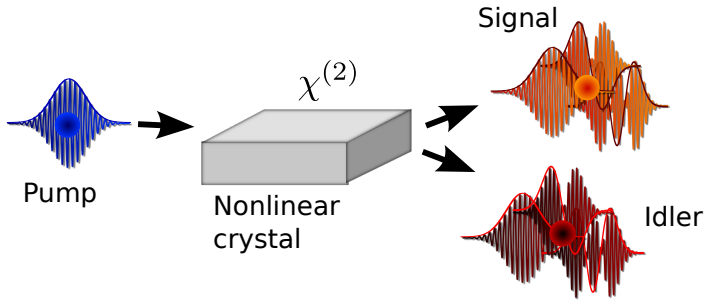

Figure 4.4.: Including the frequency degree of freedom into the description of ultrafast PDC, the pump photon featuring a certain spectral distribution decays into two photons forming a superposition of ultrafast optical pulse modes.

If the signal photon is detected in mode $\hat{A}_k$ the idler photon will be found the corresponding optical mode $\hat{B}_k$. The *effective* number of optical modes K in a PDC state is given via the relation [57, 58]:

$$K = \frac{1}{\sum_k \lambda_k^4} \tag{4.28}$$

$K = 1$ describes the PDC state with exactly one single frequency mode $|\psi\rangle = \hat{A}_0^\dagger \hat{B}_0^\dagger |0\rangle$.

For values $K \geq 1$ the created photon-pair is entangled in frequency since the detection of a idler photon in a specific mode $\hat{B}_k$ immediately reveals that the corresponding signal photon is located in the corresponding $\hat{A}_k$ mode. Rising numbers of K indicate higher and higher amounts of frequency entanglement. The overall amount of frequency entanglement in a given PDC states can be quantified via the entropy of entanglement:

$$S = -\sum_k \lambda_k^2 \log \lambda_k^2 \tag{4.29}$$

It is directly dependent on the shape of the joint spectral amplitude function $f(\omega_s, \omega_i)$. If the joint spectral amplitude $f(\omega_s, \omega_i)$ assumes a circular form or an elliptical distribution

oriented along the signal or idler axis the Schmidt decomposition will yield exactly a single optical mode for signal and idler each since the photons are not correlated in frequency. Detecting the signal photon at a certain frequency ω_s does not reveal any information about the frequency of the idler photon. However, as soon as the frequency spectrum between signal and idler becomes correlated the Schmidt decomposition will yield higher-order terms, the created photon pair is frequency entangled. For more details, please have a look at the papers [37, 52].

4.5. Quasi phase-matching

In the process of PDC it is vital to have a fine degree of control over the created signal and idler wavelengths. Depending on the application it is necessary to create both photons in the telecom regime, at 1550 nm, for transmission with minimal losses over long distances, or both at 800 nm enabling efficient detection, or signal at 1550 nm and idler at 800 nm to bridge the gap between the two wavelengths. Sometimes other, more "exotic", wavelengths like 532 nm and 1330 nm have to be generated as well.

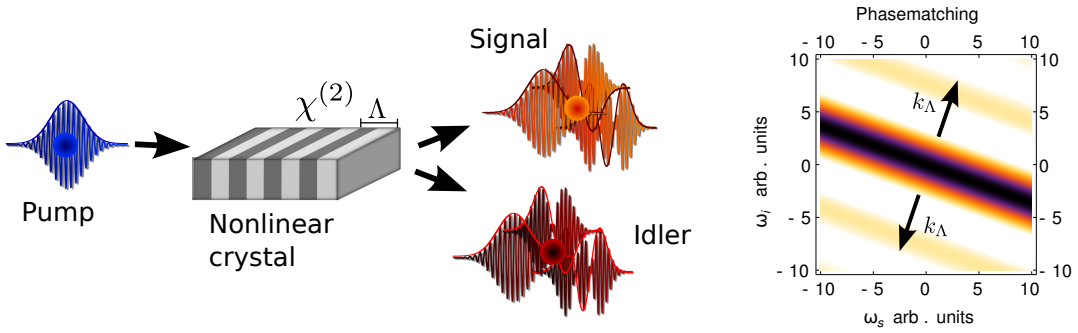

Figure 4.5.: A periodic modulation of the $\chi^{(2)}$ nonlinearity of the crystal enables an almost arbitrary displacement of the phasematching function $\Phi(\omega_s, \omega_i)$ in frequency space.

Unfortunately it is not straightforward to tune the joint-spectral-amplitude $f(\omega_s, \omega_i)$ of a given down-conversion process. While the pump function $\alpha(\omega_s+\omega_i)$ is easily adjusted by modifying the pump wavelength the position of phase-matching function $\Phi(\omega_s, \omega_i)$ is dependent on the dispersion inside the medium, which introduces a severe restriction of the available signal and idler frequencies.

To resolve this issue quasi-phase-matching was proposed in 1962, by Armstrong et. al. [59] (see Fig. 4.5). In this process an additional k-vector k_Λ is introduced in the phase mismatch $\Delta k(\omega_s, \omega_i)$ which enables an (almost) arbitrary placement of the phase-matching function in frequency space [60]. This is achieved by a periodic modulation of the crystal nonlinearity $\chi^{(2)}(z)$, i.e. the Hamiltonian from Eq. (4.11) reads:

$$\hat{H}_{PDC}(t) = \frac{\epsilon_0}{3} \int_{-\frac{L}{2}}^{\frac{L}{2}} \mathrm{d}z\, \chi^{(2)}(z) \hat{E}_p^{(+)}(z,t) \hat{E}_s^{(-)}(z,t) \hat{E}_i^{(-)}(z,t) + h.c. \tag{4.30}$$

In order to understand the physical impact of this periodic variation of $\chi^{(2)}(z)$ it is useful to consider the simplest case of a sinusoidal $\chi^{(2)}(z)$ variation with a period of Λ:

$$\chi^{(2)}(z) = \chi_0^{(2)} \sin\left(\frac{2\pi}{\Lambda} z\right) = \chi_0^{(2)} \frac{1}{2\imath} \left[\exp\left(\imath \frac{2\pi}{\Lambda} z\right) - \exp\left(-\imath \frac{2\pi}{\Lambda} z\right)\right] \tag{4.31}$$

The calculations from Sec. 4.3 using the Hamiltonian in Eq. (4.30) with $\chi^{(2)}(z)$ as given in Eq. (4.31) modify Eq. (4.11) to:

$$\begin{aligned}\int_{-\infty}^{\infty} \mathrm{d}t\, \hat{H}_{PDC}(t) = B' \int_{-\infty}^{\infty} \mathrm{d}t \int_{-\frac{L}{2}}^{\frac{L}{2}} \mathrm{d}z \iiint \mathrm{d}\omega_p \mathrm{d}\omega_s \mathrm{d}\omega_i\, \alpha(\omega_p) \exp\left[-\imath\left(\omega_p - \omega_s - \omega_i\right) t\right] \\ \times \frac{1}{2\imath} \left(\exp\left[\imath \left(k_p(\omega_p) - k_s(\omega_s) - k_i(\omega_i) + \frac{2\pi}{\Lambda}\right) z\right] \right. \\ \left. - \exp\left[\imath \left(k_p(\omega_p) - k_s(\omega_s) - k_i(\omega_i) - \frac{2\pi}{\Lambda}\right) z\right]\right) \\ \times \hat{a}^\dagger(\omega_s) \hat{b}^\dagger(\omega_i) + h.c.\end{aligned} \tag{4.32}$$

The created PDC state reads:

$$\begin{aligned}|\psi\rangle_{PDC} = |0\rangle + B' \iint \mathrm{d}\omega_s \mathrm{d}\omega_i\, \alpha(\omega_s + \omega_i) \\ \times \frac{1}{2\imath} \left[\mathrm{sinc}\left(\left[\Delta k\left(\omega_s, \omega_i\right) + \frac{2\pi}{\Lambda}\right] \frac{L}{2}\right) - \mathrm{sinc}\left(\left[\Delta k\left(\omega_s, \omega_i\right) - \frac{2\pi}{\Lambda}\right] \frac{L}{2}\right)\right] \\ \times \hat{a}^\dagger(\omega_s) \hat{b}^\dagger(\omega_i) |0\rangle\end{aligned} \tag{4.33}$$

From Eq. (4.33) it is evident that the inclusion of periodic poling modifies the k-vector mismatch Δk about $k_\Lambda = \pm\frac{2\pi}{\Lambda}$. In consequence the phase-matching function is split into two parts which are shifted into opposite directions from the original position. With an accordingly adjusted pump it is possible to select only one of the two new phase-matching functions which enables us to to drop the second term. We remain with:

$$\begin{aligned}|\psi\rangle_{PDC} = |0\rangle + B' \frac{1}{2\imath} \iint \mathrm{d}\omega_s \mathrm{d}\omega_i\, \alpha(\omega_s + \omega_i) \\ \times \mathrm{sinc}\left(\left[\Delta k\left(\omega_s, \omega_i\right) + \frac{2\pi}{\Lambda}\right] \frac{L}{2}\right) \hat{a}^\dagger(\omega_s) \hat{b}^\dagger(\omega_i) |0\rangle\end{aligned} \tag{4.34}$$

This allows the (almost) arbitrary displacement of the phase-matching function in frequency space and consequently the engineering of arbitrary signal and idler frequencies independent of the applied material. The quasi-phase-matching however comes at a cost. Since the phasematching function is split into two its amplitude is scaled down by a factor of 1/2 and each process consequently features a reduced photon-pair generation rate.

Furthermore it is currently not possible to produce a sinusoidal $\chi^{(2)}$-modulation. In practice rectangular variations of $\chi^{(2)}$ are created via the process of periodic poling. In

this procedure the $\chi^{(2)}$ nonlinearity is periodically inverted via the application of strong electric fields [61]. The resulting $\chi^{(2)}$ modulation is a square-wave function which reads:

$$\begin{aligned}\chi^{(2)}(z) &= \chi_0^{(2)}\mathrm{sgn}\left(\sin(z)\right) \\ &= \chi_0^{(2)}\frac{4}{\pi}\sum_{k=1}^{\infty}\frac{1}{(2k-1)}\sin\left(\frac{2\pi(2k-1)}{\Lambda}z\right) \\ &= \chi_0^{(2)}\frac{4}{\pi}\sum_{k=1}^{\infty}\frac{1}{(2k-1)}\frac{1}{2\imath}\left[\exp\left(\imath\frac{2\pi(2k-1)}{\Lambda}z\right)-\exp\left(-\imath\frac{2\pi(2k-1)}{\Lambda}z\right)\right] \quad (4.35)\end{aligned}$$

From its Fourier expansion in Eq. (4.35) it is evident that a rectangular periodic inversion of $\chi^{(2)}$ introduces a variety of different additional k_Λ vectors, yet with ever decreasing down-conversion efficiency scaling with $1/(2k-1)$. The first term $k=1$ directly corresponds to the discussed sinusoidal poling, whereas higher-oder terms introduce increasing quasi-phase-matching vectors $k_\Lambda = [2\pi(2k-1)]/\Lambda$.

4.6. Conclusion

The presented theoretical model of ultrafast PDC is the current workhorse for almost all experimental implementation of PDC. The first-order perturbation theory offers a straightforward modelling of the process, especially its spectral structure, while still being precise enough to describe the majority of experimental setups. Furthermore the broadband mode formalism gives direct access to the inherent ultrafast pulse mode structure of the parametric down-conversion process and enables us to evaluate the generated frequency entanglement. Finally quasi-phase-matching enables a tuning of the signal and idler wavelenghts via a displacement of the phase-matching function in frequency space. This theoretical description forms the basis for our investigations of PDC and, in the remainder of this thesis, we will successively expand the presented ideas and concepts.

Wisdom begins in wonder.

(Socrates)

5. Spatial modes in waveguided PDC

5.1. Introduction

The first PDC experiments where performed using bulk crystals and, to date, these bulk crystal PDC sources are still the most common method to create PDC states. In the past years, however, attention has fallen on enhancing the down-conversion process using waveguiding structures.[1]

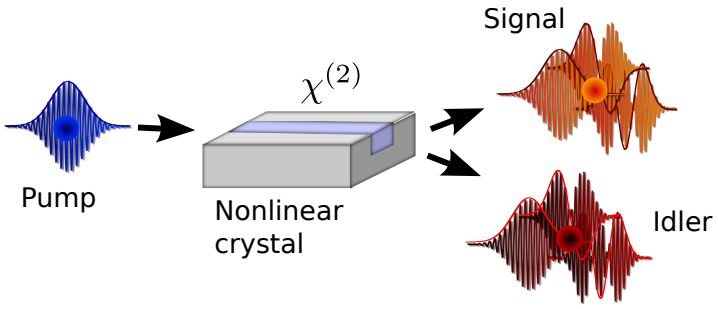

Figure 5.1.: Sketch of waveguided parametric down-conversion: A waveguide channels the light through the material, which gives rise to an enhanced down-conversion rate and a collinear propagation of all involved fields in well defined spatial modes.

The principle of waveguided PDC is sketched in Fig. 5.1: A waveguide channels the light through the nonlinear crystal which restricts the pump, signal and idler fields to a well-defined set of spatial modes. This provides a straightforward method to control the spatial emission pattern from bulk-crystal down-converters and, due to the tight confinement of the fields inside the waveguide, leads to an enhanced down-conversion efficiency [23, 62, 63, 64, 38, 65].

[1] This chapter is a summary of the paper "Spatial modes in waveguided parametric down-conversion" by Andreas Christ, Kaisa Laiho, Andreas Eckstein, Thomas Lauckner, Peter J. Mosley, and Christine Silberhorn [1] and the paper "Direct Measurement of the Spatial-Spectral Structure of Waveguided Parametric Down-Conversion" by Peter J. Mosley, Andreas Christ, Andreas Eckstein, and Christine Silberhorn [2].

5.2. Theory of PDC in waveguides

The first challenge when analysing PDC in waveguides is to calculate the eigenmodes of the system. Depending on the geometry of the waveguide, there exist various approaches: Assuming rectangular or circular waveguides with perfect conducting edges[2] is the most simplistic model and possesses an analytic solution. Including the effects of finite refractive index steps Δn a completely analytical solution is not possible any more, but a semi-analytical approach, as presented in [66], has to be applied. As soon as more complex waveguide geometries, such as non-rectangular waveguide structures with slowly varying refractive indices Δn are considered, full numerical theories have to be utilized. Mode solving techniques based on finite elements approaches [67] are common and various software packages are available for this purpose.

Having derived the eigenmodes $f^{(k)}(x,y)$ of the waveguide we are able to write down the quantized signal and idler fields in a straightforward extension of Eq. (4.6) [68]

$$\hat{E}^{(+)}_{s,i}(\vec{r},t) = \hat{E}^{(-)\dagger}_{s/i}(\vec{r},t) = A\sum_k f^{(k)}_{s,i}(x,y)\int \mathrm{d}\omega_{s,i}\exp\left[\imath\left(\beta^{(k)}_{s,i}(\omega_{s,i})z-\omega_{s,i}t\right)\right]\hat{a}^{(k)}/\hat{b}^{(k)}(\omega_{s,i}), \tag{5.1}$$

where we, similar to the frequency degree of freedom, sum over all individual waveguide modes $f^{(k)}_{s,i}(x,y)$ with corresponding longitudinal propagation vectors $\beta^{(k)}_{s,i}$. Here we neglect the frequency dependence in the spatial mode distributions $f^{(k)}_{s,i}(x,y)$, because we assume fields which are not too broad in frequency $\Delta\omega \ll \omega$. Further note that both the spatial field distribution $f^{(k)}_{s,i}(x,y)$ and the effective k-vector $\beta^{(k)}_{s,i}$ are dissimilar for the signal and idler, due to their varying wavelengths and polarizations.

Again we treat the strong pump field as a classical wave:

$$E^{(+)}_p(\vec{r},t) = E^{(-)*}_p(\vec{r},t) = A\sum_k f^{(k)}_p(x,y)\int \mathrm{d}\omega_p\,\alpha(\omega_p)\exp\left[\imath\left(\beta^{(k)}_p(\omega_p)z-\omega_p t\right)\right] \tag{5.2}$$

To calculate the two-photon state emitted during the process of waveguided parametric down-conversion we extend the PDC Hamiltonian in Eq. (4.11) to include the transverse degrees of freedom:

$$\hat{H}_{PDC}(t) = \frac{\epsilon_0}{3}\chi^{(2)}\int_V \mathrm{d}^3r\,\hat{E}^{(+)}_p(\vec{r},t)\hat{E}^{(-)}_s(\vec{r},t)\hat{E}^{(-)}_i(\vec{r},t) + h.c. \tag{5.3}$$

Following the discussion in Chap. 4 and using Eq. (5.1), Eq. (5.3) and Eq. (5.2) we arrive at the normalized waveguided PDC state:

$$|\psi\rangle_{PDC} = \frac{1}{\sqrt{N}}\sum_{klm} A_{klm}\iint \mathrm{d}\omega_s\mathrm{d}\omega_i\, f_{klm}(\omega_s,\omega_i)\hat{a}^{(l)\dagger}(\omega_s)\hat{b}^{(m)\dagger}(\omega_i)\,|0\rangle \tag{5.4}$$

[2]This corresponds to the mathematical analog of modes inside an infinitely deep potential well.

Here the joint spatio-spectral distribution $f_{klm}(\omega_s, \omega_i)$, of the created photon-pair, is defined as:

$$f_{klm}(\omega_s, \omega_i) = \alpha(\omega_s + \omega_i)\mathrm{sinc}\left[\Delta\beta_{klm}\left(\omega_s, \omega_i\right)\frac{L}{2}\right] \tag{5.5}$$

Taking into account the spatial degree of freedom in waveguided PDC, the created photon-pair is not only emitted into a superposition of frequencies ω_s and ω_i, but also into a superposition of spatial modes l and m, where the spatial and spectral degree of freedom are connected via the phase-mismatch $\Delta\beta_{klm}(\omega_s, \omega_i)$:

$$\Delta\beta^{(klm)}(\omega_s, \omega_i) = \beta_p^{(k)}(\omega_p) - \beta_s^{(l)}(\omega_s) - \beta_i^{(m)}(\omega_i) \tag{5.6}$$

This phase-mismatch $\Delta\beta^{(klm)}(\omega_s, \omega_i)$ translates different interacting spatial mode triplets of pump k, signal l and idler m into distinct signal and idler spectra. Furthermore a new overlap integral over the three interacting spatial modes appears:

$$A_{klm} = \iint \mathrm{d}x\mathrm{d}y\, f_p^{(k)}(x, y) f_s^{(l)*}(x, y) f_i^{(m)*}(x, y) \tag{5.7}$$

Hence the efficiency of the down-conversion is dependent on the spatial shapes of the interacting mode triplet. If pump, signal and idler propagate in similar modes the output state will be generated with high efficiency, but if signal and idler are dissimilar the photon pair generation efficiency will be strongly suppressed.

The derived PDC state exiting the waveguiding structure in Eq. (5.4) enables us, for the first time, to accurately model, predict and engineer the PDC process in waveguiding structures including both the spatial and the spectral degree of freedom. Depending on the application it is either necessary to ensure a spatially single-mode behaviour, for example for the heralding of single-photons from PDC (see Chap. 7), or we are able to harness the spatial degree of freedom for advanced quantum state preparation techniques, such as the creation of quantum states hyperentangled in the spatial and spectral domain [2].

5.3. Experimental investigation

In order to probe the validity of our theoretical description of waveguided PDC we put our model to the test in the laboratory and measured the spectral and spatial distribution of a spatially and spectrally multi-mode waveguided PDC source.

Fig. 5.2 (a) shows the observed spectral distribution of the signal and idler photons. The labels A to E mark the individual down-conversion processes. Each peak stems from a different triplet of interacting spatial pump, signal and idler modes, which shift the spectrum into its distinct positions. The corresponding observed spatial modes of signal and idler are presented in Fig. 5.2. These measurements are the first direct observation of the interplay between the spatial and spectral degree of freedom in waveguided PDC and in very good accordance with our theory (see [2] for details).

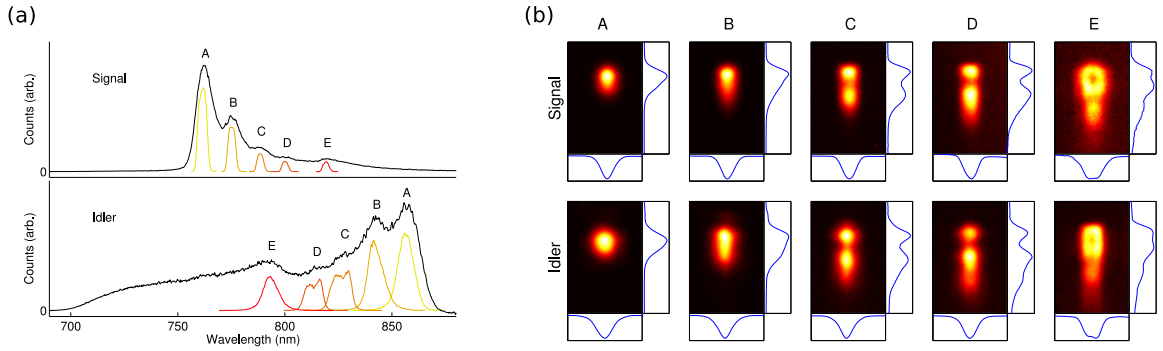

Figure 5.2.: (a) Spectrum of signal and idler photons in spatially multi-mode waveguided PDC. Each peak from A to E corresponds to a down-conversion process in different spatial modes, which shift the spectrum into the individual positions. (b) Spatial modes of the individual down-conversion processes. It is evident that higher spatial modes lead to an increasing shift in frequency with respect to the PDC process in the fundamental mode (A) [2].

5.4. Conclusion

In conclusion we developed a theoretical model of waveguided PDC, in the two-photon picture, taking into account both the spectral *and* spatial degree of freedom [1]. Our investigations revealed an intricate interplay between the spatial *and* spectral degree of freedom, which enables the design of spatially single-mode PDC sources, e.g. for the heralding pure single photon states and can be be harnessed to generate photon states hyperentangled in the spatial and spectral degree of freedom. Our theoretical investigations lead to the first direct observation of the spatial-spectral coupling in waveguided PDC [2] and has already been extended to describe two-photon quantum walks in waveguide arrays [35].

Spatial modes in waveguided parametric down-conversion

Andreas Christ,* Kaisa Laiho, Andreas Eckstein, Thomas Lauckner, Peter J. Mosley, and Christine Silberhorn
Max Planck Institute for the Science of Light, Günther-Scharowsky-Str. 1/Building 24, 91058 Erlangen, Germany
(Received 29 April 2009; published 18 September 2009)

The propagation of several spatial modes has a significant impact on the structure of the emission from parametric down-conversion in a nonlinear waveguide. This manifests itself not only in the spatial correlations of the photon pairs but also, due to new phase-matching conditions, in the output spectrum, radically altering the degree of entanglement within each pair. Here we investigate both theoretically and experimentally the results of higher-order spatial-mode propagation in nonlinear waveguides. We derive conditions for the creation of pairs in these modes and present observations of higher-order mode propagation in both the spatial and spectral domains. Furthermore, we observe correlations between the different degrees of freedom and finally we discuss strategies for mitigating any detrimental effects and optimizing pair production in the fundamental mode.

DOI: 10.1103/PhysRevA.80.033829 PACS number(s): 42.65.Tg, 42.50.Dv, 42.50.Ex

I. INTRODUCTION

The process of parametric down-conversion (PDC) is widely used in quantum optics and quantum information as a source of photon pairs. These photon pairs are generated inside a nonlinear crystal when a pump photon decays into signal and idler photons; typically the signal photon is used to herald the availability of an idler photon that can be used in subsequent experiments. The distribution of the pump photon energy between the daughter photons is determined by momentum conservation or, using the language common in optics, by the phase-matching conditions.

After some initial discussion, experiments have demonstrated that for PDC in bulk crystals the orbital angular momentum (OAM) of the pump beam is conserved [1,2]. Hence, by controlling the spatial mode of the interacting beams a new degree of freedom becomes available for quantum information processing. It can be used to generate mode-entangled [2,3] and even hyperentangled biphoton states for quantum metrology [4] or quantum information-processing applications [5,6].

In recent years attention has fallen on PDC in waveguiding structures [7–10]. The resulting implicit spatial-mode control has significant benefits for photon-pair production. Due to the tight confinement of the fields inside the waveguide (WG) the effective down-conversion rate into useful spatial modes increases substantially. This, in turn, allows such sources to be pumped at greatly reduced power levels while still achieving high photon fluxes relative to bulk crystal down-converters. In the ideal case only the fundamental spatial mode is present, and the waveguide output is naturally suited for efficient coupling to fibers yielding a robust high-brightness photon-pair source.

However, real-world waveguide sources usually deviate significantly from this ideal. Typical waveguides support the propagation of several spatial modes for the interacting pump, signal, and idler photons which can assume any of the spatial modes guided at their respective wavelengths [11]. In the standard case of a roughly rectangular waveguide, the radial symmetry of the system is broken and hence the OAM conservation condition is reduced to that of parity conservation between the spatial modes of the three fields. Therefore OAM is no longer a useful parameter. Instead the fields must be decomposed into the waveguide transverse field mode solutions.

In addition to the modification of the spatial characteristics introduced by the waveguide, the spectral properties of the PDC process are also affected. The energy distribution between the signal and idler photons, and hence their wavelengths, is governed by the phase matching of the longitudinal components of the wave vector. Every spatial mode corresponds to a different transverse—and therefore also longitudinal—momentum, so for every set of three spatial modes of pump, signal, and idler we observe photon pairs with a specific distribution of wavelengths. The resulting output from the waveguide contains many of these distributions coherently superimposed on one another. For various applications this can be a significant problem if a heralded single photon in a single well-defined spatiotemporal mode is needed. Likewise second-harmonic generation (SHG), the reverse process of PDC, is affected.

In this paper, we present a study of the impact of discrete spatial-mode structure on PDC in a nonlinear waveguide. We consider the connection between the spatial and spectral degrees of freedom as well as both the challenges and benefits that arise from using a waveguided PDC photon-pair source in quantum information processing. In Secs. II and III we present the theoretical groundwork for dealing with discrete spatial modes in PDC. In Sec. IV we investigate the spatiospectral mode structure of our waveguide utilizing SHG. We present experimental results on the spectral impact of spatial multi-mode PDC and theoretical predictions in Sec. V. Section VI discusses our findings with respect to spatiospectral correlations.

II. THEORETICAL BACKGROUND

We analyze the process of PDC in the interaction picture. In order to derive the two-photon state of the down-

*andreas.christ@mpl.mpg.de; URL: http://mpl.mpg.de

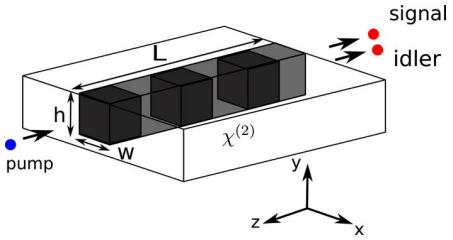

FIG. 1. (Color online) Schematic picture of waveguided PDC in a periodically poled rectangular waveguide.

converted fields we follow an approach used in [12–14]. Assuming a nonlinear dielectric crystal with length L, a constant waveguide cross section A, and propagation along the z direction (Fig. 1), the down-converted biphoton quantum state $|\psi\rangle$ (within first-order perturbation theory) is then given by

$$|\psi\rangle \sim \int_0^{t'} dt \int_V dV \chi^{(2)}(z) \hat{E}_p^{(+)} \hat{E}_s^{(-)} \hat{E}_i^{(-)} |0,0\rangle. \tag{1}$$

The susceptibility $\chi^{(2)}(z)$ indicates the second-order nonlinearity, V is the volume of the waveguide, and t' denotes the interaction time. The three interacting fields $\hat{E}_\mu(\mu=p,s,i)$ identify the pump field and the down-converted signal and idler waves, respectively. Note that we neglected the vacuum state which is of no interest in the scope of this paper.

The boundary conditions imposed on the fields propagating inside a waveguide define a discrete and finite set of allowed transverse field modes. This is in contrast to the infinite continuous set of transverse modes possible in bulk crystal PDC. We derive the joint spatio-spectral wave function of the photon pair by quantizing the fields of the signal and idler beams in the waveguide basis [15]. For a fixed frequency we denote the spatial waveguide modes in terms of a discrete set of orthonormal mode functions $u_n(\boldsymbol{r})$ $(n=1,\ldots,N)$, where $\boldsymbol{r}=(x,y)$ is the position in the transverse direction and z is the propagation direction of the pump beam. The vector $\boldsymbol{q}_n=(k_x,k_y)$ indicates the transverse momentum associated with the nth spatial mode of the field, and the reduced longitudinal wave numbers of pump, signal, and idler beams are given by $\beta_n^{(p,s,i)}(\omega)=\sqrt{[\omega n(\omega)/c]^2-|\boldsymbol{q}_n|^2}$. Their positive and negative frequency parts can now be written as

$$\begin{aligned}\hat{E}_\mu^{(-)}(\boldsymbol{r},z,t) &= \hat{E}_\mu^{(+)\dagger}(\boldsymbol{r},z,t) \\ &= B' \sum_n \int d\omega_\mu u_n^{(\mu)}(\boldsymbol{r}) \\ &\quad \times \exp\{\imath[\beta_n^{(\mu)}(\omega_\mu)z - \omega_\mu t]\} \hat{a}_n^{(\mu)\dagger}(\omega_\mu),\end{aligned} \tag{2}$$

where $\mu=(s,i)$ labels the signal and idler fields and the sum embraces all spatial modes propagating inside the waveguide. In Eq. (2) all constants and slowly varying field amplitudes have been merged into the overall parameter B', and the operator $\hat{a}_n^{(\mu)\dagger}(\omega_\mu)$ corresponds to the creation of one photon with a given frequency in one discrete spatial mode.

If we treat the electric field of the strong pump beam classically with the approximation of an undepleted pump it can be written as

$$\begin{aligned}E_p(\boldsymbol{r},z,t) &= \sum_l \int_0^\infty d\omega \alpha(\omega) A_l^{(p)} u_l^{(p)}(\boldsymbol{r}) \\ &\quad \times \exp\{\imath[\beta_l^{(p)}(\omega)z - \omega t]\} + \text{c . c.}\end{aligned} \tag{3}$$

In the general case of ultrashort pump pulses the laser source can exhibit a broad-band frequency structure which is modeled by the pump function $\alpha(\omega)$. In the following the field amplitude of each pump spatial mode $u_l^{(p)}(\boldsymbol{r})$ is denoted by $A_n^{(p)}$ (in the experiment this may be tuned by changing the coupling into the waveguide).

Using Eqs. (1)–(3) and following Grice and Walmsley [13] we find for the two-photon state,

$$\begin{aligned}|\psi\rangle = B \sum_{lmn} A_l^{(p)} \int \int_0^\infty d\omega_s d\omega_i \\ \times \underbrace{\int_A d\boldsymbol{r} u_l^{(p)}(\boldsymbol{r}) u_m^{(s)}(\boldsymbol{r}) u_n^{(i)}(\boldsymbol{r})}_{A_{lmn}} \alpha(\omega_s+\omega_i) \\ \times \underbrace{\text{sinc}[\Delta k_{lmn}(\omega_s,\omega_i)L/2] \exp[\imath \Delta\beta_{lmn}(\omega_s,\omega_i)L/2]}_{\phi_{lmn}(\omega_s,\omega_i)} \\ \times \hat{a}_m^{(s)\dagger}(\omega_s) \hat{a}_n^{(i)\dagger}(\omega_i) |0,\end{aligned} \tag{4}$$

with B defining an overall constant. The indices lmn label the triplet of the pump mode l, signal mode m, and idler mode n.

In Eq. (4) we introduced the value $\Delta\beta_{lmn}(\omega_s,\omega_i) = \beta_l^{(p)}(\omega_s+\omega_i) - \beta_m^{(s)}(\omega_s) - \beta_n^{(i)}(\omega_i) - \beta_{QPM}$, which corresponds to a momentum mismatch between the different propagation constants. This is corrected by the quasi-phase-matching vector β_{QPM} arising from a periodic variation in the $\chi^{(2)}$ nonlinearity in the z direction fabricated in the waveguide to achieve perfect phase-matching [16]. The spectrum of the down-converted photon pairs is given by the joint spectral amplitude (JSA) $f_{lmn}(\omega_s,\omega_i)=\alpha(\omega_s+\omega_i)\times\phi_{lmn}(\omega_s,\omega_i)$, where $\alpha(\omega_s+\omega_i)$ is the pump distribution and $\phi_{lmn}(\omega_s,\omega_i)$ is the phase-matching function.

Note that Eq. (4) is similar to the two-photon state of collinear plane-wave PDC, neglecting the spatial structure of the propagating waves [13]. However, by explicitly considering the spatial modes propagating inside the waveguiding material, we can see that the generated biphotonic state is emitted into a superposition of interacting mode triplets (lmn). Each triplet typically exhibits a different overall down-conversion generation efficiency due to the overlap between the three interacting fields A_{lmn}. Moreover the triplet possesses a unique spectrum $f_{lmn}(\omega_s,\omega_i)$ because of the different longitudinal wave vectors satisfying the phase-matching condition $\Delta\beta_{lmn}(\omega_s,\omega_i)=0$. In the experiment the spread of the photons into different spatial modes can be tuned by controlling the preparation of the incoming pump wave into different waveguide modes $A_l^{(p)}$. In conclusion the multi-mode PDC state is represented as

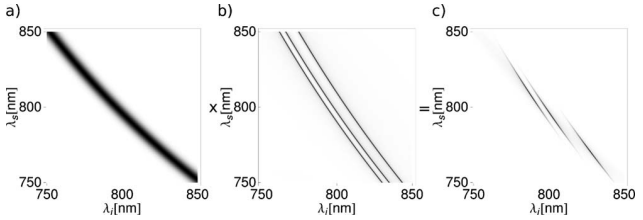

FIG. 2. Different spatial modes excited in the down-conversion process lead to a superposition of Gaussian shaped frequency distributions in the generated two-photon state. (a) pump function, (b) phase-matching function, and (c) JSA.

$$|\psi\rangle = B\sum_{lmn} A_l^{(p)} A_{lmn} \int \int_0^\infty d\omega_s d\omega_i f_{lmn}(\omega_s,\omega_i) \times \hat{a}_n^{(s)\dagger}(\omega_s)\hat{a}_m^{(i)\dagger}(\omega_i)|0,0\rangle. \quad (5)$$

The JSA of a typical two-photon state with only three different mode triplets is plotted in Fig. 2. As can be seen the differences in the momentum mismatch lead to slightly shifted phase-matching functions and the photons are generated in a superposition of these three frequency amplitudes. Hence the down-converted photon pairs are emitted into a composite state entangled in frequency and spatial mode (or transverse momentum).

III. WAVEGUIDE MODEL

To model numerically the properties of the generated two-photon state for a given waveguide architecture and down-conversion process, we assume a rectangular waveguide with width W, height H, a difference in the refractive index between the waveguide and substrate materials of Δn and a poling period Λ. The waveguide dimensions and the difference in the index of refraction are deduced from a measurement of waveguide's numerical aperture. The extracted parameters suggest a rectangular waveguide with parameters $H=6$ μm, $W=4$ μm, and $\Delta n=0.01$. In addition to the refractive index difference Δn between the waveguide and the substrate, our model also takes into account the air boundary at the upper edge of the waveguide. The waveguides have an effective poling period of $\Lambda=7.59$ μm. The estimates for the waveguide dimensions were verified with a microscope as shown in Fig. 3.

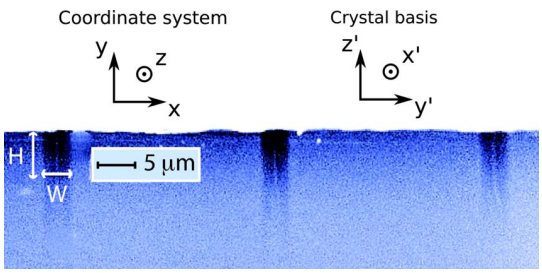

FIG. 3. (Color online) Microscope image of the waveguide cross section. The height and the width ($H\times W=6\times 4$ μm^2) given by the numerical aperture measurement are in good agreement with the image. Note the different nomenclature for the biaxial crystal basis and the coordinate system used for the calculations.

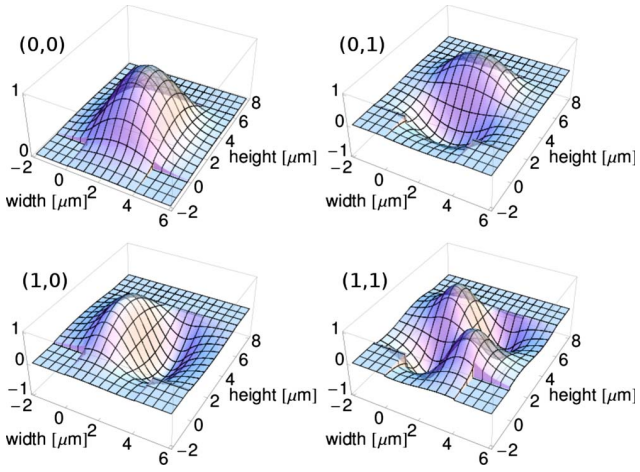

FIG. 4. (Color online) The first four z' polarized spatial field modes at 800 nm propagating in our waveguide.

In our type-II PDC process y' polarized pump photons near 400 nm are down converted into y' and z' polarized signal and idler photons around 800 nm. The spatial modes propagating in this waveguide architecture can be calculated with a semi-analytical dielectric waveguide model [17]. The solutions of the transverse wave equations correspond to sine and cosine functions followed by an exponential decay into the surrounding material (see Fig. 4).

The spatial modes and their respective transverse momenta can be conveniently labeled by the number of nodes in the transverse x and y directions (x nodes, y nodes). Our waveguide architecture shows multi-mode behavior at the spectral range of interest and supports spatial modes from (0,0) up to (3,5) and (1,2) at 400 and 800 nm, respectively. For given field modes we can readily evaluate both the propagation constant $\beta_\nu^{(p,s,i)}$ ($\nu=l,m,n$) and the coupling constant A_{lmn} for each mode triplet in Eq. (4) (cf. Table I).

In the special case of a rectangular waveguide the parity between the interacting modes is conserved ($l_i+n_i+m_i=2N$, $N\in\mathbb{N}$) similarly to the conversion of OAM in bulk crystal PDC. All down-conversion processes violating the parity conservation exhibit a vanishing coupling coefficient A_{lmn}. However perfect parity conservation would only be given if signal, idler, and pump waves propagate in the same mode basis, which in general is not the case due to their different polarizations and wavelengths. Hence weak cou-

TABLE I. Five selected coupling constants for different down-conversion processes possible in our WG architecture.

$E^{(p)}(l_x,l_y)\rightarrow E^{(s)}(m_x,m_y)+E^{(i)}(n_x,n_y)$	$A_{(lmn)}(10^{-4})$
$(0,0)\rightarrow(0,0)+(0,0)$	53.96
$(0,0)\rightarrow(0,1)+(0,0)$	0.11
$(0,0)\rightarrow(0,1)+(0,1)$	53.66
$(1,0)\rightarrow(1,0)+(0,0)$	42.55
$(0,2)\rightarrow(0,0)+(0,0)$	4.72

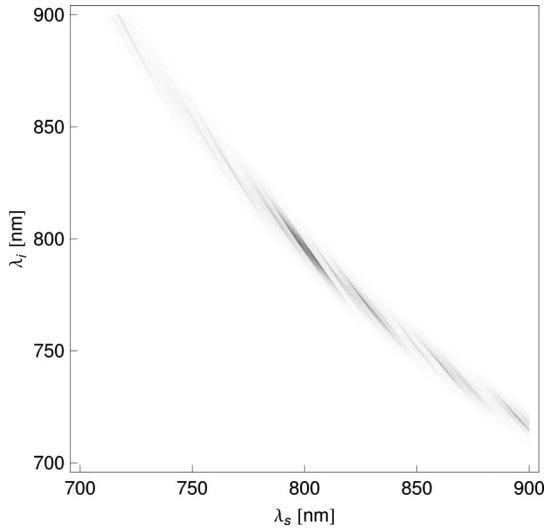

FIG. 5. Frequency distribution of the two-photon state for the 60 most important mode triplets. The PDC spectra are spread over a range of more than 200 nm.

pling exists between mode triplets that do not conserve parity.

Altogether we expect for this configuration that the down-converted fields will be emitted in a superposition of 720 different mode triplets each having a distinct JSA and coupling efficiency. With a 1.14 nm pump bandwidth the frequency spectra are spread over 200 nm in wavelength as can be seen in Fig. 5.

IV. STUDY OF SPATIAL STRUCTURE BY SECOND-HARMONIC MEASUREMENTS

SHG is a useful tool to analyze the spectral effects of spatial-mode propagation in our waveguides because, unlike PDC, all three fields are intense. Hence it is easy to measure both their spectral and spatial characteristics. In this way we can anticipate the spatio-spectral structure of the PDC emission from the waveguide by studying its SH response. The rich modal structure of the potassium titanyl phosphate (KTP) waveguides has been studied in the past by Roelofs *et al.*, who reported the existence of higher-order spatial modes by investigating frequency doubling [18].

In SHG, the signal and idler modes at the fundamental frequency are combined to form a second-harmonic mode at the doubled frequency. Thus the wavelengths of pump and output are reversed and in analogy to PDC this process is phase matched at the same frequencies: an SHG signal will only be present at wavelengths where pump and phase-matching functions overlap. Tuning the pump (fundamental) frequency moves the pump function along a +45° line in the joint frequency space as shown in Fig. 6. As this pump function crosses each individual phase-matching function a SH signal will be observed. If we use a pump with a sufficiently narrow bandwidth and align the pump beam such that we excite multiple waveguide modes, we can probe the position of the phase-matching functions for each spatial-mode triplet.

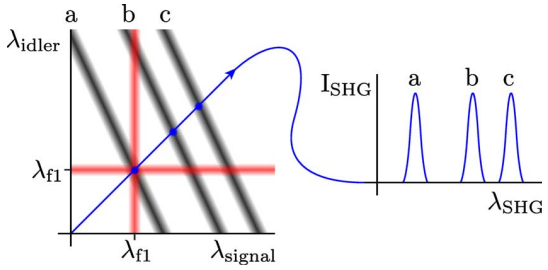

FIG. 6. (Color online) Schematic of SHG. The two gray (red) lines represent the two pump fields and the three black curves are three different phase-matching functions for three mode triplets. The black (blue) line at 45° is the locus of points picked out by the pump function as the fundamental wavelength is scanned. SH signal can be generated at the intersections of this line and the three phase-matching functions.

In our first experiment we pumped a 2.1-mm-long type-II PP-KTP (periodically poled) waveguide with a narrow-band Ti:sapphire laser [0.6 nm full width at half maximum (FWHM), 2.6 ps autocorrelation length, and ~1.5 MHz repetition rate] and measured the second-harmonic response with a spectrometer (Ocean Optics, Mikropack) while tuning the pump from 780 to 820 nm. Simultaneously, we recorded the spatial structure of the frequency doubled mode with a beam profiler charge-coupled device (CCD) camera (uEye, IDS Imaging). We observed a SH response at four different wavelengths (Table II). The corresponding spatial modes can be identified as (0,2), (0,0), (0,1), and (0,0) as shown in Fig. 7 and the SH spectra of the different spatial modes lie 2–5 nm apart. These modes propagate in the waveguide and could therefore be exploited to pump down-conversion processes.

With the help of the SH signal we verified the results of our model (Sec. III), specifically that it correctly predicts the separation between different SH peaks. In order to match exactly the absolute wavelength values from our model with the measured values, we introduced a small correction into the pump momentum. This was used as a fitting parameter to correct a discrepancy between the Sellmeier equations [19] calculated for a rectangular waveguide and those for the real waveguide used in the experiment. It should be noted that the value of this correction was only around 0.4% of the pump momentum and was the only free parameter in the model.

TABLE II. Spectral correspondence of different spatial modes in SHG. The second column states the mode triplets that yield the recorded wavelengths. The third and fourth columns show the measured and predicted positions of the SH modes.

		Experiment	Theory
Mode	$E^{(f_2)}+E^{(f_1)}\rightarrow E^{(\mathrm{SHG})}$	λ_{SHG} (nm)	λ_{SHG} (nm)
1	$(0,0)+(0,0)\rightarrow(0,2)$	393.9	395.1
2	$(0,0)+(0,0)\rightarrow(0,0)$	397.9	398.0
3	$(0,0)+(0,1)\rightarrow(0,1)$	400.0	399.3
4	$(0,1)+(0,2)\rightarrow(0,0)$	404.6	404.1

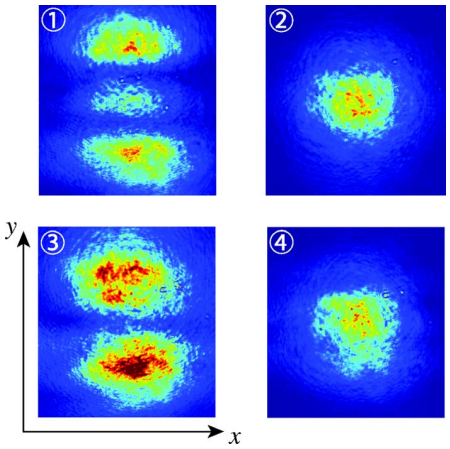

FIG. 7. (Color online) Observed second-harmonic modes. The modes (1) (0,2), (2) (0,0), (3) (0,1), and (4) (0,0) were recorded at wavelengths of 393.9, 397.9, 400.0, and 404.6 nm, respectively. (Axis labels correspond to the coordinate system in Fig. 3.)

The measured and predicted positions of the SH peaks were then in very good agreement as shown in Table II.

V. MEASUREMENT OF SPATIAL-TO-SPECTRAL COUPLING IN PDC

In our next experiment we investigated the spatial structure of the signal and idler photons from PDC more directly by measuring the spectrum of the single counts in both signal and idler arms. Measuring the single counts of only one arm discards the events in the other. However the corresponding spectral peaks of the two measured down-conversion distributions can be connected by energy conservation. This type of spectral marginal measurement corresponds to an integration over one spectral dimension of the JSA.

We pumped our down-converter with the SH of a mode-locked Ti:sapphire laser (798 nm, 10 nm FWHM, and 250 kHz repetition rate). A fairly narrow-band pump was required in order to resolve the spectral peaks arising in the marginal distributions from different spatial modes; hence the SH had a spectral width of 1.1 nm centered around 399 nm. Our nonlinear medium was a 3.5-mm-long type-II PPKTP waveguide similar to the one studied in Sec. IV. Signal and idler were separated at a polarizing beam splitter; one arm was coupled into a single-mode (SM) fiber, while the other was coupled into a multi-mode (MM) fiber. The fiber outputs were connected to a high-sensitivity spectrograph (Andor) as shown in Fig. 8. By rotating a half-wave plate before the polarizing beam splitter we could direct either signal or idler beam to the MM or SM fiber.

Coupling to MM fibers allowed the spectra of all of the different PDC spatial modes to be observed simultaneously. The large number of spectral peaks indicates that several spatial modes were excited inside the WG (Fig. 9). As expected, the peaks in the multi-mode signal and idler spectra could be accurately paired according to energy conservation. When coupling to SM fiber the main spectral peak corresponding to (0,0) mode in signal (790 nm) and idler (806 nm) dominates indicating that only the fundamental spatial mode is efficiently coupled.

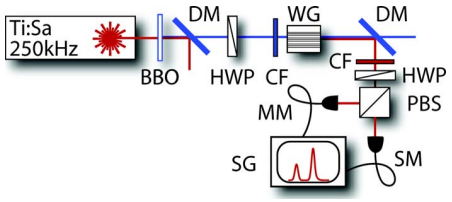

FIG. 8. (Color online) Experimental setup for measuring the spectral marginals of the signal and idler. BBO, β-barium borate crystal for SHG; DM, dichroic mirror; CF, color glass filter; HWP, half-wave plate; WG, waveguide; PBS, polarizing beam splitter; MM, multi-mode fiber; SM, single-mode fiber; and SG, spectrograph with CCD camera.

A crucial factor in influencing the structure of the photon pairs is the coupling of the pump mode into the waveguide. We examined the overlap between the incident free-space Gaussian pump mode and the corresponding pump modes in the waveguide basis, $A_l^{(p)}=\int_A d\boldsymbol{r} u_l^{(p)}(\boldsymbol{r})E_{ext.}^{(p)}(\boldsymbol{r})$. For a Gaussian pump beam with the correct beam waist properly aligned with the center of the waveguide almost all of the energy is deposited into the (0,0) waveguide mode and very little is coupled into higher-order waveguide modes. Nevertheless given that small pump misalignments were present we estimated a relative coupling into each higher-order pump mode of 10% of the energy coupled into the (0,0) mode. Taking into account this coupling of the beam into the waveguide in conjunction with the conversion efficiency of all the interacting mode triplets and their respective phase-matching functions, we calculated the generated JSA. Hence we were also able to predict the measured marginal spectra with very high

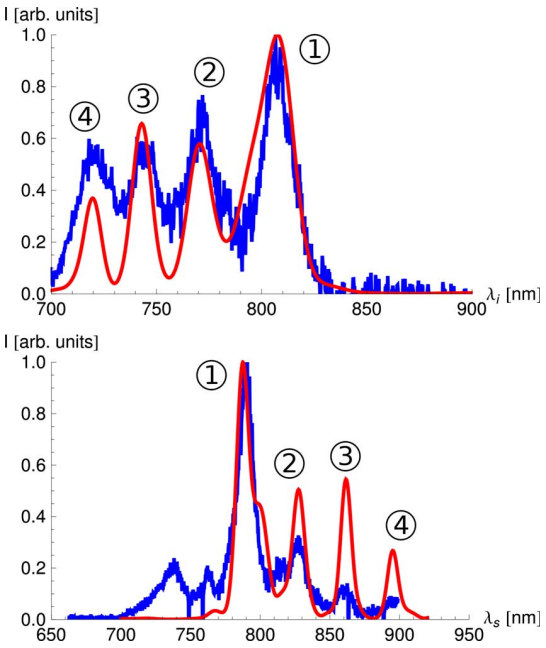

FIG. 9. (Color online) The observed noise-subtracted signal and idler marginals in black (blue) are in very good accordance with the predicted spectra in gray (red).

TABLE III. Spectral correspondence of different spatial modes observed in the marginal measurements of the PDC.

Proc.	$E^{(p)} \rightarrow E^{(s)} + E^{(i)}$	λ_s (nm)	λ_i (nm)
1	$(0,0) \rightarrow (0,0) + (0,0)$	788.1	806.2
2	$(0,0) \rightarrow (0,1) + (0,1)$	827.0	700.3
3	$(0,0) \rightarrow (1,0) + (1,0)$	816.5	742.9
4	$(0,0) \rightarrow (1,1) + (1,1)$	895.0	719.4

accuracy. We observed that the output is dominated by four main down-conversion processes (Table III); the coupling to other possible down-conversion processes is suppressed such that they cannot be seen above the noise level in the measurement. The remaining small deviations from the predicted marginal measurements can be explained by the different coupling efficiencies of the various modes into the MM fibers and the differences between the real waveguide investigated and our rectangular waveguide model. Note that the predicted spectra of the SHG and the PDC measurements are in very good agreement with each other. Our model requires only one fitting parameter which is the small constant offset in the effective Sellmeier equations for the waveguide.

VI. DISCUSSION

Our results from the previous sections demonstrate that higher-order spatial-mode propagation has significant consequences for photon-pair generation in waveguide architectures. The majority of quantum optics experiments require single photons in a well-controlled single mode in any given degree of freedom [20,21]. Consequently, in most single photon experiments, it is desirable to suppress all higher-order spatial-mode processes and to promote the emission of the photon pairs into the fundamental mode $[(0,0) \rightarrow (0,0) + (0,0)]$.

In order to achieve this with waveguided PDC, we first turn our attention to the measures one can take to promote the coupling of the pump beam into the fundamental waveguide mode. The pump beam should be spatially filtered to have a Gaussian profile either by the use of a pinhole and lens pair or a single-mode fiber. This mode should be carefully matched to the waveguide diameter either by choosing the appropriate lenses for efficient coupling into the waveguide or by directly butt coupling a single-mode fiber tip to the waveguide. In general a spot size with a diameter larger than the waveguide profile provides pump propagation that is closer to single mode, whereas a smaller beam will tend to exhibit more multi-mode effects. Fine tuning the coupling of the pump beam into the waveguide has a large impact on the modal structure of the pump and the optimum position can be found by monitoring the PDC spectrum. In our experiments we have found that this careful pump coupling can very effectively suppress all down-conversion processes originating from higher-order pump modes.

Having implemented these changes, any spectral peaks observed in the output spectrum beyond those of the fundamental modes originate from the down-conversion of the pump photons from the fundamental mode into higher-order signal and idler modes, as already shown in Fig. 9. Due to the different spectra connected to the different spatial modes, the output can be filtered in the spatial *or* the spectral domain to ensure collection of emission from the fundamental signal and idler mode only. By coupling the output beams into single-mode fibers one can affect a spatial-mode filter with relatively high contrast. The impacts on the frequency spectrum of such a spatial-mode filter can clearly be seen in Fig. 10 where the coupling of the down-converted photons was changed from MM to SM fiber. This demonstrates that the spectra of the beam can be manipulated by operations in the spatial domain. On the other hand, a frequency filter may be used to operate on the spatial structure of the photon pairs and could be adjusted to only transmit photons with spectra originating from fundamental mode propagation.

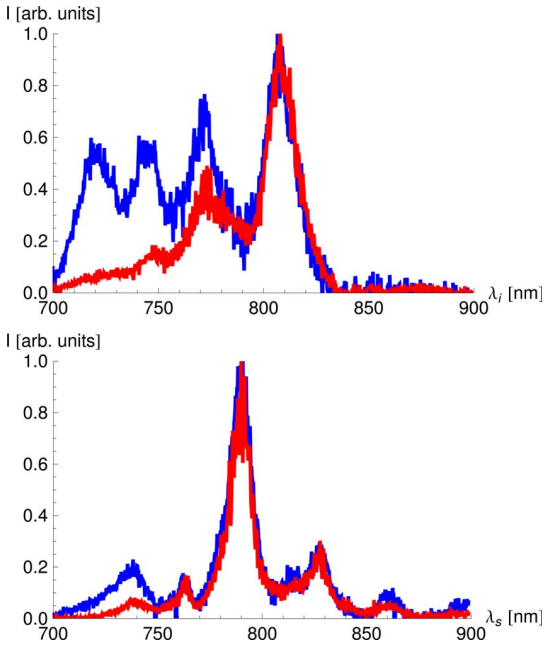

FIG. 10. (Color online) Noise subtracted SM fiber measurement (gray, red) and MM fiber (black, blue) marginal measurements. In these graphs the impact of spatial filtering on the spectral measurements can clearly be seen. The SM fibers select the signal and idler photons in the ground mode and suppress the side peaks from higher-order spatial-mode signal and idler photons.

Alternatively this problem can be addressed in the production process by reducing the size of waveguide cross section to only guide signal and idler beams in the fundamental mode. However since the wavelength of the down-converted pairs is approximately twice that of the pump, the light inevitably propagates not only in the fundamental waveguide mode but also in several higher-order spatial modes. Therefore multi-mode propagation effects still have to be taken into account, yet the number or the excited different down-conversion processes will be significantly reduced.

It is conceivable that the high down-conversion efficiency possible with a waveguide source in addition to these additional degrees of freedom may be used to create a multiplexed photon-pair source by simple spatial or spectral filter

operations on the generated biphotonic states. On the other hand these modes could be utilized as an information-processing degree of freedom and hence achieving control over the spatial emission profile is of paramount importance. For example, the spatial correlations may be applied in the generation of hyperentangled states offering new possibilities in the production of Bell states and additional robustness in quantum error correction due to the enlarged Hilbert space.

VII. CONCLUSION

In this paper we have derived the two-photon state generated in waveguided parametric down-conversion, explicitly taking into account the spatial mode propagating inside the waveguide material. We have shown how the propagation of a multitude of pump, signal, and idler modes affects the spatial *and* spectral structure of photon pairs emitted from a nonlinear waveguide. We have observed these effects both through measurements of the spectra of second-harmonic light generated in a KTP waveguide as well as in marginal measurements of down-converted photon pairs. The spectra derived from the multi-mode treatment of the SHG and the down-conversion fit the measured data extremely well, yielding the possibility to precisely engineer further experiments. Furthermore we have shown that we can influence the spectra of the generated biphotonic states by operations in the spatial domain.

We suggested how these effects may be controlled to give a truly single-mode photon source in the spatial domain by either careful experimental design or waveguide engineering. These findings are of significance for quantum information experiments where nonlinear waveguides are used to generate photon pairs and may be harnessed to generate hyperentangled photon states or may be applied to design multiplexed photon-pair sources.

Note added: Recently, we became aware of an independent theoretical examination of spatial entanglement in waveguided PDC [22]. Furthermore a recent experimental investigation of higher-order spatial modes in KTP waveguides with sum frequency generation was brought to our attention [23].

ACKNOWLEDGMENT

This work was supported by the EC under the FET-Open grant agreement CORNER, (Grant No. FP7-ICT-213681).

[1] J. Arlt, K. Dholakia, L. Allen, and M. J. Padgett, Phys. Rev. A **59**, 3950 (1999).
[2] A. Mair, A. Vaziri, G. Weihs, and A. Zeilinger, Nature (London) **412**, 313 (2001).
[3] H. H. Arnaut and G. A. Barbosa, Phys. Rev. Lett. **85**, 286 (2000).
[4] S. P. Walborn, S. Padua, and C. H. Monken, Phys. Rev. A **68**, 042313 (2003).
[5] J. P. Torres, Y. Deyanova, L. Torner, and G. Molina-Terriza, Phys. Rev. A **67**, 052313 (2003).
[6] J. C. Garcia-Escartin and P. Chamorro-Posada, Phys. Rev. A **78**, 062320 (2008).
[7] J. Chen, A. J. Pearlman, A. Ling, J. Fan, and A. L. Migdall, Opt. Express **17**, 6727 (2009).
[8] M. E. Anderson, M. Beck, M. G. Raymer, and J. D. Bierlein-siolb, Opt. Lett. **20**, 620 (1995).
[9] A. B. U'Ren, C. Silberhorn, K. Banaszek, and I. A. Walmsley, Phys. Rev. Lett. **93**, 093601 (2004).
[10] S. Tanzilli, H. D. Riedmatten, H. Tittel, H. Zbinden, P. Baldi, M. D. Micheli, D. Ostrowsky, and N. Gisin, Electron. Lett. **37**, 26 (2001).
[11] K. Banaszek, A. B. URen, and I. A. Walmsley, Opt. Lett. **26**, 1367 (2001).
[12] M. Fiorentino, S. M. Spillane, R. G. Beausoleil, T. D. Roberts, P. Battle, and M. W. Munro, Opt. Express **15**, 7479 (2007).
[13] W. P. Grice and I. A. Walmsley, Phys. Rev. A **56**, 1627 (1997).
[14] Y. M. Mikhailova, P. A. Volkov, and M. V. Fedorov, Phys. Rev. A **78**, 062327 (2008).
[15] D. Walls and G. Milburn, *Quantum Optics* (Springer, New York, 1995).
[16] G. D. DiGiuseppe, M. Atature, M. D. Shaw, A. V. Sergienko, B. E. A. Saleh, and M. C. Teich, Phys. Rev. A **66**, 013801 (2002).
[17] D. Marcuse, *Theory of Dielectric Optical Waveguides* (Academic Press, New York, 1974).
[18] M. G. Roelofs, A. Suna, W. Bindloss, and J. D. Bierlein, J. Appl. Phys. **76**, 4999 (1994).
[19] K. Kato and E. Takaoka, Appl. Opt. **41**, 5040 (2002).
[20] A. Eckstein and C. Silberhorn, Opt. Lett. **33**, 1825 (2008).
[21] A. Martin, V. Cristofori, P. Aboussouan, H. Herrmann, W. Sohler, D. B. Ostrowsky, O. Alibart, and S. Tanzilli, Opt. Express **17**, 1033 (2009).
[22] M. F. Saleh, B. E. A. Saleh, and M. C. Teich, Phys. Rev. A **79**, 053842 (2009).
[23] M. Karpinski, C. Radzewicz, and K. Banaszek, Appl. Phys. Lett. **94**, 181105 (2009).

Direct Measurement of the Spatial-Spectral Structure of Waveguided Parametric Down-Conversion

Peter J. Mosley, Andreas Christ, Andreas Eckstein, and Christine Silberhorn

Max Planck Institute for the Science of Light, Günther-Scharowsky Strasse 1/Bau 24, 91058 Erlangen, Germany

(Received 27 August 2009; published 2 December 2009)

We present a study of the propagation of higher-order spatial modes in a waveguided parametric down-conversion photon-pair source. Observing the multimode photon-pair spectrum from a periodically poled $KTiOPO_4$ waveguide allowed us to isolate individual spatial modes through their distinctive spectral properties. We have measured directly the spatial distribution of each mode of the photon pairs, confirming the findings of our waveguide model, and demonstrated by coincidence measurements that the total parity of the modes is conserved in the nonlinear interaction. Furthermore, we show that we can combine the advantages of a waveguide source with the potential to generate spatially entangled photon pairs as in bulk-crystal down-converters.

DOI: 10.1103/PhysRevLett.103.233901 PACS numbers: 42.65.Lm, 03.65.Ta, 03.67.−a, 42.50.Dv

The prevalence of parametric down-conversion (PDC) as a source of photon pairs is due not only to the high quality of the photons produced but also its experimental simplicity relative to other methods of generating single photons. Its ubiquity may lead one to believe that PDC is a technique with little scope for improvement. However, bulk-crystal down-conversion sources suffer from a significant drawback: the photon pairs are emitted in a cone-shaped pattern making efficient collection difficult. This limits both the absolute count rate for a given pump power (stimulating the purchase of ever larger and more expensive laser systems) and, more importantly, the heralding efficiency of any bulk-crystal PDC source.

By confining photon-pair generation to a channel waveguide in a nonlinear optical material one can restrict the down-converted light to a well-defined set of spatial modes rather than allowing the emission to propagate at the natural phase-matching angles. This provides a straightforward method of controlling the messy spatial emission pattern from bulk-crystal down-converters and increases the down-conversion collection rate significantly [1–5]. However, as the wavelength of the down-converted pairs is approximately twice that of the pump, the light inevitably propagates not only in the fundamental waveguide mode but also in several higher-order spatial modes [6–8]. Because of the coupling between the spatial and spectral properties of the photon pairs imposed by phase matching, these higher-order waveguide modes have a significant impact on the spectrum of the photon pairs and can markedly degrade source performance [9,10]. Optimal source design requires that we both understand and control the interaction of higher-order modes in waveguides [11]. On the other hand, the multimode spatial structure in the down-converted beams offers new opportunities for advanced quantum state preparation [12]. Recent experiments utilize entanglement of the orbital angular momentum of the photon pairs prepared by bulk-crystal PDC, but they rely on heavy filter operations by means of holographic state selection [13,14]. Waveguided PDC can directly provide entangled higher-order spatial modes in analogy to orbital angular momentum (OAM) entangled modes of photon pairs generated in bulk PDC experiments. OAM modes and their applications have been extensively studied recently [15–18] with a view to accessing higher-dimensional Hilbert spaces via the generation of hyperentangled photon pairs [19–24].

In this Letter we report the first direct observation of photon pairs generated in higher-order spatial modes by waveguided parametric down-conversion. We assign specific mode labels to each process by applying a numerical model and confirm parity conservation between the interacting mode triplets. Furthermore, we show that our source can generate spatially entangled two-photon states, while retaining the virtues of a waveguided device.

In general, down-converted photon pairs from waveguides are entangled in both frequency and spatial mode. Because of the dependence of the mode propagation constants on wavelength, spatial mode and spectrum are linked through the phase-matching conditions. Hence entanglement in these degrees of freedom cannot usually be separated [11]. A key property of our source presented in this Letter is its particular modal dispersion inside the waveguide which fulfills all the requirements to generate Bell-states in the spatial domain. By spectrally filtering the down-converted beams this source allows for the generation of photon pairs whose spatial entanglement is separated from the spectral domain. Hence hyperentangled photon-pairs are emitted:

$$|\psi\rangle_{\text{filtered}} = B' \sum_k \lambda_k |\psi_s^{(k)}, \phi_i^{(k)}\rangle \otimes |\Psi\rangle_{\text{Bell}} \qquad (1)$$

with $|\psi_s^{(k)}\rangle$ and $|\phi_i^{(k)}\rangle$ denoting the spectral properties and $|\Psi\rangle_{\text{Bell}}$ denoting a Bell state for higher-order spatial modes. Equation (1) is derived by applying a spectral Schmidt

decomposition and introducing broadband frequency modes $|\hat{\psi}_s^{(k)}\rangle$, $|\hat{\phi}_i^{(k)}\rangle$ to highlight the decoupling of the spectral and spatial degrees of freedom [25].

Our source is a 10 mm z-cut periodically poled $KTiOPO_4$ (PPKTP) waveguide from AdvR with a nominal poling period of 8.72 μm, pumped by a spatially filtered pulsed diode laser at 403.3 nm with a bandwidth of 0.8 nm. Input coupling was through a 20× microscope objective and the pump was observed to be mainly (though not exclusively) in the fundamental mode of the waveguide. Output coupling was by an aspheric lens with a focal length of 6.24 mm, set to image the output face of the waveguide to a plane about 800 mm away. The type-II phase-matching conditions ensured that we obtained almost degenerate photon pairs, with the horizontally polarized pump (y-polarized in the crystal basis) yielding signal and idler with horizontal (y) and vertical (z) polarizations, respectively. After the crystal the pump was removed with long-pass filters and the signal and idler photons were separated at a polarizing beam splitter (PBS).

Initially, signal and idler beams were coupled into two multimode fibers attached to a spectrometer with single-photon sensitivity. The multimode fibers allowed us to monitor simultaneously a range of spatial modes generated in the waveguide. The spectra for signal and idler are shown in Fig. 1. The spectral signatures of several spatial modes are clearly present: five individual peaks can be identified in both spectra. The peaks in the signal arm are paired with those in the idler through energy conservation. Each pair of peaks corresponds to a particular spatial mode set of pump, signal, and idler. Using the single-photon spectra, two sets of spectral filters (one for the signal with central wavelengths of 808 and 830 nm and bandwidths of 3 nm and the other for the idler with central wavelengths 810, 830, and 860 nm and bandwidths of 10 nm) were calibrated such that each spectral peak could be individually selected by inserting and angle tuning a particular filter.

In order to assign specific mode labels to peaks A to E we developed a model of down-conversion in a step-index waveguide with a rectangular profile, bounded by a uniform dielectric on three sides and by air at the fourth. Although the production method of the waveguides results in a graded index distribution orthogonal to the air interface [4] our model yielded a simplified, semianalytic solution which has been proven as sufficient to describe the experimental results [11]. Although a more precise model would cause slight alterations to the predicted peak heights and spatial mode distributions, the more salient features—the central wavelengths of the spectral peaks—would remain virtually unchanged. By adjusting the index contrast, the waveguide dimensions, and the poling period as free parameters we fitted the calculated spectra to the measured marginal spectra of signal and idler (Fig. 2). Note that the spectral widths of the signal and idler marginal distributions are set by the overlap of the pump bandwidth with the modal phase-matching functions of the crystal. Here the relatively broadband pump results in photon pairs with wider bandwidths than in similar experiments utilizing continuous-wave lasers [4]. From the theoretical modeling we identified each of the mode triplets listed in Table I; they are labeled with the number of nodes in the horizontal and vertical directions (x, y), respectively.

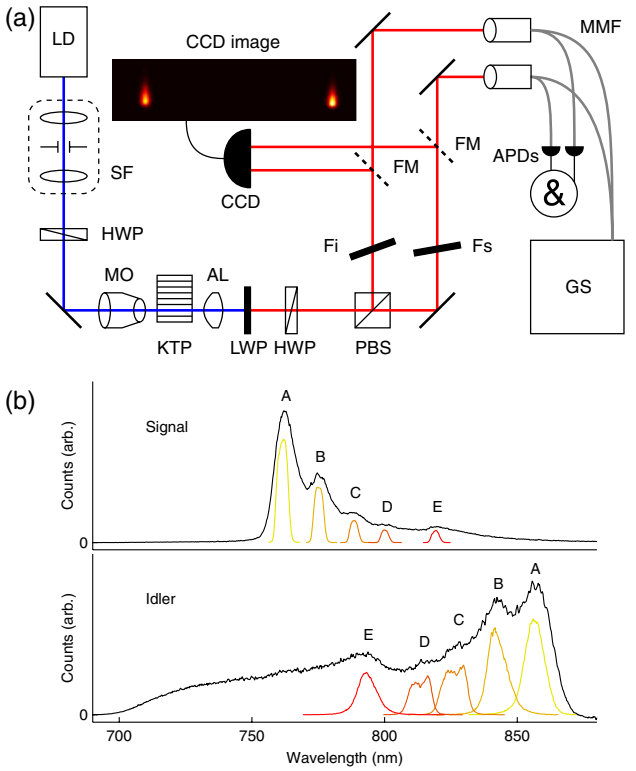

FIG. 1 (color online). (a) Experimental setup. LD, laser diode; SF, spatial filter; HWP, half-wave plate; MO, microscope objective; KTP, PPKTP waveguide; AL, aspheric lens; LWP, long-wave pass filter; PBS, polarizing beam splitter; Fs, Fi, interference filters; FM, flipper mirrors; MMF, multimode fiber; APD, avalanche photodiode; GS, grating spectrometer. (b) Background-subtracted spectra with correlated peaks labeled A to E. Colored lines show filtered spectral peaks (heights adjusted for ease of viewing).

The principal mode pair A, is the result of the interaction between the fundamental modes of all three fields. This triplet has the most widely separated spectral components and was fitted by adjusting the poling period in the model. This effective poling period of 8.92 μm serves as a global correction to allow for the difference between the waveguide in the lab and the empirical Sellmeier equations [26]. The remaining free parameters were adjusted to reproduce the observed marginal spectra of the photon pairs. With waveguide dimensions of 4.1 × 9.3 μm and an index contrast of 0.008 we obtained a very good agreement between

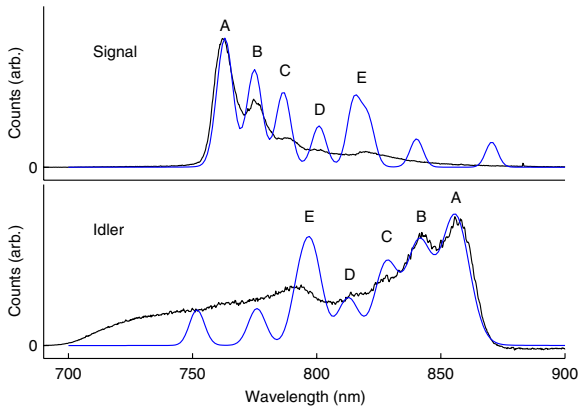

FIG. 2 (color online). Comparison of modeled spectra with measured data. Labels A to E correspond to labels in Fig. 1.

theory and experiment (see Fig. 2). These dimensions were verified under an optical microscope.

According to our model, mode pairs A, C, and E originate from the (0,0) component of the pump (see Table I). E stems from photon pairs generated both in modes (1,0) and (0,2) with overlapping spectral distributions. As a result of this frequency degeneracy and the coherence of the PDC process, the signal and idler pairs in E are entangled in spatial mode. Further mode pairs occur at B and D pumped by the fraction of the pump intensity in the (0,1) mode (37.5%). In these cases, the signal and idler are in different—though still parity conserving—modes. Peaks B and D each consist of two down-conversion processes with almost identical spectra each entangled in spatial mode. The two pairs of peaks in the modeled spectra not mirrored in the measured data are from down-conversion events into higher-order spatial modes [up to (1,2)]. These modes couple poorly into the collection fibers and hence are not seen in the data. The discrepancies in peak height between theory and experiment in Fig. 2 stem from our rectangular waveguide model and the falling collection efficiencies for higher-order spatial modes.

Next the high-sensitivity CCD camera was removed from the spectrometer and placed in the image plane of the $f = 6.24$ mm aspheric to measure the spatial intensity distribution of each mode. Both output beams from the waveguide were directed simultaneously to separate areas of the sensor yielding magnified images (approximately 130×) of the spatial modes of both signal and idler in the waveguide. Figure 3 shows the characteristic distributions of individual spatial modes, recorded by tuning the spectral filters to pick out spatial modes through their unique spectra. This demonstrates the strong correlation between the spatial and spectral degrees of freedom in this system.

TABLE I. Processes giving rise to the five observed mode spectra.

A	$(0,0)_p \rightarrow (0,0)_s + (0,0)_i$
B	$(0,1)_p \rightarrow (0,0)_s + (0,1)_i$ and $(0,1)_s + (0,0)_i$
C	$(0,0)_p \rightarrow (0,1)_s + (0,1)_i$
D	$(0,1)_p \rightarrow (0,1)_s + (0,2)_i$ and $(0,2)_s + (0,1)_i$
E	$(0,0)_p \rightarrow (1,0)_s + (1,0)_i$ and $(0,2)_s + (0,2)_i$

In these measurements, a high level of background was present from the long-lived, unphasematched fluorescence emitted by the waveguide that could not be removed by time gating due to the slow speed of the camera. Instead the fluorescence level was measured for each spatial mode by rotating the pump polarization to vertical, hence removing any phase matching. However, this background could not be subtracted directly as the fluorescence was higher for a vertically polarized pump. Therefore, auxiliary measurements for both polarizations were made with an unpoled waveguide in which no phasematched processes could take place. The ratio between these fluorescence signals allowed us to introduce a correction for the scaling of the background in the PDC spatial mode images recorded with the poled waveguide. Subtracting this adapted background from the spatial mode images yielded a realistic measurement of the true distribution of the PDC in the various spatial modes as shown in Fig. 3.

It is apparent from Fig. 3 that each of the five mode pairs A to E has its own characteristic spatial intensity distribution, with peaks B to E exhibiting obvious signs of higher-order mode propagation. All of the recorded spatial distributions agree very well with those found in the spectral degree of freedom through the model as listed in Table I: A and C are pure (0,0) and (0,1), respectively; B is a sum of (0,0) and (0,1) where two processes overlap spectrally; D is also a sum of two processes, (0,1) and (0,2); E, the superposition of the (1,0) and (0,2) modes, is the only case to show a higher-order mode in the horizontal direction. Furthermore one can see the deviation of the waveguide from a rectangular structure: the fundamental mode sits at the top of the guide close to the air boundary, while higher-order modes spread down into the chip where there is an exponential decay in the refractive index contrast not present in our model.

Finally, we performed a coincidence measurement between the different spatial modes. With both beams once again coupled into the multimode fibers the photons were sent to two silicon avalanche photodiodes (APD). The time-gated single count rate of each APD was monitored along with the rate of coincidence counts between the two as the filters were set to select every combination of the five spatial modes in both the signal and idler arms. The results are shown in Fig. 3 with the background of accidental coincidences—calculated as the product of the singles rates divided by the laser repetition rate (1 MHz)—subtracted from the coincidence rates. The presence of only diagonal elements in the corrected coincidence rates demonstrates the strict correlation between the spatial modes: if the signal photon is emitted into a particular spatial mode

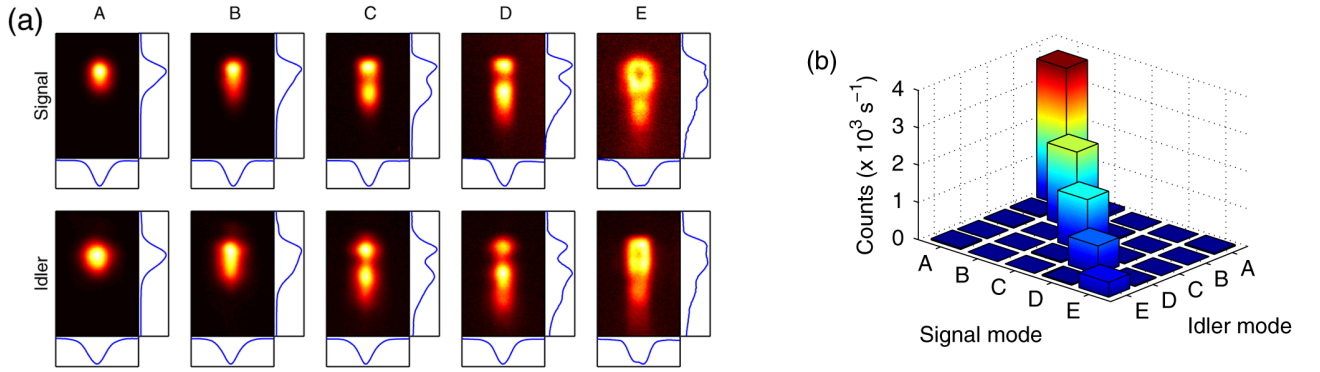

FIG. 3 (color online). (a) Plots of the background-subtracted spatial mode distributions for signal (top) and idler (bottom) arms along with their marginal distributions. The air interface is towards the top of each frame, and the decay of the waveguide structure into the chip can clearly be observed towards the bottom. (b) Coincidence count rate between different pairs of spatial modes. Labels *A* to *E* correspond to labels in Fig. 1.

then the idler will always be found in the corresponding mode. This confirms the requirement for parity conservation between the three interacting modes.

Our measurements demonstrate that the generation of higher-order spatial mode entanglement can be easily accomplished in waveguided PDC. For our source this can be achieved by filtering processes B, D, or E and postselecting on successful coincidence events. For example, by choosing only process B we find

$$|\psi\rangle_B = B' \sum_k \lambda_k |\psi_s^{(k)}, \phi_i^{(k)}\rangle \otimes \underbrace{(|(0,1)_s,(0,0)_i\rangle + |(0,0)_s,(0,1)_i\rangle)}_{|\Psi^+\rangle}. \quad (2)$$

Similarly, filtering peaks D and E yields the Bell states $|\Psi^+\rangle$ and $|\Phi^+\rangle$, respectively.

In conclusion, we have directly imaged spectrally resolved spatial modes of PDC in a PPKTP waveguide. We have identified the individual spatial mode contributions and demonstrated that our model accurately reproduces the photon-pair spectra. This shows that waveguided PDC sources have the potential to be used as bright sources of photon pairs entangled in spatial mode. These photon pairs may have many applications from testing the Bell inequalities in the spatial domain to distributing Bell pairs over free space links for quantum key distribution applications.

This work was supported by the EC under the FET-Open grant agreement CORNER, No. FP7-ICT-213681.

[1] A. B. U'Ren, C. Silberhorn, K. Banaszek, and I. A. Walmsley, Phys. Rev. Lett. **93**, 093601 (2004).
[2] J. Chen *et al.*, Opt. Express **17**, 6727 (2009).
[3] S. Tanzilli *et al.*, Electron. Lett. **37**, 26 (2001).
[4] M. Fiorentino *et al.*, Opt. Express **15**, 7479 (2007).
[5] T. Zhong, F. N. Wong, T. D. Roberts, and P. Battle, Opt. Express **17**, 12019 (2009).
[6] M. G. Roelofs, A. Suna, W. Bindloss, and J. D. Bierlein, J. Appl. Phys. **76**, 4999 (1994).
[7] K. Banaszek, A. B. U'Ren, and I. A. Walmsley, Opt. Lett. **26**, 1367 (2001).
[8] M. Karpinski, C. Radzewicz, and K. Banaszek, Appl. Phys. Lett. **94**, 181105 (2009).
[9] A. Eckstein and C. Silberhorn, Opt. Lett. **33**, 1825 (2008).
[10] A. Martin *et al.*, Opt. Express **17**, 1033 (2009).
[11] A. Christ, K. Laiho, A. Eckstein, T. Lauckner, P. J. Mosley, and C. Silberhorn, Phys. Rev. A **80**, 033829 (2009).
[12] M. F. Saleh, B. E. A. Saleh, and M. C. Teich, Phys. Rev. A **79**, 053842 (2009).
[13] A. Mair, A. Vaziri, G. Weihs, and A. Zeilinger, Nature (London) **412**, 313 (2001).
[14] J. Arlt, K. Dholakia, L. Allen, and M. J. Padgett, Phys. Rev. A **59**, 3950 (1999).
[15] G. Molina-Terriza, J. P. Torres, and L. Torner, Nature Phys. **3**, 305 (2007).
[16] M. Lassen *et al.*, Phys. Rev. Lett. **98**, 083602 (2007).
[17] J. C. Garcia-Escartin and P. Chamorro-Posada, Phys. Rev. A **78**, 062320 (2008).
[18] S. Franke-Arnold, L. Allen, and M. J. Padgett, Laser Photon. Rev. **2**, 299 (2008).
[19] J. T. Barreiro, N. K. Langford, N. A. Peters, and P. G. Kwiat, Phys. Rev. Lett. **95**, 260501 (2005).
[20] S. P. Walborn, S. Pádua, and C. H. Monken, Phys. Rev. A **68**, 042313 (2003).
[21] S. Franke-Arnold, S. M. Barnett, M. J. Padgett, and L. Allen, Phys. Rev. A **65**, 033823 (2002).
[22] G. Molina-Terriza, J. P. Torres, and L. Torner, Phys. Rev. Lett. **88**, 013601 (2001).
[23] S. S. R. Oemrawsingh *et al.*, Phys. Rev. Lett. **95**, 240501 (2005).
[24] A. Vaziri, G. Weihs, and A. Zeilinger, Phys. Rev. Lett. **89**, 240401 (2002).
[25] P. P. Rohde, W. Mauerer, and C. Silberhorn, New J. Phys. **9**, 91 (2007).
[26] K. Kato and E. Takaoka, Appl. Opt. **41**, 5040 (2002).

Any fool can make something complicated.
It takes a genius to make it simple.

(Woody Guthrie)

6. PDC and FC in the high gain regime

6.1. Introduction

To date most theoretical treatments of PDC restrict themselves to the application of first-order perturbation theory. However, with the advent of waveguided PDC and high power laser sources, the first-order perturbation theory approaches are not sufficient any more. Higher-order terms, which describe the emission of multiple photon-pairs, have to be taken into account.[1]

In this chapter we address this problem and build two theoretical models for PDC including higher-order photon-number effects: a rigorous numerical model, based on the theoretical framework of Kolobov [69], and a simplified analytical approach. We analyse their performance and the quality of their predictions which enables us to suggest when a simple analytic modelling of PDC is sufficient and when the rigorous approach has to be applied.

Furthermore, we extended the developed theoretical framework to frequency conversion (FC) processes. These frequency conversion setups enable us to build quantum pulse gates [49, 70, 71], where our theoretical model enables us to benchmark their performance.

6.2. The PDC process in the high-gain regime

In Chap. 4 (Eq. (4.13)) we already stated that the unitary transformation generated by the PDC process is given by the formula

$$\hat{U}_{PDC} = \mathcal{T} \exp\left[-\frac{\imath}{\hbar}\int_{-\infty}^{\infty} \mathrm{d}t\, \hat{H}_{PDC}(t)\right], \tag{6.1}$$

but restricted ourselves to a discussion of PDC using perturbation theory, i.e. we only considered the generation of a single photon-pair. In the high gain regime, however, we have to take into account the possibility that two or more pump photons can simultaneously decay into several photon-pairs.

[1] This chapter is a summary of the paper "Theory of quantum frequency conversion and parametric down-conversion in the high gain regime" by Andreas Christ, Benjamin Brecht, Wolfgang Mauerer, and Christine Silberhorn [3].

PDC in the high gain regime has already been studied in detail using simplified representations [46, 72] and continuous-wave laser sources [69]. Here we go beyond these standard monochromatic descriptions and consider ultrafast broadband PDC in the high gain regime.

In order to mathematically describe this situation we develop a rigorous model of the process. For this purpose it is useful to consider PDC in the Heisenberg picture, as depicted in Fig. 6.1: in this picture two input beams $\hat{a}^{(in)}$ (signal) and $\hat{b}^{(in)}$ (idler) are, via the process of parametric down-conversion, converted into the two output beams $\hat{a}^{(out)}$ and $\hat{b}^{(out)}$.

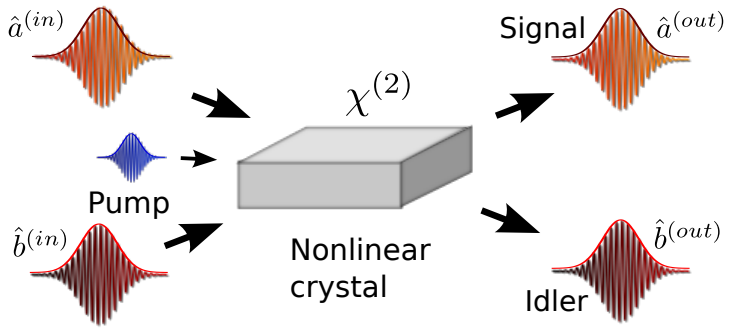

Figure 6.1.: Type-II PDC in the Heisenberg picture: two input beams $\hat{a}^{(in)}$ and $\hat{b}^{(in)}$ are, via the process of parametric down-conversion, converted into the two output beams $\hat{a}^{(out)}$ and $\hat{b}^{(out)}$.

The PDC Hamiltonian in Eq. (4.11) already gives valuable information about the properties of PDC. Treating the strong pump as a classical field PDC is described by a bilinear Hamiltonian mixing photon creation and destruction operators from different optical modes. Hence the solution is a linear operator transformation of the form [73, 74]

$$\begin{aligned}\hat{a}^{(out)}(\omega) &= \int \mathrm{d}\omega' U_a(\omega,\omega')\,\hat{a}^{(in)}(\omega') + \int \mathrm{d}\omega' V_a(\omega,\omega')\,\hat{b}^{(in)\dagger}(\omega') \\ \hat{b}^{(out)}(\omega) &= \int \mathrm{d}\omega' U_b(\omega,\omega')\,\hat{b}^{(in)}(\omega') + \int \mathrm{d}\omega' V_b(\omega,\omega')\,\hat{a}^{(in)\dagger}(\omega'),\end{aligned} \tag{6.2}$$

where the matrices U_a, U_b, V_a and V_b carry the physical properties of the system.

Furthermore Eq. (6.2) has to form a canonical transformation. Under this constraint, and with the help of the singular-value decomposition, we are able to rewrite it as (see appendix in [3])

$$\begin{aligned}\hat{A}_k^{(out)} &= \cosh(r_k)\,\hat{A}_k^{(in)} + \sinh(r_k)\,\hat{B}_k^{(in)} \\ \hat{B}_k^{(out)} &= \cosh(r_k)\,\hat{B}_k^{(in)} + \sinh(r_k)\,\hat{A}_k^{(in)},\end{aligned} \tag{6.3}$$

where $\hat{A}_k$ and $\hat{B}_k$ are broadband single-photon destruction operators as defined in Eq. (4.26). Consequently, without actually solving the PDC process, we are able to deduce

that a PDC source emits a multitude of EPR states or twin-beam squeezed states in ultrafast optical pulse modes with squeezing parameters r_k [33].

If we assume that the input and output modes are of identical shape, we are able to recast Eq. (6.3), from the Heisenberg picture, into the general unitary transformation[2]:

$$\hat{U}_{PDC} = \bigotimes_k \exp\left[r_k \left(\hat{A}_k^\dagger \hat{B}_k^\dagger - \hat{A}_k \hat{B}_k\right)\right] \tag{6.4}$$

6.2.1. PDC process parameters

Eq. (6.3) and Eq. (6.4) fully describe the PDC process and directly give its most important parameters: The individual mode distributions $\hat{A}_k$ and $\hat{B}_k$ and the squeezing amplitudes r_k. The r_k distribution gives both the number of excited optical modes and the amount of generated squeezing. In order to be able to investigate the number of emitted squeezers independent of the efficiency of the down-conversion process we separate the r_k distribution as follows:

$$r_k = B\lambda_k \tag{6.5}$$

Here λ_k is a normalized mode distribution satisfying $\sum_k \lambda_k^2 = 1$ and B depicts the overall optical gain. From this λ_k distribution we are able to evaluate the *effective* number of optical modes K emitted from the PDC state via [57, 58]:

$$K = \frac{1}{\sum_k \lambda_k^4} \tag{6.6}$$

This normalized λ_k distribution is then transformed into the actual squeezer distribution r_k via the overall optical gain B. This splitting of r_k enables us to treat the efficiency of the down-conversion process B separately from the number of excited modes λ_k and benchmarks PDC states via two simple numbers.[3]

6.3. Theory of PDC in the high gain regime

In order to obtain the actual squeezing amplitudes r_k and mode shapes $\hat{A}_k$, $\hat{B}_k$ we have to evaluate Eq. (6.1). Here the main issue is the time-ordering operator $\mathcal{T}$, which takes into account that the electric fields, in the PDC Hamiltonian, do not commute in time.[4]

[2] This is a subtle approximation. It is, in fact, not required that the shapes of the input modes $\hat{A}_k^{(in)}$ / $\hat{B}_k^{(in)}$ are identical to the output modes $\hat{A}_k^{(out)}$ / $\hat{B}_k^{(out)}$. We are, however, not aware of any actual physical PDC processes where this takes place.

[3] How to determine these benchmarks from an actual PDC source is described in Chap. 9.

[4] A detailed discussion of the time-ordering effects in PDC, using a Dyson series approach, was performed by Agata M. Brańczyk in [51, 75]).

6.3.1. Analytic model

The most straightforward method to obtain the PDC parameters from Eq. (6.1) is to simply neglect the effects from the time-ordering operator $\mathcal{T}$. We remain with:

$$\hat{U}_{PDC} = \exp\left[-\frac{\imath}{\hbar}\int_{-\infty}^{\infty} \mathrm{d}t\, \hat{H}_{PDC}(t)\right] \tag{6.7}$$

This enables us to directly perform the time-integration in the exponent of Eq. (6.7). Following Sec. 4.3 we obtain:

$$\hat{U}_{PDC} = \exp\left[-\frac{\imath}{\hbar}\left(\int \mathrm{d}\omega_a \int \mathrm{d}\omega_b\, f(\omega_a,\omega_b)\hat{a}^\dagger(\omega_a)\hat{b}^\dagger(\omega_b) + h.c.\right)\right] \tag{6.8}$$

Using the singular-value decomposition, similar to Sec. 4.4, we are able to rewrite Eq. (6.8) in the broadband mode formalism [6]

$$\hat{U}_{PDC} = \bigotimes_k \exp\left[r_k\left(\hat{A}_k^\dagger \hat{B}_k^\dagger - \hat{A}_k\hat{B}_k\right)\right], \tag{6.9}$$

which is exactly the form requested in Eq. (6.4) and directly yields the desired PDC parameters.

This "no time-ordering" approximation enables the straightforward analytic solution of the PDC process in the high gain regime, at the expense of neglecting the time-ordering effects.

6.3.2. Rigorous numerical model

To obtain a rigorous solution of the PDC process, including time-ordering effects, we follow the approach by Mikhail I. Kolobov in [69] and perform our calculations using the Heisenberg equation of motion. As a first step we transform the electric field operators from Eq. (4.6) to the simplified electric fields [69]:

$$\hat{a}(z,t) = \frac{1}{\sqrt{2\pi k_0}}\int \mathrm{d}k\, \sqrt{\omega(k)}\exp\left[\imath\left(kz-\omega(k)t\right)\right]\hat{a}(k) \tag{6.10}$$

$$\hat{b}(z,t) = \frac{1}{\sqrt{2\pi k_0}}\int \mathrm{d}k\, \sqrt{\omega(k)}\exp\left[\imath\left(kz-\omega(k)t\right)\right]\hat{b}(k) \tag{6.11}$$

The time-dependence of the electric field operators $\hat{a}(z,t)$ is then given via the relation

$$\frac{d}{dt}\hat{a}(z,t) = \frac{\imath}{\hbar}\left[\hat{H}_0(t) + \hat{H}_{PDC}(t), \hat{a}(z,t)\right], \tag{6.12}$$

where we have to include the effects of free propagation via the Hamiltonian $\hat{H}_0(t)$ [69].

Solving Eq. (6.12) and moving into the interaction picture

$$\begin{aligned}\hat{\epsilon}_a(z,t) &= \hat{a}(z,t)\exp\left[-\imath k_a(\omega)\right]\\ \hat{\epsilon}_b(z,t) &= \hat{b}(z,t)\exp\left[-\imath k_b(\omega)\right],\end{aligned} \tag{6.13}$$

we obtain two operator valued integro-differential equations describing the down-conversion process

$$\begin{aligned}\frac{\partial}{\partial z}\hat{\epsilon}_a(z,\omega) &= \int \mathrm{d}\omega' f(\omega,\omega',z)\,\hat{\epsilon}_b^\dagger(z,\omega') \\ \frac{\partial}{\partial z}\hat{\epsilon}_b(z,\omega) &= \int \mathrm{d}\omega' f^*(\omega',\omega,z)\,\hat{\epsilon}_a^\dagger(z,\omega'),\end{aligned} \tag{6.14}$$

with $f(\omega,\omega',z)$ defined as

$$f(\omega,\omega',z) = -\frac{\imath}{\hbar} D\epsilon_p^{(+)}(z,\omega+\omega')\exp\left[\imath\Delta k(\omega,\omega')z\right], \tag{6.15}$$

where D collects all constants and $\epsilon_p^{(+)}(z,\omega+\omega')$ describes the pump distribution. The structure of this result is very similar to the equations derived by [76, 77, 78], which serves as a cross check of our calculations.

One method to solve linear operator valued differential equations is the widely used split-step Fourier inversion technique [78, 79]. We use a different approach, based on our knowledge of the structure of the PDC process: using Eq. (6.2) and Eq. (6.14) we obtain the four classical differential equations [76]

$$\begin{aligned}\frac{\partial}{\partial z}U_a(z,\omega,\omega'') &= \int \mathrm{d}\omega' f(\omega,\omega',z)V_b^*(z,\omega',\omega'') \\ \frac{\partial}{\partial z}V_b(z,\omega,\omega'') &= \int \mathrm{d}\omega' f(\omega',\omega,z)U_a^*(z,\omega',\omega'')\end{aligned} \tag{6.16}$$

and

$$\begin{aligned}\frac{\partial}{\partial z}U_b(z,\omega,\omega'') &= \int \mathrm{d}\omega' f(\omega',\omega,z)V_a^*(z,\omega',\omega'') \\ \frac{\partial}{\partial z}V_a(z,\omega,\omega'') &= \int \mathrm{d}\omega' f(\omega,\omega',z)U_b^*(z,\omega',\omega''),\end{aligned} \tag{6.17}$$

which we solve using the iterative approach put forward by Mauerer in [77].[5]

6.3.3. Comparison between analytical and rigorous approach

In order to quantify the discrepancies between the simplified analytical and rigorous numerical model we simulated an (almost) uncorrelated PDC process. The resulting squeezing values ($\text{squeezing}\,[\text{dB}] = -10\log_{10}(e^{-2r_k})$) and broadband modes shapes are depicted in Fig. 6.2 (a) to (c). In the low gain regime of about 2 dB of squeezing both models yield identical results (Fig. 6.2 (a)). When squeezing values of about 12 dB are reached the two models start to differ from each other (Fig. 6.2 (b)). The rigorous model predicts higher squeezing values and broader mode shapes, than the simplified analytical model. Significant discrepancies occur in the high gain regime about 20 dB of squeezing (Fig. 6.2 (c)).

[5] The program code is available online and can be downloaded from the publications section on our website. The current url is `https://physik.uni-paderborn.de/ag/ag-silberhorn/publications/`

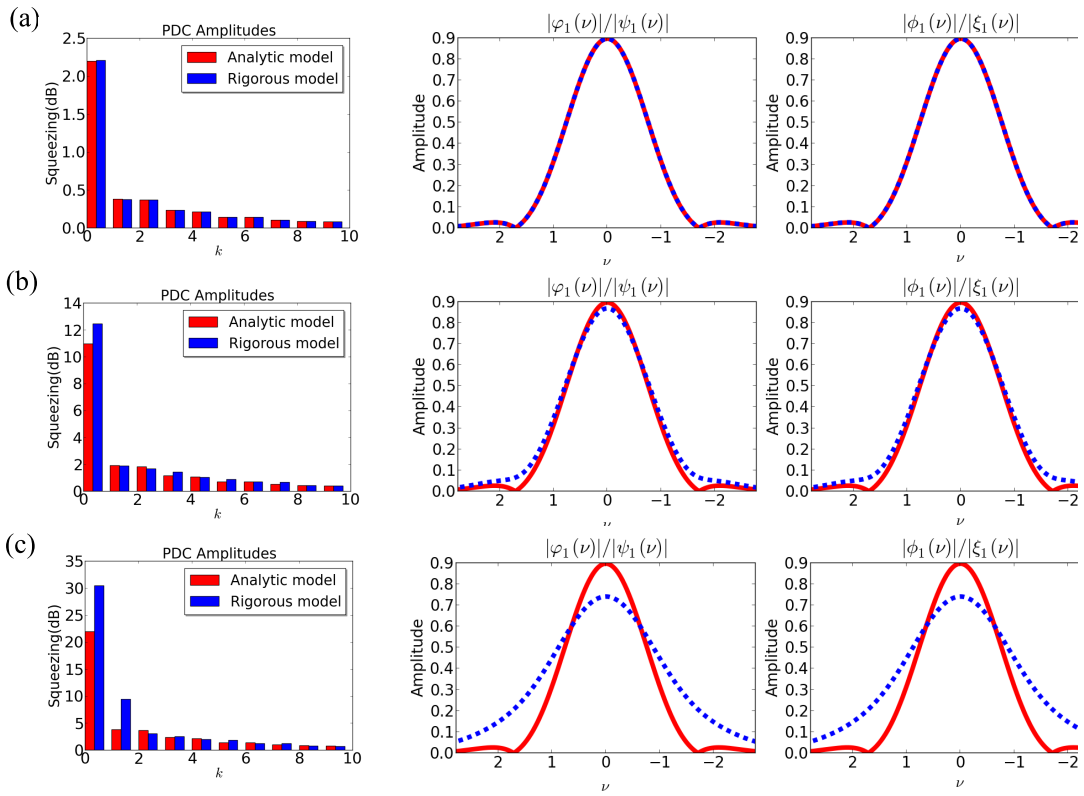

Figure 6.2.: Comparison between the rigorous and the analytical approach for an (almost) uncorrelated parametric down-conversion process. For low down-conversion rates, presented in (a), both approaches evaluate to identical results. Only in the case of rising squeezing values in (b), with squeezing values about 12dB, the two approaches start to show minor differences, which become more prominent when even higher squeezing values are considered (c).

6.4. Expansion to frequency conversion

The presented approaches to solve PDC in the high gain regime, are not restricted to parametric down-conversion processes. They are, in fact, applicable to all bilinear Hamiltonians. This enables us to adapt the presented methods to the process of quantum frequency conversion [3].

6.4.1. The frequency conversion process

The general frequency conversion process is depicted in Fig. 6.3: driven by a strong pump field two input beams $\hat{a}^{(in)}$ and $\hat{c}^{(in)}$ are, inside a medium featuring a $\chi^{(2)}$-nonlinearity,

interconverted into the two output beams $\hat{a}^{(out)}$ and $\hat{c}^{(out)}$.[6]

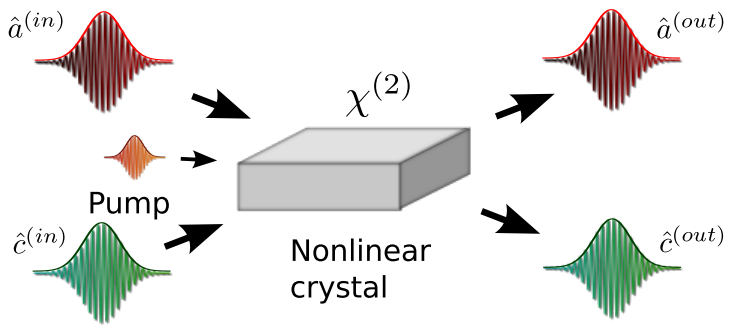

Figure 6.3.: Frequency conversion process: two input beams $\hat{a}^{(in)}$ and $\hat{c}^{(in)}$ are interconverted into the two output beams $\hat{a}^{(out)}$ and $\hat{c}^{(out)}$.

The Hamiltonian of the frequency conversion process is very similar to the PDC Hamiltonian[7] and given by

$$\hat{H}_{FC} = \frac{\epsilon_0}{3}\chi^{(2)} \int_{-\frac{L}{2}}^{\frac{L}{2}} \mathrm{d}z\, E_p^{(+)}(z,t)\hat{E}_a^{(+)}(z,t)\hat{E}_c^{(-)}(z,t) + h.c.\,, \tag{6.18}$$

where we again assume a strong, undepleted, classical pump field. Similar to parametric down-conversion the bilinear frequency conversion Hamiltonian gives rise to a linear operator transformation:

$$\begin{aligned}\hat{a}^{(out)}(\omega) &= \int \mathrm{d}\omega' U_a(\omega,\omega')\,\hat{a}^{(in)}(\omega') + \int \mathrm{d}\omega' V_a(\omega,\omega')\,\hat{c}^{(in)}(\omega') \\ \hat{c}^{(out)}(\omega) &= \int \mathrm{d}\omega' U_c(\omega,\omega')\,\hat{c}^{(in)}(\omega') + \int \mathrm{d}\omega' V_c(\omega,\omega')\,\hat{a}^{(in)}(\omega')\end{aligned} \tag{6.19}$$

Here the matrices U_a, U_c, V_a and V_c carry the physical properties of the system. However, unlike parametric down-conversion in Eq. (6.2), frequency conversion creates a passive linear optical transformation, i.e. the overall photon-number is preserved. In the broadband mode picture, and under the constraint that Eq. (6.19) must form a canonical transformation, we are able to recast the frequency conversion process in the broadband mode picture:

$$\begin{aligned}\hat{A}_k^{(out)} &= \cos(r_k)\,\hat{A}_k^{(in)} + \sin(r_k)\,\hat{C}_k^{(in)} \\ \hat{C}_k^{(out)} &= \cos(r_k)\,\hat{C}_k^{(in)} + \sin(r_k)\,\hat{A}_k^{(in)}\end{aligned} \tag{6.20}$$

[6] When the input photon fuses with the pump photon to create the output photon this process is labelled sum-frequency conversion $\omega_{out} = \omega_p + \omega_{in}$. When an output photon with frequency $\omega_{out} = \omega_{in} - \omega_p$ is emitted this process is referred to as difference frequency generation. Every crystal always supports both process and we consequently refer to the overall process as frequency conversion.

[7] In fact the frequency conversion Hamiltonian is already present in Eq. (4.10).

If we, again, assume that the input and output modes are of the same shape we are able to write the frequency conversion unitary as

$$\hat{U}_{FC} = \bigotimes_k \exp\left[(-r_k)\left(\hat{A}_k\hat{C}_k^\dagger - \hat{A}_k^\dagger\hat{C}_k\right)\right]. \tag{6.21}$$

According to Eq. (6.20) and Eq. (6.21) frequency conversion acts similar to a beam-splitter operation on the ultrafast pulse modes $\hat{A}_k$ and $\hat{C}_k$.

6.4.2. Frequency conversion as a quantum pulse gate

Depending on the efficiency of the process the ultrafast pulses are partly transmitted through the crystal and partly converted into another optical mode. This enables the creation of quantum pulse gates [49, 70, 71], which convert, from a multi-mode input $\{\hat{A}_k\}$, a single optical mode $\hat{A}_i$ with unit efficiency into the mode $\hat{C}_i$ (see Fig. (6.4)), whereas the remaining $\{\hat{A}_k\} \setminus \hat{A}_i$ are transmitted unperturbed.

This can be achieved by engineering a single-mode frequency conversion process, i.e. all r_k elements in Eq. (6.21), but one, are zero. By adjusting the pump amplitude to yield unit conversion efficiency for the remaining process we obtain the desired result.

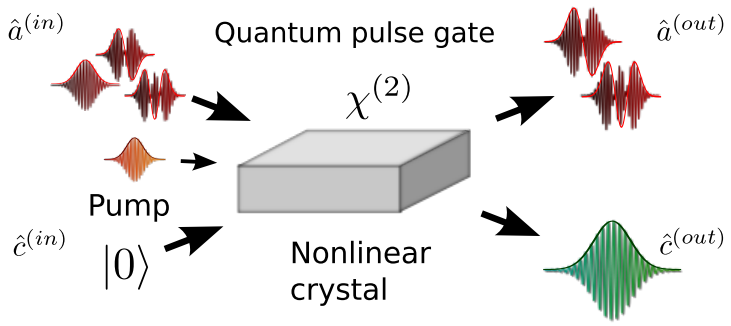

Figure 6.4.: Frequency conversion enables the creation of an ultrafast quantum pulse gate, where one optical pulse, of a multi-mode input beam, is converted with unit efficiency, whereas the rest is transmitted through the crystal unperturbed.

Since the Hamiltonians of frequency conversion in Eq. (6.18) and of parametric down-conversion Eq. (4.11) are very similar we are able to directly extend our developed theoretical framework for PDC to frequency conversion. Following the discussion in 6.3 we build a simplified analytical model, neglecting time-ordering effects, and rigorous numerical model, including time-ordering effects, of frequency conversion in the high gain regime [3].

6.4.3. Quantum pulse gate performance

This developed theoretical framework enables us to benchmark frequency conversion as a quantum pulse gate. For this purpose we engineered an almost uncorrelated frequency conversion process with varying pump powers and evaluated the achievable conversion amplitudes $\sin(r_k)$ and mode functions $\hat{A}_k$ and $\hat{C}_k$. The results are depicted in Fig. (6.5).

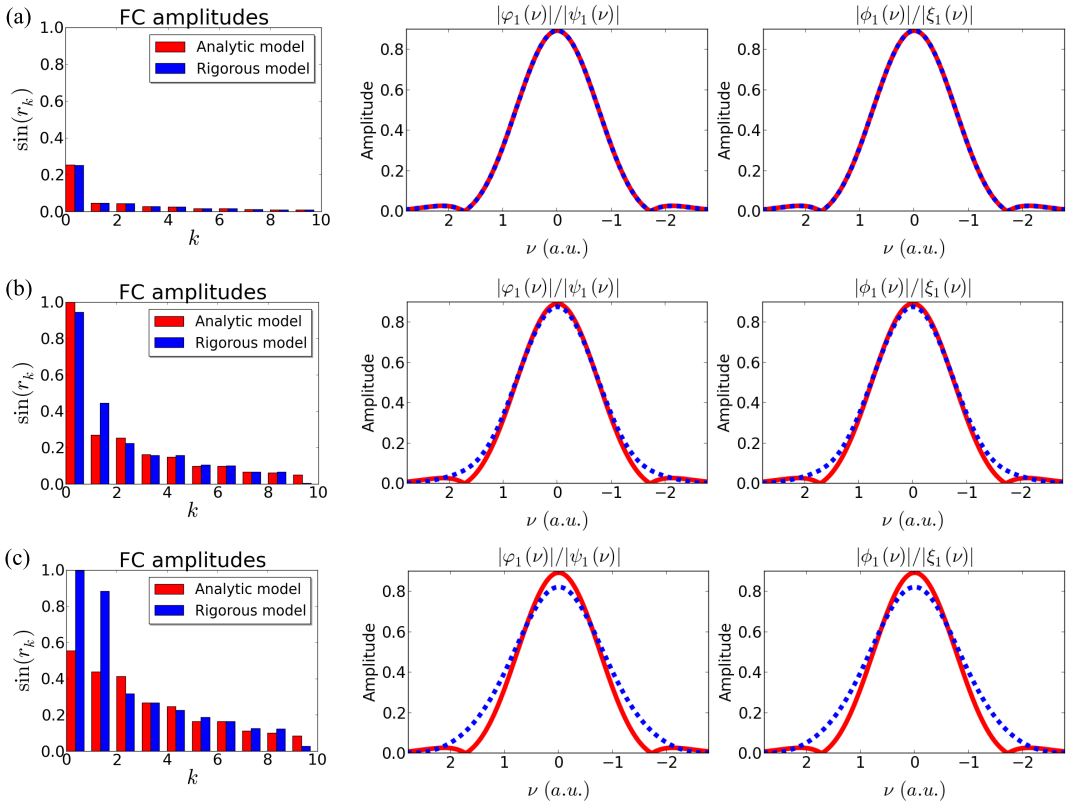

Figure 6.5.: Comparison between the rigorous numerical and simplified analytical model for an (almost) uncorrelated frequency conversion process. For rising conversion efficiencies the time-ordering effects introduce additional multi-mode contributions, which decrease the performance of quantum pulse gates, based on frequency conversion processes.

In principle we aim at engineering a single-mode frequency conversion process, where only the very first r_k mode r_0 is excited. However already in the low gain regime, depicted in Fig. (6.5) (a), the frequency conversion process is not perfectly single-mode. This multi-mode character stems from the side-peaks introduced by the sinc function in the phase-matching function, which can, in principle, be removed via the use of hypergrating structures [80]. In the high gain regime however (Fig. (6.5) (b) and (c)), it is evident that the time-ordering effects, considered in the rigorous numerical model, introduce an

additional multi-mode character when unit conversion efficiency is approached.

Consequently, our investigations revealed, that standard frequency conversion processes will not be able to create a perfect quantum pulse gate. Both the sinc side-peaks, as well as the time-ordering effects limit its performance. Whether hypergrating structures, adapted pump shapes or other enhancements are able to resolve this issue remains an open research question.

6.5. Conclusion

In conclusion we developed two models for ultrafast PDC in the high-gain regime: A simplified analytical and a rigorous numerical model. Our analysis revealed that the analytical model yields the correct PDC process parameters up to squeezing values about 12 dB.

The developed theoretical framework permits us to effectively work with PDC in the high gain regime (see Chap. 9 and 10) and enables us to perform new benchmarks of PDC in the framework of quantum information applications (see Chap. 10).

Furthermore we were able to extend the presented theoretical framework to the process of frequency conversion, which enabled us to benchmark the prospects of engineered frequency processes to serve as a quantum pulse gate.

Theory of quantum frequency conversion and parametric down-conversion in the high gain regime

Andreas Christ[1], **Benjamin Brecht**[1], **Wolfgang Mauerer**[2,3], **and Christine Silberhorn**[1,2]

[1]Applied Physics, University of Paderborn, Warburger Straße 100, 33098 Paderborn, Germany
[2]Max Planck Institute for the Science of Light, Günther-Scharowsky Straße 1/Building 24, 91058 Erlangen, Germany
[3]Siemens AG, Corporate Research and Technologies, Wladimirstrasse 3, 91058 Erlangen, Germany

E-mail: andreas.christ@uni-paderborn.de

Abstract. Frequency conversion (FC) and parametric down-conversion (PDC) are among the most widely used nonlinear processes for the implementation of quantum optical experiments. Parametric down-conversion enables the efficient creation of quantum states ranging from photon-number states over squeezers to EPR-states. Frequency conversion gives rise to technologies enabling efficient atom-photon coupling, ultrafast pulse gates and enhanced detection schemes. However, despite their widespread deployment, their theoretical treatment remains challenging. Especially the multi-photon components in the high gain regime, as well as the explicit time-dependence of the involved Hamiltonians hamper an efficient theoretical description of these nonlinear optical processes.

In this paper we investigate these effects and put forward two models which enable a full description of FC and PDC in the high gain regime. We present a rigorous numerical model relying on the solution of coupled integro-differential equations which covers the complete dynamics of the process. And, as an alternative, we develop a simplified model that, at the expense of neglecting time-ordering effects, enables an analytical solution which approximates the correct solution with high fidelity in a broad parameter range.

The developed fundamental understanding of frequency conversion and parametric down-conversion gives valuable insights into the quantum properties of the processes, extends the current theoretical descriptions, and simplifies considerably the engineering process for future quantum information applications using FC and PDC.

1. Introduction

A fundamental building block of quantum information and quantum communication applications are nonlinear optical processes. In experimental implementations of photonic quantum systems parametric down-conversion (PDC) and frequency conversion (FC) are omnipresent. Parametric down-conversion enables the generation of various quantum states ranging from single photons [1, 2, 3, 4, 5] over entangled photon-pairs [6, 7, 8] up to squeezers [9, 10] and EPR-states [11, 12]. Frequency conversion is applied for frequency translations between different wavelengths [13, 14, 15] which enables interfaces between quantum systems, in particular atom-photon coupling [16, 17], quantum pulse gates [18, 19, 20], and efficient quantum state detection [21, 22, 23, 24, 25].

Their deployment in quantum enhanced applications requires a detailed theoretical understanding of the corresponding nonlinear interactions. A variety of models have been developed for PDC [26, 27, 28, 29, 12, 30] and FC [18, 19, 20, 15, 31]. They vary from straightforward perturbation approaches to much more rigorous treatments. The crucial issue in these derivations is firstly the fact that multi-photon effects have to be considered during the interaction, and secondly the problem that the involved electric field operators and consequently Hamiltonians do *not* commute in time. In this paper we address these issues and build two theoretical models for FC and PDC: a rigorous numerical model based on the theoretical framework of Mikhail I. Kolobov [32], and a simplified analytical approach. Both models take into account higher-order photon number effects and are hence suitable to describe FC and PDC in the high gain regime. We analyse their performance and the quality of their predictions over a broad parameter range which enables us to suggest when a simple analytic modelling of the processes is sufficient and when the rigorous approach has to be applied.

The paper is structured into two main parts: In sections 2 to 9 we study frequency conversion. Our investigation of this process is divided into eight sub chapters: After a short description of the basic principles of frequency conversion in section 2, section 3 discusses the Hamiltonian of the process. The general properties of the conversion are outlined in section 4. In section 5 we introduce the no time-ordering approximation which forms the basis for the analytical solution of the frequency conversion process and elaborate on its implications. In section 6 we derive the analytic solution excluding time-ordering effects. In section 7 we put forward the rigorous approach relying on the solution of coupled integro-differential equations. The differences between the two models are quantified in section 8. Finally, in section 9, we elaborate on the impacts of our work on the design and performance of frequency conversion processes for quantum enhanced applications. The same reasoning is then applied to the process of parametric down-conversion in sections 10 onward. Section 18 concludes the paper and summarizes our findings. Appendix A to Appendix F contain additional information and further calculations.

2. FC: Overview

A general frequency conversion process is sketched in figure 1. Mediated by the nonlinearity of the crystal and a strong pump beam two input fields $\hat{a}^{(in)}$ and $\hat{c}^{(in)}$ are interconverted into two output fields $\hat{a}^{(out)}$ and $\hat{c}^{(out)}$. This frequency conversion process is more commonly known as sum frequency generation (SFG), when the input

beam in combination with the pump beam generates an output field at a higher frequency $\omega_{out} = \omega_{in} + \omega_p$, or difference frequency generation (DFG), when a field with frequency $\omega_{out} = \omega_{in} - \omega_p$ is created.‡

The distinction between sum-frequency and difference frequency generation arises via the input wave which is fed in either the $\hat{a}^{(in)}$ or $\hat{c}^{(in)}$ port. In the scope of this paper $\hat{a}^{(in)} \rightarrow \hat{c}^{(out)}$ depicts a sum-frequency generation process and $\hat{c}^{(in)} \rightarrow \hat{a}^{(out)}$ labels difference frequency generation. Each crystal configuration always supports both processes simultaneously and we refer to the overall system as frequency conversion.

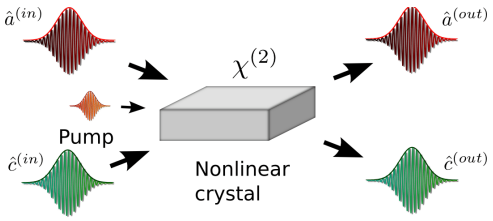

Figure 1. Sketch of the frequency conversion process. Mediated by the strong pump field and the $\chi^{(2)}$-nonlinearity of the medium parts of the fields $\hat{a}^{(in)}$ and $\hat{c}^{in}$ are interconverted into the two output fields $\hat{a}^{(out)}$ and $\hat{c}^{(out)}$.

In this paper we go beyond the standard monochromatic single-mode description of frequency conversion and consider a multitude of frequencies interacting with each other during the frequency conversion process. This becomes especially important for pulsed frequency conversion experiments where wave packets, spanning several nanometers in width, interact with each other. In the following chapters we derive the properties of this transformation and compare the accuracy of different theoretical models.

3. FC: Hamiltonian

We first define the electric field operators of an optical wave inside a nonlinear medium as [33]

$$\begin{aligned}\hat{E}^{(+)}(z,t) &= \hat{E}^{(-)\dagger}(z,t) \\ &= \imath \left(\frac{\hbar\, c}{4\pi\epsilon_0 A\, n^3(k_0)}\right)^{\frac{1}{2}} \int \mathrm{d}k\, \sqrt{\omega(k)}\, \exp\left[\imath(kz - \omega(k)t)\right] \hat{a}(k), \end{aligned} \tag{1}$$

where A labels the transverse quantization area in the material [34]. We use the slowly varying envelope approximation, i.e. the bandwidth $\Delta\omega$ of the considered electric fields is small compared to their central frequency ω_0 ($\Delta\omega \ll \omega_0$) and hence treat the dispersion term in front of the integral $n(k_0)$ in (1) as a constant, using the value at the central wave vector k_0. This approximation is justified since, in the remainder of this paper, we only consider electric fields not too broad in frequency, compared to their central frequency, and take into account the rather flat dispersion

‡ In classical nonlinear optics, DFG is understood as a stimulated process. The bright pump field has the highest frequency and the process is seeded with a weak input field, which is enhanced through continuous conversion of pump photons. We, in contrast, assume a weak input field, which has the highest frequency and the 'seed' is the bright pump field (see [18] for details).

in nonlinear crystals. Finally $\hat{a}(k)$ is the standard single-photon annihilation operator which destroys a single-photon in mode k and obeys

$$\left[\hat{a}(k), \hat{a}(k')^\dagger\right] = \delta(k-k') \qquad [\hat{a}(k), \hat{a}(k')] = 0. \tag{2}$$

In this paper we restrict ourselves to electric fields in one dimension, this means we assume a fully collinear propagation of the interacting fields along one axis in a single-spatial mode, since a three dimensional treatment does not offer further physical insight into the properties of the process and clutters the calculations.

The Hamiltonian of the frequency conversion process consists of two parts: The Hamiltonian $H_0^{(x)}$ describing the free propagation of the electromagnetic waves through the medium for each of the involved fields [32]

$$\hat{H}_0^{(x)}(t) = \frac{2\epsilon_0 A\, n_{k_0^x}^3}{c} \int \mathrm{d}z\, \hat{E}_x^{(-)}(z,t)\hat{E}_x^{(+)}(z,t), \tag{3}$$

where the factor in front of the Hamiltonian appears due to the normalization of the electric fields operators in (1) [32]. The interaction Hamiltonian of the frequency conversion process is given by [35, 36, 18, 19]

$$\hat{H}_I^{(FC)}(t) = \epsilon_0 \int \mathrm{d}z\, \chi^{(2)}(z)\, \hat{E}_p^{(+)}(z,t)\hat{E}_a^{(+)}(z,t)\hat{E}_c^{(-)}(z,t) + h.c.\,. \tag{4}$$

$\hat{E}_p^{(+)}(z,t)$ labels the pump field driving the frequency conversion process and $\hat{E}_a^{(+)}(z,t), \hat{E}_c^{(-)}(z,t)$ are the two fields which are interconverted. In the derivation of this Hamiltonian we used the rotating wave approximation and hence only regard the frequency conversion terms of the nonlinear optical process while neglecting the parametric down-conversion and further nonlinear interactions. The pump field driving the frequency conversion process is a strong optical wave. We hence treat it as a classical field:

$$E_p^{(+)}(z,t) = E_p^{(-)*}(z,t) = \mathcal{A}_p \int \mathrm{d}k\, \alpha\left[\omega(k)\right] \exp\left[\imath(kz - \omega(k)t)\right] \tag{5}$$

Here $\mathcal{A}_p$ labels the pump amplitude and $\alpha\left[\omega(k)\right]$ its spectral distribution ranging from $\delta(\omega-\omega_c)$ for cw-laser sources up to more complicated forms in the case of pulsed laser systems. We further assume that the pump field is not depleted during propagation through the crystal since only a minor part of the strong pump beam is lost during the frequency conversion process. The interaction Hamiltonian (4) becomes:

$$\hat{H}_I^{(FC)}(t) = \epsilon_0 \int \mathrm{d}z\, \chi^{(2)}(z)\, E_p^{(+)}(z,t)\hat{E}_a^{(+)}(z,t)\hat{E}_c^{(-)}(z,t) + h.c.\,. \tag{6}$$

Combining (3) and (6) the process of frequency conversion is described by the overall Hamiltonian:

$$\hat{H}_{FC}(t) = \hat{H}_0^{(a)}(t) + \hat{H}_0^{(c)}(t) + \hat{H}_I^{(FC)}(t) \tag{7}$$

There are a variety of different constants involved in the definition of the frequency conversion Hamiltonian in (7) (see (1), (3), (5) and (6)). However most are dependent on the initial definitions of the interacting fields. In the remainder of this paper we merge all of them into a coupling value depicting the overall efficiency of the frequency conversion process rendering the presented calculations independent of individual notations.

4. FC: General properties

The frequency conversion Hamiltonian in (7) generates the unitary transformation

$$\hat{U}_{FC} = \mathcal{T} \exp\left[-\frac{\imath}{\hbar}\int \mathrm{d}t\, \hat{H}_{FC}(t)\right]. \tag{8}$$

In (8) the *time-ordering* operator $\mathcal{T}$ is crucial, because the electric field operators in $\hat{H}_{FC}(t)$ are time-dependent. In turn, the Hamiltonian does not commute at different points in time, which renders finding a solution difficult. The structure of (8) already gives valuable insights into the properties of the system. The Hamiltonian in (8) is bilinear in its electric field operators — the pump is treated as a classical wave — and the solution hence takes the form of a linear operator transformation [37, 38, 39].§ In the monochromatic picture the solution is of the form [18]:

$$\begin{aligned}\hat{a}^{(out)}(\omega) &= \cos(r)\hat{a}^{(in)}(\omega) + \sin(r)\hat{c}^{(in)}(\omega')\\ \hat{c}^{(out)}(\omega') &= \cos(r)\hat{c}^{(in)}(\omega') - \sin(r)\hat{a}^{(in)}(\omega)\end{aligned} \tag{9}$$

A single frequency $\hat{a}^{(in)}(\omega)$ has a certain conversion amplitude $\sin(r)$ which defines which part of the beam will be converted to $\hat{c}^{(out)}(\omega')$, via sum-frequency or difference frequency generation, whereas the rest is transmitted without change to $\hat{a}^{(out)}(\omega)$. This mathematical structure is very similar to the transmissivity and reflectivity of a beam-splitter [40]. In the frequency conversion case, however, not two spatial modes but two optical modes at different frequencies are coupled with each other.

This behavior is not immediately visible in the multimode regime, where we have to consider the conversion of many frequencies:

$$\begin{aligned}\hat{a}^{(out)}(\omega) &= \int \mathrm{d}\omega' U_a(\omega,\omega')\,\hat{a}^{(in)}(\omega') + \int \mathrm{d}\omega' V_a(\omega,\omega')\,\hat{c}^{(in)}(\omega')\\ \hat{c}^{(out)}(\omega) &= \int \mathrm{d}\omega' U_c(\omega,\omega')\,\hat{c}^{(in)}(\omega') - \int \mathrm{d}\omega' V_c(\omega,\omega')\,\hat{a}^{(in)}(\omega')\end{aligned} \tag{10}$$

Here the functions $U_{a/c}(\omega,\omega')$ in (10) define which parts of the different frequencies of the input beams pass the crystal unperturbed, whereas the $V_{a/c}(\omega,\omega')$ functions give the portions of the beams which are converted via sum frequency or difference frequency generation.

In order to unravel the underlying structure we use the constraint that the frequency conversion process is a unitary transformation and hence (10) has to form a canonical transformation [38, 39]. This imposes several conditions on the properties of the solution which we study in detail in Appendix A. Under this constraint and with the help of the Bloch-Messiah decomposition we rewrite (10) as

$$\begin{aligned}\hat{A}_k^{(out)} &= \cos(r_k)\,\hat{A}_k^{(in)} + \sin(r_k)\,\hat{C}_k^{(in)}\\ \hat{C}_k^{(out)} &= \cos(r_k)\,\hat{C}_k^{(in)} - \sin(r_k)\,\hat{A}_k^{(in)},\end{aligned} \tag{11}$$

where $\hat{A}_k$ and $\hat{C}_k$ are broadband single-photon destruction operators [41] defined as:

$$\begin{aligned}\hat{A}_k^{(out)} &= \int \mathrm{d}\omega\, \varphi_k(\omega)\,\hat{a}^{(out)}(\omega) \qquad & \hat{C}_k^{(out)} &= \int \mathrm{d}\omega\, \xi_k(\omega)\,\hat{c}^{(out)}(\omega)\\ \hat{A}_k^{(in)} &= \int \mathrm{d}\omega\, \psi_k(\omega)\,\hat{a}^{(in)}(\omega) \qquad & \hat{C}_k^{(in)} &= \int \mathrm{d}\omega\, \phi_k(\omega)\,\hat{c}^{(in)}(\omega)\end{aligned} \tag{12}$$

§ Solving the process via the Heisenberg equation of motion (see section 7), yields a linear operator valued differential equation. Linear operator valued differential equations are solved by linear Bogoliubov transformation, i.e. the solution will be of the form (10). Furthermore with the help of the Bloch-Messiah reduction, discussed in Appendix A, we are able to rewrite the general linear Bogoliubov transformation [39] into the form depicted in (11).

This means that broadband frequency conversion is equivalent to the transformation of an orthonormal set of optical pulses given by the broadband mode shapes in (12). Each individual pulse is, independently from the rest, partially converted and partially transmitted. According to (11) we consequently are able to regard the overall frequency conversion process as a quantum pulse gate [19, 18, 20] which, depending on the efficiency of the process, transmits the incoming pulses unperturbed or switches them via frequency conversion.

The crucial parameters of this transformation are firstly the conversion amplitudes r_k which give the efficiency of the process — conversion efficiency $= \sin^2(r_k)$ — and secondly the broadband mode shapes $\varphi_k(\omega)$, $\xi_k(\omega)$, $\psi_k(\omega)$ and $\phi_k(\omega)$ that define the range of frequencies which are interconverted.

5. FC: Time-ordering approximation

In order to obtain some first insights into the frequency conversion process we use perturbation theory. In the case of a time-dependent Hamiltonian a Dyson series expansion is necessary [42]. This approach was studied in detail by Agata M. Brańczyk in [30] and [43]. Here we shortly recapitulate the general approach, starting with the Dyson series expansion of (8):

$$\begin{aligned}\hat{U}_{FC} &= \mathcal{T}\exp\left[-\frac{\imath}{\hbar}\int \mathrm{d}t\,\hat{H}_{FC}(t)\right]\\ &= \mathbb{1} - \frac{\imath}{\hbar}\int_{-\infty}^{\infty}\mathrm{d}t_1\,\hat{H}_{FC}(t_1)\\ &\quad + \left(\frac{\imath}{\hbar}\right)^2\int_{-\infty}^{\infty}\mathrm{d}t_1\,\hat{H}_{FC}(t_1)\int_{-\infty}^{t_1}\mathrm{d}t_2\,\hat{H}_{FC}(t_2) + \cdots\end{aligned} \tag{13}$$

In our case we regard the system long after the interaction in the crystal has taken place and consequently use plus and minus infinity as the overall bounds for the time-integration.

Unfortunately it is not trivial to perform the Dyson series expansion for FC, because coupled time integrals appear. To simplify this evaluation we introduce the time-ordering approximation. Hereby we approximate (8) by ignoring the time-ordering operator $\mathcal{T}$. By dropping $\mathcal{T}$ in (8) a simple Taylor series expansion becomes sufficient:

$$\begin{aligned}\hat{U}_{FC} &= \exp\left[-\frac{\imath}{\hbar}\int \mathrm{d}t\,\hat{H}_{FC}(t)\right]\\ &= \mathbb{1} - \frac{\imath}{\hbar}\int_{-\infty}^{\infty}\mathrm{d}t_1\,\hat{H}_{FC}(t_1)\\ &\quad + \frac{1}{2}\left(\frac{\imath}{\hbar}\right)^2\int_{-\infty}^{\infty}\mathrm{d}t_1\,\hat{H}_{FC}(t_1)\int_{-\infty}^{\infty}\mathrm{d}t_2\,\hat{H}_{FC}(t_2) + \cdots\end{aligned} \tag{14}$$

Note the differences in the integration ranges and the expansion coefficients in (13) and (14) when terms of second order and higher are considered.

To investigate the differences between the two approaches we explicitly calculate the perturbation series up to second order. For this purpose it is beneficial to work with the electric field operators of (1) in the ω-representation [33]:

$$\hat{E}^{(+)}(z,t) = \hat{E}^{(-)\dagger}(z,t)$$

$$= \imath \left(\frac{\hbar}{4\pi\epsilon_0 c\, A\, n(\omega_0)} \right)^{\frac{1}{2}} \int \mathrm{d}\omega \, \sqrt{\omega} \exp\left[\imath(k(\omega)z - \omega t)\right] \hat{a}(\omega) \tag{15}$$

We also perform our calculations in the interaction picture, this means we move into a new reference frame where the effects of free propagation are not present and hence do not need to consider the free propagation Hamiltonians. Finally we assume a crystal featuring a constant $\chi^{(2)}$-nonlinearity extending from $-\frac{L}{2}$ to $\frac{L}{2}$. The frequency conversion Hamiltonian from (7) takes the form

$$\begin{aligned} \hat{H}^{(FC)}(t) &= \epsilon_0 \chi^{(2)} \int_{-\frac{L}{2}}^{\frac{L}{2}} \mathrm{d}z \, E_p^{(+)}(z,t_1) \hat{E}_a^{(+)}(z,t_1) \hat{E}_c^{(-)}(z,t_1) + h.c. \\ &= \epsilon_0 \chi^{(2)} L \int \mathrm{d}\omega_p \int \mathrm{d}\omega_a \int \mathrm{d}\omega_c \, \alpha(\omega_p) \operatorname{sinc}\left(\frac{\Delta k(\omega_p, \omega_a, \omega_c) L}{2} \right) \\ &\times \exp\left(-\imath \Delta\omega t\right) \hat{a}(\omega_a) \hat{c}^\dagger(\omega_c) + h.c. \end{aligned} \tag{16}$$

where we introduced the two abbreviations $\Delta k(\omega_p, \omega_a, \omega_c) = k_p(\omega_p) + k_a(\omega_a) - k_c(\omega_c)$ and $\Delta\omega = \omega_p + \omega_a - \omega_c$.

The approximations performed when ignoring time-ordering effects are located in the time-integrations in the term $\exp(-\imath\Delta\omega t)$. The time-integration of the first-order term gives identical results for both the Taylor and Dyson series expansion:

$$\int_{-\infty}^{\infty} \exp\left(-\imath\Delta\omega t\right) = 2\pi\delta(\Delta\omega) \tag{17}$$

From a physical point of view the obtained delta function $\delta(\Delta\omega)$ describes the energy conservation between the three interacting photons: the input, the pump, and the output photon.

In the second order expansion the time integrals in two perturbation approaches start to deviate from each other. The time-integration of the Taylor series in (14) yields

$$\begin{aligned} &\int_{-\infty}^{\infty} \mathrm{d}t_1 \int_{-\infty}^{\infty} \mathrm{d}t_2 \exp\left(-\imath\Delta\omega t_1\right) \exp\left(-\imath\Delta\omega' t_2\right) \\ &= \delta(\Delta\omega)\delta(\Delta\omega') \end{aligned} \tag{18}$$

which is just two times the result of the first-order expansion. In the Dyson series however we obtain a different result [30]:

$$\begin{aligned} &\int_{-\infty}^{\infty} \mathrm{d}t_1 \int_{-\infty}^{t_1} \mathrm{d}t_2 \, \exp\left[-\imath\Delta\omega t_1\right] \exp\left[-\imath\Delta\omega' t_2\right] \\ &= 2\pi^2 \, \delta(\Delta\omega + \Delta\omega') \left(\delta(\Delta\omega - \Delta\omega') + \frac{1}{\pi} \frac{1}{\Delta\omega - \Delta\omega'} \right) \end{aligned} \tag{19}$$

This term shows the crucial difference between the inclusion and the exclusion of time-ordering effects. When we exclude time-ordering effects the time-integrations in every order yield delta functions $\delta(\omega_p + \omega_a - \omega_c)$ between three different frequencies. We can interpret this mathematical expression by a physical process where only three photons interact with each other. This means that even in the case of a multitude of photon conversions take place in the overall process the energy is still conserved in each photon triplet. Effectively this means that the spectral properties of the interacting photons are identical in every order of the perturbation series.

This is quite different from the Dyson expansion. Here delta functions of the form $\delta(\Delta\omega + \Delta\omega')$ appear in the second-order expansion. From a physical point of view this delta function describes energy conservation which does not occur between the three but between six photons. Either the SFG (DFG) of two photons takes place simultaneously or a SFG (DFG) with successive DFG (SFG) conversion of a single-photon takes place.‖ This enables an enhanced flexibility in the available energy range and modifies the solution, especially its spectral properties, with respect to the Taylor expansion. Since the energy, in these terms, only has to be conserved for the *overall* process and not the individual photon triplets the constraints imposed by energy conservation are relaxed. A graphical representation of this effect in the third-order expansion is shown in figure 2.

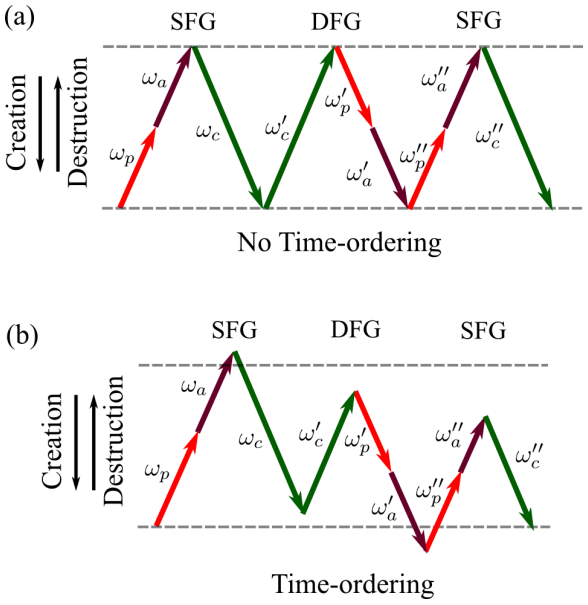

Figure 2. Schematic diagrams depicting the energy conservation during successive SFG and DFG processes neglecting time-ordering effects (Analytic model) (a) and including time-ordering (Rigorous model) (b). Neglecting time-ordering effects the energy is conserved between the three photons in each individual SFG/DFG process, whereas the rigorous model including time-ordering effects only requires energy conservation during the overall process [30].

The time-ordering approximation will consequently give accurate results as long as the conversion efficiency is not too high and the first-order perturbation expansion is the dominant term in the solution.

6. FC: Analytic model excluding time-ordering effects

The huge advantage of neglecting time-ordering effects in frequency conversion is the fact that it enables us to build an analytical model of frequency conversion, which

‖ The individual orders n of the perturbation expansion do not directly correspond to the conversion of n photons, multiple back and forth conversions of a single-photon can appear as well. In order to obtain the full dynamics of the process all orders have to be considered.

is highly beneficial since it enables quick and straightforward access to the process properties:

$$\hat{U}_{FC} = \exp\left[-\frac{\imath}{\hbar}\int \mathrm{d}t\, \hat{H}_I^{(FC)}(t)\right] \tag{20}$$

This formula is identical to (8) except that we dropped the time-ordering operator $\mathcal{T}$ and work in the interaction picture. It enables us to directly perform the time-integration in the exponential function. As in the previous section we perform our calculations in the ω-representation and again we assume a crystal featuring a constant $\chi^{(2)}$-nonlinearity extending from $-\frac{L}{2}$ to $\frac{L}{2}$. After a straightforward calculation we obtain

$$\begin{aligned}\int \mathrm{d}t\, \hat{H}_I^{(FC)}(t) =& \int \mathrm{d}t\, \epsilon_0\chi^{(2)} \int_{-\frac{L}{2}}^{\frac{L}{2}} \mathrm{d}z\, E_p^{(+)}(z,t)\hat{E}_a^{(+)}(z,t)\hat{E}_c^{(-)}(z,t) + h.c.\\ =& B\int \mathrm{d}\omega_a \int \mathrm{d}\omega_c\, \alpha\left(\omega_c-\omega_a\right)\\ &\times \operatorname{sinc}\left(\frac{\Delta k(\omega_a,\omega_c)L}{2}\right)\hat{a}(\omega_a)\hat{c}^\dagger(\omega_c) + h.c.\end{aligned} \tag{21}$$

where we merged all constants into the overall factor B and $\Delta k(\omega_a,\omega_c) = k_p(\omega_c - \omega_a) + k_a(\omega_a) - k_c(\omega_c)$. Details of this calculation are given in [18]. Defining

$$f(\omega_a,\omega_c) = B\,\alpha\left(\omega_c-\omega_a\right)\operatorname{sinc}\left(\frac{\Delta k(\omega_a,\omega_c)L}{2}\right), \tag{22}$$

the unitary transformation generated by (20) takes on the form:

$$\hat{U}_{FC} = \exp\left[-\frac{\imath}{\hbar}\left(\int \mathrm{d}\omega_a \int \mathrm{d}\omega_c\, f(\omega_a,\omega_c)\hat{a}(\omega_a)\hat{c}^\dagger(\omega_c) + h.c.\right)\right] \tag{23}$$

With the help of the singular-value-decomposition theorem [44] we recast this solution in the broadband mode formalism presented in (11). At first we diagonalize the Hamiltonian by decomposing the exponent in (23), via a Schmidt decomposition, as:

$$\begin{aligned}-\frac{\imath}{\hbar}f(\omega_a,\omega_c) &= \sum_k (-r_k)\psi_k(\omega_a)\phi_k^*(\omega_c)\\ -\frac{\imath}{\hbar}f^*(\omega_a,\omega_c) &= \sum_k r_k\psi_k^*(\omega_a)\phi_k(\omega_c)\end{aligned} \tag{24}$$

Here both $\{\psi_k(\omega_a)\}$ and $\{\phi_k(\omega_c)\}$ each form a complete set of orthonormal functions and $r_k \in \mathcal{R}^+$. Employing equation (24) we rewrite the unitary frequency conversion transformation in (23) as:

$$\begin{aligned}\hat{U}_{FC} = \exp\Bigg[&\sum_k (-r_k)\int \mathrm{d}\omega_a\, \psi_k(\omega_a)\hat{a}(\omega_a)\int \mathrm{d}\omega_c \phi_k^*(\omega_c)\hat{c}^\dagger(\omega_c)\\ &+ r_k\int \mathrm{d}\omega_a \psi_k^*(\omega_a)\hat{a}^\dagger(\omega_a)\int \mathrm{d}\omega_c\phi_k(\omega_c)\hat{c}(\omega_c)\Bigg]\end{aligned} \tag{25}$$

With the help of the broadband mode operators defined in (12) it takes on the form

$$\begin{aligned}\hat{U}_{FC} &= \exp\left[\sum_k (-r_k)\left(\hat{A}_k\hat{C}_k^\dagger - \hat{A}_k^\dagger\hat{C}_k\right)\right]\\ &= \bigotimes_k \exp\left[(-r_k)\left(\hat{A}_k\hat{C}_k^\dagger - \hat{A}_k^\dagger\hat{C}_k\right)\right].\end{aligned} \tag{26}$$

The solution of (26) is well known and, in the Heisenberg pictures, it reads [37]:

$$\begin{aligned}\hat{A}_k^{(out)} &= \cos(r_k)\hat{A}_k^{(in)} + \sin(r_k)\hat{C}_k^{(in)} \\ \hat{C}_k^{(out)} &= \cos(r_k)\hat{C}_k^{(in)} - \sin(r_k)\hat{A}_k^{(in)}\end{aligned} \tag{27}$$

This simplified analytic model features exactly the structure required by the canonical commutation relations discussed in section 4. Only the additional fact that the input modes and output modes in this simplified model are always of identical shape differs from the general solution (11).

It is evident that this treatment ignoring time-ordering effects enables a straightforward analytic solution of the frequency conversion process. In contrast to the perturbation approach in section 5 we do not require to evaluate a perturbation series up to infinite order and, in some cases, even the SVD can be performed analytically and hence no computational effort is required at all [45]. This enables the efficient engineering and design of frequency conversion processes as long as the applied approximations hold.

7. FC: Rigorous theory including time-ordering effects

In order to obtain a rigorous solution of frequency conversion we have to include the effects of time-ordering and the corresponding relaxed energy conservation conditions into our calculations. For this purpose we change our analysis method and regard the frequency conversion process in the Heisenberg picture. This approach was already utilized for frequency conversion in nonlinear optical fibers in [14, 20] and is common for parametric down-conversion [32, 29, 27, 28, 46, 47, 48, 49, 50]. In order to solve the corresponding Heisenberg equations of motion we adapt the work of Mikhail I. Kolobov on PDC in [32] to frequency conversion. It enables the complete time-ordered solution of the frequency conversion process without having to perform the Dyson series expansion up to infinite orders. As a first step we redefine the electric field operators in (1) according to [32]

$$\hat{a}(z,t) = \frac{1}{\sqrt{2\pi k_0}} \int \mathrm{d}k \, \sqrt{\omega(k)} \exp\left[\imath \left(kz - \omega(k)t\right)\right] \hat{a}(k) \tag{28}$$

$$\hat{c}(z,t) = \frac{1}{\sqrt{2\pi k_0}} \int \mathrm{d}k \, \sqrt{\omega(k)} \exp\left[\imath \left(kz - \omega(k)t\right)\right] \hat{c}(k) \tag{29}$$

The Heisenberg equation of motion for $\hat{a}(z,t)$ reads:

$$\frac{d}{dt}\hat{a}(z,t) = \frac{\imath}{\hbar}\left[\hat{H}_{FC}(t), \hat{a}(z,t)\right] \tag{30}$$

We first calculate the commutator of $\hat{a}(z,t)$ with the free space Hamiltonian $\hat{H}_0^{(a,c)}(t)$. The commutation relation with the free space Hamiltonian $\hat{H}_0^{(c)}(t)$ directly results in zero whereas the commutator with $\hat{H}_0^{(a)}(t)$ yields [32]:

$$\begin{aligned}\frac{\imath}{\hbar}\left[\hat{H}_0^{(a)}(t), \hat{a}(z,t)\right] &= \frac{\imath}{\hbar}\left[\hbar k_0 \int \mathrm{d}z' \hat{a}^\dagger(z',t)\hat{a}(z',t), \hat{a}(z,t)\right] \\ &= \imath k_0 \int \mathrm{d}z' \, \left[\hat{a}^\dagger(z',t), \hat{a}(z,t)\right] \hat{a}(z',t)\end{aligned} \tag{31}$$

The crucial part in (31) is the commutator between the electric fields, at the same time, but at two different points in the medium:

$$\left[\hat{a}(z,t), \hat{a}^\dagger(z',t)\right] = \frac{1}{2\pi} \int \mathrm{d}k \, \frac{\omega(k)}{k_0} \exp\left[\imath k(z-z')\right] \tag{32}$$

In order to solve the integral in (32) we Taylor expand the dispersion relation up to first-order and obtain:

$$\begin{aligned}
&\left[\hat{a}(z,t), \hat{a}^\dagger(z',t)\right] \\
&= \frac{1}{2\pi}\frac{\omega_0}{k_0}\int \mathrm{d}k \left(1 + \frac{k-k_0}{k_0}\right) \exp\left[\imath k(z-z')\right] \\
&= \frac{1}{2\pi}\frac{\omega_0}{k_0}\int \mathrm{d}k \frac{k}{k_0} \exp\left[\imath k(z-z')\right] \\
&= \frac{1}{2\pi}\frac{\omega_0}{k_0}\int \mathrm{d}k \frac{-\imath}{k_0}\frac{\partial}{\partial z} \exp\left[\imath k(z-z')\right] \\
&= \frac{-\imath}{k_0}\frac{c}{n_0}\frac{\partial}{\partial z}\delta(z-z')
\end{aligned} \tag{33}$$

Using (33) the free space commutation relation in (31) evaluates to:

$$\frac{\imath}{\hbar}\left[\hat{H}_0^{(a)}(t), \hat{a}(z,t)\right] = -\frac{c}{n_0}\frac{\partial}{\partial z}\hat{a}(z,t) \tag{34}$$

Next we calculate the commutator of $\hat{a}(z,t)$ with the nonlinear interaction Hamiltonian $\hat{H}_I^{(FC)}(t)$ in (6). To simplify this problem we treat $\omega(k)$ as a constant $\omega(k_0)$ using the slowly varying amplitude approximation. The commutator consequently evaluates to a delta function:

$$\left[\hat{a}(z,t), \hat{a}^\dagger(z',t)\right] = \frac{c}{n_0}\delta(z-z')$$

We obtain:

$$\begin{aligned}
&\frac{\imath}{\hbar}\left[\hat{H}_I^{(FC)}(t),\, \hat{a}(z,t)\right] = \\
&= \frac{\imath}{\hbar}\left[D\int \mathrm{d}z'\, E_p^{(+)}(z',t)\hat{a}(z',t)\hat{c}^\dagger(z',t) + h.c.\,, \hat{a}(z,t)\right] \\
&= \frac{\imath}{\hbar}D^*\int \mathrm{d}z'\, \left[\hat{a}^\dagger(z',t), \hat{a}(z,t)\right] E_p^{(-)}(z',t)\,\hat{c}(z',t) \\
&= \frac{\imath}{\hbar}D^*\int \mathrm{d}z'\, E_p^{(-)}(z',t)\,\hat{c}(z',t)\left(-\frac{c}{n_0}\right)\delta(z-z') \\
&= -\frac{\imath}{\hbar}\frac{c}{n_0}D^*\, E_p^{(-)}(z,t)\,\hat{c}(z,t)
\end{aligned} \tag{35}$$

Here we merged all constants into the overall variable D. The Heisenberg equation of motion in (30) then reads:

$$\frac{d}{dt}\hat{a}(z,t) = -\frac{c}{n_0}\frac{\partial}{\partial z}\hat{a}(z,t) - \frac{\imath}{\hbar}\frac{c}{n_0}D^* E_p^{(-)}(z,t)\hat{c}(z,t) \tag{36}$$

Since we are interested in the spectral distribution of the output we perform a Fourier transformation into the frequency domain. We regard the created electric fields long after the interaction and therefore integrate the time dependence from minus to plus infinity, as already performed in the analytic solution in section 6:

$$\begin{aligned}
&\mathcal{F}\left[\frac{d}{dt}\hat{a}(z,t)\right] = \mathcal{F}\left[-\frac{c}{n_0}\frac{\partial}{\partial z}\hat{a}(z,t)\right] - \frac{\imath}{\hbar}\frac{c}{n_0}\mathcal{F}\left[D^* E_p^{(-)}(z,t)\hat{c}(z,t)\right] \\
&-\imath\omega\hat{a}(z,\omega) = -\frac{c}{n_0}\frac{\partial}{\partial z}\hat{a}(z,\omega) - \frac{\imath}{\hbar}\frac{c}{n_0}D^*\int \mathrm{d}\omega' E_p^{(-)}(z,\omega'-\omega)\hat{c}(z,\omega')
\end{aligned} \tag{37}$$

We further separate the interaction from the propagation effects by transforming our operators into the interaction picture, similar to the analytic solution in section 6. For this purpose we introduce the electric fields:

$$\begin{aligned}
\hat{\epsilon}_a(z,\omega) &= \hat{a}(z,\omega)\exp\left[-\imath k_a(\omega)z\right] \\
\hat{\epsilon}_c(z,\omega) &= \hat{c}(z,\omega)\exp\left[-\imath k_c(\omega)z\right] \\
\epsilon_p^{(-)}(z,\omega) &= E_p^{(-)}(z,\omega)\exp\left[\imath k_p(\omega)z\right]
\end{aligned} \tag{38}$$

With the help of (38) we transform the differential equation in (37) into the interaction picture:

$$\begin{aligned}
\frac{\partial}{\partial z}\hat{\epsilon}_a(z,\omega) = &-\frac{\imath}{\hbar}D^*\int \mathrm{d}\omega'\epsilon_p^{(-)}(z,\omega'-\omega)\hat{\epsilon}_c(z,\omega') \\
&\times\exp\left\{-\imath\left[k_p(\omega'-\omega)-k_c(\omega')+k_a(\omega)\right]z\right\}
\end{aligned} \tag{39}$$

In a similar manner we calculate the differential equation of the second beam and obtain:

$$\begin{aligned}
\frac{\partial}{\partial z}\hat{\epsilon}_c(z,\omega) = &-\frac{\imath}{\hbar}D\int \mathrm{d}\omega'\epsilon_p^{(+)}(z,\omega-\omega')\hat{\epsilon}_a(z,\omega') \\
&\exp\left\{\imath\left[k_p(\omega-\omega')+k_a(\omega')-k_c(\omega)\right]z\right\}
\end{aligned} \tag{40}$$

Finally we introduce the abbreviation $\Delta k(\omega,\omega') = k_p(\omega'-\omega) - k_c(\omega') + k_a(\omega)$. The two coupled differential equations describing the frequency conversion process read:

$$\begin{aligned}
\frac{\partial}{\partial z}\hat{\epsilon}_a(z,\omega) &= -\frac{\imath}{\hbar}D^*\int \mathrm{d}\omega'\epsilon_p^{(-)}(z,\omega'-\omega)\exp\left[-\imath\Delta k(\omega,\omega')z\right]\hat{\epsilon}_c(z,\omega') \\
\frac{\partial}{\partial z}\hat{\epsilon}_c(z,\omega) &= -\frac{\imath}{\hbar}D\int \mathrm{d}\omega'\epsilon_p^{(+)}(z,\omega-\omega')\exp\left[\imath\Delta k(\omega',\omega)z\right]\hat{\epsilon}_a(z,\omega')
\end{aligned} \tag{41}$$

Note the inversion of the ω and ω' factors in the Δk and ϵ_p functions between the two formulas. By defining

$$f(\omega,\omega',z) = -\frac{\imath}{\hbar}D^*\epsilon_p^{(-)}(z,\omega'-\omega)\exp\left[-\imath\Delta k(\omega,\omega')z\right] \tag{42}$$

we may write (41) in a more compact notation:

$$\begin{aligned}
\frac{\partial}{\partial z}\hat{\epsilon}_a(z,\omega) &= \int \mathrm{d}\omega' f(\omega,\omega',z)\,\hat{\epsilon}_c(z,\omega') \\
\frac{\partial}{\partial z}\hat{\epsilon}_c(z,\omega) &= -\int \mathrm{d}\omega' f^*(\omega',\omega,z)\,\hat{\epsilon}_a(z,\omega')
\end{aligned} \tag{43}$$

7.1. Solving the differential equations

In order to obtain the dynamics of the frequency conversion process the differential equations in (43) have to be solved. Usually operator valued differential equations cannot readily be evaluated and, in the case of FC, this is complicated by the fact that we have to solve integro-differential equations, since we consider the conversion of many frequencies simultaneously. Note, that (41) is linear in its operators and hence classical solution methods like the split-step Fourier inversion method have been applied [20, 27, 28]. In the special case of a cw-pump laser the integral in (41) vanishes and it is even possible to find analytic solutions [32].

In this paper we apply a different approach — introduced by Wolfgang Mauerer in [46] — exploiting the fact that the structure of the solution is already known: it

is a linear operator transformation (10). Using (10) and (43) we obtain two pairs of classical integro-differential equations [29]

$$\begin{aligned}\frac{\partial}{\partial z}U_a(z,\omega,\omega'') &= -\int \mathrm{d}\omega' f(\omega,\omega',z)V_c(z,\omega',\omega'')\\ \frac{\partial}{\partial z}V_c(z,\omega,\omega'') &= \int \mathrm{d}\omega' f^*(\omega',\omega,z)U_a(z,\omega',\omega'')\end{aligned} \tag{44}$$

and

$$\begin{aligned}\frac{\partial}{\partial z}U_c(z,\omega,\omega'') &= -\int \mathrm{d}\omega' f^*(\omega',\omega,z)V_a(z,\omega',\omega'')\\ \frac{\partial}{\partial z}V_a(z,\omega,\omega'') &= \int \mathrm{d}\omega' f(\omega,\omega',z)U_c(z,\omega',\omega'')\end{aligned} \tag{45}$$

which cover the complete dynamics of the frequency conversion process.

We solve these coupled integro-differential equations using an iterative approach. For the pair in (44) this means we first formally integrate both differential equations along z, where we assume a medium of length L, as in in the analytic solution discussed in section 6,

$$\begin{aligned}U_a(z,\omega,\omega'') &= \delta(\omega-\omega') - \int_{-\frac{L}{2}}^{\frac{L}{2}} \mathrm{d}z \int \mathrm{d}\omega' f(\omega,\omega',z)V_c(z,\omega',\omega'')\\ V_c(z,\omega,\omega'') &= \int_{-\frac{L}{2}}^{\frac{L}{2}} \mathrm{d}z \int \mathrm{d}\omega' f^*(\omega',\omega,z)U_a(z,\omega',\omega'').\end{aligned} \tag{46}$$

Here we also included our knowledge about the initial solution. If no interaction takes place the process is described by the identity operation $\hat{a}^{(out)}(\omega) = \hat{a}^{(in)}(\omega)$ and $\hat{c}^{(out)}(\omega) = \hat{c}^{(in)}(\omega)$ from which follows:

$$\begin{aligned}U_a(z,\omega,\omega'') &= U_c(z,\omega,\omega'') = \delta(\omega-\omega'')\\ V_a(z,\omega,\omega'') &= V_c(z,\omega,\omega'') = 0\end{aligned} \tag{47}$$

Starting with the initial solution for $U_a(z,\omega,\omega'')$ we then perform the two integrations in (46) and obtain a preliminary $V_c(z,\omega,\omega'')$. This is then used to obtain a new $U_a(z,\omega,\omega'')$. We repeat this iterative procedure till the functions converge.

The same method is applied to the second set of differential equations defining $U_c(z,\omega,\omega'')$ and $V_a(z,\omega,\omega'')$ which gives us the complete time-ordered solution of the frequency conversion process. The implementation of this algorithm is discussed in Appendix D, where we also elaborate on the numerical accuracy of the applied method. The program code is available on our website.¶

8. FC: Comparison between simplified analytical and rigorous approach

In sections 6 and 7 we presented two models describing frequency conversion taking into account the higher-order moments: a simplified analytic model excluding time-ordering effects and a rigorous numerical model including time-ordering. While the analytic method is straightforward and only requires minimal computational effort, it is only an approximation to the rigorous model. In this section we compare these two approaches in order to investigate the validity of the simplified theory for the

¶ The program code can be downloaded from the publications section on our website. The current url is `http://physikwww.uni-paderborn.de/ag/ag-silberhorn/publications.html`.

modelling of frequency conversion processes and the effects of time-ordering present in the rigorous solution.

From the discussion in section 6 we are able to directly deduce that the analytic solution features constant mode shapes connected to conversion amplitudes which oscillate with a sinusoidal pattern. In the low gain regime, when a first-order expansion is sufficient, the rigorous solution of section 7 gives the identical result. However, as soon as the higher-order moments yield a significant contribution to the frequency conversion process, the rigorous solution will feature a reshaped frequency spectrum due to the relaxed energy conservation condition discussed in section 5.

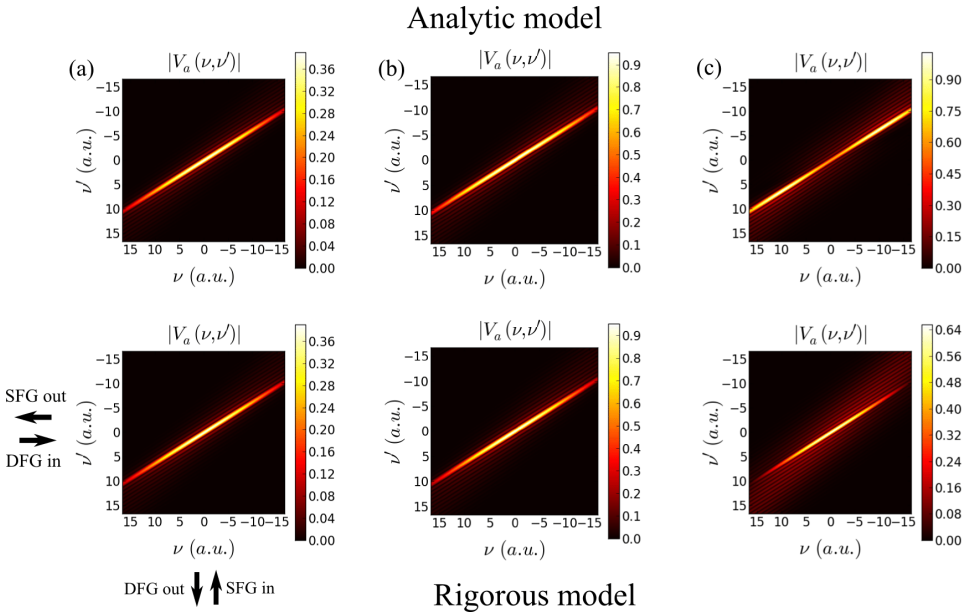

Figure 3. Comparison of the conversion amplitudes $|V_a(\omega,\omega')|$ between the rigorous and the simplified analytical model of a correlated frequency conversion process, with rising conversion efficiencies from (a) to (c). For low conversion efficiencies depicted in (a) both models yield identical results. When conversion efficiencies of unity are approached in (b) the rigorous model starts to deviate from the analytic approach due to the relaxed energy conservation condition. Significant differences occur when conversion efficiencies beyond unity are considered (c).

In order to quantify the discrepancies between the two approaches we simulate two frequency conversion processes: a correlated frequency conversion where many optical modes r_k are converted and an almost uncorrelated frequency conversion process where only a few optical modes r_k are present [18]. The frequency conversion process is defined by the incoming pump laser and the applied nonlinear crystal, i.e. the length of the material and its dispersion properties. These parameters can be represented by just six values: The length of the crystal, the group velocities of the three beams and the width and the amplitude of the Gaussian pump beam of our ultrafast laser system driving the frequency conversion process. The details of this procedure and the applied process properties are given in Appendix C.

The crucial parameter in the solution are the $\left|V_{a/c}(\omega,\omega')\right|$ amplitudes in the

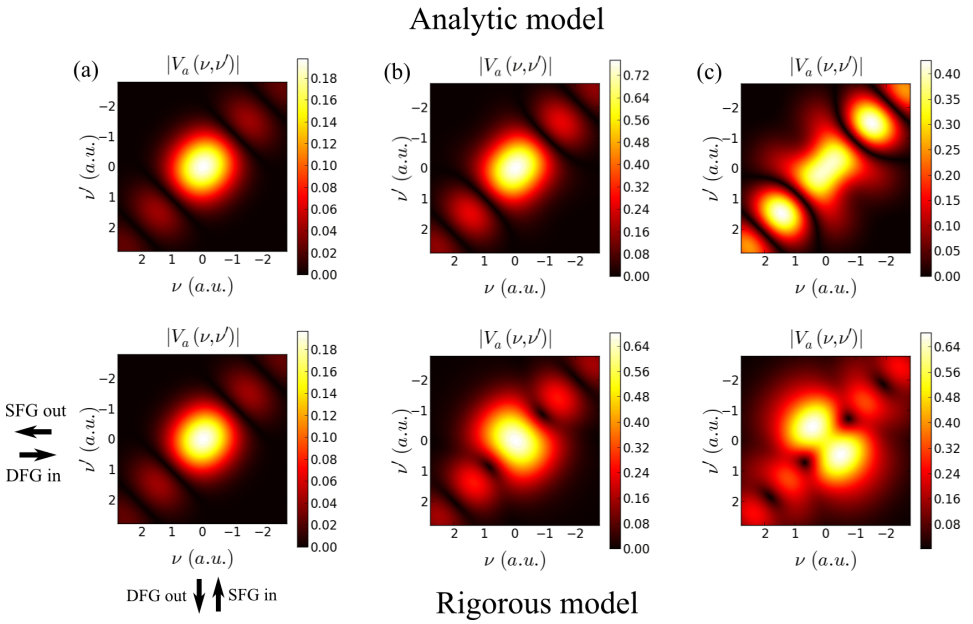

Figure 4. Comparison of the conversion amplitudes $|V_a(\omega,\omega')|$ between the rigorous and the simplified analytical model of an uncorrelated frequency conversion process, with rising conversion efficiencies from (a) to (c). For low conversion efficiencies in depicted in (a) both models yield identical results. When conversion efficiencies of unity are approached in (b) the rigorous model starts to deviate from the analytic approach due to the relaxed energy conservation condition. Significant differences occur when conversion efficiencies beyond unity are considered (c).

general solution in (10) which describe the conversion amplitude — conversion efficiency = |conversion amplitude|^2 — at individual frequencies. The $|V_a(\omega,\omega')|$ amplitudes for the correlated frequency conversion case are presented in figure 3. Figure 3(a) gives $|V_a(\omega,\omega')|$ at a low conversion rate. In this regime both models yield identical results. At efficiencies approaching unity, as depicted in figure 3 (b), minor deviations between the two models appear. Figure 3 (c) shows $|V_a(\omega,\omega')|$ for a conversion efficiency beyond unity. In this regime the time-ordering approximation breaks down and the two theories predict significantly different results. While the analytic model predicts a dip in the conversion efficiency about the central frequencies, the rigorous model still shows a Gaussian shape.

For the case of uncorrelated frequency conversion the $|V_a(\omega,\omega')|$ amplitudes are given in figure 4. As in the correlated case 4 (a) presents the process at low conversion efficiencies where both models are identical, (b) depicts near unit conversion efficiency with minor deviations between the two approaches and (c) visualizes the discrepancies between the two models arising at conversion rates beyond unity. In this uncorrelated frequency conversion case the discrepancies between the different models are much more prominent than in the correlated frequency conversion case. In the analytic model the side peaks are much more prominent as in the rigorous model. Furthermore the rigorous model shows a broadening and along the +45° axis, which is a direct result

of the relaxed energy conservation conditions in this model.

The corresponding frequency conversion amplitudes $\sin(r_k)$ and mode shapes are displayed in figure 5 for correlated and in figure 6 for uncorrelated frequency conversion. The figures in the column on the left show the conversion amplitudes $\sin(r_k)$ — conversion efficiency = $\sin^2(r_k)$ — whereas the two columns on the right present the corresponding mode functions $\varphi_1(\nu), \psi_1(\nu), \phi_1(\nu)$ and $\xi_1(\nu)$ for the first optical mode featuring the highest conversion efficiency, where $\varphi_1(\nu)$ and $\psi_1(\nu)$ as well as $\phi_1(\nu)$ and $\xi_1(\nu)$ are of identical shape.

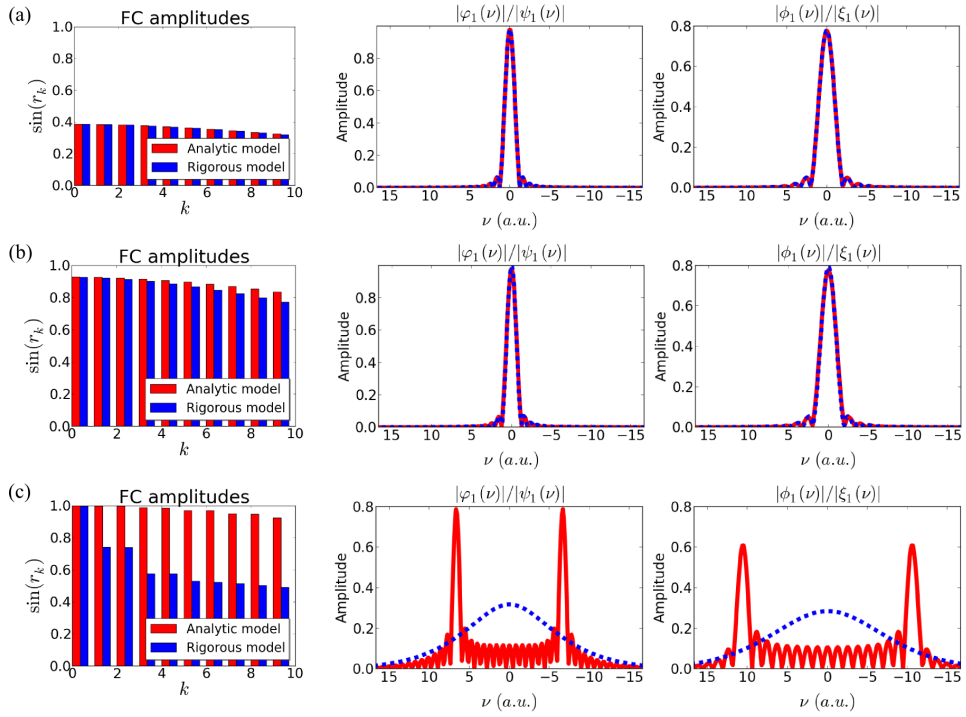

Figure 5. Comparison between the rigorous and the analytical approach in correlated many mode ultrafast frequency conversion. In the low conversion regime, presented in (a) (15%/15% conversion efficiency in the first mode in the analytic / rigorous model), both approaches evaluate to identical results. Approaching unit efficiency in (b) (86%/86% conversion efficiency in the first mode) the two approaches start to show differences, which become significant when optical gains beyond unity are considered in (c). (100%/99% conversion efficiency in the first mode)

In the conversion regime up to unity (a) both approaches yield almost identical conversion amplitudes $\sin(r_k)$ and corresponding mode functions $\varphi_1(\nu), \psi_1(\nu), \phi_1(\nu)$ and $\xi_1(\nu)$. At conversion rates about unity minor discrepancies in the mode shapes and $\sin(r_k)$ amplitudes start to appear. Significant differences between the two theories, however, are only present when we consider rates beyond unit conversion efficiency as depicted in (c).

Interestingly the time-ordering effects affect the correlated and uncorrelated frequency conversion in a different manner: in the correlated case the rigorous

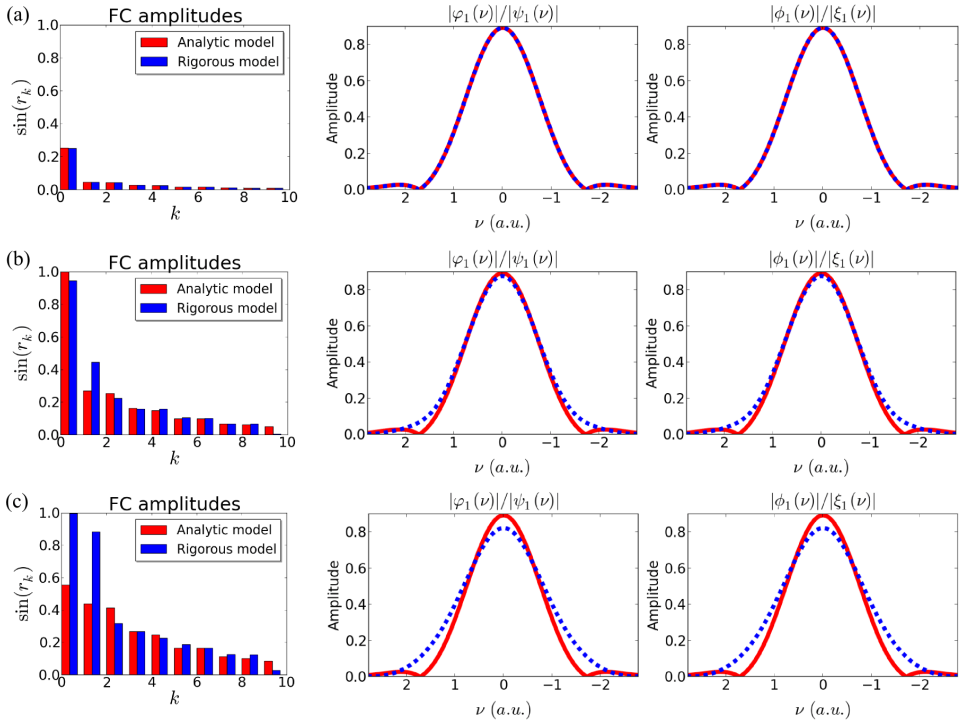

Figure 6. Comparison between the rigorous and the analytical approach in uncorrelated few mode ultrafast frequency conversion. In the low conversion regime, presented in (a), both approaches evaluate to identical results (6.4%/6.3% conversion efficiency in the first mode in the analytic / rigorous model). Approaching unit efficiency in (b) the two approaches start to show differences (100%/89% conversion efficiency in the first mode), which become significant when optical gains beyond unity are considered in (c) (30%/99% conversion efficiency in the first mode).

model predicts a considerably faster drop of the conversion amplitudes $\sin(r_k)$ than the analytical approach. Diamentral to this behaviour the $\sin(r_k)$ amplitudes of decorrelated case in the rigorous model, presented in 6(c), remain at unit conversion efficiency once they reach this value. In general it is not possible to associate the time-ordering effects with a specific behaviour of the broadband conversion amplitudes $\sin(r_k)$. Consequently each frequency conversion process has to be investigated individually.

Both correlated and uncorrelated down-conversion, however, share the property that the rigorous model predicts a significant broadening in the corresponding mode shapes in the high gain regime. Please note, that in figure 5 (c) the first mode of the analytic model is not the Gaussian from 5 (a) and (b) any more since we always plot the modes with the highest conversion efficiency and, in this power regime, this is not a Gaussian any more.

In summary the analytical model accurately describes frequency conversion in the low gain regime up to unit conversion efficiency, where minor deviations start

to appear. Only in the high gain regime, when conversion efficiencies beyond unity are reached, complicated non-trivial deviations from the analytical model have to be taken into account and a rigorous treatment of frequency conversion is required. For most experimental setups and applications it is hence perfectly justified to apply the simplified analytic model to minimize the computational effort, as long as its limitations are kept in mind.

9. FC: Outlook

These time-ordering effects have practical implications for the deployment of frequency conversion processes. Especially affected are frequency conversion processes which serve as quantum pulse gates [18, 19, 20]. In theory a perfect quantum pulse gate converts a single optical mode with unit efficiency. Actually building a quantum pulse gate, however, is complicated by time-ordering effects. As is evident from figure 6 the relaxed energy conditions move the frequency process from the single-mode regime towards a more multimode behaviour. This effect fundamentally limits the gate performance at high conversion efficiencies. One could, in principle, use advanced engineering techniques, such as hypergrating structures to reduce the amount of multimodeness in the state [51], yet still the time-ordering effects seem to remain a fundamental limitation. Whether or not it is actually possible to engineer single-mode pulse gates including the effects of time-ordering remains an open research question.

10. PDC: Overview

Having discussed frequency conversion we now extend our investigations to the second important nonlinear optical process: parametric down-conversion. The principle of PDC is sketched in figure 7. A strong pump beam decays inside a nonlinear optical material into two beams commonly labelled signal and idler. The output state formed by the two beams is known as finitely squeezed EPR-state or twin-beam state[+]. As

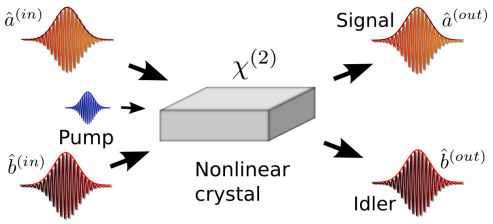

Figure 7. Sketch of the parametric down-conversion process. A strong pump beam decays inside the nonlinear optical material into two beams usually labelled signal $\hat{a}$ and idler $\hat{b}$, forming a finitely squeezed EPR-state.

in the frequency conversion case, we do not restrict ourselves to a discussion of the parametric down-conversion process in the monochromatic picture, but extend the theories to the multimode picture including the interaction of many frequencies. This is especially important when the PDC process is pumped by pulsed laser systems.

[+] PDC is also able to create squeezed states. This process is discussed in [27, 28].

11. PDC: Hamiltonian

The interaction Hamiltonian of the PDC process — using electric field operators as defined in (1) and the rotating wave approximation — takes on the form:

$$\hat{H}_I^{(PDC)}(t) = \epsilon_0 \int \mathrm{d}z\, \chi^{(2)}(z)\, \hat{E}_p^{(+)}(z,t)\hat{E}_a^{(-)}(z,t)\hat{E}_b^{(-)}(z,t) + h.c.\,. \tag{48}$$

As in the frequency conversion process we assume a strong pump field exceeding the amplitudes of the signal and idler fields by several orders of magnitude and hence treat it as a classical field propagating undepleted through the medium (see (5)). This transforms the interaction Hamiltonian to:

$$\hat{H}_I^{(PDC)}(t) = \epsilon_0 \int \mathrm{d}z\, \chi^{(2)}(z)\, E_p^{(+)}(z,t)\hat{E}_a^{(-)}(z,t)\hat{E}_b^{(-)}(z,t) + h.c.\,. \tag{49}$$

Using the free space propagation Hamiltonian from (3) and the interaction Hamiltonian from (49) the process of parametric downconversion is given by the overall Hamiltonian:

$$\hat{H}_{PDC}(t) = \hat{H}_0^{(a)}(t) + \hat{H}_0^{(b)}(t) + \hat{H}_I^{(PDC)}(t) \tag{50}$$

While, at first glance, the process of parametric down-conversion seems very different from the process of frequency conversion, comparing the interaction Hamiltonian of PDC in (49) and FC in (6) reveals that they both feature bilinear Hamitonians — the pump is treated as a classical field — with an almost identical structure and hence share many mathematical properties.

It is therefore straightforward to extend our presented calculations corresponding frequency conversion to parametric down-conversion. In order to avoid repetition we are going to only state the results and elaborate on the differences and similarities to the process of frequency conversion. The detailed calculations will be presented in [52].

12. PDC: General properties

The general solution of (50) takes on the form of a linear operator transformation [38, 39]:

$$\begin{aligned}
\hat{a}^{(out)}(\omega) &= \int \mathrm{d}\omega' U_a(\omega,\omega')\, \hat{a}^{(in)}(\omega') + \int \mathrm{d}\omega' V_a(\omega,\omega')\, \hat{b}^{(in)\dagger}(\omega') \\
\hat{b}^{(out)}(\omega) &= \int \mathrm{d}\omega' U_b(\omega,\omega')\, \hat{b}^{(in)}(\omega') + \int \mathrm{d}\omega' V_b(\omega,\omega')\, \hat{a}^{(in)\dagger}(\omega')
\end{aligned} \tag{51}$$

This solution is constrained by the fact that it has to form a canonical transformation [38, 39, 27]. Under this restriction we are able to rewrite it as:

$$\begin{aligned}
\hat{A}_k^{(out)} &= \cosh(r_k)\hat{A}_k^{(in)} + \sinh(r_k)\hat{B}_k^{(in)\dagger} \\
\hat{B}_k^{(out)} &= \cosh(r_k)\hat{B}_k^{(in)} + \sinh(r_k)\hat{A}_k^{(in)\dagger}
\end{aligned} \tag{52}$$

where $\hat{A}_k$ and $\hat{B}_k$ are defined as broadband single-photon destruction operators [41]:

$$\begin{aligned}
\hat{A}_k^{(out)} &= \int \mathrm{d}\omega\, \varphi_k(\omega)\, \hat{a}^{(out)}(\omega) & \hat{B}_k^{(out)} &= \int \mathrm{d}\omega\, \xi_k(\omega)\, \hat{b}^{(out)}(\omega) \\
\hat{A}_k^{(in)} &= \int \mathrm{d}\omega\, \psi_k(\omega)\, \hat{a}^{(in)}(\omega) & \hat{B}_k^{(in)} &= \int \mathrm{d}\omega\, \phi_k(\omega)\, \hat{b}^{(in)}(\omega)
\end{aligned} \tag{53}$$

The details of this procedure are given in Appendix B.

According to (52) the parametric downconversion process is a broadband twin-beam squeezer transformation. However, not a single finitely squeezed EPR state, but a multitude of twin beam states are emitted into broadband ultrafast pulse modes $\hat{A}_k$ and $\hat{B}_k$. The crucial parameters of this transformation are firstly the amplitudes r_k which give both the amount of generated EPR entanglement — squeezing[dB] $= -10\log_{10}\left(e^{-2r_k}\right)$ — and the number of emitted EPR states, and secondly the mode shapes $\varphi_k(\omega)$, $\xi_k(\omega)$, $\psi_k(\omega)$, and $\phi_k(\omega)$ which define the form of the optical modes in which the states are created.

13. PDC: Time-ordering approximation

To obtain some first insights into the parametric down-conversion process given by (50) we applied perturbation theory, as performed in the case of frequency conversion, discussed in section 5. The mathematics are identical to the ones presented in section 5. Including time-ordering and performing a Dyson series expansion is involved yet gives an enhanced flexibility in the energy conservation condition, whereas neglecting time-ordering enables a straightforward Taylor expansion. An extensive discussion of Dyson series vs. Taylor series for PDC was performed by Agata M. Brańczyk in [30] and [43].

14. PDC: Analytic model excluding time-ordering effects

As in the frequency conversion case, presented in section 6, we first solve the process excluding time-ordering effects. Again we use the electric fields in the frequency domain (15) and move into the interaction picture:

$$\hat{U}_{PDC} = \exp\left[-\frac{\imath}{\hbar}\int \mathrm{d}t\, \hat{H}_I^{(PDC)}(t)\right] \tag{54}$$

Retracting the steps from section 6 we obtain

$$\hat{U}_{PDC} = \exp\left[-\frac{\imath}{\hbar}\left(\int \mathrm{d}\omega_a \int \mathrm{d}\omega_b\, f(\omega_a,\omega_b)\hat{a}^\dagger(\omega_a)\hat{b}^\dagger(\omega_b) + h.c.\right)\right], \tag{55}$$

where $f(\omega_a,\omega_b)$ is defined as

$$f(\omega_a,\omega_b) = B\,\alpha(\omega_a+\omega_b)\,\mathrm{sinc}\left(\frac{\Delta k(\omega_a,\omega_b)L}{2}\right) \tag{56}$$

and $\Delta k(\omega_a,\omega_b) = k_p(\omega_a+\omega_b) - k_a(\omega_a) - k_b(\omega_b)$.

In the broadband mode formalism this process evaluates to

$$\begin{aligned}\hat{U}_{PDC} &= \exp\left[\sum_k r_k\left(\hat{A}_k^\dagger\hat{B}_k^\dagger - \hat{A}_k\hat{B}_k\right)\right] \\ &= \bigotimes_k \exp\left[r_k\left(\hat{A}_k^\dagger\hat{B}_k^\dagger - \hat{A}_k\hat{B}_k\right)\right] = \bigotimes_k \hat{S}_k^{ab}(-r_k)\end{aligned} \tag{57}$$

which, in the Heisenberg formalism (57), takes on the form:

$$\begin{aligned}\hat{A}_k^{(out)} &= \cosh(r_k)\hat{A}_k^{(in)} + \sinh(r_k)\hat{B}_k^{\dagger(in)} \\ \hat{B}_k^{(out)} &= \cosh(r_k)\hat{B}_k^{(in)} + \sinh(r_k)\hat{A}_k^{\dagger(in)}\end{aligned} \tag{58}$$

The details of this calculation are given in [12].

This result exhibits exactly the structure imposed by the canonical commutation relation in (52), except for the fact that, as in the frequency conversion case, the input and output modes are of identical shape.

In conclusion the analytic model ignoring time-ordering effects enables a straightforward solution of the parametric down-conversion process, which enables the efficient engineering and design of frequency conversion processes as long as the applied approximations hold.

15. PDC: Rigorous theory including time-ordering effects

Having elaborated on solving parametric down-conversion neglecting time-ordering effects we now explicitly include these effects into our analysis. For this purpose we adapt the approach presented in section 7. We first define new electric field operators according to [32]

$$\begin{aligned}\hat{a}(z,t) &= \frac{1}{\sqrt{2\pi k_0}} \int \mathrm{d}k \, \sqrt{\omega(k)} \exp\left[\imath \left(kz - \omega(k)t\right)\right] \hat{a}(k) \\ \hat{b}(z,t) &= \frac{1}{\sqrt{2\pi k_0}} \int \mathrm{d}k \, \sqrt{\omega(k)} \exp\left[\imath \left(kz - \omega(k)t\right)\right] \hat{b}(k). \end{aligned} \tag{59}$$

In terms of (59) the Heisenberg equation of motion for $\hat{a}(z,t)$ takes on the form:

$$\frac{d}{dt}\hat{a}(z,t) = \frac{\imath}{\hbar}\left[\hat{H}_{PDC}(t), \hat{a}(z,t)\right] \tag{60}$$

Repeating exactly the same steps as in section 7 we obtain two operator valued integro-differential equations describing the downconversion process

$$\begin{aligned}\frac{\partial}{\partial z}\hat{\epsilon}_a(z,\omega) &= -\frac{\imath}{\hbar} D \int \mathrm{d}\omega' \exp\left[\imath \Delta k(\omega,\omega') z\right] E_p^{(+)}(z, \omega+\omega') \, \hat{\epsilon}_b^\dagger(z,\omega') \\ \frac{\partial}{\partial z}\hat{\epsilon}_b(z,\omega) &= -\frac{\imath}{\hbar} D \int \mathrm{d}\omega' \exp\left[\imath \Delta k(\omega',\omega) z\right] E_p^{(+)}(z, \omega+\omega') \, \hat{\epsilon}_a^\dagger(z,\omega') \end{aligned} \tag{61}$$

where we introduced the shorthand $\Delta k(\omega,\omega') = k_p(\omega+\omega') - k_a(\omega) - k_b(\omega')$. The structure of this result is very similar to the equations derived by [29, 46, 27] which serves as a nice cross check of our calculations. Also please take note of the switch of ω and ω' in the second equation.

By defining

$$f(\omega,\omega',z) = -\frac{\imath}{\hbar} D E_p^{(+)}(z,\omega+\omega') \exp\left[\imath \Delta k(\omega,\omega') z\right] \tag{62}$$

we rewrite the differential equations in a compact form:

$$\begin{aligned}\frac{\partial}{\partial z}\hat{\epsilon}_a(z,\omega) &= \int \mathrm{d}\omega' f(\omega,\omega',z) \, \hat{\epsilon}_b^\dagger(z,\omega') \\ \frac{\partial}{\partial z}\hat{\epsilon}_b(z,\omega) &= \int \mathrm{d}\omega' f(\omega',\omega,z) \, \hat{\epsilon}_a^\dagger(z,\omega') \end{aligned} \tag{63}$$

15.1. Solving the differential equations

Since the structure of the two differential equations describing the PDC process in (63) is identical to the ones describing the frequency conversion process (41) and (43), we apply the same solution method as presented in section 7.1.

We obtain four classical integro-differential equations. Two for $U_a(z,\omega,\omega')$ and $V_b(z,\omega,\omega')$:

$$\begin{aligned}\frac{\partial}{\partial z}U_a(z,\omega,\omega'') &= \int \mathrm{d}\omega' f(\omega,\omega',z)V_b^*(z,\omega',\omega'')\\ \frac{\partial}{\partial z}V_b(z,\omega,\omega'') &= \int \mathrm{d}\omega' f(\omega',\omega,z)U_a^*(z,\omega',\omega'')\end{aligned} \tag{64}$$

And two for $U_b(z,\omega,\omega')$ and $V_a(z,\omega,\omega')$:

$$\begin{aligned}\frac{\partial}{\partial z}U_b(z,\omega,\omega'') &= \int \mathrm{d}\omega' f(\omega',\omega,z)V_a^*(z,\omega',\omega'')\\ \frac{\partial}{\partial z}V_a(z,\omega,\omega'') &= \int \mathrm{d}\omega' f(\omega,\omega',z)U_b^*(z,\omega',\omega'')\end{aligned} \tag{65}$$

The initial conditions are:

$$\begin{aligned}U_a(z,\omega,\omega'') &= U_b(\omega,\omega'',z) = \delta(\omega-\omega'')\\ V_a(z,\omega,\omega'') &= V_b(\omega,\omega'',z) = 0\end{aligned} \tag{66}$$

As in the frequency conversion case they can be solved via an iterative approach. Details of this calculation and the numerical errors in the solution method are give in Appendix F. The program code is available, together with the frequency conversion code, on our website.

16. PDC: Comparison between simplified analytical and rigorous approach

In sections 14 and 15 we presented two models describing parametric down-conversion: a simple analytic model excluding time-ordering effects and a complex numerical model including time-ordering. As in the frequency conversion case the analytic method is straightforward and only requires minimal computational effort while the rigorous approach demands the solution of coupled integro-differential equations. In this section we compare these two approaches in order to test the validity of our simplified theory for the modelling of parametric down-conversion and the effects of time-ordering present in the rigorous approach.

As in the frequency conversion case, presented in section 8, we consider a correlated and an almost uncorrelated process pumped by ultrafast pump lasers (see Appendix E for the process properties and Appendix F for details on the numerical implementation).

The crucial parameters in the solution are the $\left|V_{a/b}(\omega,\omega')\right|$ amplitudes in the general solution in (51) which describe the amount of EPR-squeezing that is generated during the nonlinear interaction.

The resulting $|V_a(\omega,\omega')|$ for a correlated parametric down-conversion process is depicted in figure 8. The results for uncorrelated parametric down-conversion are visualized in figure 9. Similar to the frequency conversion case we choose to depict the low down-conversion regime in (a), the regime where first discrepancies occur in (b) and the effects in the high down-conversion regime in (c).

The corresponding EPR squeezing values and mode shapes are depicted in figures 10 and 11 for rising down-conversion rates from (a) to (c). The figures in the column on the left shows the squeezing squeezing values obtained via the relation: squeezing[dB] $= -10\log_{10}\left(e^{-2r_k}\right)$ and the corresponding mean-photon number of the

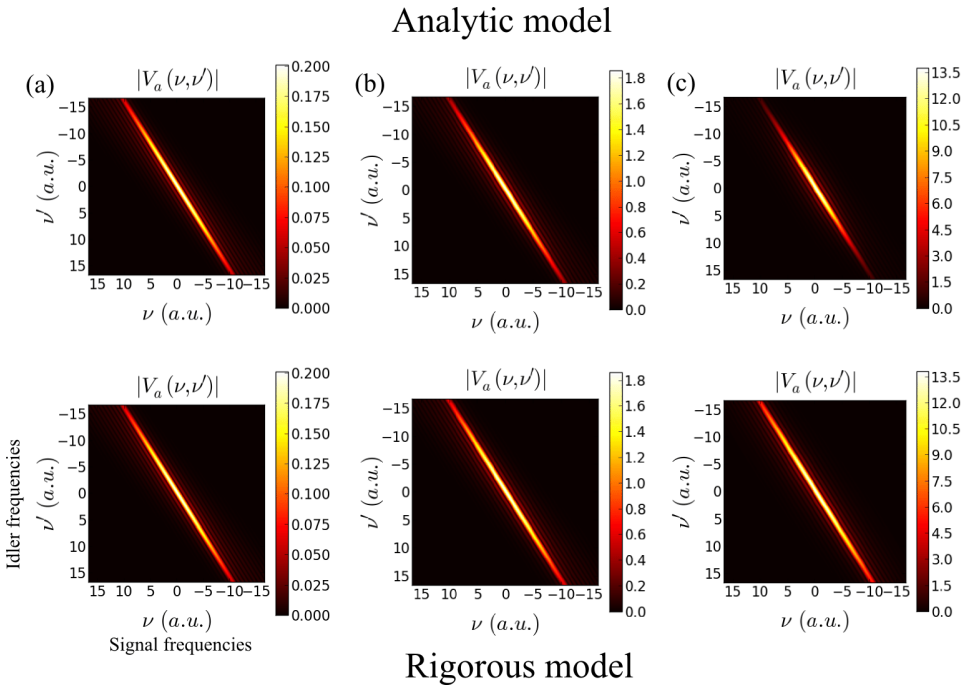

Figure 8. Comparison of the process amplitudes $|V_a(\omega,\omega')|$ between the rigorous and the simplified analytical model for a correlated parametric down-conversion process. In the low squeezing regime in (a) both models yield identical results ($\langle n\rangle = 0.59/0.60$ in the analytic / rigours model.). Only at EPR squeezing values of 12 dB, presented in (b), minor discrepancies start to appear ($\langle n\rangle = 44.14/53.18$). Significant differences are only present for extremely high down-conversion rates visualized in (c) ($\langle n\rangle = 1708.16/3328.27$).

complete state, whereas the two columns on the right present the corresponding mode functions $\varphi_1(\nu), \psi_1(\nu), \phi(\nu)$ and $\xi_1(\nu)$ for the first optical mode, where $\varphi_1(\nu)$ and $\psi_1(\nu)$ as well as $\phi_1(\nu)$ and $\xi_1(\nu)$ are of identical shape. "Analytic model" labels the solution excluding time-ordering effects, as presented in section 14 and the "Rigorous model" label marks the rigorous solution from section 15.

Up to squeezing values of 12dB presented in (b) the two approaches give identical results, only when squeezing values beyond this bound are considered significant differences between the two models start to appear. The rigorous model predicts more squeezing than the analytic model and the relaxed energy conservation condition induces a broadening of the spectral distributions $\left|V_{a/b}(\omega,\omega')\right|$ which leads to a broadening of the mode shapes in the high gain regime. In general the impacts of time-ordering on correlated PDC are much weaker than the changes present in the uncorrelated PDC case.

In summary the analytical model accurately describes parametric down-conversion in the low gain regime up to two-mode squeezing values of 12dB, where minor deviations start to appear. Only for extremely high squeezing values, in the range of 20dB and higher, complicated non-trivial deviations from the analytical appear and give significant contribution which require a rigorous treatment of

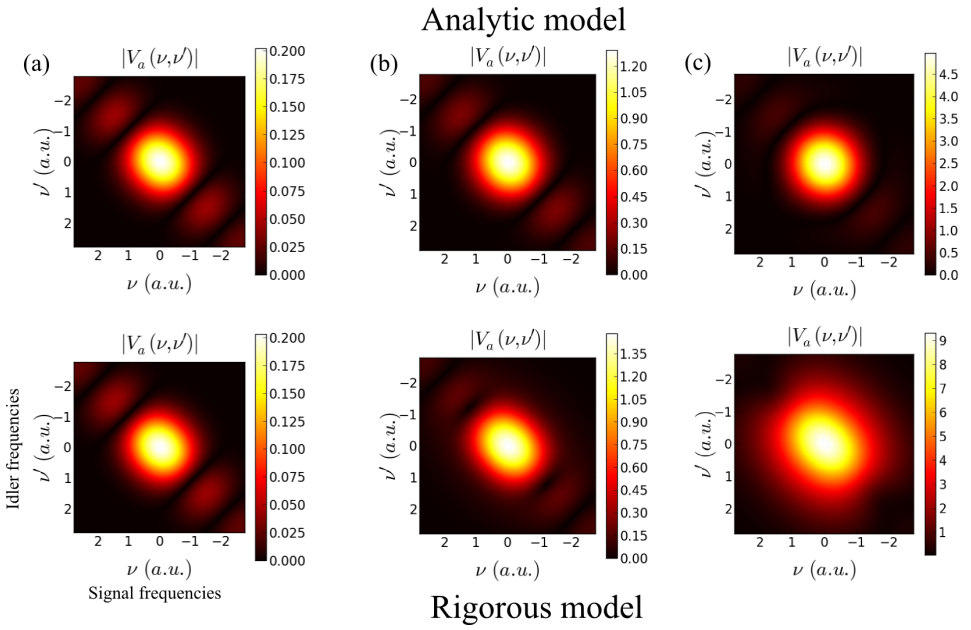

Figure 9. Comparison of the process amplitudes $|V_a(\omega,\omega')|$ between the rigorous and the simplified analytical model for an almost uncorrelated parametric down-conversion process. In the low squeezing regime in (a) both models yield identical results ($\langle n\rangle$ = 0.07/0.07 in the analytic / rigours model.). Only at EPR squeezing values of 12 dB, presented in (b), minor discrepancies start to appear ($\langle n\rangle$ = 2.80/4.08). Significant differences are only present for extremely high down-conversion rates visualized in (c) ($\langle n\rangle$ = 39.39/279.87).

parametric down-conversion. For most experimental setups and applications it is hence perfectly justified to apply the simplified analytic model to minimize the computational effort, as long as its limitations are kept in mind.

17. PDC: Outlook

The time-ordering effects on PDC have practical implementations for the deployment of PDC sources in quantum optical experiments. In contrast to FC, however, the time-ordering effects are beneficial to the performance of the sources. They lead to much higher EPR squeezing values as predicted by the simplified analytic model.

18. Conclusion

In conclusion we developed two models for the nonlinear optical processes of frequency conversion and parametric down-conversion taking into account higher-order photon number effects. The presented rigorous numerical model relies on the solution of coupled differential equations, whereas ignoring time-ordering effects enabled us to construct an analytical solution.

Our analysis revealed that the analytic model gives accurate results for frequency conversion processes up to unit conversion efficiency and parametric down-conversion

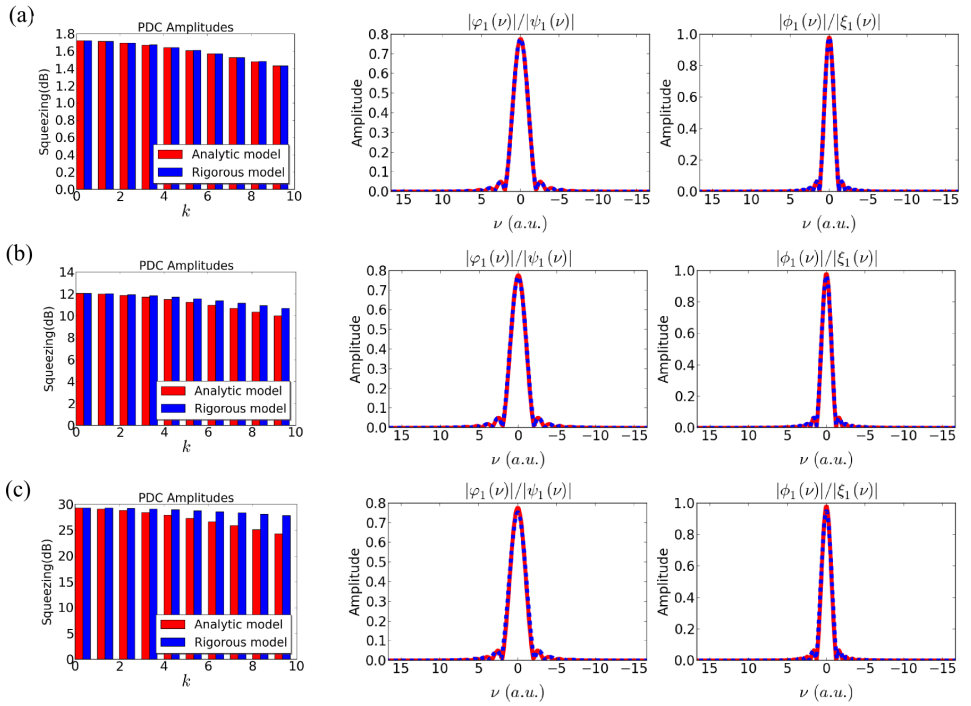

Figure 10. Comparison between the rigorous and the analytical approach in correlated many mode parametric down-conversion. For low down-conversion rates, presented in (a), both approaches evaluate to identical results. Only in the case of rising squeezing values in (b), with squeezing values about 12dB, the two approaches start to show minor differences, which become more prominent when even higher squeezing values are considered (c).

process up to 12dB of squeezing. However as soon as we go beyond these bounds, the relaxed energy conservation conditions, induced by the time-ordering effects, require a rigorous treatment of these processes.

The developed fundamental understanding of frequency conversion and parametric down-conversion gives valuable insights into the quantum properties of the nonlinear optical processes, extends the current theoretical descriptions of FC and PDC, and simplifies considerably the engineering process for future quantum information applications.

19. Acknowledgments

The authors thank Agata M. Brańczyk and Regina Kruse for useful discussions and helpful comments.

The research leading to these results has received funding from the European Community's Seventh Framework Programme FP7/2007-2013 under the grant agreement Q-Essence 248095.

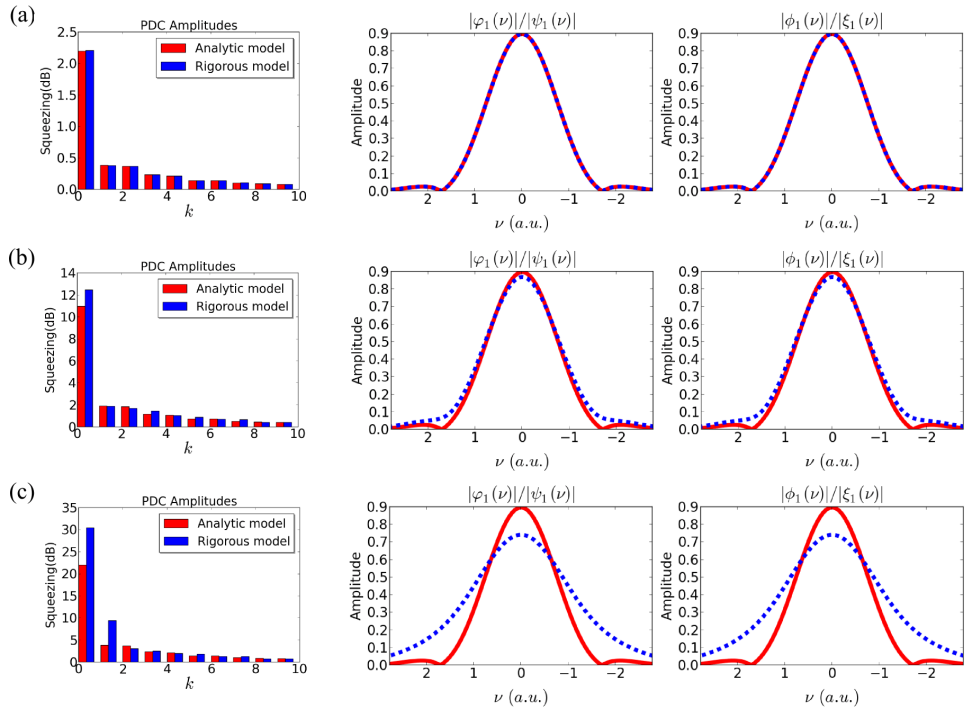

Figure 11. Comparison between the rigorous and the analytical approach in (almost) uncorrelated few mode parametric down-conversion. For low down-conversion rates, presented in (a), both approaches evaluate to identical results. Only in the case of rising squeezing values in (b), with squeezing values about 12dB, the two approaches start to show minor differences, which become more prominent when even higher squeezing values are considered (c).

Appendix A. FC: Canonical transformation conditions

The frequency conversion process in (10) is a unitary transformation, hence the generated output modes must preserve the canonical commutation relations. This imposes several restrictions on the structure of the solution. We evaluate these by extending the calculations from [38, 39] to frequency conversion. At first we rewrite (10) in the more compact notation

$$\begin{aligned}\hat{a}_i^{(out)} &= u_{ij}^{(a)}\hat{a}_j^{(in)} + v_{ij}^{(a)}\hat{c}_j^{(in)} \\ \hat{c}_i^{(out)} &= u_{ij}^{(c)}\hat{c}_j^{(in)} - v_{ij}^{(c)}\hat{a}_j^{(in)}\end{aligned} \tag{A.1}$$

where i and j label the individual frequencies of the electric fields and summation over repeated indices is understood. These two input-output relations must preserve:

$$\begin{aligned}\left[\hat{a}_i, \hat{a}_j^\dagger\right] &= \left[\hat{c}_i, \hat{c}_j^\dagger\right] = \delta_{ij} \\ \left[\hat{a}_i, \hat{c}_j^\dagger\right] &= 0\end{aligned} \tag{A.2}$$

Using (A.1) and (A.2) we obtain three conditions for frequency conversion:

$$U_a U_a^\dagger + V_a V_a^\dagger \;=\; U_c U_c^\dagger + V_c V_c^\dagger \;=\; \mathbb{1} \tag{A.3}$$

$$U_a V_c^\dagger - V_a U_c^\dagger = 0 \tag{A.4}$$

Furthermore the commutation relations have to be preserved for the inverse transformation as well:

$$\begin{aligned}\hat{a}_i^{(in)} &= u_{ji}^{*(a)} \hat{a}_j^{(out)} - v_{ji}^{*(c)} \hat{c}_j^{(out)} \\ \hat{c}_i^{(in)} &= u_{ji}^{*(c)} \hat{c}_j^{(out)} + v_{ji}^{*(a)} \hat{a}_j^{(out)}.\end{aligned} \tag{A.5}$$

With (A.5) the canonical commutation conditions in (A.2) yield the restrictions:

$$U_a^\dagger U_a + V_c^\dagger V_c = U_c^\dagger U_c + V_a^\dagger V_a = \mathbb{1} \tag{A.6}$$

$$U_a^\dagger V_a - V_c^\dagger U_c = 0 \tag{A.7}$$

The equations (A.3), (A.4), (A.6) and (A.7) impose several constraints on the solution. However they are rather unintuitive representations of the symmetries governing the frequency conversion process, yet with the help of the Bloch-Messiah reduction [39] it is possible to unravel their underlying structure: As a first step we decompose the four matrices U_a, V_a, U_c, V_c as

$$\begin{aligned} U_a &= A_a^u D_a^u B_a^{u\dagger} \qquad & V_a &= A_a^v D_a^v B_a^{v\dagger} \\ U_c &= A_c^u D_c^u B_c^{u\dagger} \qquad & V_c &= A_c^v D_c^v B_c^{v\dagger} \end{aligned} \tag{A.8}$$

where A and B are unitary matrices and D is a diagonal matrix with real entries. This definition is equivalent to a singular-value decomposition except for the fact that we allow the individual elements in D to exhibit negative values.*

The matrices $U_a U_a^\dagger$ and $V_a V_a^\dagger$ are Hermitian and (A.3) implies that they commute hence both are diagonalised by the same unitary matrix P:

$$P\, U_a U_a^\dagger P^\dagger = D \qquad P\, V_a V_a^\dagger P^\dagger = D' \tag{A.9}$$

With the help of the decomposition in (A.8) they take on the form:

$$P A_a^u D_a^{u^2} A_a^{u^\dagger} P^\dagger = D \qquad P A_a^v D_a^{v^2} A_a^{v^\dagger} P^\dagger = D' \tag{A.10}$$

And we obtain $A_a^u = A_a^v$. From (A.3) using $U_c U_c^\dagger$ and $V_c V_c^\dagger$ we infer in a similar manner $A_c^u = A_c^v$. Evaluating the conditions for the inverse transformation using (A.6) yields $B_a^u = B_c^v$ and $B_c^u = B_a^v$. Consequently the decomposition in (A.8) can be written as:

$$\begin{aligned} U_a &= A_a D_a^u B_a^\dagger \qquad & U_c &= A_c D_c^u B_c^\dagger \\ V_a &= A_a D_a^v B_c^\dagger \qquad & V_c &= A_c D_c^v B_a^\dagger \end{aligned} \tag{A.11}$$

Using the matrices in (A.11) in conjunction with the conditions in (A.3) we further obtain:

$$D_a^{u^2} + D_a^{v^2} = \mathbb{1} \qquad D_c^{u^2} + D_c^{v^2} = \mathbb{1}. \tag{A.12}$$

This implies that the individual elements of the D matrices have to obey $\cos(r_k)$ and $\sin(r_k)$ behaviour. Applying the conditions in (A.6) to the transformation matrices in (A.11) results in:

$$D_a^{u2} + D_c^{v2} = \mathbb{1} \qquad D_c^{u2} + D_a^{v2} = \mathbb{1} \tag{A.13}$$

From which we conclude $D_a^{u^2} = D_c^{u^2} = D^{u^2}$ and $D_a^{v^2} = D_c^{v^2} = D^{v^2}$. Taking everything into account the final decomposed frequency conversion matrices read:

$$\begin{aligned} U_a &= A_a D^u B_a^\dagger \qquad & U_c &= A_c D^u B_c^\dagger \\ V_a &= A_a D^v B_c^\dagger \qquad & V_c &= A_c D^v B_a^\dagger \\ & & D^{u^2} + D^{v^2} &= \mathbb{1} \end{aligned} \tag{A.14}$$

* The reason for this extension of the singular-value decomposition becomes clear in (A.16).

In the original representation they take on the form:

$$\begin{aligned} U_a(\omega,\omega') &= \sum_k \varphi_k^*(\omega)\cos(r_k)\psi_k(\omega') \\ V_a(\omega,\omega') &= \sum_k \varphi_k^*(\omega)\sin(r_k)\phi_k(\omega') \\ U_c(\omega,\omega') &= \sum_k \xi_k^*(\omega)\cos(r_k)\phi_k(\omega') \\ V_c(\omega,\omega') &= \sum_k \xi_k^*(\omega)\sin(r_k)\psi_k(\omega') \end{aligned} \tag{A.15}$$

From these symmetry relations the frequency conversion process in (10) must take on the form of multiple beam-splitter relations in orthogonal modes

$$\begin{aligned} \hat{A}_k^{(out)} &= \cos(r_k)\hat{A}_k^{(in)} + \sin(r_k)\hat{C}_k^{(in)} \\ \hat{C}_k^{(out)} &= \cos(r_k)\hat{C}_k^{(in)} - \sin(r_k)\hat{A}_k^{(in)} \end{aligned} \tag{A.16}$$

where we defined:

$$\begin{aligned} \hat{A}_k^{(out)} &= \int \mathrm{d}\omega\, \varphi_k(\omega)\hat{a}^{(out)}(\omega) \qquad & \hat{C}_k^{(out)} &= \int \mathrm{d}\omega\, \xi_k(\omega)\hat{c}^{(out)}(\omega) \\ \hat{A}_k^{(in)} &= \int \mathrm{d}\omega\, \psi_k(\omega)\hat{a}^{(in)}(\omega) \qquad & \hat{C}_k^{(in)} &= \int \mathrm{d}\omega\, \phi_k(\omega)\hat{c}^{(in)}(\omega) \end{aligned} \tag{A.17}$$

Note however that the canonical commutation relations do not demand that the input and output modes are of identical shape. In principle the input modes $\hat{A}^{(in)}$ and output modes $\hat{C}^{(in)}$ could feature completely different spectral mode functions $\varphi_k(\omega)$ and $\psi_k(\omega)$ but still form a canonical and hence unitary solution.

Appendix B. PDC: Canonical transformation conditions

As in the case of frequency conversion the parametric down-conversion process is a unitary transformation, hence it must preserve the canonical commutation relations. Retracting the calculation in (Appendix A) for parametric down-conversion they read:

$$U_a U_a^\dagger - V_a V_a^\dagger \;=\; U_b U_b^\dagger - V_b V_b^\dagger \;=\; I \tag{B.1}$$

$$U_a V_b^T - V_a U_b^T \;=\; 0 \tag{B.2}$$

For the inverse transformation they evaluate to:

$$U_a^\dagger U_a - (V_b^\dagger V_b)^T \;=\; U_b^\dagger U_b - (V_a^\dagger V_a)^T \;=\; I \tag{B.3}$$

$$U_a^\dagger V_a - (U_b^\dagger V_b)^T \;=\; 0 \tag{B.4}$$

With the help of the singular-value-decomposition theorem and (B.1), (B.2) and (B.4) the four matrices of a general parametric down-conversion process in (51) take on the form:

$$\begin{aligned} U_a(\omega,\omega') &= \sum_k \varphi_k^*(\omega)\cosh(r_k)\psi_k(\omega') \\ V_a(\omega,\omega') &= \sum_k \varphi_k^*(\omega)\sinh(r_k)\phi_k^*(\omega') \\ U_b(\omega,\omega') &= \sum_k \xi_k^*(\omega)\cosh(r_k)\phi_k(\omega') \\ V_b(\omega,\omega') &= \sum_k \xi_k^*(\omega)\sinh(r_k)\psi_k^*(\omega') \end{aligned} \tag{B.5}$$

From these symmetry relations the parametric down-process (51) consists of multiple twin-beam squeezers in orthogonal optical modes:♯

$$\begin{aligned}\hat{A}_k^{(out)} &= \cosh(r_k)\hat{A}_k^{(in)} + \sinh(r_k)\hat{B}_k^{(in)\dagger} \\ \hat{B}_k^{(out)} &= \cosh(r_k)\hat{B}_k^{(in)} + \sinh(r_k)\hat{A}_k^{(in)\dagger}\end{aligned} \tag{B.6}$$

where we defined:

$$\begin{aligned}\hat{A}_k^{(out)} &= \int \mathrm{d}\omega\, \varphi_k(\omega)\hat{a}^{(out)}(\omega) \qquad & \hat{B}_k^{(out)} &= \int \mathrm{d}\omega\, \xi_k(\omega)\hat{b}^{(out)}(\omega) \\ \hat{A}_k^{(in)} &= \int \mathrm{d}\omega\, \psi_k(\omega)\hat{a}^{(in)}(\omega) \qquad & \hat{B}_k^{(in)} &= \int \mathrm{d}\omega\, \phi_k(\omega)\hat{b}^{(in)}(\omega)\end{aligned} \tag{B.7}$$

Note however that, as in the frequency conversion case, the canonical commutation relations do not demand that the input and output modes are of identical shape.

Appendix C. FC: Simulated frequency conversion processes

In our simulation of frequency conversion we did not restrict ourselves to a specific crystal material or wavelength range, but created a generic model of the process. For this purpose we first moved from the (ω, ω')-system to the parameter range (ν, ν') relative to the central frequencies of the frequency conversion process (ω_0, ω_0'). In the simulation we work with a Gaussian pump distribution, as created by pulsed laser systems. The pump distribution in (22) and (41) takes on the form

$$\alpha(\nu - \nu') = E_p \exp\left[-\frac{(\nu - \nu')^2}{2\sigma^2}\right], \tag{C.1}$$

where E_p labels the pump amplitude and σ the pump width. The second function we have to adapt is the phasematching function $\Delta k(\omega, \omega') = k_p(\omega' - \omega) - k_c(\omega') + k_a(\omega)$. As a first step we perform a Taylor expansion of the individual $k(\omega)$ terms up to first order about their central frequency ω_0:

$$k(\omega) \approx k(\omega_0) + \frac{d}{d\omega}k(\omega_0)\underbrace{(\omega - \omega_0)}_{\nu} \tag{C.2}$$

This is justified since we restrict ourselves to nonlinear processes not to broad in frequency (slowly varying envelope approximation $\Delta\omega \ll \omega_0$) far off any singularities in the dispersion relation. At the central frequencies the process, per definition, displays perfect phasematching $k_p(\omega_0' - \omega_0) - k_c(\omega_0') + k_a(\omega_0) = 0$ and the phasematching function simplifies to:

$$\Delta k(\nu, \nu') = \frac{d}{d\omega}k_p(\omega_0' - \omega_0)(\nu' - \nu) - \frac{d}{d\omega}k_c(\omega_0')\,\nu' + \frac{d}{d\omega}k_a(\omega_0)\,\nu \tag{C.3}$$

The three remaining parameters $\frac{d}{d\omega}k_p(\omega_0' - \omega_0)$, $\frac{d}{d\omega}k_c(\omega_0')$ and $\frac{d}{d\omega}k_a(\omega_0)$ — the inverse group velocities of the three interacting beams — define the material properties of the system and can be adjusted accordingly.

This compact notation enables us to simulate any frequency conversion process with the help of just 6 parameters: The width and amplitude of the pump beam, the group velocities of the three interacting waves and the length of the nonlinear medium.

♯ In principle the twin-beam squeezer has a phase degree of freedom [11] which we absorb in the definition of the electric field operators $\hat{A}_k$ and $\hat{B}_k$.

In order to evaluate a correlated FC with many modes r_k, as presented in figure 3 and 5, we use the parameters $\sigma = 4.0$, $\frac{d}{d\omega}k_p(\omega_0' - \omega_0) = 0.5$, $\frac{d}{d\omega}k_c(\omega_0') = 3.0$, $\frac{d}{d\omega}k_a(\omega_0) = 4.5$ and a crystal of length $L = 2$. The pump amplitude E_p is adjusted to give the targeted down-conversion rates.

For the (almost) uncorrelated case with few optical modes r_k, as depicted in figure 4 and 6, we applied $\sigma = 0.98190$, $\frac{d}{d\omega}k_p(\omega_0' - \omega_0) = 3.0$, $\frac{d}{d\omega}k_c(\omega_0') = 1.5$, $\frac{d}{d\omega}k_a(\omega_0) = 4.5$ and a crystal of length $L = 2$. Again the pump amplitude E_p is adjusted to give the desired down-conversion rates.

Appendix D. FC: Numerical implementation

In order to obtain the time-ordered solutions we solved the classical differential equations in (44) and (45) which give the functions $U_a(z, \omega, \omega'')$, $U_c(z, \omega, \omega'')$, $V_a(z, \omega, \omega'')$, and $V_c(z, \omega, \omega'')$ describing the frequency conversion process.

In the numerical implementation of frequency conversion we used a sampling of 500 points for each frequency degree of freedom and 500 points in z-direction to discretize the functions $U_a(z, \omega, \omega'')$, $U_c(z, \omega, \omega'')$, $V_a(z, \omega, \omega'')$, $V_c(z, \omega, \omega'')$ and $f(\omega, \omega', z)$. We evaluated the successive integrations in (46) via the trapezoid rule until the solutions converged. The actual solution defining the overall process properties is given by the matrices at the end of the crystal $U_a(z = \frac{L}{2}, \omega, \omega'')$, $U_c(z = \frac{L}{2}, \omega, \omega'')$, $V_a(z = \frac{L}{2}, \omega, \omega'')$, and $V_c(z = \frac{L}{2}, \omega, \omega'')$

We checked the accuracy of the result in a variety of ways: At first we evaluated the canonical transformation conditions in (A.3), (A.4), (A.6), and (A.7). For example in the case of (A.4) we calculated:

$$\begin{aligned}\int \mathrm{d}\omega' U_a(z = \frac{L}{2}, \omega, \omega') V_c(z = \frac{L}{2}, \omega'', \omega')^* \\ - \int \mathrm{d}\omega' V_a(z = \frac{L}{2}, \omega, \omega') U_c(z = \frac{L}{2}, \omega'', \omega')^* \\ = D^{(diff)}(z = \frac{L}{2}, \omega, \omega')\end{aligned} \tag{D.1}$$

and determined the distance of $D^{(diff)}(z = \frac{L}{2}, \omega, \omega')$ from the expected zero matrix and consequently the error in the solution via:

$$\text{error} = \frac{\int \mathrm{d}\omega \int \mathrm{d}\omega' D^{(diff)}(z = \frac{L}{2}, \omega, \omega')}{0.5\left[\int \mathrm{d}\omega \int \mathrm{d}\omega' |V_a(z = \frac{L}{2}, \omega, \omega')| + \int \mathrm{d}\omega \int \mathrm{d}\omega' |U_c(z = \frac{L}{2}, \omega, \omega')|\right]} \tag{D.2}$$

In all presented cases the obtained error was below 0.0085.

We also checked the numerical Schmidt decompositions of $U_a(z = \frac{L}{2}, \omega, \omega'')$, $U_c(z = \frac{L}{2}, \omega, \omega'')$, $V_a(z = \frac{L}{2}, \omega, \omega'')$, and $V_c(z = \frac{L}{2}, \omega, \omega'')$ to verify the mode properties derived in Appendix A. During this process the decompositions of $U_a(z = \frac{L}{2}, \omega, \omega'')$, $U_c(z = \frac{L}{2}, \omega, \omega'')$ showed numerical issues, these however could be resolved by decomposing $U_a(z = \frac{L}{2}, \omega, \omega'')U_a^\dagger(z = \frac{L}{2}, \omega, \omega'')$, $U_a^\dagger(z = \frac{L}{2}, \omega, \omega'')U_a(z = \frac{L}{2}, \omega, \omega'')$, $U_c(z = \frac{L}{2}, \omega, \omega'')U_c^\dagger(z = \frac{L}{2}, \omega, \omega'')$, $U_c^\dagger(z = \frac{L}{2}, \omega, \omega'')U_c(z = \frac{L}{2}, \omega, \omega'')$ instead. The obtained modes from these four matrices provided a much improved stability especially in the high gain regime. Using these Schmidt modes we verified that the obtained Schmidt values of the U and V matrices behaved like $\cos(r_k)^2 + \sin(r_k)^2 = 1$ with errors below 0.0063. We also asserted that the decompositions yielded the functions $\varphi_k, \psi_k, \phi_k, \xi_k$ with symmetries as detailed in (A.15), which were fulfilled within numerical accuracy.

The program code, published on our website, is able to directly create the investigated frequency conversion processes and also performs all mentioned tests.

Appendix E. PDC: Simulated down-conversion process

As in the simulation of frequency conversion processes in Appendix C we didn't restrict ourselves to a specific crystal material and wavelength range but created a generic model of the process. Again we first move from the (ω, ω')-system to the parameter range (ν, ν') relative to the central frequencies of the parametric down-conversion process (ω_0, ω_0'). As in the frequency conversion case we used a Gaussian pump distribution for the simulation, which in (56) and (61) take on the form

$$\alpha(\nu + \nu') = E_p \exp\left[-\frac{(\nu + \nu')^2}{2\sigma^2}\right], \tag{E.1}$$

where E_p labels the pump amplitude and σ the pump width. The second function we have to adapt is the phase-matching function $\Delta k(\omega, \omega') = k_p(\omega + \omega') - k_a(\omega) - k_b(\omega')$. As a first step we perform a Taylor expansion of the individual $k(\omega)$ terms up to first order about their central frequency ω_0:

$$k(\omega) \approx k(\omega_0) + \frac{d}{d\omega}k(\omega_0)\underbrace{(\omega - \omega_0)}_{\nu} \tag{E.2}$$

This is justified since we restrict ourselves to nonlinear processes not to broad in frequency (slowly varying envelope approximation $\Delta\omega \ll \omega_0$) far off any singularities in the dispersion. At the central frequencies the process, per definition, displays perfect phasematching $k_p(\omega_0' + \omega_0) - k_a(\omega_0) - k_b(\omega_0') = 0$ and the phasematching function simplifies to:

$$\Delta k(\nu, \nu') = \frac{d}{d\omega}k_p(\omega_0' + \omega_0)(\nu' + \nu) - \frac{d}{d\omega}k_a(\omega_0)\,\nu - \frac{d}{d\omega}k_b(\omega_0')\,\nu' \tag{E.3}$$

The three remaining parameters $\frac{d}{d\omega}k_p(\omega_0' + \omega_0)$, $\frac{d}{d\omega}k_a(\omega_0)$ and $\frac{d}{d\omega}k_b(\omega_0')$ — the inverse group velocities of the three interacting beams — define the material properties of the system and can be adjusted accordingly.

This compact notation enables us to simulate any parametric down-conversion conversion process with the help of just 6 parameters: The width and amplitude of the pump beam, the group velocities of the three interacting waves and the length of the nonlinear medium.

In order to evaluate a correlated PDC with many modes r_k, as presented in figure 8 and 10, we use the parameters $\sigma = 4.0$, $\frac{d}{d\omega}k_p(\omega_0' + \omega_0) = 0.5$, $\frac{d}{d\omega}k_a(\omega_0) = 3.0$, $\frac{d}{d\omega}k_b(\omega_0') = 4.5$ and a crystal of length $L = 2$. The pump amplitude E_p is adjusted to give the targeted conversion efficiencies.

For the (almost) uncorrelated case with few optical modes r_k, as depicted in figures 9 and 11, we applied $\sigma = 0.96231155$, $\frac{d}{d\omega}k_p(\omega_0 + \omega_0') = 3.0$, $\frac{d}{d\omega}k_a(\omega_0) = 4.5$, $\frac{d}{d\omega}k_b(\omega_0') = 1.5$ and a crystal of length $L = 2$. Again the pump amplitude E_p is adjusted to give the desired conversion efficiencies.

Appendix F. PDC: Numerical implementation

In order to obtain the time-ordered solutions we solved the classical differential equations in (64) and (65) which give the functions $U_a(z, \omega, \omega'')$, $U_b(z, \omega, \omega'')$, $V_a(z, \omega, \omega'')$, and $V_b(z, \omega, \omega'')$ describing the parametric down-conversion process.

In the numerical implementation of parametric down-conversion we used a sampling of 500 points for each frequency degree of freedom and 500 points in z-direction to discretize the functions $U_a(z,\omega,\omega'')$, $U_b(z,\omega,\omega'')$, $V_a(z,\omega,\omega'')$, $V_b(z,\omega,\omega'')$ and $f(\omega,\omega',z)$. As in the frequency conversion case we evaluated the successive integrations via the trapezoid rule until the solutions converged. The actual solution defining the overall process properties is given by the matrices at the end of the crystal $U_a(z=\frac{L}{2},\omega,\omega'')$, $U_b(z=\frac{L}{2},\omega,\omega'')$, $V_a(z=\frac{L}{2},\omega,\omega'')$, and $V_b(z=\frac{L}{2},\omega,\omega'')$

We checked the accuracy of the result in a variety of ways: At first we evaluated the canonical transformation conditions in (B.1), (B.2), (B.3), and (B.4). For example in the case of (B.2) we evaluated:

$$\begin{aligned}\int \mathrm{d}\omega' U_a(z=\frac{L}{2},\omega,\omega')V_b(z=\frac{L}{2},\omega'',\omega') \\ - \int \mathrm{d}\omega' V_a(z=\frac{L}{2},\omega,\omega')U_b(z=\frac{L}{2},\omega'',\omega') \\ = D^{(diff)}(z=\frac{L}{2},\omega,\omega')\end{aligned} \tag{F.1}$$

and determined the distance of $D^{(diff)}(z=\frac{L}{2},\omega,\omega')$ from the expected zero matrix and consequently the error in the solution via:

$$\text{error} = \frac{\int \mathrm{d}\omega \int \mathrm{d}\omega' D^{(diff)}(z=\frac{L}{2},\omega,\omega')}{0.5\left[\int \mathrm{d}\omega \int \mathrm{d}\omega' |V_a(z=\frac{L}{2},\omega,\omega')| + \int \mathrm{d}\omega \int \mathrm{d}\omega' |U_b(z=\frac{L}{2},\omega,\omega')|\right]} \tag{F.2}$$

In all presented cases the obtained error was below 0.00019.

We also checked the numerical Schmidt decompositions of $U_a(z,\omega,\omega'')$, $U_b(z,\omega,\omega'')$, $V_a(z,\omega,\omega'')$, and $V_b(z,\omega,\omega'')$ to verify the mode properties derived in Appendix B. During this process the decompositions of $U_a(z,\omega,\omega'')$, $U_b(z,\omega,\omega'')$ showed numerical issues, these however could be resolved by decomposing $U_a(z,\omega,\omega'')U_a^\dagger(z,\omega,\omega'')$, $U_a^\dagger(z,\omega,\omega'')U_a(z,\omega,\omega'')$, $U_b(z,\omega,\omega'')U_b^\dagger(z,\omega,\omega'')$, $U_b^\dagger(z,\omega,\omega'')U_b(z,\omega,\omega'')$ instead. The obtained modes from these four matrices provided a much improved stability especially in the high gain regime. Using these Schmidt modes we verified that the obtained Schmidt values of the U and V matrices behaved like $\cosh(r_k)^2 - \sinh(r_k)^2 = 1$ with errors below 0.00006. We also asserted that the decompositions yielded the functions $\varphi_k, \psi_k, \phi_k, \xi_k$ with symmetries as detailed in (B.5), which where fulfilled within numerical accuracy.

The program code, published on our website, is able to directly create the investigated parametric down-conversion processes and also performs all mentioned tests.

References

[1] C. K. Hong, Z. Y. Ou, and L. Mandel. Measurement of subpicosecond time intervals between two photons by interference. *Physical Review Letters*, 59(18):2044, November 1987.

[2] Alfred B. U'Ren, Christine Silberhorn, Konrad Banaszek, and Ian A. Walmsley. Efficient conditional preparation of high-fidelity single photon states for fiber-optic quantum networks. *Physical Review Letters*, 93(9):093601, 2004.

[3] Peter J. Mosley, Jeff S. Lundeen, Brian J. Smith, Piotr Wasylczyk, Alfred B. U'Ren, Christine Silberhorn, and Ian A. Walmsley. Heralded generation of ultrafast single photons in pure quantum states. *Physical Review Letters*, 100(13):133601–4, April 2008.

[4] T.B. Pittman, B.C. Jacobs, and J.D. Franson. Heralding single photons from pulsed parametric down-conversion. *Optics Communications*, 246(4-6):545–550, February 2005.

[5] A. L. Migdall, D. Branning, and S. Castelletto. Tailoring single-photon and multiphoton probabilities of a single-photon on-demand source. *Physical Review A*, 66(5):053805, November 2002.

[6] Paul G. Kwiat, Klaus Mattle, Harald Weinfurter, Anton Zeilinger, Alexander V. Sergienko, and Yanhua Shih. New high-intensity source of polarization-entangled photon pairs. *Physical Review Letters*, 75(24):4337–4341, December 1995.

[7] Paul G. Kwiat, Edo Waks, Andrew G. White, Ian Appelbaum, and Philippe H. Eberhard. Ultrabright source of polarization-entangled photons. *Physical Review A*, 60(2):R773–R776, 1999.

[8] Christian Kurtsiefer, Markus Oberparleiter, and Harald Weinfurter. High-efficiency entangled photon pair collection in type-II parametric fluorescence. *Physical Review A*, 64(2):023802, July 2001.

[9] Matthew E. Anderson, D. F. McAlister, M. G. Raymer, and Mool C. Gupta. Pulsed squeezed-light generation in chi^(2) nonlinear waveguides. *Journal of the Optical Society of America B*, 14(11):3180, November 1997.

[10] D. K. Serkland, M. M. Fejer, R. L. Byer, and Y. Yamamoto. Squeezing in a quasi-phase-matched LiNbO3 waveguide. *Optics Letters*, 20(15):1649–1651, 1995.

[11] Stephen M. Barnett and Paul M. Radmore. *Methods in theoretical quantum optics*. Oxford University Press, January 2003.

[12] Andreas Christ, Kaisa Laiho, Andreas Eckstein, Katiúscia N Cassemiro, and Christine Silberhorn. Probing multimode squeezing with correlation functions. *New Journal of Physics*, 13:033027, March 2011.

[13] Xiaorong Gu, Kun Huang, Haifeng Pan, E Wu, and Heping Zeng. Photon correlation in single-photon frequency upconversion. *Optics Express*, 20(3):2399–2407, January 2012.

[14] H. J. McGuinness, M. G. Raymer, C. J. McKinstrie, and S. Radic. Quantum frequency translation of single-photon states in a photonic crystal fiber. *Physical Review Letters*, 105(9):093604, 2010.

[15] L. Mejling, C. J. McKinstrie, M. G. Raymer, and K. Rottwitt. Quantum frequency translation by four-wave mixing in a fiber: low-conversion regime. *Optics Express*, 20(8):8367–8396, April 2012.

[16] S. Tanzilli, W. Tittel, M. Halder, O. Alibart, P. Baldi, N. Gisin, and H. Zbinden. A photonic quantum information interface. *Nature*, 437(7055):116–120, September 2005.

[17] D. Kielpinski, J. F. Corney, and H. M. Wiseman. Quantum optical waveform conversion. *Physical Review Letters*, 106(13):130501, March 2011.

[18] Benjamin Brecht, Andreas Eckstein, Andreas Christ, Hubertus Suche, and Christine Silberhorn. From quantum pulse gate to quantum pulse shaper—engineered frequency conversion in nonlinear optical waveguides. *New Journal of Physics*, 13(6):065029, June 2011.

[19] Andreas Eckstein, Benjamin Brecht, and Christine Silberhorn. A quantum pulse gate based on spectrally engineered sum frequency generation. *Optics Express*, 19(15):13770–13778, July 2011.

[20] H. J. McGuinness, M. G. Raymer, and C. J. McKinstrie. Theory of quantum frequency translation of light in optical fiber: application to interference of two photons of different color. *Optics Express*, 19(19):17876–17907, 2011.

[21] H. Kamada, M. Asobe, T. Honjo, H. Takesue, Y. Tokura, Y. Nishida, O. Tadanaga, and H. Miyazawa. Efficient and low-noise single-photon detection in 1550 nm communication band by frequency upconversion in periodically poled LiNbO3 waveguides. *Optics Letters*, 33(7):639–641, April 2008.

[22] J. S. Pelc, L. Ma, C. R. Phillips, Q. Zhang, C. Langrock, O. Slattery, X. Tang, and M. M. Fejer. Long-wavelength-pumped upconversion single-photon detector at 1550 nm: performance and noise analysis. *Optics Express*, 19(22):21445–21456, October 2011.

[23] J. S. Pelc, Q. Zhang, C. R. Phillips, L. Yu, Y. Yamamoto, and M. M. Fejer. Cascaded frequency upconversion for high-speed single-photon detection at 1550 nm. *Optics Letters*, 37(4):476–478, February 2012.

[24] R. Clark, Taehyun Kim, and Jungsang Kim. Double-stage frequency down-conversion system for distribution of ion-photon entanglement over long distances. In *Photonics Society Summer Topical Meeting Series, 2011 IEEE*, pages 45 –46, July 2011.

[25] S. Ramelow, A. Fedrizzi, A. Poppe, N. K. Langford, and A. Zeilinger. Polarization-entanglement-conserving frequency conversion of photons. *Physical Review A*, 85(1):013845, January 2012.

[26] W. P. Grice and I. A. Walmsley. Spectral information and distinguishability in type-II down-conversion with a broadband pump. *Physical Review A*, 56(2):1627, 1997. Copyright (C) 2009 The American Physical Society; Please report any problems to prola@aps.org.

[27] Wojciech Wasilewski, A. I. Lvovsky, Konrad Banaszek, and Czeslaw Radzewicz. Pulsed squeezed light: Simultaneous squeezing of multiple modes. *Physical Review A (Atomic, Molecular, and Optical Physics)*, 73(6):063819–12, June 2006.

[28] A. I. Lvovsky, Wojciech Wasilewski, and Konrad Banaszek. Decomposing a pulsed optical parametric amplifier into independent squeezers. *Journal of Modern Optics*, 54(5):721, 2007.

[29] E. Brambilla, A. Gatti, M. Bache, and L. A. Lugiato. Simultaneous near-field and far-field spatial quantum correlations in the high-gain regime of parametric down-conversion. *Physical Review A*, 69(2):023802, February 2004. Copyright (C) 2009 The American Physical Society; Please report any problems to prola@aps.org.

[30] Agata M Brańczyk. *Non-classical States of Light*. PhD thesis, University of Queensland, August 2010.

[31] Gil Porat, Yaron Silberberg, Ady Arie, and Haim Suchowski. Two photon frequency conversion. *Optics Express*, 20(4):3613–3619, February 2012.

[32] Mikhail I. Kolobov. The spatial behavior of nonclassical light. *Reviews of Modern Physics*, 71(5):1539, October 1999.

[33] K. J. Blow, Rodney Loudon, Simon J. D. Phoenix, and T. J. Shepherd. Continuum fields in quantum optics. *Physical Review A*, 42(7):4102, October 1990.

[34] Rodney Loudon. *The Quantum Theory of Light*. Oxford University Press, USA, 3 edition, November 2000.

[35] Prem Kumar. Quantum frequency conversion. *Optics Letters*, 15(24):1476–1478, December 1990.

[36] Kevin A. O'Donnell and Alfred B. U'Ren. Time-resolved up-conversion of entangled photon pairs. *Physical Review Letters*, 103(12):123602, 2009.

[37] Richard A. Campos, Bahaa E. A. Saleh, and Malvin C. Teich. Quantum-mechanical lossless beam splitter: SU(2) symmetry and photon statistics. *Physical Review A*, 40(3):1371, 1989.

[38] Artur K. Ekert and Peter L. Knight. Relationship between semiclassical and quantum-mechanical input-output theories of optical response. *Physical Review A*, 43(7):3934, April 1991. Copyright (C) 2009 The American Physical Society; Please report any problems to prola@aps.org.

[39] Samuel L. Braunstein. Squeezing as an irreducible resource. *Physical Review A*, 71(5):055801, May 2005. Copyright (C) 2009 The American Physical Society; Please report any problems to prola@aps.org.

[40] M.G. Raymer, S.J. van Enk, C.J. McKinstrie, and H.J. McGuinness. Interference of two photons of different color. *Optics Communications*, 283(5):747–752, March 2010.

[41] Peter P Rohde, Wolfgang Mauerer, and Christine Silberhorn. Spectral structure and decompositions of optical states, and their applications. *New Journal of Physics*, 9:91–91, April 2007.

[42] J. J. Sakurai. *Modern Quantum Mechanics*. Prentice Hall, revised edition. edition, August 1993.

[43] Agata M. Brańczyk, Thomas M. Stace, and T. C. Ralph. Time ordering in spontaneous parametric down-conversion. *AIP Conference Proceedings*, 1363(1):335–338, October 2011.

[44] C. K. Law, I. A. Walmsley, and J. H. Eberly. Continuous frequency entanglement: Effective finite hilbert space and entropy control. *Physical Review Letters*, 84(23):5304, June 2000.

[45] A. B U'Ren, K. Banaszek, and I. A Walmsley. Photon engineering for quantum information processing. *Quantum Info. Comput.*, 3(7):480–502, October 2003. ACM ID: 2011567.

[46] Wolfgang Mauerer. *On Colours, Keys, and Correlations: Multimode Parametric Downconversion in the Photon Number Basis*. PhD thesis, Universität Erlangen-Nürnberg, Universitätsstraße. 4, 91054 Erlangen, 2008.

[47] L. Caspani, E. Brambilla, and A. Gatti. Tailoring the spatiotemporal structure of biphoton entanglement in type-i parametric down-conversion. *Physical Review A*, 81(3):033808, March 2010.

[48] Wojciech Wasilewski and M. G. Raymer. Pairwise entanglement and readout of atomic-ensemble and optical wave-packet modes in traveling-wave raman interactions. *Physical Review A*, 73(6):063816, June 2006.

[49] Barak Dayan. Theory of two-photon interactions with broadband down-converted light and entangled photons. *Physical Review A*, 76(4):043813, October 2007.

[50] A. Gatti, R. Zambrini, M. San Miguel, and L. A. Lugiato. Multiphoton multimode polarization entanglement in parametric down-conversion. *Physical Review A*, 68(5):053807, November 2003.

[51] Agata M. Branczyk, Alessandro Fedrizzi, Thomas M. Stace, Tim C. Ralph, and Andrew G. White. Engineered optical nonlinearity for quantum light sources. *Optics Express*, 19(1):55–

65, January 2011.
[52] Andreas Christ. *Theory of waveguided parametric down-conversion: From fundamentals to applications (to be published)*. PhD thesis, University of Paderborn, 2012.

Part II.

PDC applications

It's easier to ask forgiveness
than it is to get permission.

(Grace Hopper)

7. Limits on PDC as a single-photon source

7.1. Introduction

The developed theoretical framework of PDC in Part I enables us to engineering the PDC process for the generation of photonic quantum states. Among the most important states for quantum enhanced applications are *pure* single-photon states, also known as single-photon Fock states. These are an essential ingredient for quantum information technologies such as quantum communication [81], quantum enhanced measurements [82] and quantum computing [83].[1]

There exist a variety of methods to produce *pure* single-photon states including semiconductor quantum dots [84, 85], trapped atoms [86, 87], trapped ions [88, 89] and four-wave-mixing processes [90, 91, 92, 93, 94, 95, 96, 97]. The most prominent source to create single-photon states, however, is parametric down-conversion (PDC) [21, 98, 25, 23, 99, 24, 36, 100, 101, 102].

7.2. Heralding single-photons from PDC

The general heralding process is sketched in Fig. 7.1. As already discussed in Chap. 4, during the process of parametric down-conversion, a pump photon of a strong incoming pump pulse, decays inside a nonlinear optical material, into a signal and idler photon pair. Detecting the idler photon consequently enables us to herald the presence of a signal photon and effectively creates a heralded single-photon source.

PDC however has two main limitations which impede its use as a deterministic *pure* single-photon source, both depicted in Fig. 7.1: firstly it is not guaranteed that only a single photon-pair is emitted.[2] Only vacuum or multiple-pairs simultaneously might leave the crystal as well. Furthermore most detectors are not able to discriminate between the arrival of a single or several idler photons. Hence the heralded signal state is projected into a mixture of photon-number states [103, 104, 105, 106, 107, 108, 109, 110, 111, 112].

[1] This chapter is a summary of the paper "Limits on the deterministic creation of pure single-photon states using parametric down-conversion" by Andreas Christ and Christine Silberhorn [4].

[2] PDC is a unitary transformation and completely deterministic. The detection of the photons, however is not. For pedagogical purposes it is useful to move this non-deterministic detection into the source and talk about the number of photon-pairs leaving the crystal, even if this description is formally not correct.

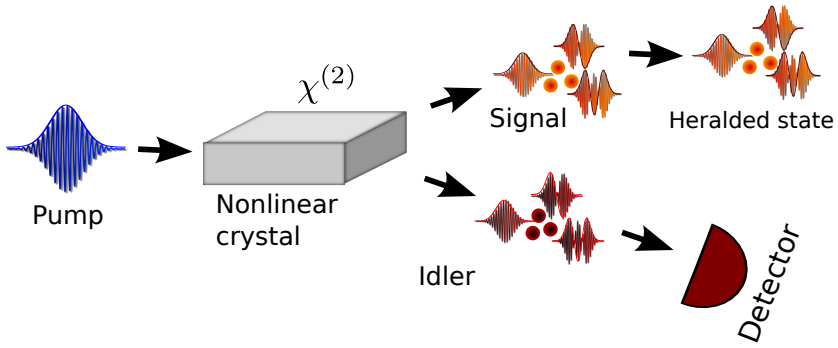

Figure 7.1.: Herald single-photon states using PDC: one or more photons of an incoming pump pulse decay, inside a nonlinear medium, into several signal and idler photon pairs in multiple optical modes. Detecting the idler photons enables us to herald the presence of the signal.

The second feature of the PDC process detrimental to the heralding of single-photons is its multi-mode spatio-spectral nature already discussed in Sec. 4.4 and Chap. 5. Standard single-photon detectors are not able to resolve in which spatial or spectral mode the heralded photon resides consequently they herald the signal state into a mixture of spatio-spectral modes, which limits the fidelity of the heralded signal state against a *pure* single-photon state [52, 24].

To quantify the achievable rates and *pure* single-photon fidelities we perform a rigorous investigation of single-photon state creation via PDC, which enables us to determine the limits of PDC to serve as a source of deterministic *pure* single-photon states.

7.2.1. PDC in the Schrödinger picture

In order to investigate the photon-number properties of the PDC states it is useful to work in the Schrödinger picture. In this picture the spectral multi-mode PDC state, as derived in Chap. 6 is given by [33]:

$$\begin{aligned} |\psi\rangle_{PDC} = \hat{U}_{PDC}\,|0\rangle &= \bigotimes_k \exp\left[r_k\left(\hat{A}_k^\dagger \hat{B}_k^\dagger - \hat{A}_k \hat{B}_k\right)\right]|0\rangle \\ &= \bigotimes_k \operatorname{sech}(r_k) \sum_{n=0}^{\infty} \tanh(r_k)^n\, |n_k^{(A)}, n_k^{(B)}\rangle \end{aligned} \tag{7.1}$$

From this equation the photon-number properties of PDC are not immediately recognizable so we explicitly write down the first few terms of Eq. (7.1)

$$\begin{aligned}|\psi\rangle_{PDC} &= A\,|0\rangle \\ &+ A\sum_k \tanh(r_k)\,|1_k^{(A)};1_k^{(B)}\rangle \\ &+ A\sum_{k\le k'} \tanh(r_k)\tanh(r'_k)\,|1_k^{(A)},1_{k'}^{(A)};1_k^{(B)},1_{k'}^{(B)}\rangle + \\ &+ A\sum_{k\le k'\le k''} \tanh(r_k)\tanh(r'_k)\tanh(r'_k)\,|1_k^{(A)},1_{k'}^{(A)},1_{k''}^{(A)};1_k^{(B)},1_{k'}^{(B)},1_{k''}^{(B)}\rangle \\ &+ \dots\,, \end{aligned} \tag{7.2}$$

where A and $|0\rangle$ equal to

$$A = \prod_k \operatorname{sech}(r_k) \qquad |0\rangle = \bigotimes_k |0\rangle_k\,. \tag{7.3}$$

From this formula it is evident that PDC always emits photons in pairs. Depending on the efficiency of the process it is possible to detect vacuum, a single pair, two pairs, three pairs and so on, where each pair is completely independent form the other. Furthermore the spectral properties of the generated photons are independent from the number of generated photon-pairs. The signal and idler photons always reside in the same set of signal modes $\{\hat{A}_k\}$ and idler $\{\hat{B}_k\}$.

7.2.2. Heralding single-photons from single-mode PDC sources

As a first step we regard the heralding of single-photons from a spatially and spectrally pure PDC state, which yields:

$$|\psi\rangle_{PDC} = \exp\left[r\hat{A}^\dagger\hat{B}^\dagger - r\hat{A}\hat{B}\right]|0\rangle = \operatorname{sech}(r)\sum_{n=0}^{\infty}\tanh^n(r)\,|n_s,n_i\rangle \tag{7.4}$$

The positive-operator valued measure (POVM) of a binary avalanche photodetector with detection efficiency η is defined as [113]:

$$\begin{aligned}\hat{\Pi}_{\text{"NoClick"}} &= \sum_{n=0}^{\infty}(1-\eta)^n\,|n\rangle\langle n| \\ \hat{\Pi}_{\text{"Click"}} &= \sum_{n=0}^{\infty}\left[1-(1-\eta)^n\right]|n\rangle\langle n| \end{aligned} \tag{7.5}$$

The POVM elements of a photon-number resolving detector are given by [114, 105]

$$\hat{\Pi}(n) = \sum_{N=n}^{\infty}\binom{N}{n}(1-\eta)^{N-n}\,\eta^n\,|N\rangle\langle N|\,, \tag{7.6}$$

where we assume for each photon the equal loss probability η. Comparing Eq. (7.5) and Eq. (7.6) we notice that both are of identical form and can be expressed as

$$\hat{\Pi}_{c_n} = \sum_{n=0}^{\infty} c_n \left|n\right\rangle \left\langle n\right|, \tag{7.7}$$

where the c_n coefficients define the efficiency and type of the detector. Using the definition of single-mode PDC state in Eq. (7.4) and the general POVM in Eq. (7.7) we are able to calculate the heralding probability:

$$p\left(r, c_n\right) = {}_{PDC}\left\langle\psi\right| \hat{\Pi}_{c_n} \left|\psi\right\rangle_{PDC} = \operatorname{sech}^2(r) \sum_{n=0}^{\infty} c_n \tanh^{2n}(r) \tag{7.8}$$

The fidelity of the heralded signal state ρ_s against a pure single-photon state is defined as:

$$F(r, c_n) = \left\langle 1\right| \rho_s \left|1\right\rangle = \frac{c_1 \tanh^2(r)}{\sum_{n=0}^{\infty} c_n \tanh^{2n}(r)} \tag{7.9}$$

These two values, the heralding probability $p\left(r, c_n\right)$ and the fidelity $F(r, c_n)$ of the heralded state, enable us to benchmark the performance of our PDC sources.

In Fig. 7.2 (a) we visualized these two benchmarks using a binary detector with varying detection efficiency η and in Fig. 7.2 (b) using a photon-number resolving detector with efficiency η. On the x-axis we plotted the achievable fidelity $F(r, c_n)$ and on the y-axis the heralding probability $p\left(r, c_n\right)$. A perfect pure and deterministic single-photon source resides in the upper right corner of these graphs. The shaded areas in the graphs give the achievable regions using either binary or photon-number resolved detection.

Binary detection, depicted Fig. 7.2 (a), features an inherent trade-off between the fidelity and the heralding. The reason for this behaviour is the fact that a binary detector cannot distinguish between the arrival of a single or multiple photons. Hence, in order to get rid of higher-order photon-number contributions we have to reduce the pump power to ensure that only photon-pairs are created. This achieves unit fidelity, yet at the cost of vanishing heralding probabilities. Similarly we are able to achieve unit heralding probability, but at the cost of a vanishing fidelity, because a huge mean-photon number is required to ensure a deterministic triggering of the heralding detector.

Photon-number resolved detectors, as depicted in Fig. 7.2(b), perform much better, since they are able to distinguish single-pair from multi-pair emissions. Using a perfect photon number resolving detector they enable the heralding of *pure* single-photons with a probability of 25%. This constraint stems directly from the thermal photon-pair distribution of a single-mode PDC source. The corresponding optimal PDC source features an amplitude of $r = 0.88$, corresponding to a squeezing value of 7.64 dB and a mean-photon number of $\langle n_{ph}\rangle = 1$.

From Fig. 7.2 it is further evident that equally important to driving a single-mode PDC source with the optimal parameters is using detectors with high detection efficiencies, since detectors with non-unit detection efficiency η severely diminish the achievable rates and fidelities, as depicted by the dashed and dotted lines in Fig. 7.2 (a) and (b).

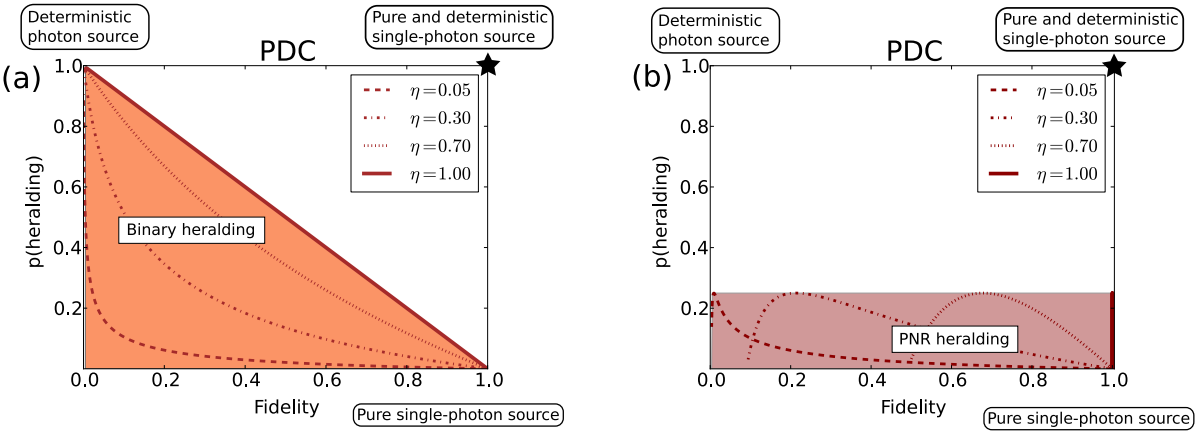

Figure 7.2.: Heralding probabilities, $p(heralding)$, and single-photon Fock-state fidelities, $Fidelity$, of the state created using a single-mode PDC source in conjunction with an (a) binary and (b) photon-number-resolving detector featuring various detection efficiencies, η.

7.2.3. Heralding single-photons from multi-mode PDC

In order to investigate the impacts of multi-mode effects on the heralding probabilities $p\,(r, c_n)$ and *pure* single-photon fidelities $F(r, c_n)$ we extended our model from Sec. 7.2.2 to incorporate spectral multi-mode effects. According to Eq. (7.1) a multi-mode PDC state, in the Schrödinger picture, is of the form:

$$|\psi\rangle_{PDC} = \bigotimes_k \operatorname{sech}(r_k) \sum_{n=0}^{\infty} \tanh^n(r_k)\, |n_k^{(s)}, n_k^{(i)}\rangle \tag{7.10}$$

In this case, not a single twin-beam squeezed state, as depicted in Eq. (7.4), is generated, but a multitude of twin-beam squeezers with amplitudes r_k in broadband frequency modes $\hat{A}_k$ and $\hat{B}_k$ [56] are emitted.

Extending our calculations from the previous section we arrive at the heralding probability

$$p(r_k, c_n) = c_0 A^2 + c_1 A^2 \sum_k \tanh^2(r_k) + c_2 A^2 \sum_{k \le k'} \tanh^2(r_k) \tanh^2(r_{k'}) + \dots\,, \tag{7.11}$$

where $A = \prod_l \operatorname{sech}(r_l)$. The fidelity of the heralded state evaluates to

$$F(r_k, c_n) = \frac{1}{N} c_1 \tanh^2(r_0), \tag{7.12}$$

with the normalization constant N defined as:

$$N = c_0 + c_1 \sum_k \tanh^2(r_k) + c_2 \sum_{k \le k'} \tanh^2(r_k) \tanh^2(r_{k'}) + \dots \tag{7.13}$$

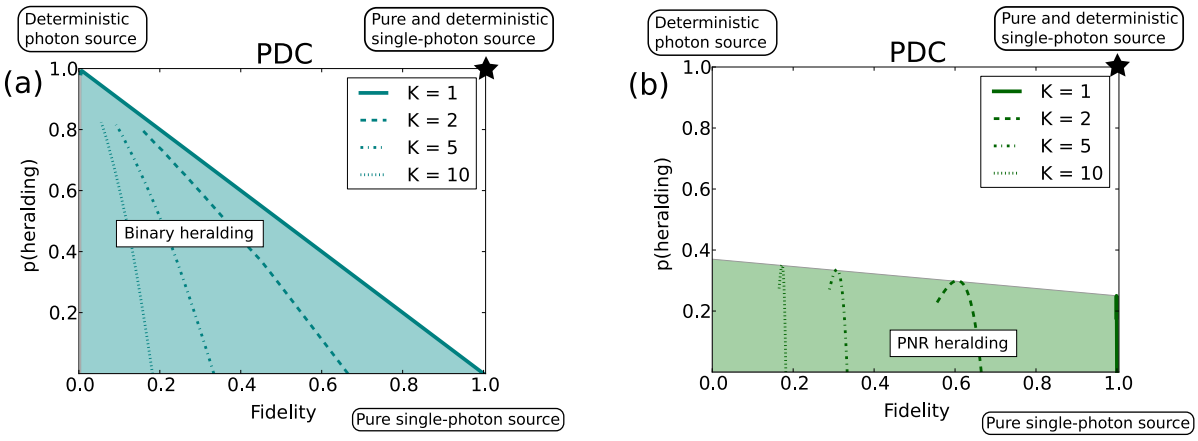

Figure 7.3.: Heralding probabilities, $p(heralding)$, and single-photon Fock-state fidelities, $Fidelity$, of the state created using various multi-mode PDC sources in conjunction with an (a) binary and (b) photon-number resolving detector featuring unit detection efficiency $\eta = 1$. Multiple frequency modes $K = 2, 5, 10$ severely limit the achievable maximum fidelities

.

We visualized the achievable rates in Fig. 7.3 using a variety of *effective* optical mode numbers $K = 1, 2, 5, 10$ and binary as well as photon-number resolved detection with unit efficiency $\eta = 1$. It is evident that the introduced frequency mixing in the heralded signal states severely reduces the achievable fidelities of the heralded states. It is hence of utmost importance to engineer PDC sources with a spectrally and spatially single-mode emission for the heralding of *pure* single-photon states. Alternatively filtering the idler beam can be applied, yet at the expense of severe losses which lead to reduce heralding rates in the idler arm and additional photon-number components in the heralded signal state, since only a fraction of the idler photons are transmitted trough the filter and impinge on the detector [108, 115, 116].

These multi-mode effects in the spectral degree of freedom can be directly extended to the spatial degree of freedom, which is, from a mathematical point of view, identical. The same detrimental effects to the fidelity of the heralded signal state are present.

7.2.4. Deterministic pure single-photon generation with switched PDC sources

While it is impossible to deterministically create *pure* single-photon states using a single PDC source it has been noted that multiple PDC sources in a switched configuration are able to solve this issue [26, 117, 118, 119]. In this approach we use multiple PDC sources to herald single-photons. When one successfully signals the heralding a pure single-photon this photon is routed to the output. Given a photon heralding probability of ν and lossless routing the overall heralding probability in a switched setup—as a

function of the number of applied PDC sources n—is:

$$p(\text{"switched"}) = 1 - (1 - \nu)^n \tag{7.14}$$

Given our optimal PDC sources with perfect photon-number resolved-detection ($\nu = 25\%$) 17 PDC setups are required to approximate a deterministic pure single-photon source ($> 99\%$).

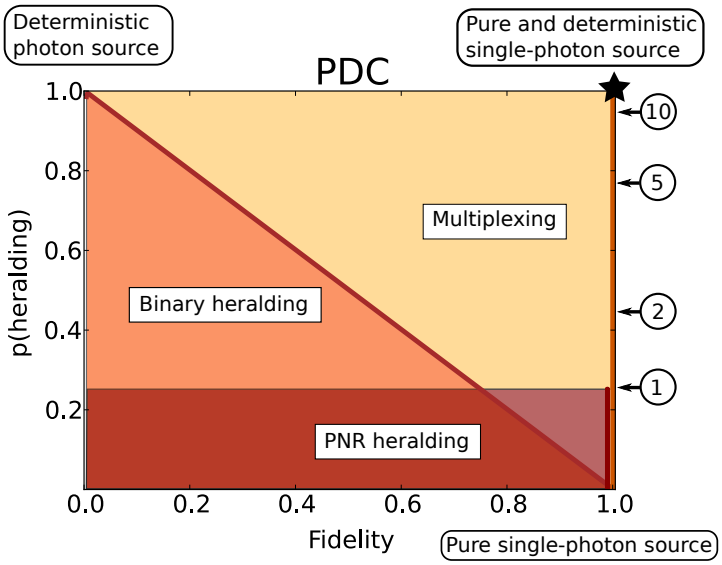

Figure 7.4.: Heralding probabilities, $p(heralding)$, and fidelities, $Fidelity$, accessible using a single-mode PDC source in conjunction with a binary detector (orange-shaded region), a photon-number resolving detector (red-shaded region), and multiplexing (yellow-shaded region). For an optimal source and a perfect photon-number-resolving detector with heralding probability of $\nu = 25\%$ 17 PDC sources are required to obtain a deterministic single-photon source ($> 99\%$ emission probability). The arrows point out the achievable heralding rates using a multiplexed setup of 1, 2, 5, and 10 single photon sources.

Fig. 7.4 summarizes our findings and shows the achievable rates using a multiplexed setup of 1, 2, 5, and 10 single photon sources and classifies the different regimes accessible using "Binary heralding", "Photon-number resolved heralding", and "Multiplexing".

In order to create a *pure* deterministic single-photon source based on PDC it is firstly necessary to build bright single-mode PDC sources which achieve the necessary mean photon-number $\langle n \rangle = 1$ and secondly to move from the current binary detection to efficient photon number resolved detectors. Finally, once these are in place, multiplexing several sources and the efficient routing of single photons will enable the final goal of building a deterministic *pure* single-photon source based on PDC.

7.3. Conclusion

In conclusion we investigated the prospects and limitations for PDC to serve as a source of *pure* deterministic single-photon states and, for the first time, included the spatio-spectral as well as the photon-number degree of freedom into the analysis. Our calculations revealed that an optimal single-mode PDC source, in conjunction with a perfect photon-number resolving detector is able to herald *pure* single-photon states with a probability of 25%. Consequently an array of 17 individual sources is necessary to approximate a pure deterministic single-photon source with $> 99\%$ emission probability. While the requested sources and detectors are beyond the reach of current technology our work clearly lays out the path for further engineering and research towards creation of a deterministic *pure* single photon source using PDC.

PHYSICAL REVIEW A **85**, 023829 (2012)

Limits on the deterministic creation of pure single-photon states using parametric down-conversion

Andreas Christ* and Christine Silberhorn
Applied Physics, University of Paderborn, Warburger Straße 100, D-33098 Paderborn and
Max Planck Institute for the Science of Light, Günther-Scharowsky-Str. 1/Building 24, D-91058 Erlangen, Germany
(Received 17 November 2011; published 22 February 2012)

Parametric down-conversion (PDC) is one of the most widely used methods to create pure single-photon states for quantum information applications. However, little attention has been paid to higher-order photon components in the PDC process, yet these ultimately limit the prospects of generating single photons of high quality. In this paper we investigate the impact of higher-order photon components *and* multiple frequency modes on the heralding rates and single-photon fidelities. This enables us to determine the limits of PDC sources for single-photon generation. Our results show that a perfectly single-mode PDC source in conjunction with a photon-number-resolving detector is ultimately capable of creating single-photon Fock states with unit fidelity and a maximal state creation probability of 25%. Hence, an array of 17 switched sources is required to build a deterministic (>99% emission probability) pure single-photon source.

DOI: 10.1103/PhysRevA.85.023829 PACS number(s): 42.65.Lm, 42.50.Ar, 42.50.Dv, 42.50.Ex

I. INTRODUCTION

Pure single-photon states are an essential ingredient for quantum information technologies such as quantum communication [1], quantum enhanced measurements [2], and quantum computing [3]. In the past decades various sources have been investigated to produce the required *pure* single-photon states, including semiconductor quantum dots [4,5], trapped atoms [6,7], trapped ions [8,9], and four-wave-mixing processes [10–17]. To date, however, the most widely used sources for the creation of single photons are still based on parametric down-conversion (PDC) [18–22] where substantial efforts haven been made over the past several years to engineer photon pairs with single-mode characteristics [23–27].

PDC sources feature many advantages: The setups are compact, cost-effective, robust, operate at room temperature, and can be integrated in optical circuits. However, they also possess some inherent drawbacks: First, the photon heralding is a statistical process and, hence, PDC always only approximates a deterministic single-photon source. Second, multi-photon-pair emission [28–37] limits the heralding rates and the fidelity of the generated single-photon states. Finally, the spectral properties of the source may lead to a heralding of single photons in a mixture of frequency modes, diminishing the purity of the heralded state.

In this paper we investigate the trade-off between heralding rates and the fidelity of the heralded states using PDC processes extending the work presented in Refs. [38] and [30]. We consider both binary avalanche photodiode detectors, as currently employed in laboratories, but also extend our analysis to incorporate the rapidly growing field of photon-number-resolved detection [39–43]. Our results quantify the definitive limits of parametric down-conversion sources to create pure single-photon states and show how well they are able to approximate deterministic behavior.

*andreas.christ@uni-paderborn.de

II. PDC STATE GENERATION

Figure 1 sketches the process of parametric down-conversion using a pulsed laser system. The incoming pump interacts with the crystal material featuring a $\chi^{(2)}$ nonlinearity creating two down-converted beams usually labeled signal and idler. These two beams exhibit perfect correlation in photon number, which means that during the interaction a certain number of photon pairs is generated, depending on the efficiency of the PDC.

The process is, in the interaction picture, described by the following Hamiltonian:

$$\hat{H}_{\mathrm{PDC}} \propto \chi^{(2)} \int d^3r\, \hat{E}_p^{(-)}(\vec{r},t)\hat{E}_s^{(+)}(\vec{r},t)\hat{E}_i^{(+)}(\vec{r},t) + \mathrm{H.c.},$$

where we consider both the spatial and spectral-temporal degree of freedom. Solving this Hamiltonian [44,45], assuming a nondepleted classical pump laser to drive the down-conversion process, we obtain the following PDC state:

$$|\psi\rangle_{\mathrm{PDC}} = \exp\left[-\frac{i}{\hbar}\left(B\sum_{k,l}\int\int d\omega_s\, d\omega_i\; f_{k,l}(\omega_s,\omega_i) \times\; \hat{a}_k^{(s)\dagger}(\omega_s)\hat{a}_l^{(i)\dagger}(\omega_i) + \mathrm{H.c.}\right)\right]|0\rangle\,. \qquad (1)$$

The operators $\hat{a}_k^{(s)\dagger}(\omega_s)$ and $\hat{a}_l^{(i)\dagger}(\omega_i)$ create photons with spatial mode numbers k and l and frequencies ω_s and ω_i into the signal and idler beam, respectively. The exact form of the output state is given by the function $f_{k,l}(\omega_s,\omega_i)$ describing its spectral and spatial structure depending on the applied pump beam and nonlinear optical material [46].

The spectral and spatial degrees of freedom are the first obstacle for the heralding of pure single-photon states. Since the photons are emitted into a multitude of spatial and spectral modes the detection of the idler beam to herald the presence of the signal results in a projection of the signal state into a mixture of spatial and spectral modes. Hence, the heralded signal does *not* form a *pure* single-photon state.

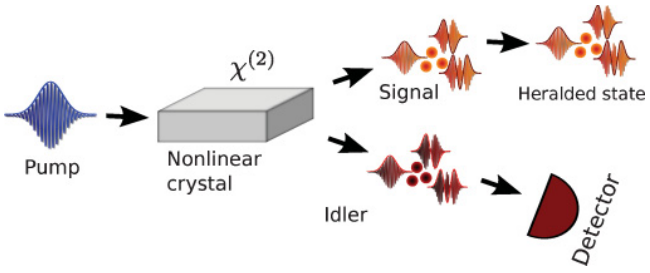

FIG. 1. (Color online) Schematic of the PDC process used to herald single-photon states: An incoming pump pulse decays inside a nonlinear medium into two beams labeled signal and idler which feature a perfect photon-number correlation. The idler beam is subsequently detected to herald the presence of the signal state.

The easiest solution to cope with this problem is to apply heavy spectral and spatial filtering in the heralding arm [33,47,48]. This will eliminate all distinguishing features and project the heralded signal into a spectrally as well as spatially pure state. However, one should be aware of the fact that the applied filter absorbs the main part of the generated idler photons and, hence, leads to significantly lower heralding rates and, furthermore, increases the higher-order photon components in the signal arm, negatively affecting the state fidelity in the photon number degree of freedom.

A more elegant approach relies on engineering the down-conversion process to emit PDC states occupying a single spectral and spatial mode. In the spatial degree of freedom waveguides can be used to restrict the signal and idler beams to the fundamental mode [45]. In the spectral degree of freedom, however, a pulsed laser system, appropriately chosen materials and wavelengths have to be applied [23,49].

For PDC processes which are engineered to emit beams into a *single* spatial and spectral mode, the generated output state corresponds to a twin-beam squeezed state [50]

$$\begin{aligned} |\psi\rangle_{\mathrm{PDC}} &= \exp[r\hat{A}^{\dagger}\hat{B}^{\dagger} - r\hat{A}\hat{B}]\,|0\rangle \\ &= \operatorname{sech}(r)\sum_{n=0}^{\infty}\tanh^{n}(r)\,|n_s,n_i\rangle\,, \end{aligned} \tag{2}$$

where we set the phase factor to π as it is unimportant within the scope of this paper. We used capital operators $\hat{A}$ and $\hat{B}$ for the signal and idler beam [51] to highlight the pulsed nature of the output state. With this state devoid of multiple spatial and spectral modes the remaining limitations for the heralding of single photons stem from higher-order photon-number components: Detecting the photons in idler projects the signal into a mixture of photon-number states and, hence, decreases the purity of the heralded state.

III. HERALDING SINGLE PHOTONS FROM SINGLE-MODE PDC SOURCES

Following the discussion of PDC in the previous chapter we now calculate the attainable heralding rates and single-photon fidelities using the state in Eq. (2) and either binary or photon-number-resolving detectors.

The most common method to herald single-photon states from PDC employs binary avalanche photo detection. Depending on its efficiency η it yields a "Click" event when photons are measured and a "NoClick" event when no photons are detected. Its measurement operators—as a positive operator valued measure (POVM)—are given by [52]

$$\begin{aligned} \hat{\Pi}_{\text{“No Click”}} &= \sum_{n=0}^{\infty}(1-\eta)^{n}\,|n\rangle\,\langle n| \\ \hat{\Pi}_{\text{“Click”}} &= \sum_{n=0}^{\infty}[1-(1-\eta)^{n}]\,|n\rangle\,\langle n|\,. \end{aligned} \tag{3}$$

Another approach relies on performing photon-number-resolved measurements in the heralding arm, which are able to enhance the heralding of single-photon states by suppressing the higher photon number components. In past years great advances have been made in photon-number-resolved detection and state-of-the-art detectors feature high detection efficiencies and exhibit an increasing fidelity resolving higher photon numbers. The POVM elements of a general photon-number-resolving detector measuring n photons are given by [30,53]

$$\hat{\Pi}(n) = \sum_{N=n}^{\infty}\binom{N}{n}(1-\eta)^{N-n}\eta^{n}\,|N\rangle\,\langle N|\,, \tag{4}$$

where we assume that each photon has a loss probability of η. Individual detection systems may differ from this POVM but all converge to $\hat{\Pi}(n) = |n\rangle\,\langle n|$ for perfect photon-number-resolved detection. In the scope of this paper we restrict ourselves to the heralding of single photons, hence, $n = 1$.

Comparing Eqs. (3) and (4) we notice that both operations have the same structure and are of the form

$$\hat{\Pi}_{c_n} = \sum_{n=0}^{\infty} c_n\,|n\rangle\,\langle n|\,, \tag{5}$$

where the c_n coefficients depend on the applied detector and its efficiency η. We note that in this formalism dark count events of imperfect detectors could also be included by adapting the c_0 coefficient.

Starting with the single-mode PDC state in Eq. (2) and the general measurement operator in Eq. (5), we calculate the probability of a successful heralding event to be

$$\begin{aligned} p(r,c_n) &= {}_{\mathrm{PDC}}\langle\psi|\,\hat{\Pi}_{c_n}\,|\psi\rangle_{\mathrm{PDC}} \\ &= \operatorname{sech}^{2}(r)\sum_{n=0}^{\infty} c_n\tanh^{2n}(r) \end{aligned} \tag{6}$$

and the heralded signal state after a successful detection takes the form

$$\begin{aligned} \rho_s(r,c_n) &= \frac{\mathrm{tr}_i(\hat{\Pi}_{c_n}|\psi\rangle_{\mathrm{PDC}\,\mathrm{PDC}}\langle\psi|)}{{}_{\mathrm{PDC}}\langle\psi|\,\hat{\Pi}_{c_n}\,|\psi\rangle_{\mathrm{PDC}}} \\ &= \frac{\sum_{n=0}^{\infty} c_n\tanh^{2n}(r)\,|n_s\rangle\,\langle n_s|}{\sum_{n=0}^{\infty} c_n\tanh^{2n}(r)}. \end{aligned} \tag{7}$$

The fidelity of the heralded signal state in Eq. (7) against a pure single photon is [54]:

$$F(r,c_n) = \langle 1|\,\rho_s\,|1\rangle = \frac{c_1\tanh^{2}(r)}{\sum_{n=0}^{\infty} c_n\tanh^{2n}(r)}. \tag{8}$$

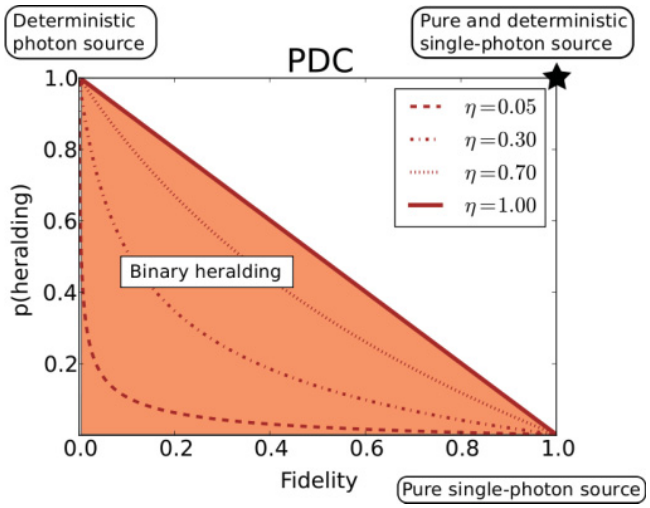

FIG. 2. (Color online) Heralding probabilities, $p(heralding)$, and single-photon Fock-state fidelities, *Fidelity*, of the state created using a single-mode PDC source in conjunction with a binary detector featuring various detection efficiencies, η. In this configuration one has to balance either high single-photon fidelities or high state generation rates.

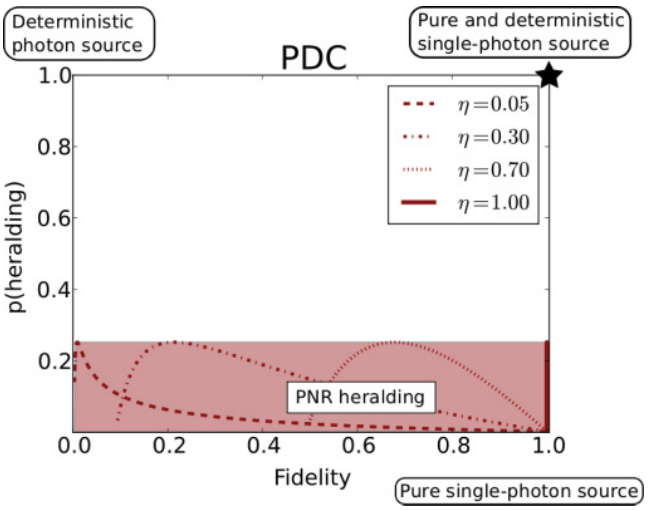

FIG. 3. (Color online) Heralding probabilities, $p(heralding)$, and single-photon Fock-state fidelities, *Fidelity*, of the state created using a single-mode PDC source in conjunction with a photon-number-resolving detector featuring various detection efficiencies, η. These detectors suppress higher-order photon numbers and, hence, enable high fidelities in conjunction with heralding rates ranging up to 25%.

Equations (6) and (8) form our benchmarks for the state generation: The heralding probability per pulse $p\,(r,c_n)$ and the fidelity of the generated signal state $F(r,c_n)$.

In Fig. 2 we plotted these benchmarks for a binary detector as given in Eq. (3) exhibiting various detection efficiencies η. The x axis depicts the achievable fidelities and the y axis the corresponding heralding probabilities. A source creating perfectly pure single-photon Fock states would appear on the right a source with unit creation probability on the top of the figure. The desired pure deterministic single-photon source resides in the upper right corner of the graphic. The shaded region in Fig. 2 depicts the general area available using PDC in conjunction with binary detectors and presents an inherent trade-off between signal creation rate and fidelity of the heralded state. Even with perfect detectors $\eta = 1$, either the PDC process only emits photon pairs ($r \leqslant 0.1$), which yields near unit fidelities but low heralding rates, or one can choose PDC states with higher-order photon-number components leading to heralding probabilities approaching unity ($r \geqslant 2$) yet at the cost of low fidelities due to the occurring mixing in photon number.

In Fig. 3 we plotted the heralding probability $p(r,c_n)$ and the state fidelity $F(r,c_n)$ using a photon-number-resolving detector as defined in Eq. (4) for various detection efficiencies η. It is evident that photon-number-resolving detectors are superior to binary detectors. They enable unit fidelities in conjunction with heralding rates up to 25% only constrained by the thermal photon-number distribution emitted by the down-conversion process ($p_{\mathrm{th}}^{(\mathrm{max})}(1) = 25\%$). In the case of perfect detection $\eta = 1$, this figure gives the fundamental limit of PDC sources. Creating perfectly pure single-photon Fock states the maximum achievable heralding rate is 25%. The corresponding PDC source features an amplitude of $r = 0.88$, corresponding to a squeezing value of 7.64 dB and a mean-photon number of $\langle n_{\mathrm{ph}}\rangle = 1$.

IV. HERALDING SINGLE PHOTONS FROM MULTIMODE PDC SOURCES

We now turn our attention to the impact of spectral multimode effects on the heralding rates and single-photon fidelities. While it is relatively straightforward to get rid of spatial multimode effects in the PDC state emission, it is not trivial to construct a source which only emits into a single spectral mode [23,24]. Hence, we extend our analysis and investigate spectrally multimode PDC as a source of single-photon states in order to evaluate to which degree multimode spectral components can be tolerated.

Including multiple spectral modes the PDC state in Eq. (2) takes the form [44]:

$$
\begin{aligned}
|\psi\rangle_{\mathrm{PDC}} &= \exp\left[-\frac{i}{\hbar}\left(B\int\!\!\int d\omega_s d\omega_i\, f(\omega_s,\omega_i)\right.\right.\\
&\qquad \left.\left.\times\ \hat{a}^{(s)\dagger}(\omega_s)\hat{a}^{(i)\dagger}(\omega_i) + \mathrm{H.c.}\right)\right]|0\rangle\\
&= \bigotimes_k \exp[r_k \hat{A}_k^\dagger \hat{B}_k^\dagger - r_k \hat{A}_k \hat{B}_k]\,|0\rangle\,, \qquad (9)\\
&= \bigotimes_k \mathrm{sech}\,(r_k) \sum_{n=0}^{\infty} \tanh^n(r_k)\,\left|n_k^{(s)}, n_k^{(i)}\right\rangle. \qquad (10)
\end{aligned}
$$

In this case, not a single twin-beam squeezed state, as depicted in Eq. (2), is generated, but a multitude of twin-beam squeezers with amplitudes r_k in broadband frequency modes $\hat{A}_k$ and $\hat{B}_k$ [51] are emitted. For common PDC sources the squeezer distribution r_k follows an exponential decay [55] and is defined by

$$
\begin{aligned}
r_k &= B\lambda_k\\
\lambda_k &= \sqrt{1-\mu}\,\mu^k \quad 0 \leqslant \mu \leqslant 1,
\end{aligned} \qquad (11)
$$

where B is optical gain depending on the applied nonlinearity, on the pump power in the PDC process and λ_k corresponds to the normalized mode distribution. The *effective* number of optical modes in the state is quantified by the parameter $K = 1/\sum_k \lambda_k^4$ [56].

The properties of the PDC state in Eq. (10) become clearer if we sort the terms according to their photon-number components,

$$|\psi\rangle_{\mathrm{PDC}} = A\,|0\rangle + A\sum_k \tanh(r_k)\,|1_k;1_k\rangle + A\sum_{k\leqslant k'} \tanh(r_k)\tanh(r_{k'})\,|1_k,1_{k'};1_k,1_{k'}\rangle + \cdots, \tag{12}$$

where $A = \prod_l \operatorname{sech}(r_l)$, $|0\rangle = \bigotimes_k |0_k\rangle$ and $\varphi_k = \pi$. According to Eq. (12) the PDC state now consists of multiple photon-pair components emitted into an array of spectral modes k.

Given a multimode PDC state as defined in Eqs. (10) and (12), we calculate the heralding rates and fidelities similar to Sec. III. In order to perform this calculation we extend the measurement operators given in Eqs. (3), (4), and (5) to the multimode regime:

$$\hat{\Pi}_{c_n} = c_0\,|0\rangle\langle 0| + c_1\sum_k |1_k\rangle\langle 1_k| + c_2\sum_{k\leqslant k'} |1_k,1_{k'}\rangle\langle 1_k,1_{k'}| + \cdots, \tag{13}$$

where the c_n terms are identical to the single-mode case as we assume that the detector cannot distinguish different frequencies due to limited time resolution. Using Eqs. (12) and (13) we obtain a multimode heralding probability of

$$p(r_k,c_n) = c_0A^2 + c_1A^2\sum_k \tanh^2(r_k) + c_2A^2\sum_{k\leqslant k'} \tanh^2(r_k)\tanh^2(r_{k'}) + \cdots \tag{14}$$

and the heralded signal state takes on the form,

$$\rho_s = \frac{1}{N}c_0\,|0\rangle\langle 0| + c_1\sum_k \tanh^2(r_k)\,|1_k\rangle\langle 1_k| + c_2\sum_{k\leqslant k'} \tanh^2(r_k)\tanh^2(r_{k'})\,|1_k,1_{k'}\rangle\langle 1_k,1_{k'}| + \cdots \tag{15}$$

with the normalization constant N defined as

$$N = c_0 + c_1\sum_k \tanh^2(r_k) + c_2\sum_{k\leqslant k'} \tanh^2(r_k)\tanh^2(r_{k'}) + \cdots. \tag{16}$$

The corresponding fidelity of the heralded photon state against a single-photon Fock state evaluates to

$$F(r_k,c_n) = \frac{1}{N}c_1\tanh^2(r_0). \tag{17}$$

Equations (14) and (17) enable us to benchmark multimode PDC processes as a source of heralded single-photon states via the heralding probability $p(r_k,c_n)$ and the fidelity $F(r_k,c_n)$ of a heralded state including *both* the spectral and photon-number degree of freedom. Note that the performance of spectrally filtered PDC states will lie below a spectrally single-mode source.

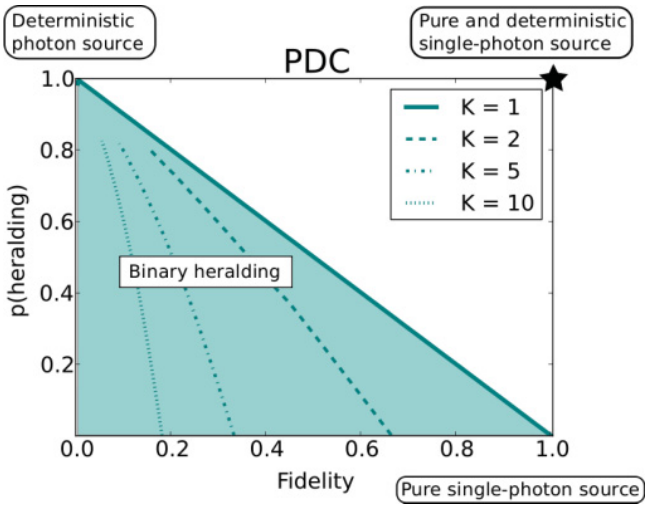

FIG. 4. (Color online) Heralding probabilities, $p(heralding)$, and single-photon Fock-state fidelities, *Fidelity*, of the state created using various multimode PDC sources in conjunction with a binary detector featuring unit detection efficiency $\eta = 1$. Multiple frequency modes $K = 2,5,10$ severely limit the achievable maximum fidelities.

We visualized the obtained rates and fidelities using a binary detector with efficiency $\eta = 1$ in Fig. 4. In this figure we use four exemplary PDC states with rising *effective* mode numbers $K = 1,2,5,10$, where $K = 1$ corresponds to the single-mode case discussed in Sec. III. Figure 4 shows that the mixing in frequency diminishes the maximal attainable fidelities over the

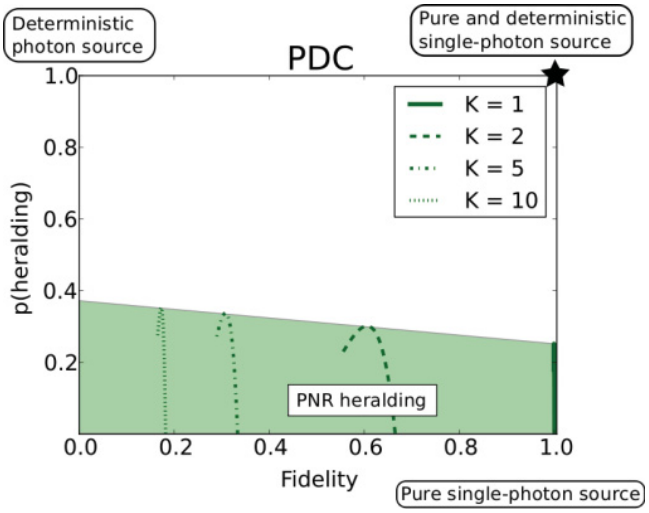

FIG. 5. (Color online) Heralding probabilities, $p(heralding)$, and single-photon Fock-state fidelities, *Fidelity*, of the state created using various multimode PDC sources in conjunction with a photon-number-resolving detector featuring unit detection efficiency $\eta = 1$. Again, multiple frequency modes $K = 2,5,10$ severely limit the achievable maximum fidelities.

whole range of heralding rates ($K = 2$, 5, and 10 plotted up to $B = 1.36$).

This mixing in frequency modes also negatively affects photon-number-resolved detection. Figure 5 depicts the heralding of single photons from a multimode PDC state using a photon-number-resolving detector with efficiency $\eta = 1$. Again the maximum achievable fidelities are constrained by the number of optical modes in the PDC.

In total multimode spectral effects ultimately limit the achievable heralded single-photon fidelities. This issue consequently must be addressed by generating the PDC state in a single spectral mode as discussed in Sec. III. Alternatively, filtering the idler beam can be applied to create single photons in a single spectral mode, yet at the expense of severe losses in photon number.

V. DETERMINISTIC PURE-SINGLE-PHOTON GENERATION WITH SWITCHED PDC SOURCES

Our previous calculations showed that it is impossible to build a pure deterministic single-photon source using a single PDC process. However, it has been noted that multiple PDC sources in a switched setup may be able to create a source approximating deterministic behavior [57–60]. This approach employs multiple PDC single-photon sources: When one signals the successful heralding of a single-photon state, the photon is routed to the output. Given a photon heralding probability of ν and lossless routing the overall heralding probability in a switched setup—as a function of the number of applied PDC sources n—is

$$p(\text{“switched”}) = 1 - (1 - \nu)^n. \tag{18}$$

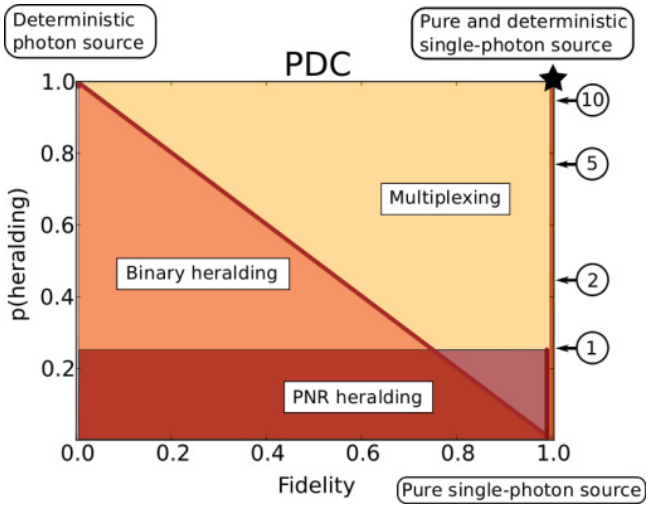

FIG. 6. (Color online) Heralding probabilities, $p(\textit{heralding})$, and fidelities, *Fidelity*, accessible using a single-mode PDC source in conjunction with a binary detector (orange-shaded region), a photon-number-resolving detector (red-shaded region), and multiplexing (yellow-shaded region). For an optimal source and a perfect photon-number-resolving detector with heralding probability of $\nu = 25\%$ 17 PDC sources are required to obtain a deterministic single-photon source (>99% emission probability). The arrows point out the achievable heralding rates using a multiplexed setup of 1, 2, 5, and 10 single photon sources.

Figure 6 presents the impacts of multiplexing on the rates and fidelities and summarizes our results. A single-mode PDC source in conjunction with binary detectors suffers from an inherent trade-off between high heralding rates and high fidelities (orange-shaded region). Photon-number-resolving detectors solve this issue and enable heralding efficiencies up to 25% and unit fidelities (red-shaded region). Multiplexing these single PDC setups enables access to sources featuring high heralding rates in conjunction with unit fidelities (yellow-shaded region). The achievable rates for the multiplexing of 1, 2, 5, and 10 PDC sources are displayed in Fig. 6.

The overhead in the number of PDC sources is, of course, quite significant. Hence, the most practicable route to create deterministic pure single-photon Fock states using PDC is first to move from binary to photon-number-resolved detection which enables unit fidelities and significant heralding rates for a single source. Multiplexing these setups gives access to the desired pure deterministic behavior. Given optimal PDC sources with perfect photon-number-resolved detection ($\nu = 25\%$) 17 PDC setups are required to approximate a deterministic pure single-photon source (>99%).

VI. CONCLUSION

In conclusion, we determined the prospects for PDC to serve as a *pure* deterministic single-photon source. We investigated the effects of the spectral *and* the photon-number degree of freedom on heralding pure single-photon states from PDC. Our findings show that the spectral degree of freedom limits the achievable fidelities of the heralded signal states and, hence, spectral effects have to be negated by engineering of the PDC process to occupy a single spectral mode.

For a PDC state free of multiple spectral modes the remaining limitations stem from the higher-order photon components and the applied detectors. Binary detectors feature an inherent trade-off between high heralding probability and near unit state fidelity, whereas photon-number-resolving detectors are able to herald *pure* single-photon Fock states with a probability of up to 25%, given unit detection efficiencies and an optimal PDC state with a twin-beam squeezing of 7.64 dB ($\langle n_{\text{ph}} \rangle = 1$). This forms the fundamental limit on heralding pure single-photon states using PDC. Applying a switched PDC setup to increase the heralding rate 17 individual sources are, hence, required to approximate a pure deterministic single-photon source (>99% emission probability).

ACKNOWLEDGMENTS

The research leading to these results has received funding from the European Community's Seventh Framework Programme FP7/2007-2013 under the grant agreement Q-Essence 248095. The authors thank Kaisa Laiho, Malte Avenhaus, Helge Rütz, and Benjamin Brecht for useful discussions and helpful comments.

[1] N. Gisin and R. Thew, Nat. Photon. **1**, 165 (2007).
[2] V. Giovannetti, S. Lloyd, and L. Maccone, Science **306**, 1330 (2004).
[3] I. A. Walmsley and M. G. Raymer, Science **307**, 1733 (2005).
[4] P. Michler, A. Kiraz, C. Becher, W. V. Schoenfeld, P. M. Petroff, L. Zhang, E. Hu, and A. Imamoglu, Science **290**, 2282 (2000).
[5] C. Santori, D. Fattal, J. Vuckovic, G. S. Solomon, and Y. Yamamoto, Nature **419**, 594 (2002).
[6] A. Kuhn, M. Hennrich, and G. Rempe, Phys. Rev. Lett. **89**, 067901 (2002).
[7] J. Beugnon, M. P. A. Jones, J. Dingjan, B. Darquié, G. Messin, A. Browaeys, and P. Grangier, Nature **440**, 779 (2006).
[8] P. Maunz, D. L. Moehring, S. Olmschenk, K. C. Younge, D. N. Matsukevich, and C. Monroe, Nat. Phys. **3**, 538 (2007).
[9] H. G. Barros, A. Stute, T. E. Northup, C. Russo, P. O. Schmidt, and R. Blatt, New J. Phys. **11**, 103004 (2009).
[10] J. Rarity, J. Fulconis, J. Duligall, W. Wadsworth, and P. Russell, Opt. Express **13**, 534 (2005).
[11] J. Chen, K. F. Lee, C. Liang, and P. Kumar, Opt. Lett. **31**, 2798 (2006).
[12] J. Fan and A. Migdall, Opt. Express **15**, 2915 (2007).
[13] J. Fulconis, O. Alibart, J. L. O'Brien, W. J. Wadsworth, and J. G. Rarity, Phys. Rev. Lett. **99**, 120501 (2007).
[14] B. J. Smith, P. Mahou, O. Cohen, J. S. Lundeen, and I. A. Walmsley, Opt. Express **17**, 23589 (2009).
[15] A. Ling, J. Chen, J. Fan, and A. Migdall, Opt. Express **17**, 21302 (2009).
[16] C. Söller, B. Brecht, P. J. Mosley, L. Y. Zang, A. Podlipensky, N. Y. Joly, P. S. J. Russell, and C. Silberhorn, Phys. Rev. A **81**, 031801 (2010).
[17] C. Söller, O. Cohen, B. J. Smith, I. A. Walmsley, and C. Silberhorn, Phys. Rev. A **83**, 031806 (2011).
[18] C. K. Hong, Z. Y. Ou, and L. Mandel, Phys. Rev. Lett. **59**, 2044 (1987).
[19] S. Castelletto, I. P. Degiovanni, V. Schettini, and A. Migdall, Metrologia **43**, S56 (2006).
[20] T. Pittman, B. Jacobs, and J. Franson, Opt. Commun. **246**, 545 (2005).
[21] A. B. U'Ren, C. Silberhorn, K. Banaszek, and I. A. Walmsley, Phys. Rev. Lett. **93**, 093601 (2004).
[22] A. I. Lvovsky, H. Hansen, T. Aichele, O. Benson, J. Mlynek, and S. Schiller, Phys. Rev. Lett. **87**, 050402 (2001).
[23] P. J. Mosley, J. S. Lundeen, B. J. Smith, P. Wasylczyk, A. B. U'Ren, C. Silberhorn, and I. A. Walmsley, Phys. Rev. Lett. **100**, 133601 (2008).
[24] A. Eckstein, A. Christ, P. J. Mosley, and C. Silberhorn, Phys. Rev. Lett. **106**, 013603 (2011).
[25] T. Gerrits, M. J. Stevens, B. Baek, B. Calkins, A. Lita, S. Glancy, E. Knill, S. W. Nam, R. P. Mirin, R. H. Hadfield, R. S. Bennink, W. P. Grice, S. Dorenbos, T. Zijlstra, T. Klapwijk, and V. Zwiller, Optics Express **19**, 24434 (2011).
[26] P. G. Evans, R. S. Bennink, W. P. Grice, T. S. Humble, and J. Schaake, Phys. Rev. Lett. **105**, 253601 (2010).
[27] H. S. Poh, J. Lim, I. Marcikic, A. Lamas-Linares, and C. Kurtsiefer, Phys. Rev. A **80**, 043815 (2009).
[28] P. Sekatski, N. Sangouard, F. Bussieres, C. Clausen, N. Gisin, and H. Zbinden, e-print arXiv:1109.0194 (2011).
[29] J. Huang and P. Kumar, Phys. Rev. A **40**, 1670 (1989).
[30] M. N. O'Sullivan, K. W. C. Chan, V. Lakshminarayanan, and R. W. Boyd, Phys. Rev. A **77**, 023804 (2008).
[31] P. P. Rohde, J. G. Webb, E. H. Huntington, and T. C. Ralph, New J. Phys. **9**, 233 (2007).
[32] P. P. Rohde, e-print arXiv:quant-ph/0703238 (2007).
[33] Y. P. Huang, J. B. Altepeter, and P. Kumar, Phys. Rev. A **84**, 033844 (2011).
[34] W. Wasilewski, C. Radzewicz, R. Frankowski, and K. Banaszek, Phys. Rev. A **78**, 033831 (2008).
[35] D. Achilles, C. Silberhorn, and I. A. Walmsley, Phys. Rev. Lett. **97**, 043602 (2006).
[36] W. Mauerer, M. Avenhaus, W. Helwig, and C. Silberhorn, Phys. Rev. A **80**, 053815 (2009).
[37] M. A. Broome, M. P. Almeida, A. Fedrizzi, and A. G. White, Optics Express **19**, 22698 (2011).
[38] S. Virally, S. Lacroix, and N. Godbout, Phys. Rev. A **81**, 013808 (2010).
[39] M. J. Fitch, B. C. Jacobs, T. B. Pittman, and J. D. Franson, Phys. Rev. A **68**, 043814 (2003).
[40] A. Divochiy, F. Marsili, D. Bitauld, A. Gaggero, R. Leoni, F. Mattioli, A. Korneev, V. Seleznev, N. Kaurova, O. Minaeva, G. Gol'tsman, K. G. Lagoudakis, M. Benkhaoul, F. Levy, and A. Fiore, Nat. Photon. **2**, 302 (2008).
[41] B. E. Kardynal, Z. L. Yuan, and A. J. Shields, Nat. Photon. **2**, 425 (2008).
[42] M. Mičuda, O. Haderka, and M. Ježek, Phys. Rev. A **78**, 025804 (2008).
[43] M. Fujiwara and M. Sasaki, Appl. Phys. Lett. **86**, 111119 (2005).
[44] A. Christ, K. Laiho, A. Eckstein, K. N. Cassemiro, and C. Silberhorn, New J. Phys. **13**, 033027 (2011).
[45] A. Christ, K. Laiho, A. Eckstein, T. Lauckner, P. J. Mosley, and C. Silberhorn, Phys. Rev. A **80**, 033829 (2009).
[46] In the high-gain regime time-ordering effects have to be considered in the derivation of Eq. (1) [61].
[47] J. Smirr, M. Deconinck, R. Frey, I. Agha, E. Diamanti, and I. Zaquine, e-print arXiv:1108.5884 (2011).
[48] A. M. Brańczyk, T. C. Ralph, W. Helwig, and C. Silberhorn, New J. Phys. **12**, 063001 (2010).
[49] W. P. Grice and I. A. Walmsley, Phys. Rev. A **56**, 1627 (1997).
[50] S. M. Barnett and P. M. Radmore, *Methods in Theoretical Quantum Optics* (Oxford University Press, Oxford, 2003).
[51] P. P. Rohde, W. Mauerer, and C. Silberhorn, New J. Phys. **9**, 91 (2007).
[52] C. Silberhorn, Contemp. Phys. **48**, 143 (2007).
[53] P. Kok, W. J. Munro, K. Nemoto, T. C. Ralph, J. P. Dowling, and G. J. Milburn, Rev. Mod. Phys. **79**, 135 (2007).
[54] R. Jozsa, J. Mod. Opt. **41**, 2315 (1994).
[55] A. B. U'Ren, K. Banaszek, and I. A. Walmsley, Quantum Inf. Comput. **3**, 480 (2003).
[56] J. H. Eberly, Laser Phys. **16**, 921 (2006).
[57] A. L. Migdall, D. Branning, and S. Castelletto, Phys. Rev. A **66**, 053805 (2002).
[58] T. B. Pittman, B. C. Jacobs, and J. D. Franson, Phys. Rev. A **66**, 042303 (2002).
[59] X.-s. Ma, S. Zotter, J. Kofler, T. Jennewein, and A. Zeilinger, Phys. Rev. A **83**, 043814 (2011).
[60] T. Jennewein, M. Barbieri, and A. G. White, J. Mod. Opt. **58**, 276 (2011).
[61] W. Wasilewski, A. I. Lvovsky, K. Banaszek, and C. Radzewicz, Phys. Rev. A **73**, 063819 (2006).

Dass ich erkenne, was die Welt
Im Innersten zusammenhält.

(Faust I, Vers 382 f)

8. PDC source engineering

8.1. Introduction

As we have discussed in Chap. 7, any multi-mode PDC character poses a severe hindrance for the heralding of pure single-photon states from PDC. Furthermore most PDC states are not suitable for quantum communication applications due to the fact that the multitude of generated EPR-states from a PDC source share only marginal squeezing amplitudes (see Chap. 10). It is hence vital to develop PDC sources which emit, depending on the intended application, all their photons into a single or very few optical modes. For this purpose a multitude of approaches have been investigated under the label of *source engineering*.[1,2]

In waveguided PDC, however, all current approaches rely on favorable dispersion properties, only present in a few nonlinear crystal materials. Especially the widely deployed lithium niobate crystals do not allow for a single-mode emission

In this chapter put forward an alternative approach and explore a promising method to create single-mode PDC-states at arbitrary signal and idler wavelengths almost independent of the applied nonlinear material by generating the signal and idler beams into opposite directions. Our investigations reveal that these down-converted PDC states carry minimal spectral correlations and further feature the additional advantage of an inherent separation of the signal and idler beams.

8.2. Source engineering

As discussed in Sec. 4.4 we require a PDC process with a phase-matching function featuring a positive slope, or being aligned along one axis, in frequency space. Using an appropriately shaped pump beam this enables us to create a decorrelated frequency spectrum $f(\omega_s, \omega_i)$ which, in turn, leads to single-mode emission. The exact slope of the phase-matching function is given by the formula [52]

$$\theta = -\arctan\left[\frac{\nu_\mathrm{s} - \nu_\mathrm{p}}{\nu_\mathrm{i} - \nu_\mathrm{p}}\frac{\nu_\mathrm{i}}{\nu_\mathrm{s}}\right], \tag{8.1}$$

[1] While the term *source engineering* could in principle refer to any engineering of the down-conversion process it has been established as a label for the design of PDC sources emitting a single optical mode.

[2] This chapter is a summary of the paper "Pure single photon generation by type-I PDC with backward-wave amplification" by Andreas Christ, Andreas Eckstein, Peter J. Mosley, and Christine Silberhorn [5].

where ν labels the group velocity of the individual beams. From Eq. (8.1) it is evident that we require a PDC process where the group velocities of the signal ν_s *or* the idler ν_i pulse are as fast or slower than the pump pulse ν_p. This leads to a phase-matching function which has a positive slope, or is aligned along one axis in frequency space.

Achieving this, however, is not an easy feat. In all standard nonlinear optical materials the dispersion is monotonically decreasing with wavelength. In consequence beams at higher wavelengths travel faster through the material than waves at lower wavelengths. Since the signal and idler waves are approximately at double the wavelengths of the pump it seems impossible to achieve group velocity matching. Fortunately a lot of nonlinear optical materials are birefringent, which enables us to slow down the group velocity of the signal or idler wave by emitting the field in a polarization orthogonal to the pump. Still the range of the available materials is restricted. As of now only KTP has been shown to emit *waveguided* PDC states with single-mode characteristics [37, 52, 24, 36, 100]. Alternatively Bragg waveguides can be applied to modify the effective dispersion properties for the involved optical beams [120]. A review of group velocity matching is given in [52].

8.3. Source engineering via counterpropagating PDC

From the discussion in Sec. 8.2 one would naively suggest, that the constraint that either the signal or idler wave has to travel through the crystal beyond the pump wave, can alternatively be fulfilled by generating the signal and idler beams in opposite directions. While this suggestion seems, at first glance, ridiculous, it in fact gives, as we will show, the desired result.

The idea to generate signal and idler photons in opposite directions is almost as old as the first theoretical description of PDC and was first proposed in 1966 by S. E. Harris in the framework of three-wave-mixing processes [121]. For the generation of counterpropagating photon pairs in PDC this approach was revisited by Booth et. al. in 2002 [122].

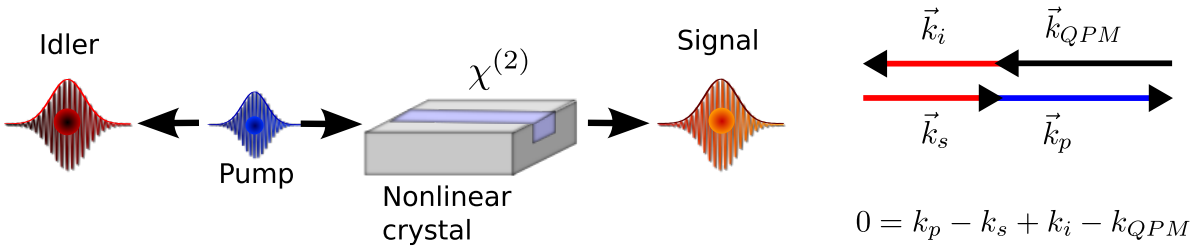

Figure 8.1.: Counterpropagating waveguided PDC. Signal and idler are leaving the crystal at opposite ends.

The general counterpropagating PDC process is sketched in Fig. 8.1. In this scenario the signal and idler photons are leaving the waveguide at opposite ends. This has a drastic effect on the phase-matching conditions. In the standard configuration, discussed

in Chap. 4 the momentum of the pump pulse has to be compensated by the momentum of the signal and idler photons, with a small additional quasi-phase-matching vector. In the counterpropagating scenario, however, the situation is different. As depicted in Fig. 8.1 the idler photon is propagating backwards, which means that now the signal and idler momenta almost cancel each other and the pump momentum has to be accounted for by the quasi-phase-matching. This requires grating periods in the sub-micron regime about 0.2 -0.6 μm. While technologically challenging these have already been demonstrated in planar semiconductor waveguides [123, 124] and KTP crystals [125].

Mathematically we have to alter the phase-mismatch Δk from Sec. 4.3 to take into account the backward propagation of the idler photon. We obtain

$$\Delta k = k_p - k_s + k_i - 2\pi/\Lambda, \tag{8.2}$$

where we included a plus instead of a minus sign in front of k_i to model the backward propagating of the idler photon. This minus sign affects the angle θ of the phase-matching function in frequency space:

$$\theta = -\arctan\left[\frac{\nu_\mathrm{s} - \nu_\mathrm{p}}{\nu_\mathrm{i} + \nu_\mathrm{p}} \frac{\nu_\mathrm{i}}{\nu_\mathrm{s}}\right] \tag{8.3}$$

Considering the relative group velocities of the signal, idler and pump beams the terms in the numerator will almost cancel each other, while the denominator will have a significant value. We hence obtain a horizontal phase-matching function ($\theta \approx 0$).

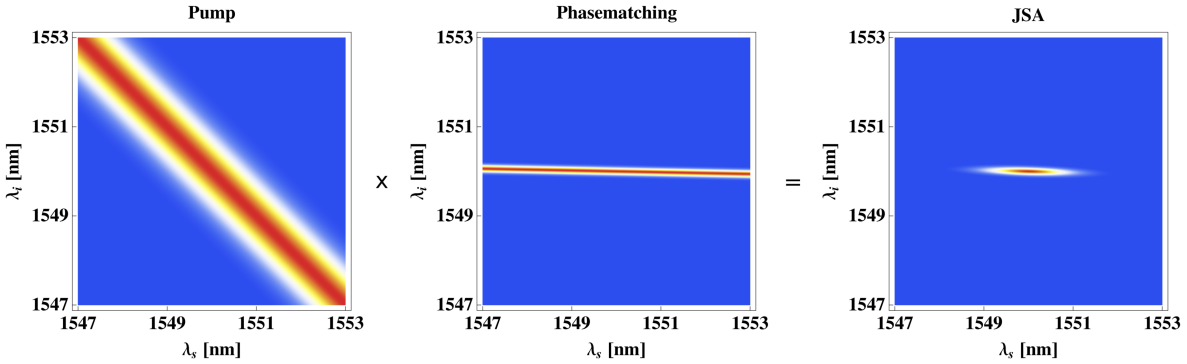

Figure 8.2.: Pump envelope, Phasematching function and JSA plotted in the Gaussian approximation; Parameters: LN, type-I PDC, e-polarized rays, pump central wavelength $\lambda_p = 775\,\mathrm{nm}$, FWHM of the pump intensity distribution $\Delta\lambda_p = 0.58\,\mathrm{nm}$, waveguide dimensions: $4\,\mu$m x $4\,\mu$m x 5 mm, grating period $\Lambda = 0.35\,\mu$m.

Fig. 8.2 illustrates the pump distribution and phase-matching function of a counterpropagating PDC process in periodically poled LN. The narrow horizontal phase-matching function together with the broad pump beam yields a decorrelated JSA distribution oriented along the signal axis. The generated photon pairs are decorrelated and consequently the source emits PDC states in a single optical mode.

We further note that this decorrelation process is independent from the material and its dispersion properties since the angle of the phase-matching is no longer determined by the material properties but, in the first place, by the counterpropagating nature of the signal and idler beams.

8.4. Numerical analysis

We quantify the single-mode character of counterpropagating signal and idler photons by numerically investigating periodically poled KTP and periodically poled LN (PPLN) in a waveguided PDC setup.

In PPLN we chose the type-I down-conversion process with the highest nonlinearity, where extraordinary-polarized pump photons decay into extraordinary-polarized signal and idler photons ($\chi^{(2)}_{eee} = 63\,\mathrm{pm/V}$). In KTP we analyzed strictly z-polarized signal, idler and pump waves making use of the largest tensor element $\chi^{(2)}_{zzz} = 27.4\,\mathrm{pm/V}$ [47].

We investigated two different scenarios, depicted in Fig. 8.3. In Fig. 8.3 (a) we tune the signal and idler wavelengths from 800 nm to 1600 nm, with corresponding pump wavelength $\lambda_p = \lambda_{s,i}/2$ and grating period $\Lambda = 2\pi/(k_p - k_s + k_i)$ about $\Lambda \approx 0.5\,\mu$m. For each parameter set we adjust the pump width $\Delta\lambda_p$ in the range $\Delta\lambda_p = 0.02 - 0.35\,$nm to give a maximal decorrelation. The figure gives the probability of the photon-pairs to be emitted in the first-optical mode.

Similarly we quantified the amount of decorrelation in Fig. 8.3 (b), yet here we fixed the idler wavelength at 1550 nm and only adjusted the signal wavelength optimizing the pump width from $\Delta\lambda_p = 0.02 - 0.35\,$nm.

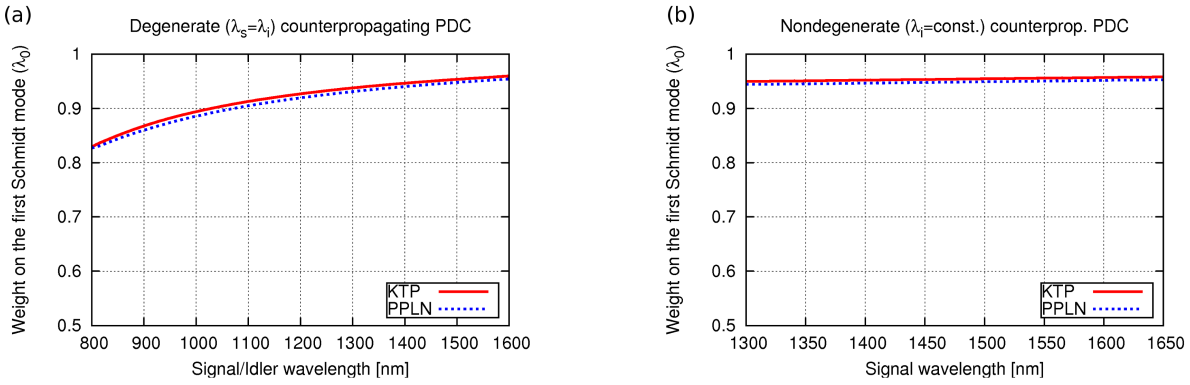

Figure 8.3.: (a) In counterpropagating PDC it is possible to generate separable degenerate signal and idler photons in the range from 800 to 1600 nm. (b) The separability is maintained for nondegenerate PDC ($\lambda_i = 1550\,$nm).

Our results show that this approach achieves a high degree of separability in a broad frequency range, almost independent of the applied material and dispersion relations.

8.5. Conclusion

In conclusion we presented a new method to create single-mode PDC sources based on emitting the signal and idler photon pairs in opposite directions. This enables us to use almost every nonlinear material, independent of its dispersion relation, in a broad frequency range for single-mode PDC, as long as the required grating periods can be produced.

Pure single photon generation by type-I PDC with backward-wave amplification

A. Christ, A. Eckstein, P. J. Mosley and C. Silberhorn

Max-Planck Institute for the Science of Light
Günther Scharowsky-Str.1 / Bau 24, 91054 Erlangen, Germany
Andreas.Christ@mpl.mpg.de

Abstract: We explore a promising method of generating pure heralded single photons. Our approach is based on parametric downconversion in a periodically-poled waveguide. However, unlike conventional downconversion sources, the photon pairs are counter-propagating: one travels with the pump beam in the forward direction while the other is backpropagating towards the laser source. Our calculations reveal that these downconverted two-photon states carry minimal spectral correlations within each photon-pair. This approach offers the possibility to employ a new range of downconversion processes and materials like PPLN (previously considered unsuitable due to its unfavorable phasematching properties) to produce heralded pure single photons over a broad frequency range.

OCIS codes: (190.4410) Nonlinear optics, parametric processes.

References and links

1. S. L. Braunstein and P. van Loock, "Quantum information with continuous variables," Rev. Mod. Phys. **77**, 513–577 (2005).
2. T. C. Ralph, A. G. White, W. J. Munro, and G. J. Milburn, "Simple scheme for efficient linear optics quantum gates," Phys. Rev. A **65**, 012314–012320 (2001).
3. P. J. Mosley, J. S. Lundeen, B. J. Smith, P. Wasylczyk, A. B. U'Ren, C. Silberhorn, and I. A. Walmsley, "Heralded Generation of Ultrafast Single Photons in Pure Quantum States," Phys. Rev. Lett. **100**, 133601–133605 (2008).
4. M. Fiorentino, S. M. Spillane, R. G. Beausoleil, T. D. Roberts, P. Battle, and M. W. Munro, "Spontaneous parametric down-conversion in periodically poled KTP waveguides and bulk crystals," Opt. Express **15**, 7479–7488 (2007).
5. G. Di Giuseppe, M. Atatüre, M. D. Shaw, A. V. Sergienko, B. E. A. Saleh, and M. C. Teich, "Entangled-photon generation from parametric down-conversion in media with inhomogeneous nonlinearity," Phys. Rev. A **66**, 013801–013818 (2002).
6. D. S. Hum and M. M. Fejer, "Quasi-phasematching," Comptes Rendus Physique **8**, 180–198 (2007).
7. W. P. Grice and I. A. Walmsley, "Spectral information and distinguishability in type-II down-conversion with a broadband pump," Phys. Rev. A **56**, 1627–1634 (1997).
8. A. B. U'Ren, C. Silberhorn, R. Erdmann, K. Banaszek, W. P. Grice, I. A. Walmsley, and M. G. Raymer, "Generation of Pure-State Single-Photon Wavepackets by Conditional Preparation Based on Spontaneous Parametric Downconversion," Laser Phys. Lett. **15**, 146–160 (2005).
9. C. K. Law, I. A. Walmsley, and J. H. Eberly, "Continuous Frequency Entanglement: Effective Finite Hilbert Space and Entropy Control," Phys. Rev. Lett. **84**, 5304–5307 (2000).
10. S. E. Harris, "Proposed backward wave oscillation in the infrared," Appl. Phys. Lett. **9**, 114–116 (1966).
11. M. C. Booth, M. Atature, G. Di Giuseppe, A. V. Sergienko, B. E. A. Saleh, and M. C. Teich, "Counter-propagating entangled photons from a waveguide with periodic nonlinearity," Phys. Rev. A **66**, 023815–02323 (2002).
12. L. Lanco, S. Ducci, J.-P. Likforman, X. Marcadet, J. A. W. van Houwelingen, H. Zbinden, G. Leo, and V. Berger, "Semiconductor Waveguide Source of Counterpropagating Twin Photons," Phys. Rev. Lett. **97**, 173901–173905 (2006).
13. M. Ravaro, Y. Seurin, S. Ducci, G. Leo, V. Berger, A. de Rossi, and G. Assanto, "Nonlinear AlGaAs waveguide for the generation of counterpropagating twin photons in the telecom range," J. Appl. Phys. **98**, 063103–063109 (2005).

14. J. P. Jr., "Quantum properties of counterpropagating two-photon states generated in a planar waveguide," Phys. Rev. A **77**, 013803–013817 (2008).
15. C. Canalias and V. Pasiskevicius, "Mirrorless optical parametric oscillator," Nat Photon **1**, 459–462 (2007).
16. M. Minakata, M. Islam, S. Nagano, S. Yoneyama, T. Sugiyama, and H. Awano, "Nanometer size periodic domain inversion in LiNbO3 substrate using circular form full cover electrodes," Solid-State Electron. **50**, 848–852 (2006).
17. A. N. Vamivakas, B. E. A. Saleh, A. V. Sergienko, and M. C. Teich, "Theory of spontaneous parametric downconversion from photonic crystals," Phys. Rev. A **70**, 043810-043817 (2004).
18. D. Marcuse, "Theory of dielectric optical waveguides", 49–59 (1974).
19. A. Christ, A. Eckstein, K. Laiho, T. Lauckner, P. J. Mosley, C. Silberhorn, "Spatial to spectral mode mapping in waveguided PDC," to be published, (2009).

1. Introduction

Linear optical quantum computing (LOQC) schemes, such as continuous variable entanglement distillation [1] or single photon quantum gates [2] require sources of pure heralded single photons. Such single photon sources may be realized via photon pair generation by parametric downconversion (PDC). The photon number correlation between the resulting fields, typically labelled signal and idler, can be exploited to herald the existence of one photon by detection of its partner. However the purity of the heralded photon is limited by spatial and spectral correlations within each photon pair arising from energy and momentum conservation between pump, signal and idler photons. One possibility of generating pure heralded single photons without spectral filtering and a reduction in the source brightness is group velocity matching [3]. However this approach to generate separable photon pairs is limited to a few materials and wavelength ranges.

Most PDC experiments to date have been performed in bulk crystals, yet lately a lot of attention has been focused on PDC in waveguides. The main advantage of PDC in rectangular waveguides is the strict collinear propagation of the pump, signal and idler fields, in contrast to angular dispersion in bulk crystal setups. Along with the high modal confinement inside the waveguide this leads to a large increase in collection efficiency [4] and the elimination of spatial correlations. Furthermore, due to the strict collinear propagation of pump, signal and idler beams these sources are much more convenient to handle in the laboratory.

The spectral properties of PDC states are governed by the phasematching properties of the nonlinear material and this determines the frequencies of the downconverted photons. In a bulk nonlinear crystal one can exploit noncollinear PDC to achieve perfect phasematching, but this approach cannot be used in a waveguide structure as the direction of propagation is fixed. Instead, one must adopt quasi-phasematching (QPM) [5, 6]: A spatial periodic variation of the $\chi^{(2)}_{ijk}$-nonlinearity in the crystal introduces a new so called quasiphasematching vector ($k_{QPM} = 2\pi/\Lambda$), for a sinusoidal poling with period Λ. In that way it is in principle possible to choose the signal and idler wavelengths freely, under the restriction of energy conservation.

The generation of backward-wave oscillations in three-wave-mixing processes was proposed in 1966 [10]. For the generation of correlated photon pairs in waveguided PDC this approach was revisited in 2002 by Booth et. al. [11]. In this configuration almost all the momentum of the pump photon has to be compensated by the QPM poling structure within the crystal. This requires grating periods in the sub-micron range (0.2 -0.6 μm) for signal and idler photons generated in the range from 800 to 1600 nm.

Quasiphasematched PDC processes with counterpropagating signal and idler photons and a perpendicularly propagating pump in planar semiconductor waveguides have already been observed [12, 13], and their respective quantum properties have been studied [14]. However, to date, the high absorption in semiconductor materials and tiny interaction volume limit the achievable photon flux. In dielectric materials a breakthrough has been made towards sub-

micron poling periods in the past year: Backward-wave oscillation in potassium titanyl phosphate (KTP) has been reported [15], and simultaneously in lithium niobate (LN) new submicron poling techniques have been explored [16]. Therefore the required crystals are within reach.

In this paper, we consider a collinear waveguided PDC setup with counterpropagating signal and idler fields. We show that this configuration allows the generation of pure heralded single photons in a large range of nonlinear materials and wavelengths.

2. The PDC state

The frequency structure of a downconverted *copropagating* two-photon state is found to be [7]:

$$|\psi_{s,i}\rangle \approx |0\rangle + A\int\int \mathrm{d}\omega_s \mathrm{d}\omega_i \underbrace{\exp\left[-\frac{(\omega_s+\omega_i-\omega_p)^2}{2\sigma^2}\right]}_{\alpha(\omega_s+\omega_i)} \underbrace{\mathrm{sinc}\left(\frac{\mathrm{L}}{2}\Delta\mathrm{k}\right)\exp\left[-\imath\frac{\mathrm{L}}{2}\Delta\mathrm{k}\right]}_{\phi(\omega_s,\omega_i)} \hat{\mathrm{a}}_s^\dagger(\omega_s)\hat{\mathrm{a}}_i^\dagger(\omega_i)\,|0\rangle \tag{1}$$

The pump distribution $\alpha(\omega_s+\omega_i)$ is given by the incoming laser. In our case we assume a mode-locked pulsed laser system with a Gaussian frequency distribution, centered around ω_p with width σ. The phasematching function $\phi(\omega_s,\omega_i)$ is governed by the waveguide dimensions and crystal dispersion, ensuring momentum conservation ($\Delta k = k_p - k_s - k_i - k_{QPM}$). Because of the strict collinear propagation inside the waveguide the transverse wavevector mismatch does not enter Eq. (1). The product of these two functions gives the joint spectral amplitude (JSA): $f(\omega_s,\omega_i) = \alpha(\omega_s+\omega_i)\cdot\phi(\omega_s,\omega_i)$. For analytic calculations the two-photon state is often simplified with the Gaussian approximation ($\mathrm{sinc}(\mathrm{x}) \approx \exp(-\gamma \mathrm{x}^2)$ where $\gamma \approx 0.193$).

Heralding one photon of this PDC-state will in general lead to a mixed heralded single photon state, due to correlations in the JSA ($f(\omega_s,\omega_i)$) [8]. Pure heralded single photons are created if and only if the downconverted two-photon state can be written as a product state $|\psi_{s,i}\rangle = |\psi_s\rangle \otimes |\psi_i\rangle$. This requires a separable JSA: $f(\omega_s,\omega_i) = f(\omega_s)f(\omega_i)$. In order to quantify the separability of the generated PDC states one has to perform a Schmidt decomposition [9], i.e. a basis transformation into a set of orthonormal Schmidt modes, $|\psi_s^n(\omega_s)\rangle$ and $|\psi_i^n(\omega_i)\rangle$:

$$|\psi_{s,i}(\omega_s,\omega_i)\rangle = \sum_n \sqrt{\lambda_n}\,|\psi_s^n(\omega_s)\rangle \otimes |\psi_i^n(\omega_i)\rangle \tag{2}$$

The probability to emit a photon pair into one specific pair of Schmidt modes $|\psi_s^n(\omega_s)\rangle \otimes |\psi_i^n(\omega_i)\rangle$ is given by λ_n, which is monotonically decreasing for successive higher order modes. Thus a perfectly separable state corresponds to a state where the full weight of the probability distribution accumulates on the first pair of Schmidt modes ($\lambda_0 = 1$).

3. Backward-wave oscillations

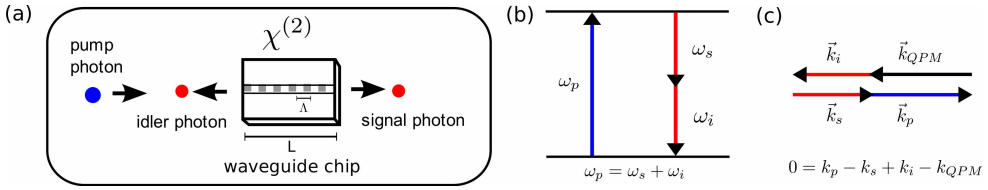

Fig. 1. Waveguided parametric downconversion with one backward-wave oscillation: (a) Process scheme, (b) Energy conservation, (c) Momentum conservation.

Figure 1 illustrates the generation of *counterpropagating* photon pairs and the corresponding energy and momentum conservation conditions. To account for the backward propagating wave in our formalism (Eq.(1)), we have to alter the momentum conservation condition:

$$\Delta k = k_p - k_s + k_i - 2\pi/\Lambda. \tag{3}$$

This has a significant effect on the properties of the generated two-photon-states. The biggest advantage over copropagating PDC are the different requirements to generate separable two-photon states. With the Gaussian approximation and expansion of the wave vector mismatch Δk as a Taylor series up to the first order, we are able to analytically derive a condition for separability from Eq. (1) and (3) (analogous to [8]):

$$0 = \frac{2}{\sigma^2} + \left(k'_p - k'_s\right)\left(k'_p + k'_i\right) = \frac{2}{\sigma^2} + \left(\frac{1}{v_p} - \frac{1}{v_s}\right)\left(\frac{1}{v_p} + \frac{1}{v_i}\right). \tag{4}$$

Therefore a waveguide in which the pump pulses propagate faster than the downconverted forward propagating signal pulses ($v_s < v_p$) will generate separable photon pairs. Note that this requirement is much easier to satisfy than that for the usual copropagating case, where the group velocities must satisfy either $v_s < v_p < v_i$ or $v_i < v_p < v_s$ [8].

Further insight is obtained by deriving the angle of the phasematching function in the $\{\omega_s, \omega_i\}$-plane:

$$\theta = -\arctan\left[\frac{\mathrm{k'_p} - \mathrm{k'_s}}{\mathrm{k'_p} + \mathrm{k'_i}}\right] = -\arctan\left[\frac{v_\mathrm{s} - v_\mathrm{p}}{v_\mathrm{i} + v_\mathrm{p}}\frac{v_\mathrm{i}}{v_\mathrm{s}}\right] \tag{5}$$

Here θ is defined as the angle between the phasematching function and the signal axis. As can be deduced from Eq. (4) and (5), the condition for factorability requires a phasematching angle between $0^\circ < \theta < 90^\circ$. Considering the relative magnitude of the numerator and denominator in Eq. (5), identical group velocities for the signal, idler and pump waves will result in a horizontally orientated phasematching function and a factorable JSA. This is in very good agreement with the small group velocity dispersion in common nonlinear materials over the relevant wavelength region $v_s(\omega_s) \approx v_i(\omega_i) \approx v_p(\omega_s + \omega_i)$. These requirements are opposed to copropagating decorrelation proposals which rely on different group velocities for the signal, idler and pump waves. In the counterpropagating case very similar group velocities are demanded, a requirement that is much more robust and easier to fulfill.

The highly nonlinear crystal LN, commonly used in PDC experiments to generate photon pairs is unable to produce factorable copropagating photon pairs, but can be used to generate separable pairs in the backward-propagating regime. Figure 2 illustrates this particular example of a separable counterpropagating two-photon state. It demonstrates several benefits of the backward-wave approach simulated using periodically poled LN (PPLN) as the nonlinear medium. The momentum mismatch changes to a much stricter condition in comparison with copropagating PDC. This leads to an extremely narrow spectral width of the backpropagating photons, almost one order of magnitude smaller than the spectral distribution of the forward propagating photon. In this case, the FWHM of the wavelength distribution is 0.09 nm for the backpropagating photon and 0.73 nm for the forward propagating photon. The narrow frequency bandwidth of the backpropagating photon makes it very well suited for long distance transmission in optical fibers.

It has to be noted that according to [17], the total photon pair production rate will decrease with respect to sources that create strictly forward propagating photons, but the effective generation rate can still exceed bulk crystal setups due to the high nonlinearity and higher collection efficiencies in a waveguide architecture.

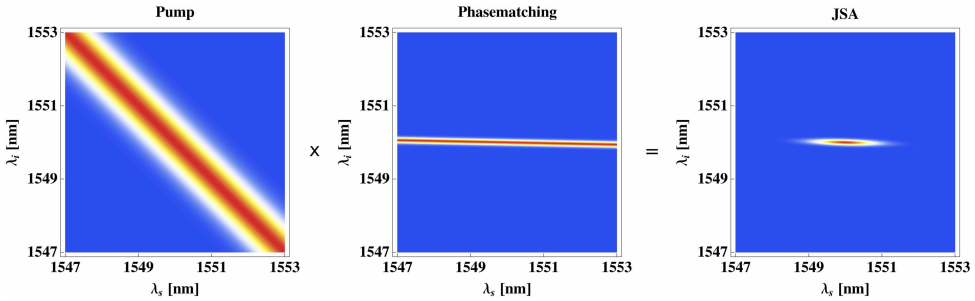

Fig. 2. Pump envelope, Phasematching function and JSA plotted in the Gaussian approximation without phase; Parameters: LN, type-I PDC, e-polarized rays, pump central wavelength λ_p = 775 nm, FWHM of the pump intensity distribution $\Delta\lambda_p = 0.58$ nm, waveguide dimensions: 4 μm x 4 μm x 5 mm, grating period $\Lambda = 0.35$ μm.

In more general terms we would like to emphasise that the separability of a downconverted photon pair is almost independent of the signal and idler frequencies (Fig. 3(a)). With appropriate grating periods it is possible to generate separable degenerate signal and idler photons from 800 nm (where detectors are most efficient) to 1550 nm (the wavelength with minimal loss in optical fibers). This can be used to create a *tuneable* pure heralded single photon source. As depicted in Fig. 3(b), for a fixed grating period different pump wavelengths lead to a change in the downconverted signal wavelength, whereas the separability and the idler frequency remain constant. Hence the wavelength of the signal photon can be tuned by changing the pump wavelength, without impact on the idler frequency and with very little change in the separability.

4. Numerical analysis

To quantify the stated benefits, we numerically investigated periodically poled LN (PPLN) and periodically poled KTP (PPKTP) as sources of separable counterpropagating photon pairs. In PPLN we chose the type-I downconversion process with the highest nonlinearity, where extraordinary-polarized pump photons decay into extraordinary-polarized signal and idler photons ($\chi^{(2)}_{eee} = 63$ pm/V). In KTP we analyzed strictly z-polarized signal, idler and pump waves making use of the largest tensor element $\chi^{(2)}_{zzz} = 27.4$ pm/V.

The rectangular waveguide embedded in the crystal material was modelled with standard dimensions of 4 μm x 4 μm x 5 mm and a realistic refractive index step between waveguide and surrounding material of 0.01 . To simulate the propagation of our signal, idler and pump waves inside the waveguide we calculated the spatial modes of signal, idler and pump fields according to [18, 19]. The resulting decomposition of the wavevector into its longitudinal and transverse components enabled us to correct the bulk crystal Sellmeier equations and to obtain a modified JSA. In the scope of this paper we assume that the signal, idler and pump fields propagate in the fundamental waveguide mode.

We investigated the possibility of generating decorrelated and degenerate photon pairs in the range of 800 nm to 1600 nm. For each studied signal and idler degeneracy wavelength the pump wavelength was chosen appropriately ($\lambda_p = \lambda_{s,i}/2$), and the grating was matched to give phasematching at the degeneracy point ($\Lambda = 2\pi/(k_p - k_i - k_s)$). For each parameter set ($\lambda_s = \lambda_i = 2\lambda_p$, $\Lambda(\lambda_s, \lambda_i)$) we optimized the pump width $\Delta\lambda_p$ in the range from $\Delta\lambda_p = 0.02 - 0.35$ nm to yield a state with maximum separability. The optimum value of $\Delta\lambda_p$ was determined by performing a Schmidt decomposition according to Eq. (2) for every set of parameters.

The results are depicted in Fig. 3(a): The overall probability of the generated photon pairs

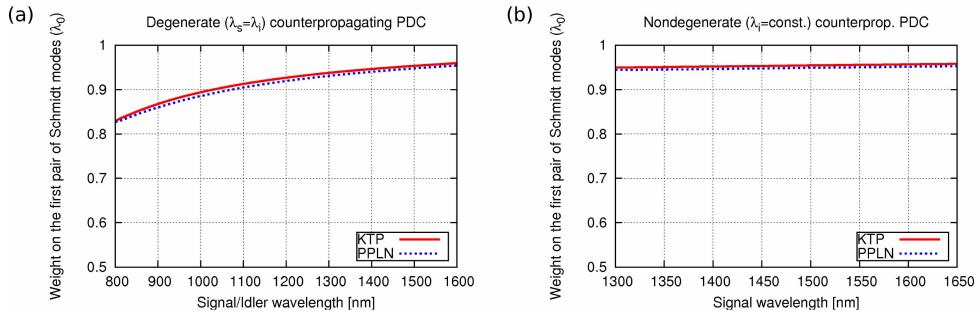

Fig. 3. (a) In counterpropagating PDC it is possible to generate separable degenerate signal and idler photons in the range from 800 to 1600 nm. (b) The separability is maintained for nondegenerate PDC ($\lambda_i = 1550$ nm).

to be emitted in the first pair of Schmidt modes (λ_0) is very high and only differs slightly for KTP and PPLN. The general improvement in separability for higher wavelengths is due to the fact that in this region the group velocities of the signal, idler and pump waves almost perfectly equal each other.

In a similar manner we checked the feasibility of this setup as a frequency-tuneable pure heralded single photon source using nondegenerate PDC (Fig. 3(b)). For a constant grating period Λ yielding phasematching at 1550 nm for signal and idler, we investigated the impacts of tuning the pump central frequency. Due to the horizontal orientation of the phasematching function the frequency distribution of the idler photons remains unchanged. However the frequency of the forward propagating signal photon shifts with the pump frequency. Again the pump width was chosen to yield a maximally separable two-photon states, now in the range from $\Delta\lambda_p = 0.22 - 0.34$ nm. Once more our results are almost independent of the chosen nonlinear crystal and the constant high level of separability shows that with this setup it will indeed be possible to create a tuneable pure heralded single photon source.

5. Conclusion

We have examined the spectral properties of downconverted counterpropagating two-photon states in rectangular waveguides. The major differences in comparison with copropagating downconverted photon-pairs allow us to exploit a wide range of processes and materials for heralded single photon generation. This technique provides separable two-photon states for a wide range of degenerate and non-degenerate signal and idler wavelengths which will be useful for practical purposes such as LOQC. Due to the progress in the production of microstructured waveguides an experimental implementation of our proposal will be feasible in the near future.

The authors would like to thank Wolfgang Mauerer for his support on the numerical analysis.

It would be so nice if something made sense for a change.

(Alice in Wonderland)

9. Probing PDC states using correlation functions

9.1. Introduction

For the deployment of parametric down-conversion sources in the laboratory it is vital to assess the quality of the generated quantum states. However, as we have seen in Sec. 4.4 the generated EPR states exhibit, in general, multi-mode characteristics. This inherent multi-mode character renders these states powerful for coding quantum information (see Chap. 10), yet the same feature impedes a proper experimental characterization. Due to the sheer vastness of the corresponding Hilbert space, standard quantum tomography methods become time-consuming and ineffective. It is neither easy to determine the degree of squeezing in each mode, nor the amount of generated twin-beam squeezers. Nonetheless, these are the key benchmarks defining the potential of a source for quantum information applications (see Sec. 6.2.1). In this chapter we present a new method to characterize ultrafast multi-mode PDC states based on broadband time-integrated correlation function measurements.[1]

9.2. Correlation functions

The n-th order (normalized) correlation function $g^{(n)}(t_1, t_1, \ldots, t_n)$ is generally defined as a time-dependent function of the electromagnetic field. It can be expressed as [126, 46, 72, 127]

$$g^{(n)}(t_1, t_2, \ldots, t_n) = \frac{\left\langle \hat{a}^\dagger(t_1) \ldots \hat{a}^\dagger(t_n)\hat{a}(t_1) \ldots \hat{a}(t_n) \right\rangle}{\langle \hat{a}^\dagger(t_1)\hat{a}(t_1)\rangle \ldots \langle \hat{a}^\dagger(t_n)\hat{a}(t_n)\rangle}, \tag{9.1}$$

and measures the (normalized) n-th order temporal correlations at different points in time independent of coupling losses and detection efficiencies [128].

The main problem with time-resolved correlation function measurements are the applied detectors which do not offer a perfect time-resolution. This impedes the measurement of time-resolved correlation functions and limits its experimental applications. We, however, exploit this exact drawback of standard correlation function measurements and

[1] This chapter is a summary of the paper "Probing multimode squeezing with correlation functions" by Andreas Christ, Kaisa Laiho, Andreas Eckstein, Katiúscia N. Cassemiro, and Christine Silberhorn [6].

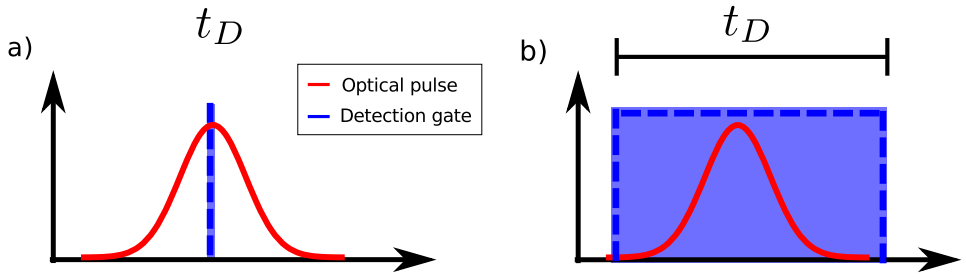

Figure 9.1.: a) perfect time-resolved detection; b) broadband time-integrated detection gate exceeding the pulse duration.

define broadband time-integrated correlation functions using photo-detectors exhibiting flat detection windows, exceeding the length of the investigated pulses. We obtain:

$$g^{(n)} = \frac{\int \mathrm{d}t_1 \ldots \mathrm{d}t_n \left\langle \hat{a}^\dagger(t_1) \ldots \hat{a}^\dagger(t_n)\hat{a}(t_1) \ldots \hat{a}(t_n) \right\rangle}{\int \mathrm{d}t_1 \left\langle \hat{a}^\dagger(t_1)\hat{a}(t_1) \right\rangle \ldots \int \mathrm{d}t_n \left\langle \hat{a}^\dagger(t_n)\hat{a}(t_n) \right\rangle} \tag{9.2}$$

In order to be able to perform straightforward calculations with our broadband time-intergrated correlation function measurements we perform a Fourier transform from the time domain into the frequency domain ($\hat{a}(t) = \int \mathrm{d}\omega\, \hat{a}(\omega) e^{-\imath\omega t}$):

$$\begin{aligned} g^{(n)} &= \frac{\int \mathrm{d}\omega_1 \ldots \mathrm{d}\omega_n \left\langle \hat{a}^\dagger(\omega_1) \ldots \hat{a}^\dagger(\omega_n)\hat{a}(\omega_1) \ldots \hat{a}(\omega_n) \right\rangle}{\int \mathrm{d}\omega_1 \left\langle \hat{a}^\dagger(\omega_1)\hat{a}(\omega_1) \right\rangle \ldots \int \mathrm{d}\omega_n \left\langle \hat{a}^\dagger(\omega_n)\hat{a}(\omega_n) \right\rangle} \\ &= \frac{\left\langle : \left(\int \mathrm{d}\omega \hat{a}^\dagger(\omega)\hat{a}(\omega) \right)^n : \right\rangle}{\left\langle \int \mathrm{d}\omega \hat{a}^\dagger(\omega)\hat{a}(\omega) \right\rangle^n} \end{aligned} \tag{9.3}$$

Here $\langle : \cdots : \rangle$ indicates normal ordering of the enclosed photon creation and destruction operators. We further adapt the correlation function measurement to the broadband mode basis discussed in Sec. 4.4 and remain with:

$$g^{(n)} = \frac{\left\langle : \left(\sum_k \hat{A}_k^\dagger \hat{A}_k \right)^n : \right\rangle}{\left\langle \sum_k \hat{A}_k^\dagger \hat{A}_k \right\rangle^n} \tag{9.4}$$

Similarly, if we want to measure the correlations between two different beams, we are able to derive broadband time-integrated cross-correlation function measurements which evaluate to:

$$\begin{aligned} g^{(n,m)} &= \frac{\left\langle : \left(\int \mathrm{d}\omega\, \hat{a}^\dagger(\omega)\hat{a}(\omega) \right)^n :: \left(\int \mathrm{d}\omega\, \hat{b}^\dagger(\omega)\hat{b}(\omega) \right)^m : \right\rangle}{\left\langle \int \mathrm{d}\omega\, \hat{a}^\dagger(\omega)\hat{a}(\omega) \right\rangle^n \left\langle \int \mathrm{d}\omega\, \hat{b}^\dagger(\omega)\hat{b}(\omega) \right\rangle^m} \\ &= \frac{\left\langle : \left(\sum_k \hat{A}_k^\dagger \hat{A}_k \right)^n :: \left(\sum_k \hat{B}_k^\dagger \hat{B}_k \right)^m : \right\rangle}{\left\langle \sum_k \hat{A}_k^\dagger \hat{A}_k \right\rangle^n \left\langle \sum_k \hat{B}_k^\dagger \hat{B}_k \right\rangle^m} \end{aligned} \tag{9.5}$$

Eq.(9.1) and Eq. (9.2) stress the key difference between time-resolved and time-integrated correlation function measurements. In a time-resolved correlation function measurement we probe the optical pulse at a specific point in time. In our broadband time-integrated correlation function measurement we probe the full pulse.

9.3. Probing PDC states via correlation functions

Using the broadband time-integrated correlation functions, as defined in Sec. 9.2, we are able to effectively probe our multi-mode PDC states. The two benchmarks we are interested in are firstly the overall optical gain B and the number of optical modes K defined in Sec. 6.2.1.

9.3.1. Probing the number of modes via $g^{(2)}$-measurements

In order to probe the number of emitted modes K we have to perform a $g^{(2)}$-measurement as depicted in Fig. 9.2.

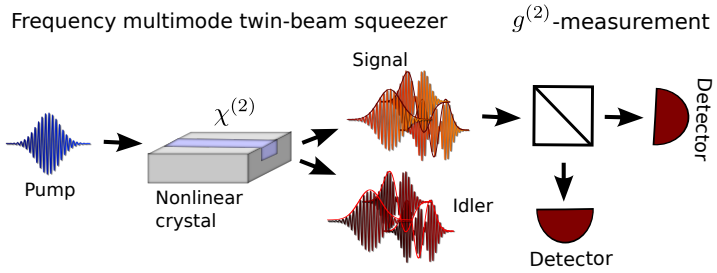

Figure 9.2.: Setup to measure $g^{(2)}$ of a multi-mode twin-beam squeezer.

Using PDC states, as defined in Eq. (6.3), we obtain:

$$g^{(2)} = 1 + \frac{\sum_k \sinh^4(r_k)}{\left[\sum_k \sinh^2(r_k)\right]^2} \tag{9.6}$$

In the low gain regime ($\sinh(r_k) \approx r_k = B\lambda_k$) Eq. (9.6) simplifies to:

$$\begin{aligned} g^{(2)} &\approx 1 + \frac{\sum_k B^4\lambda_k^4}{\left(\sum_k B^2\lambda_k^2\right)^2} = 1 + \frac{\sum_k \lambda_k^4}{\left(\sum_k \lambda_k^2\right)^2} = 1 + \sum_k \lambda_k^4 \\ &= 1 + \frac{1}{K} \end{aligned} \tag{9.7}$$

We are consequently able to directly obtain the number of modes via $K = 1/(g^{(2)} - 1)$. A single-mode PDC state ($K = 1$) yields $g^{(2)} = 2$ whereas a state with infinitely modes gives $g^{(2)} = 1$. The correspondence between K and $g^{(2)}$ is depicted in Fig. 9.3.

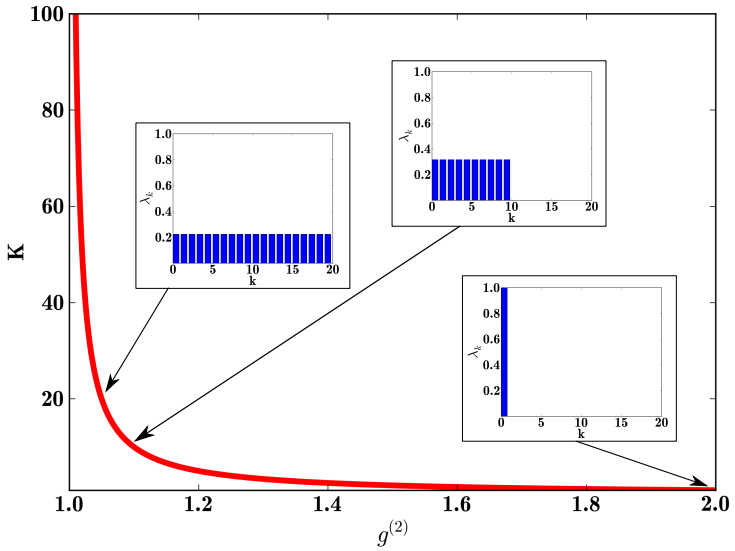

Figure 9.3.: Plot of the effective mode number K as a function of $g^{(2)}$ for various multi-mode PDC states.

Probing the optical gain B of a PDC state via $g^{(1,1)}$ measurements

To probe the optical gain B we have to perform a $g^{(1,1)}$ measurement as depicted in Fig. 9.4.

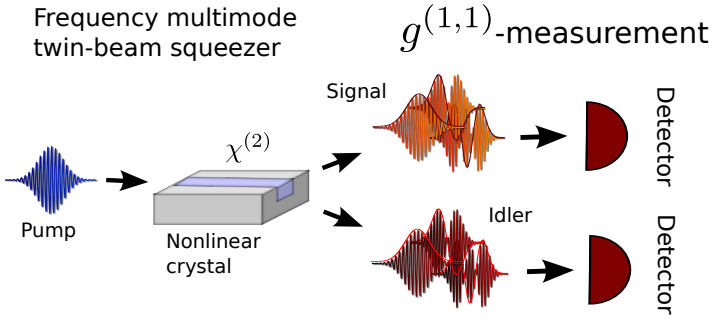

Figure 9.4.: Schematic setup to measure $g^{(1,1)}$ of a multi-mode twin-beam squeezer generated via PDC.

Using our developed broadband time-integrated correlation function formalism we

obtain:

$$g^{(1,1)} = \frac{\sum_{k,l} \sinh^2(r_k)\sinh^2(r_l) + \sum_k \sinh^2(r_k)\cosh^2(r_k)}{\left[\sum_k \sinh^2(r_k)\right]^2} = 1 + \underbrace{\frac{1}{\sum_k \sinh^2(r_k)}}_{1/\langle n\rangle} + \underbrace{\frac{\sum_k \sinh^4(r_k)}{\left[\sum_k \sinh^2(r_k)\right]^2}}_{g^{(2)}-1} \tag{9.8}$$

This measure is dependent on the optical gain B and the number of modes K via the $g^{(2)}$-measurement appearing. In the low gain regime ($\sinh(r_k) \approx r_k = B\lambda_k$), $g^{(1,1)}$ simplifies to

$$g^{(1,1)} \approx 1 + \tfrac{1}{B^2} + \underbrace{\frac{\sum_k \lambda_k^4}{\left[\sum_k \lambda_k^2\right]^2}}_{g^{(2)}-1} \approx \underbrace{g^{(2)}}_{\leq 2} + \underbrace{\frac{1}{B^2}}_{\gg 1} \approx \tfrac{1}{B^2}. \tag{9.9}$$

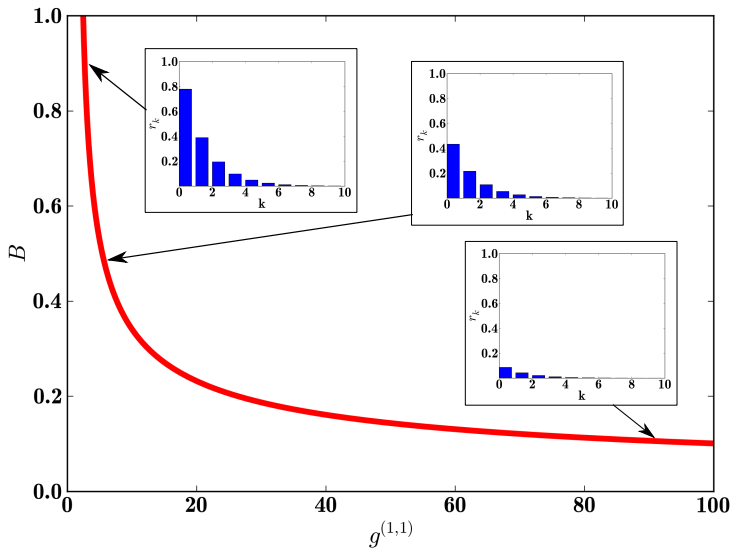

Figure 9.5.: The optical gain B plotted as a function of $g^{(1,1)}$. For small values of B the correlation function $g^{(1,1)}$ assumes a high value, yet rapidly decreases when the high gain regime is approached.

Hence, the optical gain is — in the low gain regime — obtained from the $g^{(1,1)}$-measurement via the simple relation $B \approx 1/\sqrt{g^{(1,1)}}$. In figure 9.5 we plot the dependence of the overall coupling value B on $g^{(1,1)}$which gives a high value for small optical gains B but rapidly decreases when the high gain regime is approached.

9.4. Conclusion

In conclusion we presented a new method to characterize ultrafast multi-mode PDC states using broadband time-integrated correlation function measurements. They enable a simple, straightforward and most importantly *loss independent* access to the PDC process parameters and have already be proven to be a useful tool in the laboratory [129, 36].

New Journal of Physics
The open-access journal for physics

Probing multimode squeezing with correlation functions

Andreas Christ[1,2,3], **Kaisa Laiho**[2], **Andreas Eckstein**[2], **Katiúscia N Cassemiro**[2] **and Christine Silberhorn**[1,2]

[1] Applied Physics, University of Paderborn, Warburger Straße 100, 33098 Paderborn, Germany
[2] Max Planck Institute for the Science of Light, Günther-Scharowsky Straße 1/Bau 24, 91058 Erlangen, Germany
E-mail: Andreas.Christ@uni-paderborn.de

New Journal of Physics **13** (2011) 033027 (21pp)
Received 13 December 2010
Published 18 March 2011
Online at http://www.njp.org/
doi:10.1088/1367-2630/13/3/033027

Abstract. Broadband multimode squeezers constitute a powerful quantum resource with promising potential for different applications in quantum information technologies such as information coding in quantum communication networks or quantum simulations in higher-dimensional systems. However, the characterization of a large array of squeezers that coexist in a single spatial mode is challenging. In this paper, we address this problem and propose a straightforward method for determining the number of squeezers and their respective squeezing strengths by using broadband multimode correlation function measurements. These measurements employ the large detection windows of the state of the art avalanche photodiodes in order to simultaneously probe the full Hilbert space of the generated state, which enables us to benchmark the squeezed states. Moreover, due to the structure of correlation functions, our measurements are not affected by losses. This is a significant advantage, since detectors with low efficiencies are sufficient. Our approach is less costly than tomographic methods relying on multimode homodyne detection, which is based on much more demanding measurement and analysis tools and appear to be impractical for large Hilbert spaces.

[3] Author to whom any correspondence should be addressed.

Contents

1. Introduction

The study of correlation functions has a long history and lies at the heart of coherence theory [1]. Intensity correlation measurements were first carried out by Hanbury Brown and Twiss in the context of classical optics [2]. Since then correlation functions have become a standard tool in quantum optical experiments for studying the properties of laser beams [3], parametric downconversion (PDC) sources [4, 5] or heralded single photons [6]–[8]. Current state of the art experiments are able to measure correlation functions up to the eighth order [9], giving access to diverse characteristics of photonic states. The normalized second-order correlation function $g^{(2)}(0)$ probes whether the generated photons are bunched or anti-bunched, with $g^{(2)}(0) < 1$ being a genuine sign of non-classicality [10]. The measurement of all unnormalized moments $G^{(n)}$ of a given optical quantum state provides complete access to the photon-number distribution for arbitrary single-mode input states [1]. Moreover, it is possible to perform a full state tomography with the help of correlation function measurements [11].

The measurement of these correlation functions is, in general, carried out in a time-resolved manner $g^{(n)}(t_1, t_2, \ldots, t_n)$. Limited time resolution has been considered as a detrimental effect and treated as experimental imperfection [6]. In contrast to previous work, we employ the finite-time resolution of photodetectors to gain access to the spectral character of broadband multimode quantum states. Our scheme for measuring broadband multimode correlation functions of pulsed quantum light is especially useful for probing squeezed states. These states are commonly generated via the interaction of light with a crystal exhibiting a $\chi^{(2)}$-nonlinearity, a process referred to as PDC [12]–[17] or with optical fibers featuring a $\chi^{(3)}$-nonlinearity called four-wave mixing (FWM) [18, 19].

In general, the generated squeezed states exhibit multimode characteristics in the spectral degree of freedom, i.e. a set of independent squeezed states is created with each squeezer

residing in its own Hilbert space. This inherent multimode character renders these states powerful for coding quantum information, yet the same feature impedes a proper experimental characterization in a straightforward manner. Due to the sheer vastness of the corresponding Hilbert space, standard quantum tomography methods become time consuming and ineffective. It is not easy to determine either the degree of squeezing in each mode, or the amount of generated independent squeezers. Nonetheless, these are the key benchmarks defining the potential of a source for quantum information and quantum cryptography applications. In the following, we investigate how to overcome these issues and elaborate on an alternative approach for determining the properties of multimode squeezed states based on measuring the broadband multimode correlation functions.

This paper is structured as follows. In section 2, we revisit the general structure of multimode twin-beam squeezers drawing special attention—but not restricting ourselves—to states generated by PDC and FWM. Section 3 presents the formalism of correlation functions, introduces the intricacies of finite-time resolution and defines broadband multimode correlation measurements. Section 4 combines the findings of sections 2 and 3: we analyze the relation between the number of generated squeezers, their respective squeezing strengths and broadband multimode correlation functions, which leads us to propose a scheme for characterizing multimode squeezing with the aid of broadband multimode correlation functions.

2. Multimode squeezers

In a squeezed state of light, one quadrature of the field exhibits an uncertainty below the standard quantum level at the expense of an increased variance in the conjugate quadrature, such that Heisenberg's uncertainty relation holds at its minimum attainable value. The standard description of squeezed states usually considers two different types of squeezers: single-beam squeezers and twin-beam squeezers. Single-beam squeezers create the squeezing into a single optical mode $\hat{S} = \exp(-\zeta \hat{a}^{\dagger 2} + \zeta^* \hat{a}^2)$, whereas twin-beam squeezers consist of *two* beams with inter-beam squeezing $\hat{S}^{ab} = \exp(-\zeta \hat{a}^\dagger \hat{b}^\dagger + \zeta^* \hat{a}\hat{b})$ [20]. In these equations, ζ labels the squeezing strength and the operators $\hat{a}^\dagger$ and $\hat{b}^\dagger$ create photons in distinct optical modes.

In this section, we go beyond the standard description and discuss the theory of squeezed states, which are generated by the interaction of ultrafast pump pulses with nonlinear crystals or optical fibers. Here, we concentrate on the spectral structure of the broadband output beams. In general, the utilized optical processes, typically called optical parametric amplification (OPA) or PDC, do not generate one but a variety of different squeezers in multiple frequency modes. A whole set of independent squeezed beams is generated in broadband orthogonal spectral modes within an optical beam. We refer to these states as frequency multimode single- or twin-beam squeezers [14]. Here the *multimode* prefix indicates that more than one squeezer is present in the optical beam and the term *single- or twin-beam* identifies whether one squeezed beam or two entangled squeezed beams are created. Due to the single-pass configuration of our sources, losses are negligible; hence, we restrict ourselves to the analysis of pure squeezed states.

2.1. Multimode twin-beam squeezers

The subject of our analysis is twin-beam squeezing generated by the propagation of an ultrafast pump pulse through a nonlinear medium (single-beam squeezers are discussed in appendix B). For simplicity we focus on the collinear propagation of all involved fields, each generated into

a single spatial mode. This description is rigorously fulfilled for PDC in waveguides [21, 22], but can also be applied to other experimental configurations, since the approximation carries all the complexities of the multimode propagation in the spectral degree of freedom. If the pump field is undepleted, we can neglect its quantum fluctuations and describe this OPA process by the effective quadratic Hamiltonian (see appendix A for a detailed derivation)

$$\hat{H}_{\mathrm{OPA}} = A \int \mathrm{d}\omega_{\mathrm{s}} \int \mathrm{d}\omega_{i}\; f(\omega_{\mathrm{s}}, \omega_{\mathrm{i}}) \hat{a}_{\mathrm{s}}^{\dagger}(\omega_{\mathrm{s}}) \hat{a}_{\mathrm{i}}^{\dagger}(\omega_{\mathrm{i}}) + \mathrm{h.c.}, \tag{1}$$

in which the constant A denotes the overall efficiency of the OPA, the function $f(\omega_{\mathrm{s}}, \omega_{\mathrm{i}})$ describes the normalized output spectrum of the downconverted beam, which—in many cases—is close to a two-dimensional (2D) Gaussian distribution. The operators $\hat{a}_{\mathrm{s}}^{\dagger}(\omega_{\mathrm{s}})$ and $\hat{a}_{\mathrm{i}}^{\dagger}(\omega_{\mathrm{i}})$ are the photon creation operators in the different twin-beam arms, in general labeled the signal and the idler, respectively.

The unitary transformation generated by the effective OPA Hamiltonian in equation (1) can be written in the form

$$\hat{U}_{\mathrm{OPA}} = \exp\left[-\frac{\imath}{\hbar} \left(A \int \mathrm{d}\omega_{\mathrm{s}} \int \mathrm{d}\omega_{\mathrm{i}}\; f(\omega_{\mathrm{s}}, \omega_{\mathrm{i}}) \hat{a}_{\mathrm{s}}^{\dagger}(\omega_{\mathrm{s}}) \hat{a}_{\mathrm{i}}^{\dagger}(\omega_{\mathrm{i}}) + \mathrm{h.c.} \right) \right]. \tag{2}$$

By virtue of the singular value decomposition theorem [23], we decompose the two terms in the exponential of equation (2) as

$$\begin{aligned} -\frac{\imath}{\hbar} A f(\omega_{\mathrm{s}}, \omega_{\mathrm{i}}) &= \sum_{k} r_k \psi_k^{*}(\omega_s) \phi_k^{*}(\omega_{\mathrm{i}}), \quad \text{and} \\ -\frac{\imath}{\hbar} A^{*} f^{*}(\omega_{\mathrm{s}}, \omega_{\mathrm{i}}) &= -\sum_{k} r_k \psi_k(\omega_{\mathrm{s}}) \phi_k(\omega_{\mathrm{i}}). \end{aligned} \tag{3}$$

Here both $\{\psi_k(\omega_{\mathrm{s}})\}$ and $\{\phi_k(\omega_{\mathrm{i}})\}$ each form a complete set of orthonormal functions. The amplitudes of the generated modes $\psi_k(\omega_{\mathrm{s}})$ and $\phi_k(\omega_{\mathrm{i}})$ are given by the $r_k \in \mathbb{R}^{+}$ distribution. Employing equation (3) and introducing a new broadband mode basis [24] for the generated state as

$$\hat{A}_k = \int \mathrm{d}\omega_{\mathrm{s}} \psi_k(\omega_{\mathrm{s}}) \hat{a}_{\mathrm{s}}(\omega_{\mathrm{s}}) \quad \text{and} \quad \hat{B}_k = \int \mathrm{d}\omega_{\mathrm{i}} \phi_k(\omega_{\mathrm{i}}) \hat{a}_{\mathrm{i}}(\omega_{\mathrm{i}}), \tag{4}$$

we obtain the unitary transformation [13]

$$\begin{aligned} \hat{U}_{\mathrm{OPA}} &= \exp\left[\sum_{k} r_k \hat{A}_k^{\dagger} \hat{B}_k^{\dagger} - \mathrm{h.c.} \right] \\ &= \bigotimes_{k} \exp\left[r_k \hat{A}_k^{\dagger} \hat{B}_k^{\dagger} - \mathrm{h.c.} \right] \\ &= \bigotimes_{k} \hat{S}_k^{ab}(-r_k). \end{aligned} \tag{5}$$

In total, the OPA generates a tensor product of distinct broadband twin-beam squeezers as defined in [20] with squeezing amplitudes r_k related to the available amount of squeezing via squeezing [dB] $= -10 \log_{10}(\mathrm{e}^{-2r_k})$. The Heisenberg representation of the multimode twin-beam squeezers is given by independent input–output relations for each broadband beam

$$\begin{aligned} \hat{A}_k &\Rightarrow \cosh(r_k) \hat{A}_k + \sinh(r_k) \hat{B}_k^{\dagger}, \\ \hat{B}_k &\Rightarrow \cosh(r_k) \hat{B}_k + \sinh(r_k) \hat{A}_k^{\dagger}. \end{aligned} \tag{6}$$

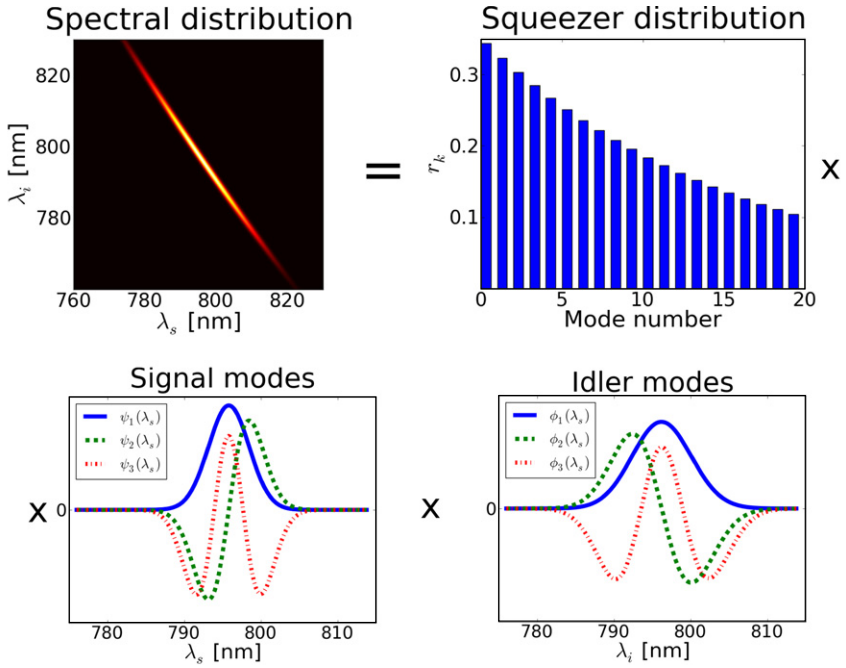

Figure 1. Visualization of the singular value decomposition in equation (3). The frequency distribution $-\frac{\imath}{\hbar}Af(\omega_\mathrm{s}, \omega_\mathrm{i})$ of the generated state defines the shape of the signal and idler modes $\psi_k(\omega_\mathrm{s})$, $\phi_k(\omega_\mathrm{i})$ and the squeezer distribution r_k.

Note that the squeezer distribution r_k and basis modes $\hat{A}_k$ and $\hat{B}_k$ are unique and well-defined properties of the generated twin beam. Their exact form is given by the Schmidt decomposition of the joint spectral amplitude $-\frac{\imath}{\hbar}Af(\omega_\mathrm{s}, \omega_\mathrm{i})$. This mathematical transformation directly yields the physical shape of the generated optical modes $\psi_k(\omega_\mathrm{s})$, $\phi_k(\omega_\mathrm{i})$ with each pair $\hat{A}_k$ and $\hat{B}_k$ being strictly correlated.

In figure 1, we illustrated one possible squeezer distribution and corresponding broadband modes. The joint spectral distribution $f(\omega_s, \omega_i)$ of the generated twin beams shown in figure 1 defines the shape of the broadband signal and idler modes $\hat{A}_k$ and $\hat{B}_k$. In the special case of a Gaussian spectral distribution, the form of the squeezing modes resembles the Hermite functions. The number of different squeezer modes is closely connected with the frequency correlations between the signal and idler beams. In the presented case, the spectrally correlated beams lead to over 20 independent squeezers. The total amount of squeezing depends on the constant A appearing in the Hamiltonian in equation (1), which is directly related to the applied pump power I and the strength of the nonlinearity $\chi^{(2)}$ in the medium ($A \propto \sqrt{I}, \chi^{(2)}$).

The OPA state is mainly characterized by the number of squeezed modes and the overall gain of the process, both being determined by the distribution of the individual squeezing amplitudes r_k. In order to analyze the number of generated squeezers independently of the amount of squeezing, we split the distribution of squeezing weights r_k into a normalized distribution λ_k ($\sum_k \lambda_k^2 = 1$) that characterizes the probability for occupation of different squeezers in the respective optical quantum state, and an overall gain of the process $B \in \mathbb{R}^+$, quantifying the total amount of generated squeezing according to

$$r_k = B\,\lambda_k. \tag{7}$$

The characterization of these two fundamental properties of a multimode twin-beam state is a major experimental challenge. While these states are easily generated in the laboratory, a tomography by means of homodyne detection would require us to match for each squeezed mode $\hat{A}_k$ and $\hat{B}_k$ different local oscillator beams with adapted temporal-spectral pulse shapes. Multimode homodyning [25] may provide a route to circumvent this difficulty; however, an experimental implementation still appears challenging.

3. Correlation functions

The nth-order (normalized) correlation function $g^{(n)}(t_1, t_1, \ldots, t_n)$ is generally defined as a time-dependent function of the electromagnetic field. For quantized electric field operators, it can be expressed as [1, 10, 26, 27]

$$g^{(n)}(t_1, t_2, \ldots, t_n) = \frac{\left\langle \hat{E}^{(-)}(t_1) \ldots \hat{E}^{(-)}(t_n) \hat{E}^{(+)}(t_1) \ldots \hat{E}^{(+)}(t_n) \right\rangle}{\left\langle \hat{E}^{(-)}(t_1) \hat{E}^{(+)}(t_1) \right\rangle \ldots \left\langle \hat{E}^{(-)}(t_n) \hat{E}^{(+)}(t_n) \right\rangle}, \tag{8}$$

and it measures the (normalized) nth-order temporal correlations at different points in time. Note that this definition of the correlation functions is independent of coupling losses and detection inefficiencies, yielding a loss resilient measure [9]. Realistic detectors, however, suffer from internal jitter and finite gating times. We accommodate these resolution effects by weighting the correlation function with the appropriate detection window $T(t)$ of the applied detectors as presented in [6], and obtain

$$g^{(n)}(t_1, t_2, \ldots, t_n) = \frac{\int \mathrm{d}t_1\, T(t_1) \ldots \int \mathrm{d}t_n T(t_n) \left\langle \hat{E}^{(-)}(t_1) \ldots \hat{E}^{(-)}(t_n) \hat{E}^{(+)}(t_1) \ldots \hat{E}^{(+)}(t_n) \right\rangle}{\int \mathrm{d}t_1\, T(t_1) \left\langle \hat{E}^{(-)}(t_1) \hat{E}^{(+)}(t_1) \right\rangle \ldots \int \mathrm{d}t_n T(t_n) \left\langle \hat{E}^{(-)}(t_n) \hat{E}^{(+)}(t_n) \right\rangle}. \tag{9}$$

If the employed photodetectors exhibit flat detection windows, exceeding the length of the investigated pulses ($T(t) \to \text{const}$), equation (9) can be simplified to

$$g^{(n)} = \frac{\int \mathrm{d}t_1 \ldots \mathrm{d}t_n \left\langle \hat{E}^{(-)}(t_1) \ldots \hat{E}^{(-)}(t_n) \hat{E}^{(+)}(t_1) \ldots \hat{E}^{(+)}(t_n) \right\rangle}{\int \mathrm{d}t_1 \left\langle \hat{E}^{(-)}(t_1) \hat{E}^{(+)}(t_1) \right\rangle \ldots \int \mathrm{d}t_n \left\langle \hat{E}^{(-)}(t_n) \hat{E}^{(+)}(t_n) \right\rangle}. \tag{10}$$

This theoretical model is adequate for the detection of ultrafast pulses with standard avalanche photodetectors. Furthermore, equation (10) exhibits the convenient property of time independence and represents our generalized broadband multimode correlation function. Despite its similarity to the common correlation functions as defined in equation (8), the broadband multimode correlation function in equation (10) should no longer be considered as a naive general measure of nth-order coherence. In figure 2, we illustrate the main difference between the time-integrated and time-resolved correlation measurements.

Equation (10) is still not optimal for our studies of squeezed light fields. We transform it further by replacing the electric field operators by photon number creation and destruction operators ($\hat{E}^{(+)}(t_n) \propto \hat{a}(t_n)$) and perform a Fourier transform from the time domain into the

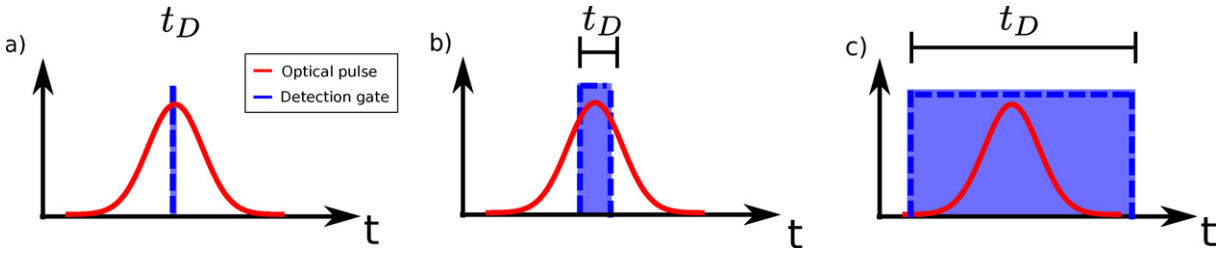

Figure 2. (a) Perfect time-resolved detection; (b) finite detection gate; (c) broadband detection gate exceeding the pulse duration giving rise to different types of correlation measures.

frequency domain ($\hat{a}(t) = \int \mathrm{d}\omega\, \hat{a}(\omega)\mathrm{e}^{-\imath\omega t}$). Equation (10) is then rewritten as

$$g^{(n)} = \frac{\int \mathrm{d}\omega_1 \ldots \mathrm{d}\omega_n \left\langle \hat{a}^\dagger(\omega_1) \ldots \hat{a}^\dagger(\omega_n)\hat{a}(\omega_1) \ldots \hat{a}(\omega_n)\right\rangle}{\int \mathrm{d}\omega_1 \left\langle \hat{a}^\dagger(\omega_1)\hat{a}(\omega_1)\right\rangle \ldots \int \mathrm{d}\omega_n \left\langle \hat{a}^\dagger(\omega_n)\hat{a}(\omega_n)\right\rangle}$$
$$= \frac{\left\langle : \left(\int \mathrm{d}\omega \hat{a}^\dagger(\omega)\hat{a}(\omega)\right)^n : \right\rangle}{\left\langle \int \mathrm{d}\omega \hat{a}^\dagger(\omega)\hat{a}(\omega)\right\rangle^n}, \tag{11}$$

in which $\langle : \cdots : \rangle$ indicates normal ordering of the enclosed photon creation and destruction operators. In addition, we adapt the correlation function to the basis of the measured quantum system, i.e. we perform a general basis transform from $\hat{a}(\omega)$ to the basis of the measured multimode twin-beam squeezers $\hat{A}_k$. This results in

$$g^{(n)} = \frac{\left\langle : \left(\sum_k \hat{A}_k^\dagger \hat{A}_k\right)^n : \right\rangle}{\left\langle \sum_k \hat{A}_k^\dagger \hat{A}_k\right\rangle^n}. \tag{12}$$

Equations (10)–(12) stress the key difference between time-resolved and time-integrated correlation function measurements. While time-resolved correlation functions probe specific temporal modes, time-integrating detectors directly measure a superposition of all the different modes. This specific feature of broadband multimode detection is essential for our analysis. The simultaneous measurement of all different optical modes gives us direct *loss-independent* access to the squeezer distribution of the probed state.

3.1. Broadband multimode cross-correlation functions

In the previous section, we restricted ourselves to intra-beam correlations. To allow for measurements of correlations between different beams we extend our analysis. The identification of such inter-beam correlations is of special importance in quantum optics and quantum information applications, since they quantify the continuous variable entanglement between different subsystems, in our case the analyzed optical beams. In section 2, we have already discussed one of the most widely employed entanglement sources: twin-beam squeezers. These states are entangled not only in their quadratures, but also in their spectral and spatial degrees of freedom [28]. To probe higher-order cross-correlations between the two different beams [27] or subsystems a and b of orders n and m, respectively, we generalize

equation (8) to

$$g^{(n,m)}(t_1^{(a)}, t_2^{(a)}, \ldots, t_n^{(a)}; t_1^{(b)}, t_2^{(b)}, \ldots, t_m^{(b)}) = \frac{\left\langle \hat{E}_a^{(-)}(t_1^{(a)}) \ldots \hat{E}_a^{(-)}(t_n^{(a)}) \hat{E}_a^{(+)}(t_1^{(a)}) \cdots \hat{E}_a^{(+)}(t_n^{(a)}) \times \hat{E}_b^{(-)}(t_1^{(b)}) \cdots \hat{E}_b^{(+)}(t_n^{(b)}) \right\rangle}{\left\langle \hat{E}_a^{(-)}(t_1^{(a)}) \hat{E}_a^{(+)}(t_1^{(a)}) \right\rangle \cdots \left\langle \hat{E}_a^{(-)}(t_n^{(a)}) \hat{E}_a^{(+)}(t_n^{(a)}) \right\rangle \times \cdots \left\langle \hat{E}_b^{(-)}(t_n^{(b)}) \hat{E}_b^{(+)}(t_n^{(b)}) \right\rangle}. \quad (13)$$

Taking into account broadband detection windows—exceeding the pulse duration—the above formula can be reformulated as

$$g^{(n,m)} = \frac{\left\langle : \left(\int \mathrm{d}t \, \hat{E}_a^{(-)}(t) \hat{E}_a^{(+)}(t) \right)^n :: \left(\int \mathrm{d}t \, \hat{E}_b^{(-)}(t) \hat{E}_b^{(+)}(t) \right)^m : \right\rangle}{\left\langle \int \mathrm{d}t \, \hat{E}_a^{(-)}(t) \hat{E}_a^{(+)}(t) \right\rangle^n \left\langle \int \mathrm{d}t \, \hat{E}_b^{(-)}(t) \hat{E}_b^{(+)}(t) \right\rangle^m}. \quad (14)$$

Again we perform the same simplifications as in equation (11) of section 3: namely we replace the electric field operators by photon creation and destruction operators, apply the Fourier transform from the time to the frequency domain and finally we adapt the measurement basis to the given optical state. We find an extended version of equations (11) and (12),

$$g^{(n,m)} = \frac{\left\langle : \left(\int \mathrm{d}\omega \, \hat{a}^\dagger(\omega) \hat{a}(\omega) \right)^n :: \left(\int \mathrm{d}\omega \, \hat{b}^\dagger(\omega) \hat{b}(\omega) \right)^m : \right\rangle}{\left\langle \int \mathrm{d}\omega \, \hat{a}^\dagger(\omega) \hat{a}(\omega) \right\rangle^n \left\langle \int \mathrm{d}\omega \, \hat{b}^\dagger(\omega) \hat{b}(\omega) \right\rangle^m}. \quad (15)$$

$$= \frac{\left\langle : \left(\sum_k \hat{A}_k^\dagger \hat{A}_k \right)^n :: \left(\sum_k \hat{B}_k^\dagger \hat{B}_k \right)^m : \right\rangle}{\left\langle \sum_k \hat{A}_k^\dagger \hat{A}_k \right\rangle^n \left\langle \sum_k \hat{B}_k^\dagger \hat{B}_k \right\rangle^m}. \quad (16)$$

Further extensions of cross-correlation measurements to systems consisting of more than two different beams are possible [1], but are not necessary within the scope of this paper.

4. Probing frequency multimode squeezers via correlation functions

Using the theoretical description of squeezers as well as the derived broadband multimode correlation functions, we now combine the findings of sections 2 and 3. We establish a connection between the broadband multimode correlation functions and the properties of the squeezing, i.e. the mode distribution λ_k and the optical gain B.

4.1. Probing the number of modes via $g^{(2)}$-measurements

The most important property of frequency multimode squeezers is the number of independent squeezers in the generated twin-beam state, which is specified by the mode distribution λ_k. In contrast to the optical gain B, which is easily tuned by adjusting the pump power, the mode distribution λ_k is heavily constricted by the dispersion in the nonlinear material and hence, in general, not easily adjustable[4]. The effective number of modes in the multimode twin-beam

[4] One method for changing the mode distribution is to perform spectral filtering on the signal and idler beams [41]. However, this process leads to impurities and the generated states are not represented by pure twin-beam squeeze any more [40]. Hence, this analysis is outside the scope of this paper.

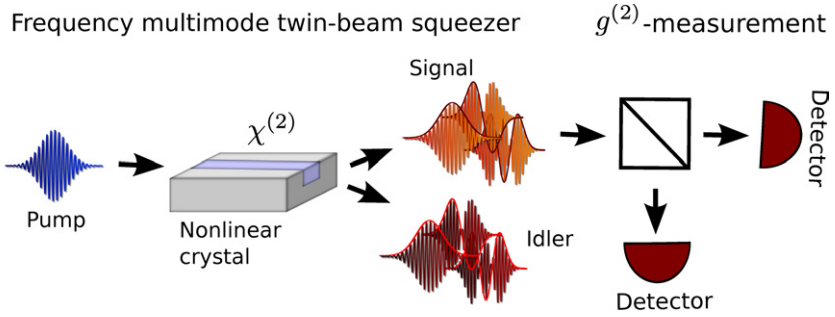

Figure 3. Setup for measuring the $g^{(2)}$ of a multimode twin-beam squeezer.

state is given by the Schmidt number or cooperativity parameter K as defined in [29, 30] with

$$K = 1/\sum_k \lambda_k^4. \tag{17}$$

Under the assumption of an independent uniform squeezer distribution, it directly reflects the number of occupied modes. The mode number K of a multimode twin-beam squeezer can be directly accessed by measuring the broadband multimode $g^{(2)}$-correlation function in the signal or idler arm as depicted in figure 3. This is a result of the structure of the second-order correlation function, which—by using (12) and (6)—can be expressed as

$$g^{(2)} = 1 + \frac{\sum_k \sinh^4(r_k)}{\left[\sum_k \sinh^2(r_k)\right]^2}. \tag{18}$$

For our further analysis, it is useful to distinguish the low gain from the high gain regime, corresponding to low and high levels of squeezing. In the low gain regime corresponding to biphotonic states typically referred to in the context of PDC experiments, $\sinh(r_k) \approx r_k = B\lambda_k$, and we are able to simplify equation (18) to

$$\begin{aligned} g^{(2)} &\approx 1 + \frac{\left(\sum_k B^4\lambda_k^4\right)}{\left(\sum_k B^2\lambda_k^2\right)^2} = 1 + \frac{\sum_k \lambda_k^4}{\left(\sum_k \lambda_k^2\right)^2} = 1 + \sum_k \lambda_k^4 \\ &= 1 + \frac{1}{K}. \end{aligned} \tag{19}$$

Consequently, the effective number of modes is directly available from the correlation function measurement via $K = 1/(g^{(2)} - 1)$. For a single twin-beam squeezer ($K = 1$) $g^{(2)} = 2$, whereas for higher numbers of squeezers ($K \gg 1$) the contributions from the term $\sum_k \lambda_k^4$ become negligible and $g^{(2)}$ approaches one. This direct correspondence between $g^{(2)}$ and the effective number of modes K is presented in figure 4(a).

Another way of interpreting equation (19) is to approach the correlation function measurement from the photon-number point of view. The $g^{(2)}$-value of a single twin-beam squeezer, which exhibits a thermal photon-number distribution, evaluates to $g^{(2)} = 2$. If more squeezers are involved the detector cannot distinguish between the different thermal distributions, i.e. it measures a convolution of all the different thermal photon streams, which gives a Poissonian photon-number distribution [13, 31]. In fact, one can show that the $g^{(2)}$-correlation function in equation (18) is the convolution of the second-order moments of each individual squeezer.

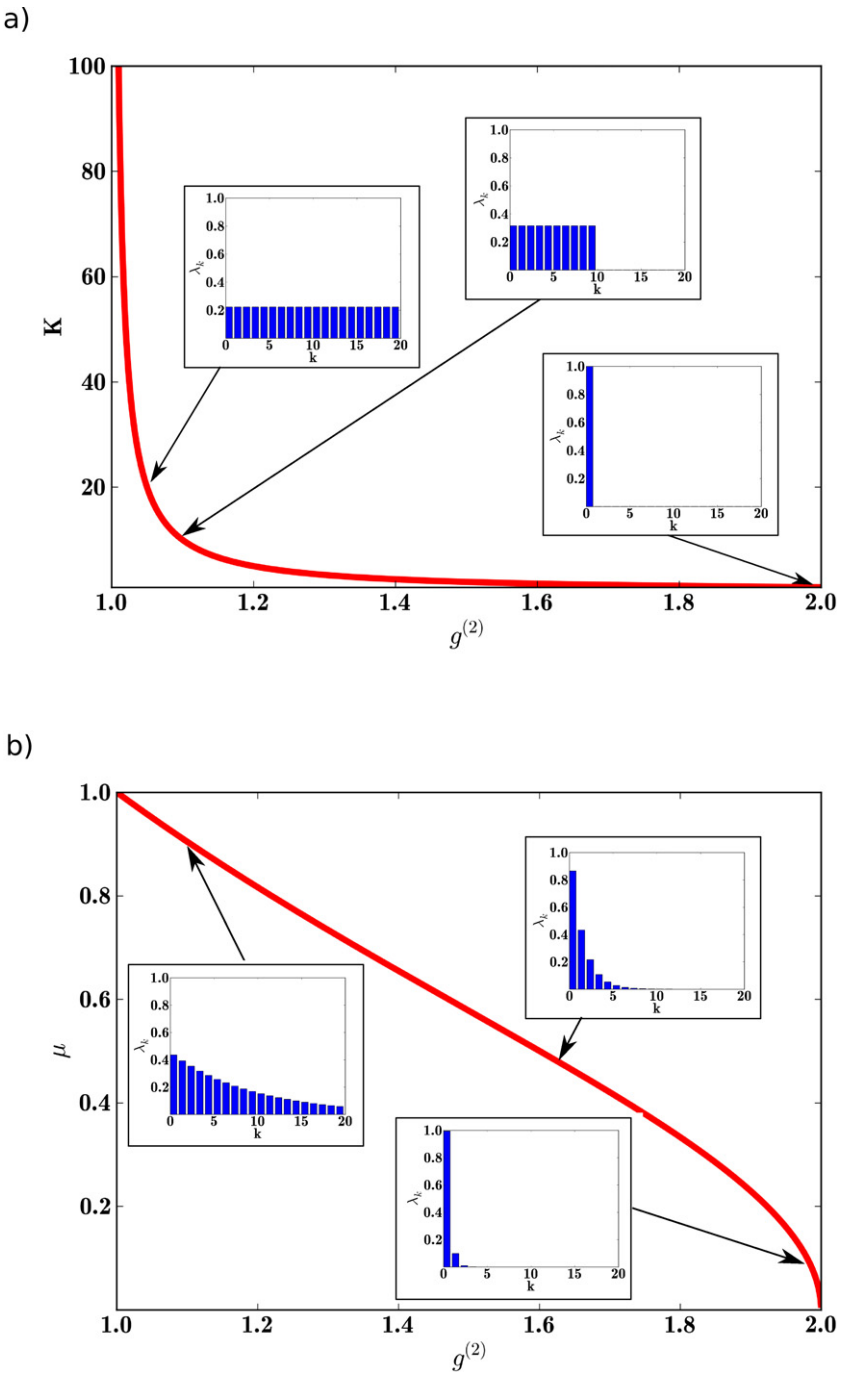

Figure 4. (a) Plot of the effective mode number K as a function of $g^{(2)}$ for various effective numbers of modes. (b) Visualization of μ as a function of $g^{(2)}$ for different thermal squeezer distributions.

Once more, we stress that the $g^{(2)}$-measurement does not give access to the exact distribution of squeezers λ_k, but to the *effective* number of modes under the assumption that all squeezed states share an identical amount of squeezing. This is a rather crude model and does not fit very well to many experimental realizations. Fortunately, there is a common class

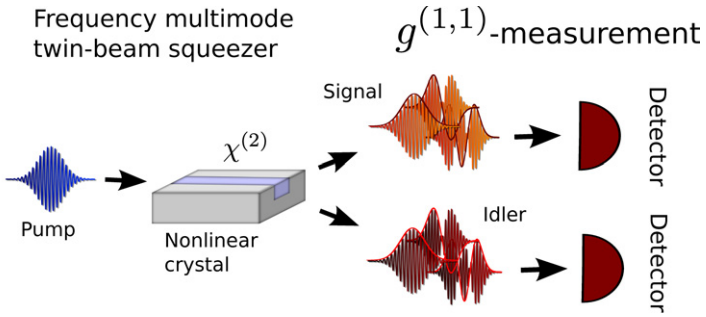

Figure 5. Schematic setup for measuring the $g^{(1,1)}$ of a multimode twin-beam squeezer generated via PDC.

of squeezed states, for which a much more refined mode distribution λ_k is accessible: in the case of a 2D Gaussian joint-spectral distribution $f(\omega_s, \omega_i)$, the distribution λ_k is thermal $\lambda_k = \sqrt{1-\mu^2}\mu^k$, and thus it can be characterized by a single distribution parameter μ [32]. The latter can be retrieved from a $g^{(2)}$-measurement via $\mu = \sqrt{2/g^{(2)} - 1}$, as depicted in figure 4(b), where we illustrate how the detection of the $g^{(2)}$-function can provide us directly with comprehensive knowledge of the underlying spectral mode structure of the analyzed state.

In conclusion, we have shown that by measuring the second-order correlation function $g^{(2)}$ of a multimode broadband twin-beam state, one can probe the corresponding distribution of spectral modes λ_k. Our method displays the advantage that correlation functions can be measured in a very practical way [33], resulting in an approach that is much easier than realizing homodyne measurements, which require addressing individual modes. As a side remark we would like to point out that one can also determine the effective number of squeezers from the higher moments $g^{(n)}$, $n \geqslant 2$, similar to the presented approach, yet $g^{(2)}$ is already sufficient for our purposes.

4.2. Probing the optical gain B of a multimode twin-beam squeezer via $g^{(1,1)}$ measurements

In section 4.1, we determined the number of modes in a loss resilient way by measuring $g^{(2)}$ for low gains B. Here we investigate the amount of the generated squeezing determined by the overall optical gain B. In order to probe this value the setup has to be changed to measure the correlation function $g^{(1,1)}$ of the generated twin-beam squeezer as presented in figure 5. Using equations (16) and (6), we obtain for $g^{(1,1)}$ the form

$$g^{(1,1)} = \frac{\sum_{k,l} \sinh^2(r_k)\sinh^2(r_l) + \sum_k \sinh^2(r_k)\cosh^2(r_k)}{\left[\sum_k \sinh^2(r_k)\right]^2}$$
$$= 1 + \underbrace{\frac{1}{\sum_k \sinh^2(r_k)}}_{1/\langle n\rangle} + \underbrace{\frac{\sum_k \sinh^4(r_k)}{\left[\sum_k \sinh^2(r_k)\right]^2}}_{g^{(2)}-1}. \tag{20}$$

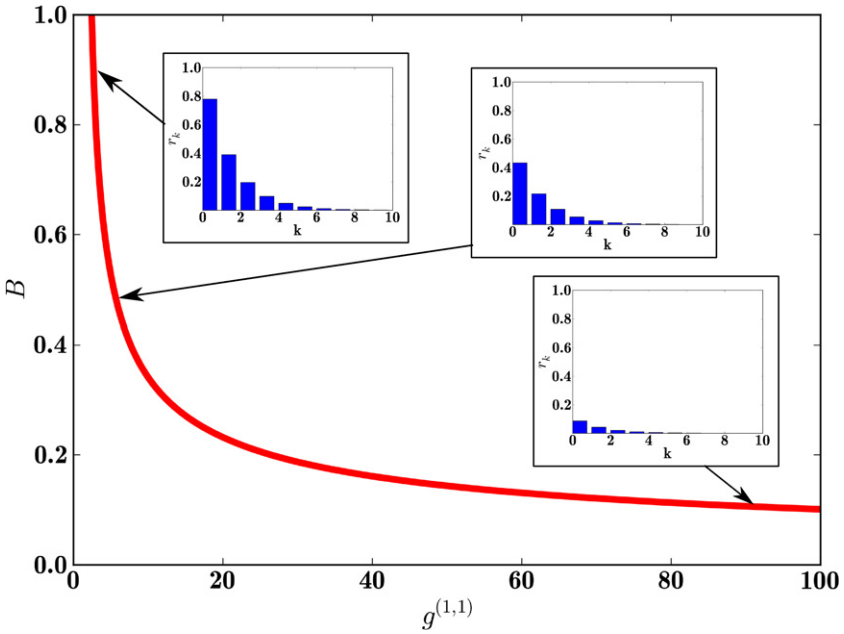

Figure 6. The optical gain B plotted as a function of $g^{(1,1)}$. For small values of B the correlation function $g^{(1,1)}$ takes on a high value, yet rapidly decreases when the high gain regime is approached.

The relevant characteristic we exploit from this measurement is its dependence on both, the number of modes in the system, as given by the $g^{(2)}$-function, and the mean photon number in each arm, which is closely connected with the coupling coefficient B. In the low gain regime ($\sinh(r_k) \approx r_k$), $g^{(1,1)}$ simplifies to

$$g^{(1,1)} \approx 1 + \frac{1}{B^2} + \underbrace{\frac{\sum_k \lambda_k^4}{\left[\sum_k \lambda_k^2\right]^2}}_{g^{(2)}-1} \approx \underbrace{g^{(2)}}_{\leqslant 2} + \underbrace{\frac{1}{B^2}}_{\gg 1} \approx \frac{1}{B^2}. \tag{21}$$

Hence, the optical gain is—in the low gain regime—obtained from the $g^{(1,1)}$-measurement via the simple relation $B \approx 1/\sqrt{g^{(1,1)}}$. Mode dependences of the coupling value B only occur at high squeezing strengths, where the relation diverges from equation (21) and takes on a more complicated form. In figure 6, we plot the dependence of the overall coupling value B on $g^{(1,1)}$—as presented in equation (20)—which takes on a high value for small optical gains B but rapidly decreases when the high gain regime is approached.

In total measuring $g^{(1,1)}$ gives direct *loss-independent* access to the optical gain B. This enables a loss tolerant probing of the generated mean photon number which, in the low gain regime, is even independent of the underlying mode structure.

Taking into account the prior knowledge we gained from section 4.1, we can now ascertain all parameters needed for fully determining the highly complex multimode state. The optical gain B defines not only the photon distribution, but quantifies the generated twin-beam squeezing, i.e. the available CV entanglement in each mode. Note that all modes exhibit different entanglement parameters. Depending on the state and its respective mode

distribution determined by the $g^{(2)}$-measurement, all the entanglement could be generated in a single spectral mode where it is readily available for quantum information experiments or in a multitude of different squeezed modes. Note, however, that after the state generation process multiple squeezers cannot be combined into a single optical mode by using only Gaussian operations, since this operation would be equivalent to continuous-variable entanglement distillation [34]–[36].

5. Outlook

In this paper, we focused on the state characterization of ultrafast twin-beam squeezers in the time domain and their experimental analysis. The presented approach, however, is not limited to twin-beam squeezers:

On the one hand, our measurement technique also applies to probing the squeezing of ultrafast multimode single-beam squeezers as presented in appendix B. On the other hand, our approach is easily adapted to spatial multimode squeezed states [37]–[39]. These are characterized by measuring correlation functions that are broadband in the spatial domain, in direct analogy to the spectral degree of freedom analyzed in this work.

6. Conclusion

We elaborated on the generation of multimode squeezed beams and their characterization with multimode broadband correlation functions. We expanded the formalism of correlation functions by including the effects of finite time resolution. These extended correlation function measurements serve as a versatile tool for characterizing optical quantum states such as twin-beam squeezers. They provide a simple, straightforward and *loss-independent* way to investigate the characteristics of multimode squeezed states. Our findings are important for the field of efficient quantum state characterization and have already proven to be a useful experimental tool in the laboratory [33, 40].

Acknowledgments

This work was supported by the EC under the grant agreements CORNER (FP7-ICT-213681) and QUESSENCE (248095). KNC acknowledges support from the Alexander von Humboldt Foundation. We thank Agata M Brańczyk, Malte Avenhaus and Benjamin Brecht for useful discussions and helpful comments.

Appendix A. Multimode twin-beam squeezer generation via nonlinear optical processes

A.1. Generation of multimode twin-beam squeezers via parametric downconversion (PDC)

In the process of PDC, squeezed states are generated by the interaction of a strong pump field with the $\chi^{(2)}$-nonlinearity of a crystal. Regarding the generation of twin-beam squeezers,

the Hamiltonian of the corresponding three-wave-mixing process is given by the equation [13, 41, 42]

$$\hat{H}_{\mathrm{PDC}} = \int_{-L/2}^{L/2} \mathrm{d}z\, \chi^{(2)} \hat{E}_{\mathrm{p}}^{(+)}(z,t)\hat{E}_{\mathrm{s}}^{(-)}(z,t)\hat{E}_{\mathrm{i}}^{(-)}(z,t) + \mathrm{h.c.}, \tag{A.1}$$

where we focused on a collinear interaction of all three beams. In equation (A.1) L labels the length of the medium, $\chi^{(2)}$ the nonlinearity of the crystal and $\hat{E}_{\mathrm{p}}^{(+)}(z,t)$, $\hat{E}_{\mathrm{s}}^{(-)}(z,t)$ and $\hat{E}_{\mathrm{i}}^{(-)}(z,t)$ the pump, the signal and the idler fields. The electric field operators used in equation (A.1) are defined as follows:

$$\hat{E}_x^{(-)}(z,t) = \hat{E}_x^{(+)\dagger}(z,t) = C \int \mathrm{d}\omega_x\, \exp[-\imath(k_x(\omega)z + \omega t)]\, \hat{a}_x^{\dagger}(\omega), \tag{A.2}$$

in which we have merged all constants and slowly varying field amplitudes in the overall parameter C. To simplify the Hamiltonian, we treat the strong pump field as a classical wave

$$\hat{E}_{\mathrm{p}}^{(+)}(z,t) \Rightarrow E_{\mathrm{p}}(z,t) = \int \mathrm{d}\omega_{\mathrm{p}}\, \alpha(\omega_{\mathrm{p}}) \exp\left[\imath\left(k_{\mathrm{p}}(\omega_{\mathrm{p}})z + \omega_{\mathrm{p}}t\right)\right]. \tag{A.3}$$

Here $\alpha(\omega_{\mathrm{p}}) = A_{\mathrm{p}}\exp[(\omega_{\mathrm{p}} - \mu_{\mathrm{p}})^2/(2\sigma_{\mathrm{p}}^2)]$ is the Gaussian pump envelope function generated by an ultrafast laser system, consisting of a field amplitude A_{p}, a central pump frequency μ_{p} and a pump width σ_{p}.

The PDC Hamiltonian in equation (A.1) generates the following unitary transformation:

$$\hat{U} = \exp\left[-\frac{\imath}{\hbar}\int_{-\infty}^{\infty} \mathrm{d}t'\, \hat{H}_{\mathrm{PDC}}(t')\right]. \tag{A.4}$$

In the low downconversion regime, we can ignore the time ordering of the electric field operators [14, 15] and directly evaluate the time integration. This yields a delta-function $2\pi\delta(\omega_{\mathrm{s}} + \omega_{\mathrm{i}} - \omega_{\mathrm{p}})$ and hence allows us to perform the integral over the pump frequency ω_{p}. Equation (A.4) can be re-expressed as

$$\hat{U} = \exp\left[-\frac{\imath}{\hbar}\left(A' \int_{-L/2}^{L/2} \mathrm{d}z \int \mathrm{d}\omega_{\mathrm{s}} \int \mathrm{d}\omega_{\mathrm{i}}\, \alpha(\omega_{\mathrm{s}} + \omega_{\mathrm{i}}) \exp[\imath\, \Delta k z]\, \hat{a}_{\mathrm{s}}^{\dagger}(\omega_{\mathrm{s}})\hat{a}_{\mathrm{i}}^{\dagger}(\omega_{\mathrm{i}}) + \mathrm{h.c.}\right)\right], \tag{A.5}$$

in which $\Delta k = k_{\mathrm{p}}(\omega_{\mathrm{s}} + \omega_{\mathrm{i}}) - k_{\mathrm{s}}(\omega_{\mathrm{s}}) - k_{\mathrm{i}}(\omega_{\mathrm{i}})$ is the so-called phase mismatch and A' accumulates all constants. Finally, we perform the integration over the length of the crystal and obtain

$$\hat{U} = \exp\left[-\frac{\imath}{\hbar}\left(A \int \mathrm{d}\omega_{\mathrm{s}} \int \mathrm{d}\omega_{\mathrm{i}}\, \alpha(\omega_{\mathrm{s}} + \omega_{\mathrm{i}})\phi(\omega_{\mathrm{s}}, \omega_{\mathrm{i}})\hat{a}_{\mathrm{s}}^{\dagger}(\omega_{\mathrm{s}})\hat{a}_{\mathrm{i}}^{\dagger}(\omega_{\mathrm{i}}) + \mathrm{h.c.}\right)\right], \tag{A.6}$$

where $\phi(\omega_{\mathrm{s}}, \omega_{\mathrm{i}}) = \mathrm{sinc}\left(\frac{\Delta k L}{2}\right)$ is referred to as the phase-matching function. The latter combined with the pump distribution $\alpha(\omega_{\mathrm{s}} + \omega_{\mathrm{i}})$ gives the overall frequency distribution or joint spectral amplitude $f(\omega_{\mathrm{s}}, \omega_{\mathrm{i}})$ of the generated state. The final unitary squeezing operator of the downconversion process is

$$\hat{U} = \exp\left[-\frac{\imath}{\hbar}\underbrace{\left(A \int \mathrm{d}\omega_{\mathrm{s}} \int \mathrm{d}\omega_{\mathrm{i}}\, f(\omega_{\mathrm{s}}, \omega_{\mathrm{i}})\hat{a}_{\mathrm{s}}^{\dagger}(\omega_{\mathrm{s}})\hat{a}_{\mathrm{i}}^{\dagger}(\omega_{\mathrm{i}}) + \mathrm{h.c.}\right)}_{\hat{H}_{\mathrm{eff}}}\right]. \tag{A.7}$$

The sinc function appearing in equation (A.7) can be approximated by a Gaussian distribution

$$\phi(\omega_s, \omega_i) = \mathrm{sinc}\left(\frac{\Delta k(\omega_s, \omega_i)L}{2}\right) \approx \exp\left[-0.193\left(\frac{\Delta k(\omega_s, \omega_i)L}{2}\right)^2\right]. \quad \text{(A.8)}$$

With this simplification the joint frequency distribution $f(\omega_s, \omega_i)$ takes on the form of a 2D Gaussian distribution. Applying this approximation the exact squeezer distribution is accessible as presented in section 4.

A.2. Generation of multimode twin-beam squeezers via four-wave mixing (FWM)

In an FWM process, two strong pump fields interact with the $\chi^{(3)}$-nonlinearity of a fiber to create two new electric fields. If the two generated fields are distinguishable, the Hamiltonian of the process is given by the equation [43]

$$\hat{H}_{\mathrm{FWM}} = \int_{-L/2}^{L/2} \mathrm{d}z\, \chi^{(3)} \hat{E}_{\mathrm{p1}}^{(+)}(z,t)\hat{E}_{\mathrm{p2}}^{(+)}(z,t)\hat{E}_{\mathrm{s}}^{(-)}(z,t)\hat{E}_{\mathrm{i}}^{(-)}(z,t) + \mathrm{h.c.} \quad \text{(A.9)}$$

Again, we assume a collinear interaction of all interacting beams. The electric fields for the signal, the idler and the pump are defined in equations (A.2) and (A.3). Performing the same steps as in appendix A.1, we obtain a similar unitary transformation

$$\hat{U} = \exp\left[-\frac{\imath}{\hbar}\underbrace{\left(A\int \mathrm{d}\omega_s \int \mathrm{d}\omega_i\, f_{\mathrm{FWM}}(\omega_s, \omega_i)\hat{a}_s^\dagger(\omega_s)\hat{a}_i^\dagger(\omega_i) + \mathrm{h.c.}\right)}_{\hat{H}_{\mathrm{eff}}}\right]. \quad \text{(A.10)}$$

Equation (A.10) resembles equation (A.7) with the exception of the joint frequency distribution $f_{\mathrm{FWM}}(\omega_s, \omega_i)$, which takes on a more complicated shape in comparison to the PDC case

$$f_{\mathrm{FWM}}(\omega_s, \omega_i) = \int \mathrm{d}\omega_p\, \alpha(\omega_p)\alpha(\omega_s + \omega_i - \omega_p)\,\mathrm{sinc}\left(\frac{\Delta k(\omega_p, \omega_s, \omega_i)L}{2}\right). \quad \text{(A.11)}$$

On a comparison of the unitary transformation in equations (A.6) and (A.10), it is apparent that the two different processes both create the same fundamental quantum state: multimode twin-beam squeezers.

Appendix B. Multimode single-beam squeezers

In the main body of the paper, we discussed the characterization of multimode twin-beam squeezers. Here we call attention to the fact that the broadband multimode correlation function formalism is also applicable to probing multimode single-beam squeezed states.

B.1. Generation of multimode single-beam squeezers

Single-beam squeezers are created by PDC and FWM processes similar to the twin-beam states. The difference between twin-beam and single-beam squeezer generation is that in the latter the generated beams are emitted into the same optical mode, whereas in the former two different optical modes are generated as discussed in appendix A.

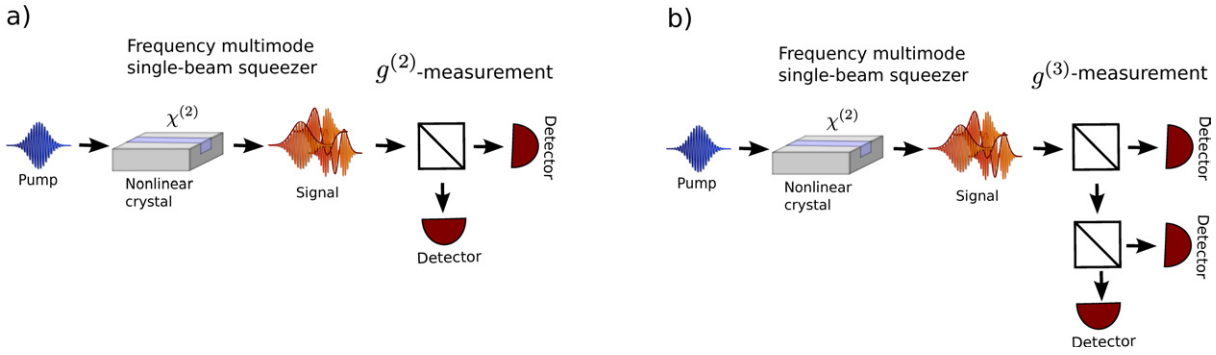

Figure B.1. Schematic setup to measure (a) $g^{(2)}$ and (b) $g^{(3)}$ of a frequency multimode single-beam squeezer.

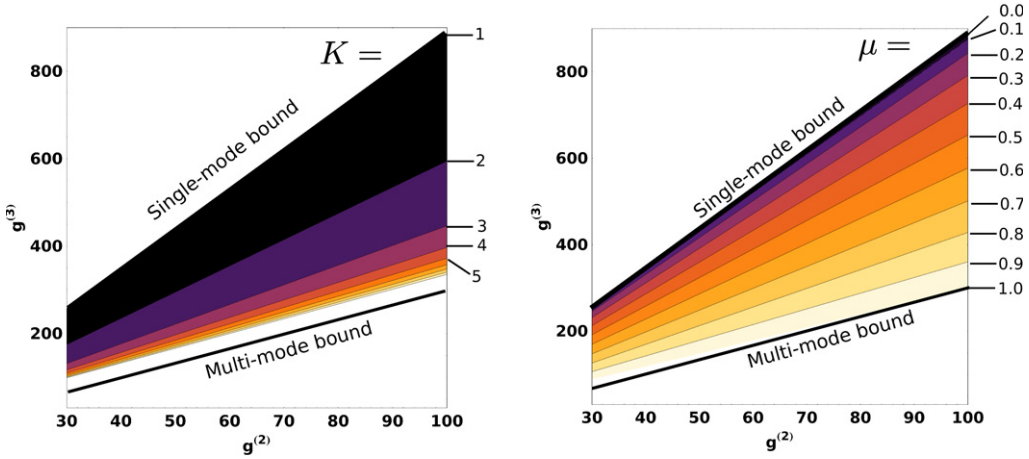

Figure B.2. $g^{(3)}$ as a function of $g^{(2)}$ for various multimode single-beam squeezers. The effective number of modes and the thermal mode distributions parameter μ of a multimode single-beam squeezer are encoded in the slope.

The PDC Hamiltonian generating a single-beam squeezer is given by

$$\hat{H} = \int_{-L/2}^{L/2} \mathrm{d}z\, \chi^{(2)} \hat{E}_{\mathrm{p}}^{(+)}(z,t)\hat{E}^{(-)}(z,t)\hat{E}^{(-)}(z,t) + \mathrm{h.c.} \tag{B.1}$$

Performing the same steps as in the case of twin-beam generation, we obtain the unitary transformation

$$\hat{U} = \exp\left[-\frac{\imath}{\hbar}\underbrace{\left(A\int \mathrm{d}\omega_{\mathrm{s}} \int \mathrm{d}\omega_{\mathrm{i}}\, f(\omega_{\mathrm{s}},\omega_{\mathrm{i}})\hat{a}^{\dagger}(\omega_{\mathrm{s}})\hat{a}^{\dagger}(\omega_{\mathrm{i}}) + \mathrm{h.c.}\right)}_{\hat{H}_{\mathrm{eff}}}\right]. \tag{B.2}$$

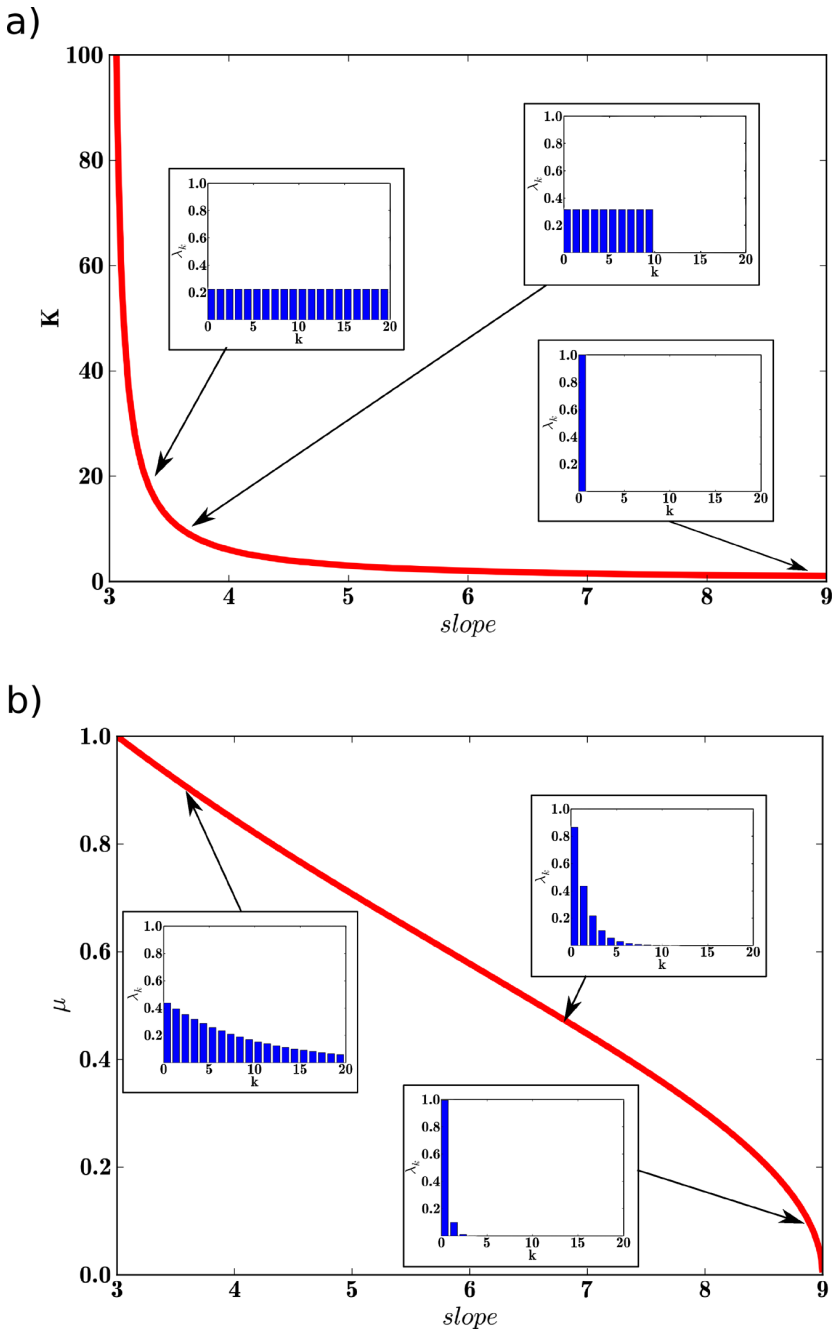

Figure B.3. (a) Effective mode number K as a function of the slope of $g^{(3)}[g^{(2)}]$. (b) Thermal mode distribution μ as a function of the slope of $g^{(3)}[g^{(2)}]$ for multimode single-beam squeezed states.

If the joint spectral distribution $f(\omega_s, \omega_i)$ is engineered to be symmetric under permutation of the signal and the idler, the Schmidt decomposition is given by

$$-\frac{\iota}{\hbar} A f(\omega_s, \omega_i) = \sum_k r_k \phi_k^*(\omega_s) \phi_k^*(\omega_i) \tag{B.3}$$

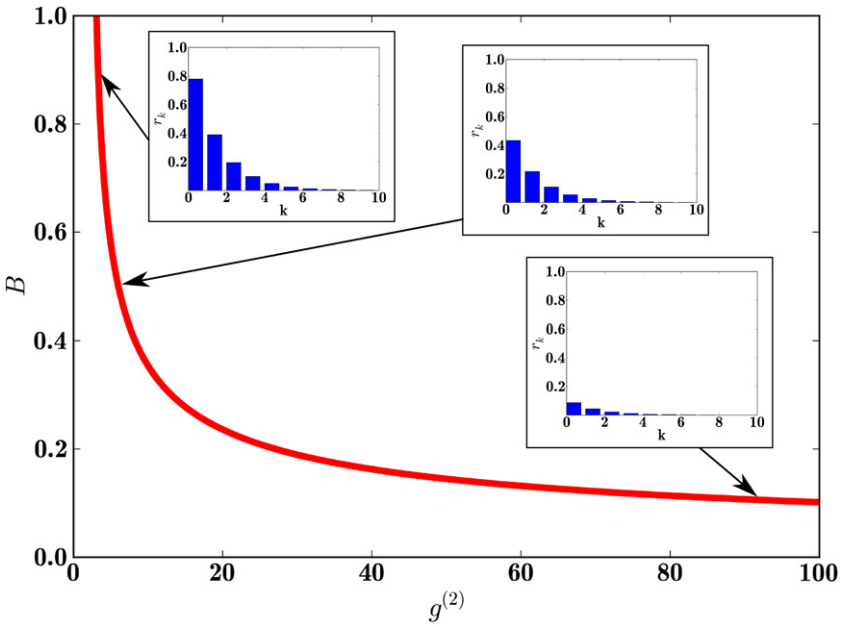

Figure B.4. Optical gain B as a function of $g^{(2)}$ for a multimode single-beam squeezed state.

and

$$-\frac{\iota}{\hbar}A^* f^*(\omega_\mathrm{s}, \omega_\mathrm{i}) = -\sum_k r_k \phi_k(\omega_\mathrm{s})\phi_k(\omega_\mathrm{i}). \tag{B.4}$$

Introducing broadband modes, we obtain the multimode broadband unitary transformation

$$\begin{aligned}\hat{U} &= \exp\left[\sum_k r_k \hat{A}_k^\dagger \hat{A}_k^\dagger - \mathrm{h.c.}\right] \\ &= \bigotimes_k \exp\left[r_k \hat{A}_k^\dagger \hat{A}_k^\dagger - \mathrm{h.c.}\right] \\ &= \bigotimes_k \hat{S}(-r_k).\end{aligned} \tag{B.5}$$

This is exactly the form of a frequency multimode single-beam squeezed state [20]. Or written in the Heisenberg picture:

$$\hat{A}_k = \cosh(r_k)\hat{A}_k + \sinh(r_k)\hat{A}_k^\dagger. \tag{B.6}$$

Single-beam squeezers are—like twin-beam squeezers—widely employed in quantum optics experiments [44, 45]. As in the twin-beam squeezer case, the same states are generated by properly engineered FWM processes.

B.2. Probing frequency multimode single-beam squeezers via correlation function measurements

To characterize the generated states, we have to determine the optical gain B and mode distribution λ_k as in the case of multimode twin-beam squeezers (see section 4). Therefore, we adapt the scheme presented in section 4 and probe the correlation functions $g^{(2)}$ and $g^{(3)}$ as sketched in figure B.1. For a multimode single-beam squeezer they can be written as

$$g^{(2)} = 1 + 2\frac{\sum_k \sinh^4(r_k)}{\left[\sum_k \sinh^2(r_k)\right]^2} + \underbrace{\frac{1}{\sum_k \sinh^2(r_k)}}_{1/\langle n\rangle} \quad \text{and} \tag{B.7}$$

$$g^{(3)} = 1 + 6\frac{\sum_k \sinh^4(r_k)}{\left[\sum_k \sinh^2(r_k)\right]^2} + 8\frac{\sum_k \sinh^6(r_k)}{\left[\sum_k \sinh^2(r_k)\right]^3} + \frac{3}{\sum_k \sinh^2(r_k)} + 6\frac{\sum_k \sinh^4(r_k)}{\left[\sum_k \sinh^2(r_k)\right]^3}. \tag{B.8}$$

In the single-beam case, however, $g^{(2)}$ does not directly yield the effective number of modes K or thermal mode distribution parameter μ as for the multimode twin-beam squeezers in equation (19). A joint measurement of $g^{(2)}$ and $g^{(3)}$ is necessary, as sketched in figure B.2. Clearly, the effective mode number K and the thermal mode distribution μ are given by the slope s of $g^{(3)}$ versus $g^{(2)}$. In figure B.3, we plotted the explicit dependence of K and μ on the slope s. Surprisingly, the functions exhibit almost the same shape as in the twin-beam squeezer case.

In order to obtain the gain of a multimode single-beam squeezer, a single $g^{(2)}$-measurement is sufficient that is sensitive to the coupling value B as presented in figure B.4 (similar to the $g^{(1,1)}$-measurement in the twin-beam squeezer case). In the low gain regime it is given via the relation $B = 1/\sqrt{g^{(2)}}$. Again, while describing a different system, the shape of the function $B[g^{(2)}]$ is very similar to the twin-beam squeezer case.

In total, the theoretical description and derivation of multimode single-beam squeezers are very similar to the mathematics behind multimode twin-beam states. These similarities translate to multimode correlation functions, which are able to probe the generated optical gain B and mode distribution λ_k as in the twin-beam case.

References

[1] Mandel L and Wolf E 1995 *Optical Coherence and Quantum Optics* (Cambridge: Cambridge University Press)

[2] Hanbury Brown R and Twiss R Q 1956 Correlation between photons in two coherent beams of light *Nature* **177** 27–9

[3] Chopra S and Mandel L 1973 Higher-order correlation properties of a laser beam *Phys. Rev. Lett.* **30** 60

[4] Blauensteiner B, Herbauts I, Bettelli S, Poppe A and Hubel H 2009 Photon bunching in parametric down-conversion with continuous-wave excitation *Phys. Rev.* A **79** 063846–6

[5] Ivanova O A, Iskhakov T Sh, Penin A N and Chekhova M V 2006 Multiphoton correlations in parametric down-conversion and their measurement in the pulsed regime *Quantum Electron.* **36** 951–6

[6] Tapster P R and Rarity J G 1998 Photon statistics of pulsed parametric light *J. Mod. Opt.* **45** 595
[7] Uren A B, Silberhorn C, Ball J L, Banaszek K and Walmsley I A 2005 Characterization of the nonclassical nature of conditionally prepared single photons *Phys. Rev.* A **72** 021802
[8] Bussires F, Slater J A, Godbout N and Tittel W 2008 Fast and simple characterization of a photon pair source *Opt. Express* **16** 17060–9
[9] Avenhaus M, Laiho K, Chekhova M V and Silberhorn C 2010 Accessing higher order correlations in quantum optical states by time multiplexing *Phys. Rev. Lett.* **104** 063602
[10] Loudon R 2000 *The Quantum Theory of Light* 3rd edn (Oxford: Oxford University Press)
[11] Shchukin E and Vogel W 2006 Universal measurement of quantum correlations of radiation *Phys. Rev. Lett.* **96** 200403
[12] Rarity J G, Tapster P R, Levenson J A, Garreau J C, Abram I, Mertz J, Debuisschert T, Heidmann A, Fabre C and Giacobino E 1992 Quantum correlated twin beams *Appl. Phys.* B **55** 250–7
[13] Mauerer W, Avenhaus M, Helwig W and Silberhorn C 2009 How colors influence numbers: photon statistics of parametric down-conversion *Phys. Rev.* A **80** 053815
[14] Wasilewski W, Lvovsky A I, Banaszek K and Radzewicz C 2006 Pulsed squeezed light: simultaneous squeezing of multiple modes *Phys. Rev.* A **73** 063819–2
[15] Lvovsky A I, Wasilewski W and Banaszek K 2007 Decomposing a pulsed optical parametric amplifier into independent squeezers *J. Mod. Opt.* **54** 721
[16] Wenger J, Tualle-Brouri R and Grangier P 2004 Pulsed homodyne measurements of femtosecond squeezed pulses generated by single-pass parametric deamplification *Opt. Lett.* **29** 1267–9
[17] Anderson M E, McAlister D F, Raymer M G and Mool Gupta C 1997 Pulsed squeezed-light generation in chi(2) nonlinear waveguides *J. Opt. Soc. Am.* B **14** 3180–90
[18] Loudon R and Knight P L 1987 Squeezed light *J. Mod. Opt.* **34** 709–59
[19] Levenson M D, Shelby R M, Aspect A, Reid M and Walls D F 1985 Generation and detection of squeezed states of light by nondegenerate four-wave mixing in an optical fiber *Phys. Rev.* A **32** 1550
[20] Barnett S M and Radmore P M 2003 *Methods in Theoretical Quantum Optics* (Oxford: Oxford University Press)
[21] Mosley P J, Christ A, Eckstein A and Silberhorn C 2009 Direct measurement of the spatial-spectral structure of waveguided parametric down-conversion *Phys. Rev. Lett.* **103** 233901
[22] Christ A, Laiho K, Eckstein A, Lauckner T, Mosley P J and Silberhorn C 2009 Spatial modes in waveguided parametric down-conversion *Phys. Rev.* A **80** 033829
[23] Law C K, Walmsley I A and Eberly J H 2000 Continuous frequency entanglement: effective finite Hilbert space and entropy control *Phys. Rev. Lett.* **84** 5304
[24] Rohde P P, Mauerer W and Silberhorn C 2007 Spectral structure and decompositions of optical states and their applications *New J. Phys.* **9** 91
[25] Beck M, Dorrer C and Walmsley I A 2001 Joint quantum measurement using unbalanced array detection *Phys. Rev. Lett.* **87** 253601
[26] Glauber R J 1963 The quantum theory of optical coherence *Phys. Rev.* **130** 2529
[27] Vogel W and Welsch D-G 2006 *Quantum Optics* 3rd edn (New York: Wiley)
[28] Braunstein S L and van Loock P 2005 Quantum information with continuous variables *Rev. Mod. Phys.* **77** 513
[29] Eberly J H 2006 Schmidt analysis of pure-state entanglement *Laser Phys.* **16** 921–6
[30] Grobe R, Rzazewski K and Eberly J H 1994 Measure of electron–electron correlation in atomic physics *J. Phys. B: At. Mol. Opt. Phys.* **27** L503
[31] Avenhaus M, Coldenstrodt-Ronge H B, Laiho K, Mauerer W, Walmsley I A and Silberhorn C 2008 Photon number statistics of multimode parametric down-conversion *Phys. Rev. Lett.* **101** 053601
[32] U'Ren A B, Banaszek K and Walmsley I A 2003 Photon engineering for quantum information processing *Quantum Inf. Comput.* **3** 480 (arXiv:quant-ph/0305192)
[33] Eckstein A, Christ A, Mosley P J and Silberhorn C 2011 Highly efficient single-pass source of pulsed single-mode twin beams of light *Phys. Rev. Lett.* **106** 013603

[34] Eisert J, Scheel S and Plenio M B 2002 Distilling Gaussian states with Gaussian operations is impossible *Phys. Rev. Lett.* **89** 137903

[35] Fiurscaronek J 2002 Gaussian transformations and distillation of entangled Gaussian states *Phys. Rev. Lett.* **89** 137904

[36] Giedke G and Cirac J I 2002 Characterization of Gaussian operations and distillation of Gaussian states *Phys. Rev.* A **66** 032316

[37] Treps N, Delaubert V, Matre A, Courty J M and Fabre C 2005 Quantum noise in multipixel image processing *Phys. Rev.* A **71** 013820

[38] Chalopin B, Scazza F, Fabre C and Treps N 2010 Multimode nonclassical light generation through the optical-parametric-oscillator threshold *Phys. Rev.* A **81** 061804

[39] Lassen M, Delaubert V, Harb C C, Lam P K, Treps N and Bachor H-A 2006 Generation of squeezing in higher order Hermite–Gaussian modes with an optical parametric amplifier *J. Eur. Opt. Soc. (Rapid Publications)* **1** 06003

[40] Laiho K, Christ A, Cassemiro K N and Silberhorn C 2010 Testing spectral filters as Gaussian quantum optical channels arXiv:1012.3123v1 [quant-ph]

[41] Braczyk A M, Ralph T C, Helwig W and Silberhorn C 2010 Optimized generation of heralded Fock states using parametric down-conversion *New J. Phys.* **12** 063001

[42] Grice W P and Walmsley I A 1997 Spectral information and distinguishability in type-II down-conversion with a broadband pump *Phys. Rev.* A **56** 1627

[43] Chen J, Lee K F and Kumar P 2007 Quantum theory of degenerate $\chi^{(3)}$ two-photon state arXiv:quant-ph/0702176

[44] Zhu C and Caves C M 1990 Photocount distributions for continuous-wave squeezed light *Phys. Rev.* A **42** 6794

[45] Sasaki M and Suzuki S 2006 Multimode theory of measurement-induced non-Gaussian operation on wideband squeezed light: analytical formula *Phys. Rev.* A **73** 043807

And now for something completely different.

(Monty Python)

10. Exponentially enhanced quantum communication rate by multiplexing CV teleportation

10.1. Introduction

As discussed in Chap. 6 PDC emits a multitude of finitely squeezed EPR states in ultrafast optical pulse modes. These multi-mode EPR-states are perfectly suited to multiplex continuous-variable (CV) quantum teleportation [130, 131], which enables a drastic increase in the corresponding quantum communication rate.[1]

10.2. Single-mode communication

The standard continuous-variable (CV) single-mode quantum teleportation protocol is depicted in Fig. 10.1. An EPR state is distributed to Alice and Bob, which use the shared entanglement in conjunction with classical communication to transmit an unknown quantum state from the sender (Alice) to the receiver (Bob).

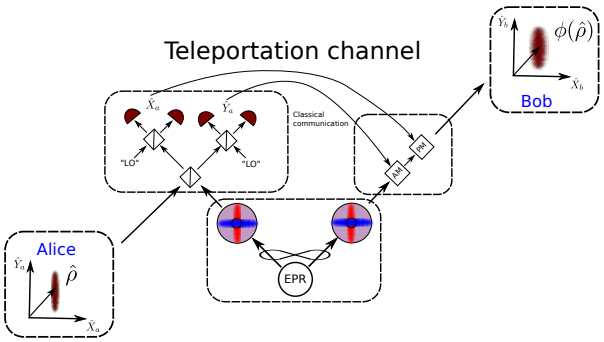

Figure 10.1.: The standard single-mode CV teleportation protocol: An EPR state in conjunction with classical communication is used to transmit an unknown quantum state from Alice to Bob.

[1] This chapter is a summary of the paper "Exponentially enhanced quantum communication rate by multiplexing continuous-variable teleportation" by Andreas Christ, Cosmo Lupo, and Christine Silberhorn [7].

This teleportation effectively creates a quantum channel between Alice and Bob. In fact continuous-variable quantum teleportation is mathematically equivalent to a thermalizing quantum channel [132]

$$\phi(\hat{\rho}) = \int dxdy f(x,y)\hat{\mathcal{D}}(x,y)\hat{\rho}\hat{\mathcal{D}}^{\dagger}(x,y), \tag{10.1}$$

where $\hat{\mathcal{D}}(x,y)$ is the displacement operator

$$\hat{\mathcal{D}}(x,y)(\hat{q}+\imath\hat{p})\hat{\mathcal{D}}^{\dagger}(x,y) = (\hat{q}-x)+\imath(\hat{p}-y), \tag{10.2}$$

which shifts the input state $\hat{\rho}$ in its quadratures $\hat{q}$ and $\hat{p}$ according to the function $f(x,y)$ given by the structure of the channel. Consequently, Bob will receive the input state from Alice plus some phase-space displacements depending on the exact form of the CV teleportation.

We are interested in the amount of quantum information which can be transmitted through the established quantum channel. In full generality the capacity of a quantum channel ϕ between Alice and Bob is given by the formula [133, 134][2]

$$Q = \max\left\{0, \lim_{\ell\to\infty}\frac{1}{\ell}\sup_{\hat{\rho}} I(\phi^{\otimes\ell},\hat{\rho})\right\}, \tag{10.3}$$

where $\phi^{\otimes\ell}$ indicates ℓ parallel uses of the quantum channel. The entropic function

$$I(\phi^{\otimes\ell},\hat{\rho}) = S[\phi^{\otimes\ell}(\hat{\rho})] - S[(\phi^{\otimes\ell}\otimes \mathrm{id}_C)(|\psi\rangle_\rho\langle\psi|)], \tag{10.4}$$

is known as the coherent information. Here, S denotes the von Neumann entropy, $S[\hat{\rho}] = -\mathrm{Tr}(\hat{\rho}\ln\hat{\rho})$ (measured in *q-nats*[3]). $|\psi\rangle_\rho$ is a purification of $\hat{\rho}$, involving an auxiliary quantum system denoted C, and id_C is the identity quantum channel acting on C.

In general, it is very hard to evaluate the quantum capacity of a given channel, since one has to optimize Eq. (10.3) over all possible input states $\hat{\rho}$ in the limit of infinite uses of the channel ϕ. An analytic formula for the quantum capacity is only known for few specimens of CV quantum channels [135]. It is however possible to evaluate upper [135] and lower bounds [136], Q_A and Q_G respectively, of the quantum channel capacity, if we restrict ourselves to the use of Gaussian resource states and a single use of the channel. For the continuous-variable teleportation protocol we obtain the upper Q_A and lower bounds Q_G:

$$Q_G = \max\{0, 2r-1\}, \tag{10.5}$$

$$Q_A = \max\{0, 2r + \ln(1-e^{-2r})\}. \tag{10.6}$$

[2]The quantum channel capacity formula works as follows: Alice starts with an entangled quantum state $\hat{\rho}$ and transmits one half through the quantum channel ϕ to Bob. The remaining entanglement optimized over all possible input states $\hat{\rho}$ in the limit of infinite uses of the channel $\phi^{\otimes l}$ gives the quantum channel capacity Q.

[3]In order to obtain compact formulas for the quantum channel capacity bounds, we use natural logarithms, $\ln = \log_e$.

10.3. Multi-mode quantum communication

Using our multi-mode PDC states we are able to multiplex the single-mode quantum communication protocol, i.e. we use our multi-mode PDC sources to simultaneously submit many EPR-states to Alice and Bob. In conjunction with multi-mode detection and displacements this enables a multiplexing of the teleportation protocol, as depicted in Fig. 10.2.

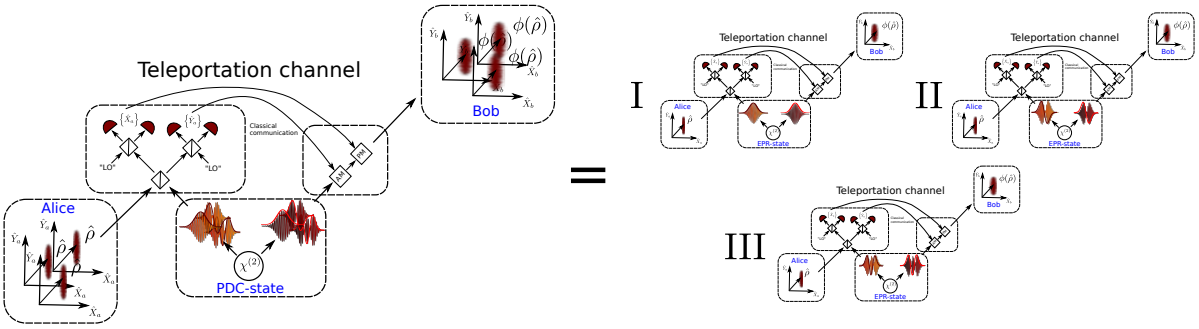

Figure 10.2.: Performing quantum teleportation using multi-mode PDC states in conjunction with multi-mode detection and displacements on Alice and Bob's side multiplexes the teleportation protocol.

Since all EPR-states are in orthogonal optical modes we are able to straightforwardly extend the upper and lower bounds obtained for single-mode quantum communication in Eq. (10.5) and Eq. (10.6) into the multi-mode domain:

$$Q_G = \sum_{k=1}^{n} \max\{0, 2r_k - 1\} \tag{10.7}$$

$$Q_A = \sum_{k=1}^{n} \max\{0, 2r_k + \ln\left(1 - e^{-2r_k}\right)\} \tag{10.8}$$

10.4. Single-mode vs. multi-mode coding

The limiting factor when performing quantum communication are firstly the losses during the quantum state distribution to Alice and Bob and secondly the amount of energy which can be transmitted between the sender (Alice) and the receiver (Bob) per use of the channel. We consequently benchmark the single vs. the multi-mode coding by comparing the upper and lower bounds of the quantum channel capacities using a fixed amount of energy or mean-photon number $\langle n_{ph} \rangle$.

A comparison between the optimal multi-mode coding and the standard single-mode coding is given in Fig. 10.3 (a) with the number of required modes K for the multi-mode coding depicted in Fig. 10.3 (b).

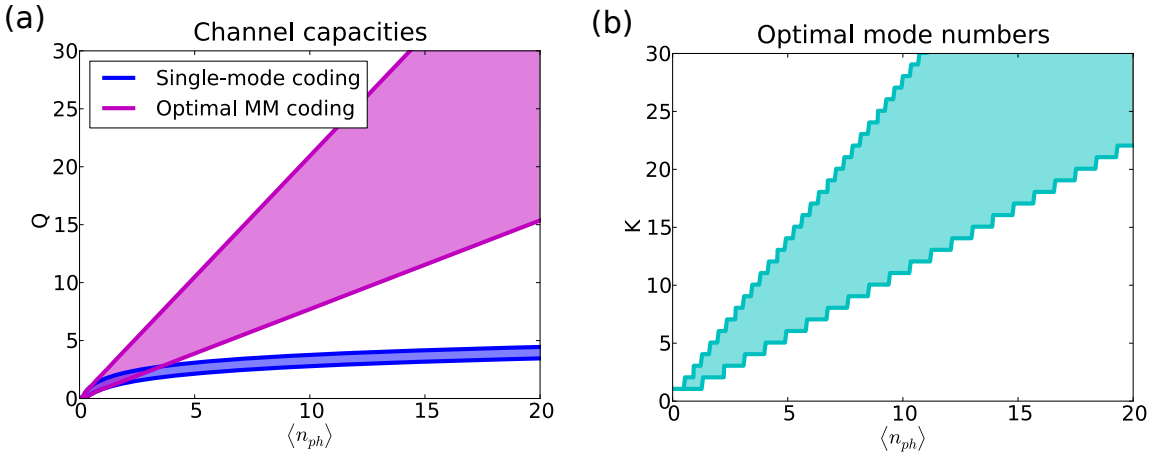

Figure 10.3.: (a) Q_A and Q_G channel capacities, measured in *q-nats*, for single-mode and optimal multi-mode coding. (b) Number of modes K required for the optimal multi-mode coding. Adapted multi-mode codes achieve quantum channel capacities outperforming single-mode approaches.

It is evident that the single-mode coding scales logarithmically with energy, whereas the multi-mode coding features a linear increase. Effectively this means that our multi-mode protocol enables *exponentially* higher quantum communication rates than the standard single-mode coding. Furthermore this exponential increase not only remains when we take into account losses during the quantum state transmission, but in fact features an enhanced loss resilience.

10.5. Conclusion

In summary we developed a multiplexed quantum communication protocol, optimally suited for ultrafast multi-mode PDC states. In comparison to the standard single-mode coding our protocol features not only an *exponentially* enhanced quantum communication rate, but also exhibits an enhanced loss resilience with respect to the standard single-mode coding.

New Journal of Physics
The open-access journal for physics

Exponentially enhanced quantum communication rate by multiplexing continuous-variable teleportation

Andreas Christ[1,4], **Cosmo Lupo**[2] **and Christine Silberhorn**[1,3]

[1] Applied Physics, University of Paderborn, Warburger Straße 100, 33098 Paderborn, Germany
[2] School of Science and Technology, University of Camerino, via Madonna delle Carceri 9, I-62032 Camerino, Italy
[3] Max Planck Institute for the Science of Light, Günther-Scharowsky Straße 1/Building 24, 91058 Erlangen, Germany
E-mail: andreas.christ@uni-paderborn.de

New Journal of Physics **14** (2012) 083007 (28pp)
Received 20 January 2012
Published 7 August 2012
Online at http://www.njp.org/
doi:10.1088/1367-2630/14/8/083007

Abstract. A major challenge of today's quantum communication systems lies in the transmission of quantum information with high rates over long distances in the presence of unavoidable losses. Thereby the achievable quantum communication rate is fundamentally limited by the amount of energy that can be transmitted per use of the channel. It is hence vital to develop quantum communication protocols that encode quantum information as energy efficiently as possible. To this aim we investigate continuous-variable quantum teleportation as a method of distributing quantum information. We explore the possibility to encode information on multiple optical modes and derive upper and lower bounds on the achievable quantum channel capacities. This analysis enables us to benchmark single-mode versus multi-mode entanglement resources. Our research reveals that multiplexing does not only feature an enhanced energy efficiency, leading to an *exponential* increase in the achievable quantum communication rates in comparison to single-mode coding, but also yields an improved loss resilience. However, as reliable quantum information transfer is only achieved for entanglement values above a certain threshold a careful optimization of the number of coding modes is needed to obtain the optimal quantum channel capacity.

[4] Author to whom any correspondence should be addressed.

Contents

1. Introduction

Quantum communication refers to the process of transferring quantum information between two parties commonly called Alice and Bob. This information transfer forms the cornerstone of many quantum information technologies, most importantly quantum cryptography [1, 2], enabling secure communication, quantum dense coding [3], boosting the data rates with respect to classical transmission and quantum networking [4]. A major challenge in all these quantum communication protocols is to achieve high rates over long distances in the presence of unavoidable losses. For this purpose, we investigate continuous-variable (CV) quantum teleportation [5, 6], as an established method of transferring an unknown quantum state between two parties, using only entanglement and classical communication, which was originally introduced in 1993 by Bennett *et al* [7] in the discrete variable regime.

In general, all quantum communication protocols are limited by the amount of energy that can be transferred between the sender (Alice) and the receiver (Bob) per use of the channel. Consequently, the challenge in quantum communication resides in encoding the information as energy efficiently as possible without sacrificing loss resilience. For this purpose, we expand the standard single-mode CV quantum teleportation protocol to incorporate multiplexing. Our research shows that by encoding the information on multiple instead of a single mode the information transfer is not only more energy efficient, leading to exponentially enhanced quantum channel capacity in comparison to the standard single-mode protocol, but it also features enhanced loss resilience.

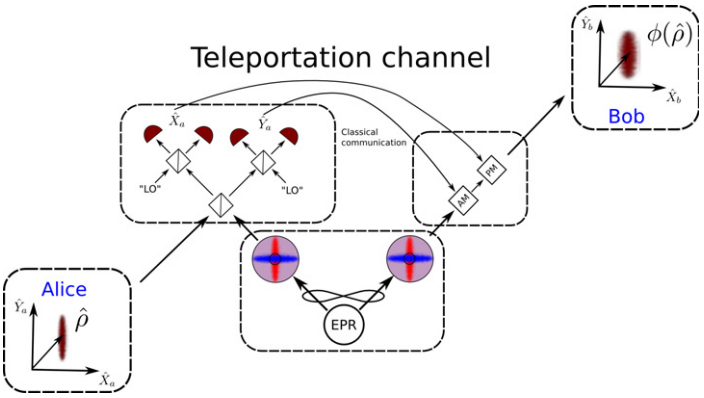

Figure 1. Sketch of the standard single-mode CV teleportation protocol. An EPR state in conjunction with classical communication is used to transmit an unknown quantum state from Alice to Bob.

Furthermore, we propose a practical setup to implement the proposed multiplexing by encoding the information on ultrafast optical pulse modes[5]. There exist a wide variety of sources capable of creating the required entangled states suitable for CV quantum teleportation, ranging from optical parametric oscillators [8–10] over four-wave mixing in optical fibers featuring a $\chi^{(3)}$ nonlinearity [11, 12] to parametric downconversion (PDC) in nonlinear $\chi^{(2)}$ crystals [13–17]. We employ—without loss of generality—an ultrafast pumped PDC source that changes a set of Einstein–Podolsky–Rosen (EPR) states into ultrafast orthogonal frequency pulse modes, that can directly be applied for multiplexed quantum teleportation.

We structured this paper into three main parts. In sections 2 and 3, we review the standard single-mode CV quantum teleportation protocol to introduce all necessary concepts and formulae. Section 4 extends the standard protocol to include multiplexing. In section 5, we compare the achievable quantum communication rates in the multiplexed regime with standard single-mode teleportation. Section 6 concludes the paper and summarizes our findings.

2. Single-mode continuous-variable (CV) quantum communication

Before we present our multiplexed quantum communication protocol we first briefly review the established single-mode CV quantum teleportation scheme and the corresponding achievable quantum communication rates in order to introduce the required concepts and formulae.

2.1. Teleportation as a quantum channel

The standard single-mode CV quantum teleportation protocol [5, 6] is illustrated in figure 1. Alice intends to teleport a (unknown) quantum state $\hat{\rho}$ from her side to Bob. To this aim,

[5] Ultrafast optical pulses are extremely short light pulses featuring durations in the femtosecond regime. Using these as carriers of quantum information enables the rapid succession of states in transmission further boosting the quantum communication rate.

Alice and Bob share a bipartite entangled state—in most cases a finitely squeezed EPR state—associated with the operators $\{\hat{a}, \hat{a}^\dagger\}$ on Alice's side, and $\{\hat{b}, \hat{b}^\dagger\}$ on Bob's side obeying canonical commutation relations $[\hat{a}, \hat{a}^\dagger] = [\hat{b}, \hat{b}^\dagger] = 1$. We denote the corresponding conjugate quadrature operators by $\hat{q}_A = (\hat{a} + \hat{a}^\dagger)/\sqrt{2}$, $\hat{p}_A = (\hat{a} - \hat{a}^\dagger)/\imath\sqrt{2}$ and $\hat{q}_B = (\hat{b} + \hat{b}^\dagger)/\sqrt{2}$, $\hat{p}_B = (\hat{b} - \hat{b}^\dagger)/\imath\sqrt{2}$ for Alice and Bob, respectively.

The CV teleportation protocol works as follows: Alice first superimposes her part of the shared bipartite state—we label it $\hat{\chi}$—with the to be teleported state $\hat{\rho}$. She then measures the resulting quantum system on her side and transmits the measurement result through classical communication to Bob. According to the data retrieved from Alice, Bob subsequently performs local operations on his part of the bipartite state $\hat{\chi}$ and obtains the teleported state $\hat{\rho}_{\text{tel}}$.

In the scope of this paper, we are not interested in the details of the apparatus; hence we regard the whole protocol as a quantum channel which enables us to send a (unknown) quantum state $\hat{\rho}$ from Alice to Bob. Then, we characterize the quantum channel defined by the teleportation protocol in terms of its quantum communication capacity. A reformulation of CV quantum teleportation as a quantum channel has been introduced by Ban *et al* [18], extending that of Bowen and Bose [19] on qubit teleportation. According to [18] the CV teleportation protocol with arbitrary resources is formally described as a generalized thermalizing channel $\phi(\hat{\rho}) = \hat{\rho}_{\text{tel}}$, in which thermal-like noise decreases the teleportation quality[6]:

$$\phi(\hat{\rho}) = \int \mathrm{d}x\, \mathrm{d}y\, f(x, y)\hat{\mathcal{D}}(x, y)\hat{\rho}\hat{\mathcal{D}}^\dagger(x, y). \tag{1}$$

Here $\hat{\mathcal{D}}(x, y)$ is the displacement operator

$$\hat{\mathcal{D}}(x, y)(\hat{q} + \imath\hat{p})\hat{\mathcal{D}}^\dagger(x, y) = (\hat{q} - x) + \imath(\hat{p} - y), \tag{2}$$

which shifts the input state $\hat{\rho}$ in its quadratures $\hat{q}$ and $\hat{p}$ according to the function $f(x, y)$ given by the structure of the channel. Consequently, Bob will receive the input state from Alice plus some extra phase-space displacements depending on the exact form of CV teleportation. The input state from Alice is distorted from its original form. The exact structure of the mapping function $f(x, y)$ is dependent on the shared bipartite state $\hat{\chi}$ and is defined as

$$f(x, y) = \mathrm{Tr}\{[\hat{\mathbb{1}} \otimes \hat{\mathcal{D}}(x, y)](|\mathrm{EPR}^*\rangle\langle\mathrm{EPR}^*|)[\hat{\mathbb{1}} \otimes \hat{\mathcal{D}}^\dagger(x, y)]\hat{\chi}\}, \tag{3}$$

where $|\mathrm{EPR}^*\rangle$ denotes the not-normalized EPR state

$$|\mathrm{EPR}^*\rangle = (2\pi)^{-1/2} \int_{-\infty}^{\infty} \mathrm{d}q\, |q\rangle_A |q\rangle_B, \tag{4}$$

and $|q\rangle_A$, $|q\rangle_B$ are the eigenstates of the quadrature operators, $\hat{q}_A|q\rangle_A = q|q\rangle_A$, $\hat{q}_B|q\rangle_B = q|q\rangle_B$.

Perfect teleportation is achieved for an infinitely squeezed EPR state $\hat{\chi} = |\mathrm{EPR}\rangle\langle\mathrm{EPR}|$, which yields $f(x, y) = \delta(x)\delta(y)$. Hence, the input state $\hat{\rho}$ from Alice is transmitted to Bob with unit fidelity, $\phi(\hat{\rho}) = \hat{\rho}$.

2.2. CV teleportation with Gaussian resources

In the remainder of this paper, we restrict ourselves to a Gaussian resource $\hat{\chi}$ shared between Alice and Bob, as is the case for the most common CV entangled state, the EPR state. The

[6] For the qubit teleportation channel, the use of non-ideal resources induces depolarization [19].

Gaussian state $\hat{\chi}$ is conveniently described in the Wigner function representation:

$$W_\chi(q_A, p_A, q_B, p_B) = \frac{1}{(2\pi)\sqrt{\det\gamma}} \exp\left[-\frac{1}{2}(\xi - m)\gamma^{-1}(\xi - m)^{\mathrm{T}}\right] = G_{(m,\gamma)}(q_A, p_A, q_B, p_B), \tag{5}$$

where ξ is defined as the vector $\xi = (q_A, p_A, q_B, p_B)$, m labels the first-order moments and γ the second-order moments or covariance matrix (CM) of the state $\hat{\chi}$, which completely characterize the Gaussian state. We have introduced short-hand notation $G_{(m,\gamma)}$ in (5), where G marks the function as Gaussian in its variables, and the subscripts m and γ inside the brackets identify the first- and second-order moments of the state.

The first step toward evaluating the output state of the teleportation channel is to derive the explicit form of the noise function $f(x, y)$ for a given Gaussian teleportation resource $\hat{\chi}$. Starting from the general form of $f(x, y)$ in (3) the function is given by the convolution integral

$$f(x, y) = \pi \int \mathrm{d}\xi\, W_{\mathrm{EPR}^*}(q_A, p_A, q_B - x, p_B - y)\, G_{(m,\gamma)}(q_A, p_A, q_B, p_B), \tag{6}$$

where $\mathrm{d}\xi = \mathrm{d}q_A\,\mathrm{d}p_A\,\mathrm{d}q_B\,\mathrm{d}p_B$ and W_{EPR^*} denotes the Wigner function of the not-normalized EPR state in (4).

To compute the convolution integral in (6), it is convenient to change to the collective quadratures (q_-, p_-, q_+, p_+), defined as

$$q_\pm := \frac{q_A \pm q_B}{\sqrt{2}}, \quad p_\pm := \frac{p_A \pm p_B}{\sqrt{2}}. \tag{7}$$

In terms of the collective variables, the Wigner function of the teleportation resource $\hat{\chi}$ now reads

$$\tilde{W}_\chi(q_-, p_-, q_+, p_+) = G_{(\tilde{m},\tilde{\gamma})}(q_-, p_-, q_+, p_+), \tag{8}$$

where $\tilde{m} = (m_{q_-}, m_{p_-}, m_{q_+}, m_{p_+}) = mR$, with

$$R = \frac{1}{\sqrt{2}}\begin{pmatrix} \mathbb{1}_2 & \mathbb{1}_2 \\ -\mathbb{1}_2 & \mathbb{1}_2 \end{pmatrix}, \tag{9}$$

$\mathbb{1}_2$ being the unit matrix of size 2, and

$$\tilde{\gamma} = R^t \gamma R = \begin{pmatrix} \tilde{\gamma}_{q_-q_-} & \tilde{\gamma}_{q_-p_-} & \tilde{\gamma}_{q_-q_+} & \tilde{\gamma}_{q_-p_+} \\ \tilde{\gamma}_{p_-q_-} & \tilde{\gamma}_{p_-p_-} & \tilde{\gamma}_{p_-q_+} & \tilde{\gamma}_{p_-p_+} \\ \tilde{\gamma}_{q_+q_-} & \tilde{\gamma}_{q_+p_-} & \tilde{\gamma}_{q_+q_+} & \tilde{\gamma}_{q_+p_+} \\ \tilde{\gamma}_{p_+q_-} & \tilde{\gamma}_{p_+p_-} & \tilde{\gamma}_{p_+q_+} & \tilde{\gamma}_{p_+p_+} \end{pmatrix}. \tag{10}$$

In terms of the collective variables, the Wigner function of the not-normalized EPR state in (4) reads

$$\tilde{W}_{\mathrm{EPR}^*}(q_-, p_-, q_+, p_+) = 2\pi\,\delta(q_-)\delta(p_+). \tag{11}$$

We arrive at the final form of the mapping function $f(x, y)$ for the shared Gaussian resources

$$\begin{aligned} f(x, y) &= \frac{1}{2}\int \mathrm{d}\xi\, \delta(q_- + x/\sqrt{2})\delta(p_+ - y/\sqrt{2}) G_{(\tilde{m},\tilde{\gamma})}(q_-, p_-, q_+, p_+) \\ &= \frac{1}{2} G_{(m_f,\gamma_f)}(x/\sqrt{2}, y/\sqrt{2}) \\ &= G_{(\sqrt{2}m_f, 2\gamma_f)}(x, y), \end{aligned} \tag{12}$$

where $m_f = (\tilde{m}_{q_-}, \tilde{m}_{p_+})$ and

$$\gamma_f = \begin{pmatrix} \tilde{\gamma}_{q_-q_-} & \tilde{\gamma}_{q_-p_+} \\ \tilde{\gamma}_{p_+q_-} & \tilde{\gamma}_{p_+p_+} \end{pmatrix}. \tag{13}$$

This gives us a convenient closed formula for $f(x, y)$ defined by the first moments m and CM γ of the shared resource $\hat{\chi}$ between Alice and Bob. In particular, given a Gaussian state $\hat{\rho}$ on Alice's side with the Wigner function

$$W_\rho(q, p) = G_{(m_\rho, \gamma_\rho)}(q, p), \tag{14}$$

the teleported state $\phi(\hat{\rho})$ arriving at Bob's side evaluates to

$$\begin{aligned} W_{\phi(\rho)}(q, p) &= \int \mathrm{d}x\, \mathrm{d}y\, f(x, y)\, G_{(m_\rho, \gamma_\rho)}(q - x, p - y) \\ &= \int \mathrm{d}x\, \mathrm{d}y\, G_{(\sqrt{2}m_f, 2\gamma_f)}(x, y) G_{(m_\rho, \gamma_\rho)}(q - x, p - y) \\ &= G_{(m_\rho + \sqrt{2}m_f, \gamma_\rho + 2\gamma_f)}(q, p). \end{aligned} \tag{15}$$

Equation (15) fully determines the CV teleportation process in the Gaussian framework (i.e. teleportation of Gaussian states using Gaussian resources). The transformation of the Gaussian input state through the teleportation channel can be calculated by adding the first moments and the CM matrix of the channel to the first moments and CM of the initial state. In the limiting case of a perfect teleportation both $\sqrt{2}m_f$ and $2\gamma_f$ are zero and the initial state is retrieved.

2.3. Information theoretical characterization of CV quantum teleportation

There exist different figures of merit to quantify the accuracy of CV teleportation. Among others there is the fidelity of quantum teleportation, detailing how closely the state arriving at Bob's side resembles the original state from Alice. Another example is the classical communication capacity, given the amount of classical information that can be pushed through the teleportation channel. In general, the choice of a figure of merit is motivated by its operational meaning.

In the scope of this paper, we characterize the teleportation channel in terms of its quantum capacity [20, 21], this means the highest rate at which quantum information can be reliably transmitted through the channel when Alice and Bob make use of error correction to convey quantum information through the noisy channel. This choice seems to be the most natural and appropriate, if quantum teleportation should be used to establish a true quantum link.

For comparison purposes, we consider the *two-way distillable entanglement* as another figure of merit in appendix B. In this scenario, Alice and Bob also exchange classical information in a two-way fashion to extract maximally entangled states. In the main part of the paper, however, we will not allow two-way classical communication between Alice and Bob, because this approach delivers tighter bounds on the properties of the required resources.

Indeed, the thermal-like noise added by non-ideal teleportation can be counteracted by employing quantum error correction codes. These can increase the quality of the communication (e.g. in terms of the fidelity) at the cost of reducing the communication rate. The highest rate of reliable quantum communication, i.e. allowing asymptotically unit fidelity, is by definition the

quantum capacity of the teleportation channel. The quantum capacity of Gaussian channels has been widely studied and characterized from an information theoretical perspective [22, 23]. In full generality, the quantum capacity of a quantum channel ϕ is given by the following expression [20, 21]:

$$Q = \max\left\{0, \lim_{\ell\to\infty}\frac{1}{\ell}\sup_{\hat{\rho}} I(\phi^{\otimes\ell}, \hat{\rho})\right\}, \tag{16}$$

where $\phi^{\otimes\ell}$ indicates ℓ parallel uses of the quantum channel. The entropic function

$$I(\phi^{\otimes\ell}, \hat{\rho}) = S[\phi^{\otimes\ell}(\hat{\rho})] - S[(\phi^{\otimes\ell}\otimes \mathrm{id}_C)(|\psi\rangle_\rho\langle\psi|)], \tag{17}$$

is known as coherent information. Here, S denotes von Neumann entropy, $S[\hat{\rho}] = -\mathrm{Tr}(\hat{\rho}\ln\hat{\rho})$ (measured in *q-nats*[7]). $|\psi\rangle_\rho$ is a purification of $\hat{\rho}$, involving an auxiliary quantum system denoted C, and id_C is the identity quantum channel acting on C. In general, it is very hard to evaluate the quantum capacity of a given channel, because one has to optimize (17) over all possible input states $\hat{\rho}$ in the limit of infinite uses of the channel ϕ. An analytic formula for quantum capacity is only known for a few specimens of CV quantum channels [23]. It is however possible to evaluate upper and lower bounds of quantum channel capacity.

In the following, we put

$$2\gamma_f = \begin{pmatrix} N & 0 \\ 0 & N \end{pmatrix}. \tag{18}$$

This thermal-like form for the channel CM is the relevant one in several cases, as for the finitely squeezed EPR states with and without losses, where the parameter N contains the entanglement properties of the resource state.

2.3.1. Lower bound. A lower bound on the quantum capacity can be obtained by restricting ourselves in (17) to maximizing over Gaussian states $\hat{\rho}_{\mathrm{G}}$, and by considering only a 'single use' of the channel, i.e.

$$Q \geqslant \max\left\{0, \sup_{\hat{\rho}_{\mathrm{G}}} I(\phi, \hat{\rho}_{\mathrm{G}})\right\} =: Q_{\mathrm{G}}. \tag{19}$$

Clearly, a lower bound on quantum capacity still provides an achievable rate of reliable communication[8]. This lower bound can be computed efficiently for Gaussian channels [22]. For the teleportation channel, it is a function of the noise CM in (13). For a thermal-like noise with CM (18), such a quantity was computed in [22], yielding:

$$Q_{\mathrm{G}} = \max\{0, -1 - \ln N\}. \tag{20}$$

The derivation of (20) is presented in appendix A.

[7] In order to obtain compact formulae for quantum channel capacity bounds, we use natural logarithms, $\ln = \log_e$.

[8] For the case of Gaussian channel, a natural conjecture is that Gaussian states saturate the maximization in (16). However, it is in principle possible that the coherent information has a global maximum on non-Gaussian states. Moreover, as the coherent information might be super-additive for parallel channels, the regularized limit over n is in general necessary for computing the quantum capacity [24].

2.3.2. Upper bound. An upper bound on the quantum capacity can be calculated by noting that the thermal-like noise with CM (18), for $N \leqslant 1$, can be simulated by the action of a linear amplifier with amplification factors $1/\eta$, followed by a linear attenuating channel with attenuating factor η. In fact, the composition of these channels transforms the input CM γ_ρ to

$$\gamma_\rho + \begin{pmatrix} 1-\eta & 0 \\ 0 & 1-\eta \end{pmatrix}, \tag{21}$$

which coincides with the thermal-like channel by setting $\eta = 1 - N$. Due to the fact that the composition of channels cannot increase the quantum capacity, the capacity of the thermal-like channel is upper bounded by that of the attenuating channel.

Using the results of [23], we can write

$$Q \leqslant \max\{0, \ln(1-N) - \ln N\} =: Q_A. \tag{22}$$

3. Single-mode quantum channel capacity analysis

With formulae (20) and (22), we are now able to evaluate bounds on the available quantum channel capacities of the standard one-mode quantum teleportation protocol.

At first, we assume that the shared bipartite entangled state is a finitely squeezed EPR state,

$$|\psi\rangle_{\mathrm{PDC}} = \exp[r(\hat{a}^\dagger \hat{b}^\dagger - \hat{a}\hat{b})]|0\rangle, \tag{23}$$

where the parameter r describes the generated squeezing amplitude (we assume without loss of generality $r \geqslant 0$), which can be transformed into the squeezing value by the relation: squeezing $[\mathrm{d}B] = -10\log_{10}(\mathrm{e}^{-2r})$. Secondly, we study the effect of losses in the quantum capacity of the teleportation channel by assuming that the modes $\{\hat{a}, \hat{a}^\dagger\}$, $\{\hat{b}, \hat{b}^\dagger\}$ are attenuated by a factor η.

3.1. Quantum channel capacity without losses

If we neglect losses, which can occur during the EPR state distribution to Alice and Bob, the parameter in CM (18) reads $N = \mathrm{e}^{-2r}$, where r labels the squeezing amplitudes of the shared EPR state. The bounds on the quantum channel capacities in (20) and (22) evaluate to the expressions:

$$Q_{\mathrm{G}} = \max\{0, 2r - 1\}, \tag{24}$$

$$Q_A = \max\{0, 2r + \ln(1 - \mathrm{e}^{-2r})\}. \tag{25}$$

The limiting factor in the CV teleportation protocol is that EPR sources are constrained by the maximum amount of entanglement, and hence energy, that they are able to emit. For the case of PDC processes, this is equivalent to the overall optical gain of the down-conversion process. Furthermore, the channels used to transmit the EPR states to Alice and Bob are constrained by the amount of energy that they can carry. For example, in the case of the ubiquitous optical fibers, the most prevalent method for quantum state distribution, transmitted pulses exceeding a certain power level undergo nonlinear optical processes in the fiber and subsequently lose part of their entanglement.

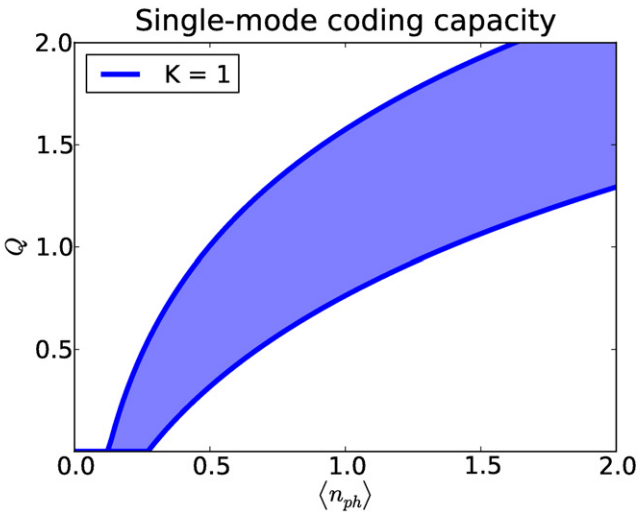

Figure 2. Upper Q_A and lower Q_{G} bounds for the quantum channel capacity (measured in *q-nats*) of CV quantum teleportation using a single-mode EPR state. The minimum squeezing required in order to reliably transmit quantum information resides between 3.01 and 4.34 dB. ($K = 1$: a single EPR state is transmitted.)

It is hence vital to develop quantum communication protocols that encode quantum information as energy efficiently as possible. For this purpose, we benchmark quantum communication by evaluating the quantum channel capacity as a function of the energy, i.e. mean-photon number $\langle n_{\mathrm{ph}} \rangle$ inside the channel. In the case of an EPR state this mean photon number is given as

$$\langle n_{\mathrm{ph}} \rangle = \sinh^2(r). \tag{26}$$

Figure 2 displays the calculated upper and lower bounds Q_A and Q_{G}, as defined in (24) and (25), as a function of the mean photon number $\langle n_{\mathrm{ph}} \rangle$ inside the channel.

This figure shows the minimum requirements for an EPR state to enable reliable quantum information transfer of the teleportation channel. The upper bound Q_A remains zero up to mean photon numbers $\langle n_{\mathrm{ph}} \rangle = 0.125$ corresponding to squeezing values of 3.01 dB, whereas the lower bound Q_{G} is zero up to $\langle n_{\mathrm{ph}} \rangle \approx 0.27$ equivalent to 4.34 dB of squeezing. Hence, the minimum squeezing in EPR state allowing reliable quantum information transfer resides in the range between 3.01 and 4.34 dB. The situation changes if additional resources—like unbounded two-way classical communication—are allowed (see discussion in appendix B).

3.2. Quantum channel capacity including losses

Analyzing quantum teleportation in the framework of realistic applications, for example, the ubiquitous quantum state $\hat{\chi}$ distribution through optical fibers, the impact of losses has to be considered. We model these losses by the standard beam splitter interactions, $\hat{a} \to \sqrt{\eta}\,\hat{a} + \sqrt{1-\eta}\,\hat{v}_a$, $\hat{b} \to \sqrt{\eta}\,\hat{b} + \sqrt{1-\eta}\,\hat{v}_b$ during the distribution of the state to Alice and Bob, as displayed in figure 3, and evaluate the robustness of state distribution as a function of the

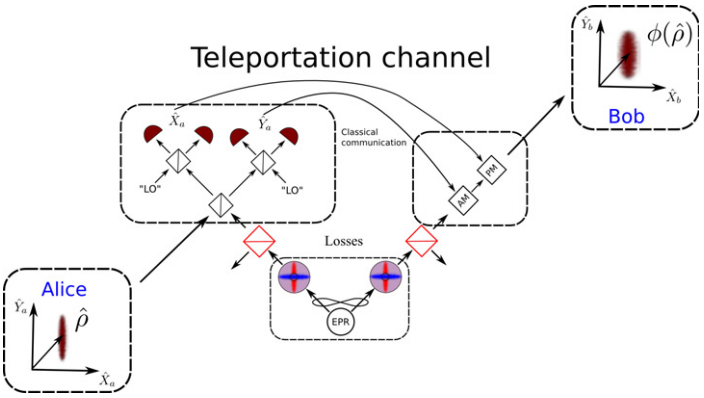

Figure 3. CV teleportation setup including standard beam splitter like losses during the distribution of the EPR state to Alice and Bob.

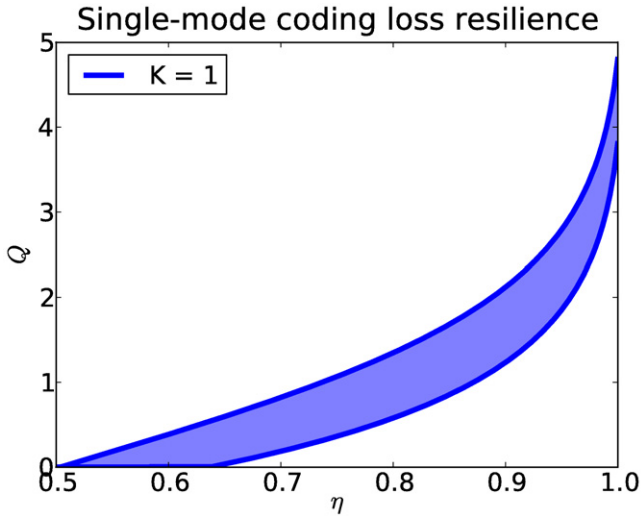

Figure 4. Upper Q_A and lower Q_{G} bounds for the quantum channel capacity (measured in *q-nats*) as a function of the transmissivity η for CV quantum teleportation using a single-mode EPR state including loss. The quantum channel capacity quickly degrades under loss until it reaches zero at loss rates exceeding 50%. ($K = 1$: a single EPR state is transmitted.)

transmissivity of channel η. With these conditions $N = \eta\,\mathrm{e}^{-2r} + (1-\eta)$, the channel capacity formulae evaluate to:

$$Q_{\mathrm{G}} = \max\{0, -1 - \ln[1 - \eta(1 - \mathrm{e}^{-2r})]\}, \tag{27}$$

$$Q_A = \max\{0, \ln[\eta(1 - \mathrm{e}^{-2r})] - \ln[1 - \eta(1 - \mathrm{e}^{-2r})]\}. \tag{28}$$

Figure 4 depicts the quantum channel capacity as a function of the transmissivity η for an EPR state with a mean photon number of $\langle n_{\mathrm{ph}}\rangle = 30$.

Starting from a quantum channel capacity between 4 and 5 *q-nats*, it quickly degrades for decreasing transmissivities η until it reaches 0 at loss rates exceeding 50%.

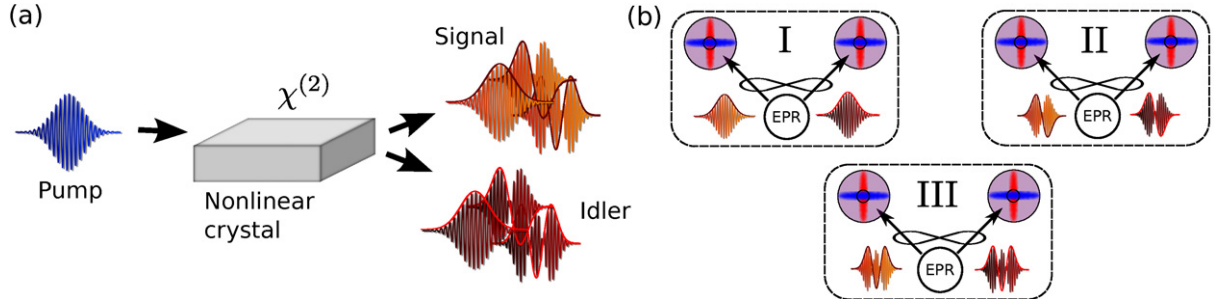

Figure 5. (a) Schematic PDC process: an incoming ultrafast pump pulse is down converted into two squeezed and entangled signal and idler waves. (b) The generated PDC state incorporates a multitude of EPR states in orthogonal ultrafast pulse modes.

4. Multi-mode Einstein–Podolsky–Rosen state generation and teleportation

Having reviewed and established CV teleportation and the corresponding quantum communication rates in the single-mode regime we now expand the protocol to incorporate multiplexing.

As discussed in the introduction there exist a variety of sources to create multi-mode EPR states. In the scope of this paper, we will focus on the properties of PDC as a source of pulsed multi-mode EPR states in ultrafast frequency modes [25, 26]. Yet our findings could also be adapted to other methods of squeezer generation as well.

Figure 5(a) sketches the state generation process. An incoming ultrafast pump pulse decays inside a medium with $\chi^{(2)}$-nonlinearity into two beams usually labeled signal and idler, which represent the two modes of the generated finitely squeezed EPR state. These states are well suited for quantum teleportation as they enable high repetition rates due to the ultrafast nature of the created pulses.

However, this PDC process pumped by a pulsed laser system produces not only a single EPR state but, as sketched in figures 5(a) and (b), also a multitude of ultrafast finitely squeezed EPR states into broadband frequency pulse modes. Each output pulse consists of a multitude of EPR states in different orthogonal modes [27, 28], formally described as

$$|\psi\rangle_{\mathrm{PDC}} = \bigotimes_{k=1}^{n} \exp\left[r_k\left(\hat{A}_k^{\dagger}\hat{B}_k^{\dagger} - \hat{A}_k\hat{B}_k\right)\right]|0\rangle, \tag{29}$$

where $\hat{A}_k$ and $\hat{B}_k$ label the different ultrafast pulse modes in the signal and idler arms, and the parameters $r_k \geqslant 0$ describe the generated squeezing amplitudes. A detailed derivation of (29) is given in [25]. For common PDC sources the squeezing parameters r_k form an exponentially decaying distribution, which can be engineered from emitting a single EPR state to creating a whole array of twin-beam squeezed states (see [29]).

The standard protocol for single-mode CV teleportation [6] requires CV Bell-measurements, one-way classical communication and local phase-space displacements. In order to multiplex the teleportation protocol, these operations have to be performed on several pulse modes parallel. There is a certain arbitrariness in that, because in principle different multi-mode orthogonal basis sets can be chosen for quantum information encoding by the communicating parties Alice and Bob. However, in the following we are focusing on broadband entangled states

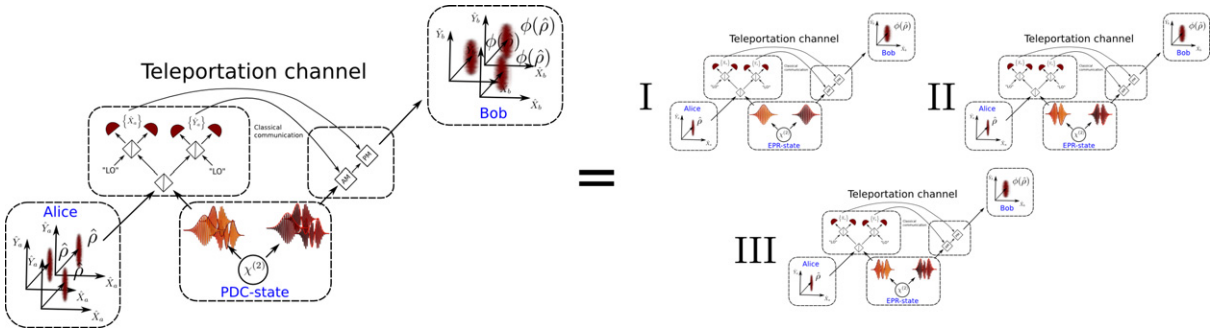

Figure 6. Performing quantum teleportation using multi-mode PDC states in conjunction with multi-mode detection and displacements on Alice and Bob's side, effectively multiplexes the teleportation protocol.

produced via PDC, for which a unique natural mode basis $\hat{A}_k$ $\hat{B}_k$ arises from the Schmidt decomposition as given in (29). In this basis each pair of modes $\hat{A}_k$ and $\hat{B}_k$ forms a finitely squeezed EPR state and we can hence treat each teleportation independently of the others. One could in principle also perform teleportation on a different basis; this however would lead to correlations between all individual modes, reduce the individual mode entanglement and consequently lower the overall quality of teleportation. It is hence natural to conjecture that the basis of the Schmidt modes optimizes teleportation capacity. A detailed discussion on this issue will be presented elsewhere [30].

These multi-mode PDC states are hence optimally suited to multiplex CV quantum teleportation as a single source is sufficient for creating many EPR states in multiple orthogonal ultrafast frequency modes. The general multiplexed protocol is depicted in figure 6. From the source a multitude of EPR states is transmitted to Alice and Bob. Alice now encodes the state she wants to teleport in the $\{\hat{A}_k\}$ modes of the source, superimposes the two beams at a beam splitter and then measures all optical modes separately. This can be implemented by either splitting the frequency modes into different spatial modes [31–34] and guiding the light to independent measurement setups or by performing multi-mode homodyne detection [35, 36]. These measurement results are then transmitted to Bob who performs the according displacements on each individual $\hat{B}_k$ mode. He then retrieves the teleported multi-mode state $\hat{\rho}_{\text{tel}}$.

The experimental implementation of multi-mode teleportation represents the main challenge for a deployment of our multi-mode coding protocol. Alice has to implement homodyne measurements in multiple orthogonal modes simultaneously on exactly the same basis as imposed by the multi-mode EPR source. Furthermore, the phase reference of the local oscillator beams has to be kept stable over all optical modes. Any errors in the measurement basis or phase mismatch between the individual modes will decrease the quantum communication rate. The same reasoning also applies to Bob who has to perform phase-locked displacements in exactly the same basis. Although experimentally challenging, this problem is already addressed by various researchers working on multi-mode homodyne detection [35, 36] and quantum pulse gates [31–34].

Eventually, this approach of expanding the EPR source and the detection apparatus to incorporate multiple modes allows us to perform multiplexed quantum teleportation. This in turn leads to several independent CV teleportation protocols being performed simultaneously.

5. Multiplexed quantum channel capacity analysis

In this section, we characterize the multiplexed CV teleportation channel in terms of its quantum capacity.

We consider two remarkable settings. Firstly, we assume that the teleportation resource is given by the multi-mode EPR state in equation (29). Secondly, we introduce a loss model in which each Schmidt mode is independently (and identically) attenuated by a standard beam splitter interaction with attenuation parameter η.

In both cases, the resulting multi-mode teleportation channel coincides with n parallel single-mode teleportations. Hence, proceeding as in sections 2.3.1 and 2.3.2 we obtain the lower bound on the multiplexed quantum channel capacity

$$Q_{\mathrm{G}} = \sum_{k=1}^{n} \max\{0, -1 - \ln N_k\}, \tag{30}$$

and the upper bound on the multiplexed quantum channel capacity

$$Q_A = \sum_{k=1}^{n} \max\{0, \ln(1 - N_k) - \ln N_k\}, \tag{31}$$

for suitable parameters $N_k \geqslant 0$.

5.1. Multi-mode teleportation

Neglecting losses during the EPR state distribution to Alice and Bob, the parameters N_k are given by $N_k = \mathrm{e}^{-2r_k}$, where r_k labels the individual squeezing amplitudes of the multi-mode squeezed state in (29). The bounds on the quantum channel capacities in (30) and (31) evaluate to the straightforward expressions:

$$Q_{\mathrm{G}} = \sum_{k=1}^{n} \max\{0, 2r_k - 1\}, \tag{32}$$

$$Q_A = \sum_{k=1}^{n} \max\{0, 2r_k + \ln(1 - \mathrm{e}^{-2r_k})\}. \tag{33}$$

The amount of energy of the multi-mode EPR state arriving at either Alice or Bob's side is related to the mean-photon number in each arm given by:

$$\langle n_{\mathrm{ph}} \rangle = \sum_{k} \sinh^2(r_k). \tag{34}$$

In analogy to the single-mode case, we analyze the teleportation channel as a function of the corresponding energy that is now expressed by the mean-photon number $\langle n_{\mathrm{ph}} \rangle$ of all the modes involved in the teleportation protocol.

In order to compare the standard single-mode teleportation with our multiplexed coding, we simulated a PDC source creating EPR states multi-mode in frequency, based on the source employed in [26]. The source is able to operate in various degrees of multi-modeness and is

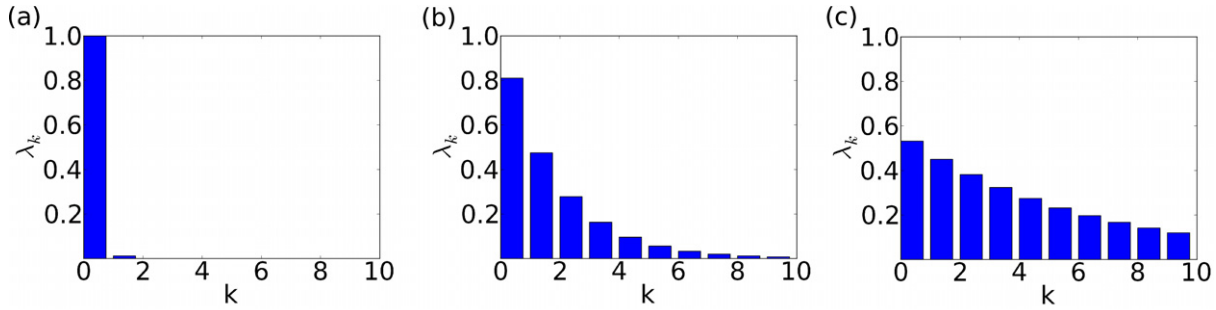

Figure 7. Three different squeezer distributions λ_k normalized via $\sum_k \lambda_k^2 = 1$ with varying degrees of multi-modeness. Depending on the source properties states ranging from a single squeezer (a) up to a whole range of EPR states in orthogonal optical modes are generated. Here k labels the number of the generated finitely squeezed EPR state and λ_k its amplitude relative to the other modes. λ_k can be converted to the actual squeezing amplitudes r_k via the overall optical gain B of the source: $r_k = B\lambda_k$.

hence perfectly suited for comparison purposes. We designed it to produce three different PDC states with varying numbers of modes as presented in figure 7, which shows the three normalized exponentially decaying mode distributions and their different weights, which we use for this analysis. These normalized mode distributions can be directly converted to the corresponding EPR state distributions, by multiplying them with the overall optical gain B of the process $r_k = B\lambda_k$ (see [26] for details on the PDC source and [25]). We first simulate a purely single-mode source (figure 7(a)), which only emits a single EPR state recreating the single-mode communication discussed in section 3 [6]. Figures 7(b) and (c) present states with rising multi-mode character, many EPR states generated in orthogonal pulse modes. Their *effective* mode numbers $K = 1/\sum_k \lambda_k^4$ [37] are $K = 1, 2$ and 6, where it should be stressed that, due to the generation process, not all modes share the same squeezing, but the entanglement follows an exponential decay toward higher-order modes.

Using (32) and (33) we derive the lower and upper quantum channel capacity bounds Q_G and Q_A for the different squeezer distributions presented in figure 7. The obtained quantities are plotted in figure 8 as a function of the mean photon number or energy inside the channel.

It is evident that multiplexed teleportation relying on several less squeezed optical modes results in significantly higher bounds on channel capacities with respect to standard single-mode coding as soon as a certain energy threshold is exceeded. While the blue shaded area, which corresponds to single-mode teleportation, with the complete energy being concentrated in a single mode, never reaches quantum channel capacities above 5 *q-nats* in the considered energy range, encoding information on multiple modes shows significantly higher quantum channel capacities[9].

The underlying reason for this behavior is the efficiency of the EPR state distribution. Following the discussion in [25] one finds that it is far more efficient, in terms of energy content, to utilize several EPR states with a low amount of squeezing than one EPR state with a high squeezing value. A similar effect is also observed in other contexts such as energy efficient

[9] As an alternative to frequency multiplexing one could also transmit multiple weakly squeezed EPR states in succession instead of one strongly squeezed EPR state. Mathematically both approaches are equivalent.

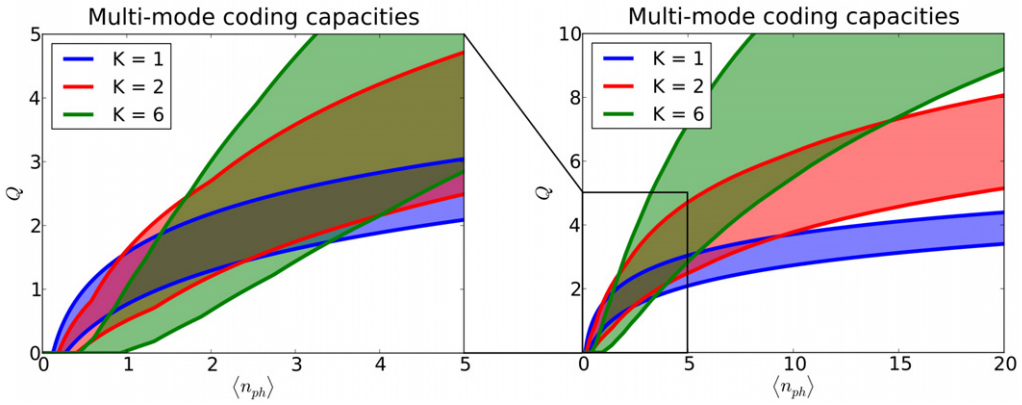

Figure 8. Quantum channel capacity bounds (in *q-nats*) for multi-mode transmission. From bottom to top $K = 1, 2, 6$. Applying multi-mode EPR states for teleportation gives a significant increase in the available quantum channel capacity as soon as a certain energy threshold is exceeded. This is due to the increased energy efficiency of multi-mode coding in conjunction with the fact that a minimum amount of squeezing has to be present in each optical mode to achieve positive quantum channel capacities (see section 3).

entanglement creation [38], quantum reading [39, 40] and entanglement distribution [41]. However, the fact that a certain energy is required to achieve a positive quantum channel capacity (see section 3) counteracts the enhanced energy efficiency of multi-mode coding and consequently there exists a trade-off between using as many optical modes as possible for enhanced energy efficiency and sufficiently few optical modes to achieve positive quantum channel capacities.

5.2. *Optimal multi-mode coding*

In order to achieve the optimal quantum channel capacity one has to carefully balance the splitting of the energy into different modes. As discussed in section 3 the upper bound Q_A will drop to zero as soon as the applied EPR state is below 3.01 dB. Hence, in order to maximize the quantum channel capacity of CV teleportation, one has to distribute the energy over as many EPR states as possible while the created EPR states still bear sufficiently high squeezing values.

We analyzed the optimal number of modes for multiplexing that achieves maximal quantum channel capacities for a given amount of energy (mean photon number $\langle n_{\mathrm{ph}} \rangle$). Our following discussion of the encoding into the optimal number of modes is split into two parts: first we will elaborate on PDC sources that can be realized in a straightforward manner by the use of existing setups, and discuss their optimal design. Then we turn our attention to the global optimum where the necessary squeezer distributions would require further engineering of the source.

5.2.1. Common EPR sources. Given a common source of multi-mode EPR states—as presented in [26]—we optimize the capacities Q_A and Q_{G} over all possible *effective* mode

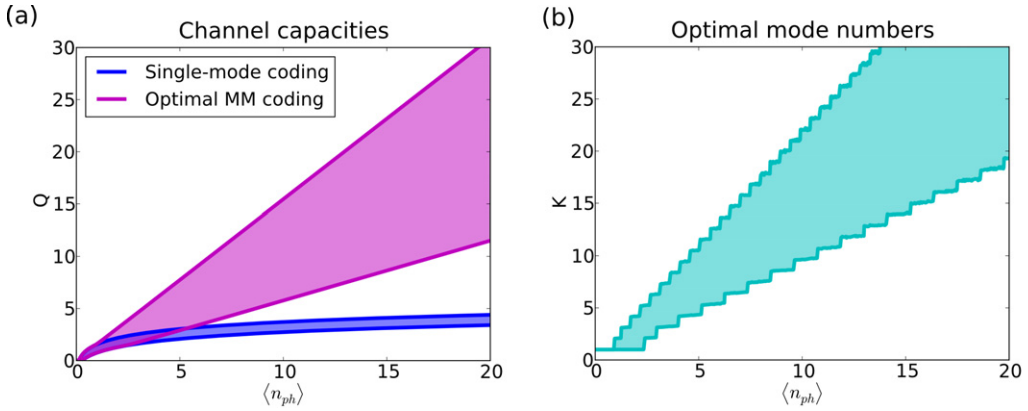

Figure 9. (a) Q_A and Q_{G} channel capacities (in *q-nats*) for single-mode and optimal multi-mode coding given a *common* EPR source. (b) Effective mode number K required for optimal multi-mode coding. Adapted multi-mode codes achieve quantum channel capacities outperforming single-mode approaches.

numbers K for each mean photon number $\langle n_{\mathrm{ph}} \rangle$ under the restriction of a mode distribution r_k given by the formula [29]:

$$r_k = B\sqrt{1-\mu^2}\mu^k, \quad 0 \leqslant \mu \leqslant 1. \tag{35}$$

The results are depicted in figure 9. Figure 9(a) shows the Q_A and Q_{G} bounds for the standard single-mode CV teleportation in comparison with the obtained optimized multi-mode coding. In the case of low energies both approaches yield identical rates. However, given mean-photon numbers above $\langle n_{\mathrm{ph}} \rangle \approx 0.94$ (7.47 dB) and $\langle n_{\mathrm{ph}} \rangle \approx 2.40$ (10.61 dB) for Q_A and Q_{G} respectively the optimized multi-mode coding outperforms the single-mode approach in each bound individually. Finally, the lower bound Q_{G} of the optimized multi-mode encoding surpasses the upper bound Q_A of single-mode coding at $\langle n_{\mathrm{ph}} \rangle \approx 5.37$ (13.70 dB).

Most importantly, however, the optimal coding bounds show a linear increase in channel capacity with energy, whereas the single-mode quantum capacity bounds exhibit a logarithmic growth for high mean photon numbers. Consequently, the multi-mode coding enables an *exponential* increase of the quantum communication rate over single-mode coding in the presence of energy constraints. The effective mode number K corresponding to the optimal bounds in figure 9(a) is presented in figure 9(b). As the channel capacities they feature a (mostly) linear increase with energy.

5.2.2. Optimal encoding with EPR sources. The main drawback of the currently available PDC sources emitting EPR states is that they feature exponentially decaying squeezing amplitudes r_k for higher-order modes, as already depicted in figure 7. This is not the optimal encoding because a certain number of squeezers will always reside below the bound to create positive quantum channel capacities. Hence, they do not contribute to the quantum communication rate while still occupying energy.

We can negate this drawback by applying multi-mode EPR states exhibiting a *flat* distribution $r_k = r$ with a mode number K. Experimentally these states can be approximated by engineering the pump pulse and phase-matching of the PDC process. This flat distribution

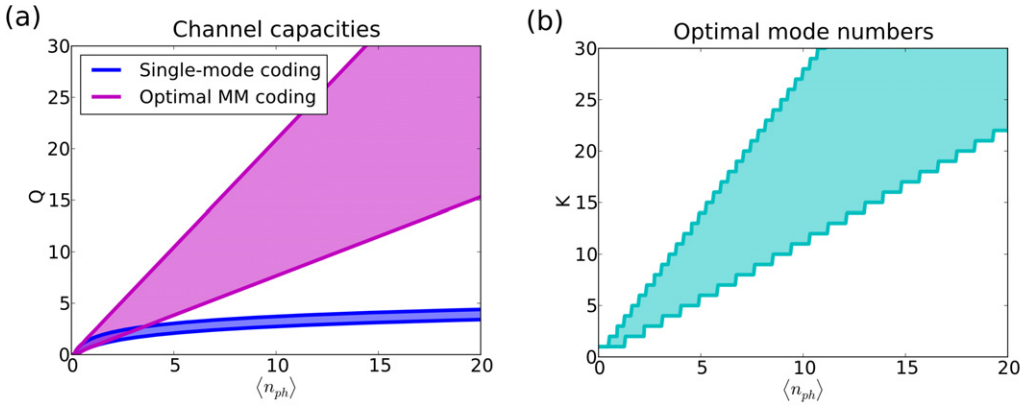

Figure 10. (a) Q_A and Q_G channel capacities, measured in *q-nats*, for single-mode and optimal multi-mode coding given a *flat* mode distribution. (b) Effective mode number K required for optimal multi-mode coding. Adapted multi-mode codes achieve quantum channel capacities outperforming single-mode approaches.

offers the great advantage that all EPR states contribute to the overall channel capacity and no energy is lost in weakly squeezed modes with zero capacity. Indeed, it can be proven to provide optimal distribution of the squeezing amplitudes, see appendix C.

In the optimal case of flat mode distributions the formulae for Q_G and Q_A, as a function of the mode number K and mean photon number $\langle n_{ph} \rangle$, evaluate to:

$$Q_G = \max\left\{0,\, K\left[2\,\mathrm{arcsinh}\left(\sqrt{\frac{\langle n_{ph}\rangle}{K}}\right) - 1\right]\right\}, \tag{36}$$

$$Q_A = \max\left\{0,\, K\left[2\,\mathrm{arcsinh}\left(\sqrt{\frac{\langle n_{ph}\rangle}{K}}\right) + \ln\left(1 - \exp\left(-2\,\mathrm{arcsinh}\left(\sqrt{\frac{\langle n_{ph}\rangle}{K}}\right)\right)\right)\right]\right\}. \tag{37}$$

We analyze the achievable channel capacities in this optimized configuration by maximizing over the mode number K for given energies or mean photon numbers $\langle n_{ph} \rangle$. The results are displayed in figure 10. Similar to the common EPR state distributions discussed in section 5.2.1 they feature the advantage of showing a linear gain with mean photon number $\langle n_{ph} \rangle$ instead of the logarithmic growth present in the single-mode coding case and hence an *exponential* growth in quantum communication rate. The achievable channel capacities surpass the quantum communication rates available using common EPR states as displayed in figure 9, since no energy is located in weakly squeezed EPR states that do not contribute to the overall quantum channel capacity.

Furthermore (36) enables us to directly assess the optimal number of modes K_{opt} required to encode information for optimal capacity given a certain mean photon number $\langle n_{ph} \rangle$:

$$K_{opt}(Q_G) \approx 1.1133\,\langle n_{ph}\rangle, \quad K_{opt}(Q_A) \approx 2.7523\,\langle n_{ph}\rangle. \tag{38}$$

From equation (38) we conclude that for the optimum mode number the squeezing of individual modes stays fixed between 4.96 and 7.33 dB. Consequently using energy to achieve squeezing

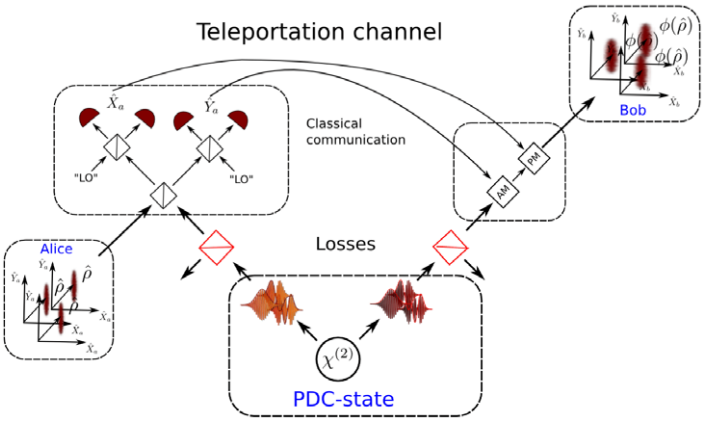

Figure 11. Frequency multi-mode teleportation setup including standard beam-splitter like losses during the distribution of the EPR states to Alice and Bob.

values above this threshold is actually detrimental for the overall quantum capacity and it is much more resourceful employing it to create EPR states in additional modes.

5.3. Multi-mode analysis under loss

We finally consider the impact of loss for multi-mode coding similar to the single-mode case discussed in section 3. For a first analysis of the robustness under losses, we assume that all the modes are attenuated by the same attenuation factor η. The more realistic setting of frequency depending attenuation will be considered elsewhere [30]. Under these conditions the channel capacity formulae evaluate to:

$$Q_{\mathrm{G}} = \sum_{k=1}^{n} \max\{0, -1 - \ln[1 - \eta(1 - \mathrm{e}^{-2r_k})]\}, \tag{39}$$

$$Q_{A} = \sum_{k=1}^{n} \max\{0, \ln[\eta(1 - \mathrm{e}^{-2r_k})] - \ln[1 - \eta(1 - \mathrm{e}^{-2r_k})]\}. \tag{40}$$

Using (39) and (40) we determine the loss resilience of the three exemplary states. We start by tuning the three test states to exhibit identical mean-photon numbers $\langle n_{\mathrm{ph}} \rangle = 30$ and study their behavior under loss. Our results are visualized in figure 12 where we plot the quantum channel capacity as a function of the transmissivity η. Clearly an enhanced loss resilience is observed for multi-mode coding with respect to the single-mode protocol, which quickly degenerates under loss. The reason for this advantage is well known: Strongly squeezed EPR states are highly susceptible to loss whereas the encoding of information on multiple weakly squeezed states is much more robust against this type of noise (see, e.g., [38]).

5.4. Optimal multi-mode coding under loss

In a similar manner to the discussion in section 5.2, we search for the optimal number of modes to encode information yet including loss during the EPR state transmission.

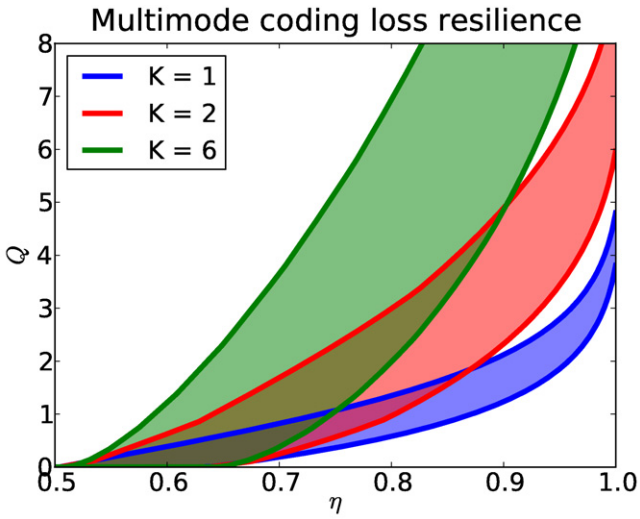

Figure 12. The loss resilience of the quantum information transmission rate visualized for multi-mode and single-mode coding. From bottom to top $K = 1, 2, 6$. Multi-mode coding offers the advantage of an increased loss resilience and gives significantly higher rates over almost the whole η range in comparison to the single-mode approach.

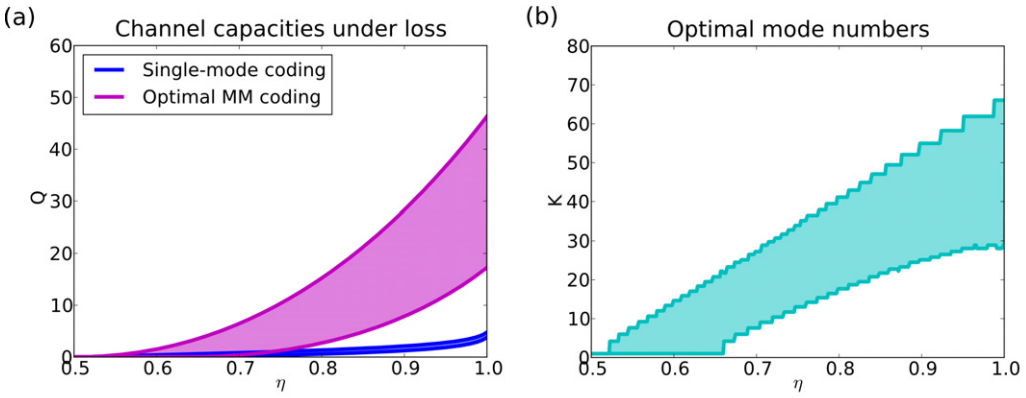

Figure 13. (a) Q_A and Q_G channel capacities (measured in *q-nats*) for single-mode and optimal multi-mode coding given a *common* mode distribution as a function of loss. (b) Effective mode number K required for optimal multi-mode coding. Adapted multi-mode codes outperform single-mode approaches in the low-loss regime.

For this purpose, we use an input state with mean photon number $\langle n_{\mathrm{ph}} \rangle = 30$ and in dependence of the transmissivity η optimize the channel capacity over all possible input mode distributions. In figure 13(a), we display the achievable rates using common squeezer distributions readily available in the lab, as already discussed in section 5.2.1. Figure 13(b) depicts the *effective* mode numbers required to achieve optimal coding. This analysis shows that in the case of losses the optimal squeezing values differ from the ones for lossless coding (see section 5.3) and the advantages of multiplexing are partially lost depending on the amount of loss in the system. In the low-loss regime the optimized multi-mode coding outperforms

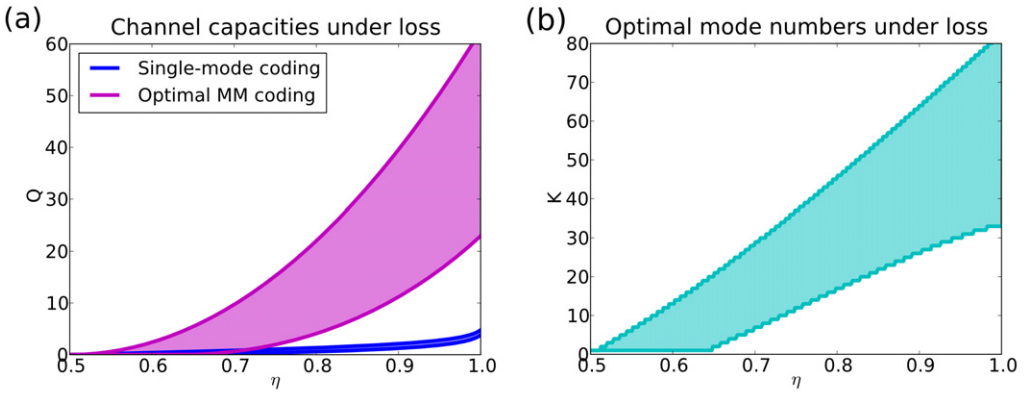

Figure 14. (a) Q_A and Q_G channel capacities (in *q-nats*) for single-mode and optimal multi-mode coding given an optimal *flat* mode distribution as a function of loss. (b) Effective mode number K required for optimal multi-mode coding. Adapted multi-mode codes outperform single-mode approaches in the low-loss regime.

the standard single-mode approach. However, in the case of high losses approaching 50%—the exact value depends on the initial energy or the mean photon number—the single-mode coding surpasses our multi-mode approach. This is to be expected for the applied CV quantum communication protocol since it is not designed for transmission under extreme loss but for low-loss applications. Its optimal operational area is the transmission of large amounts of quantum information over short distances where it excels. For quantum communication over longer distances—without repeater stations—other quantum communication protocols are more suitable.

However, these results are still not optimal. For this purpose, we investigated attainable quantum channel capacities using a flat mode distribution as discussed in section 5.2.2. The attainable rates are presented in figures 14(a) and (b). Again the optimized coding on flat mode distributions outperforms single-mode coding in the low-loss regime and achieves higher rates than the use of common squeezer distributions.

Next, we turn our attention to the quantum communication rates as a function of the energy for a constant loss rate. In figure 15(a), we plot the optimal multi-mode coding quantum channel capacities for a transmissivity of $\eta = 0.8$ for *common* squeezer distributions as a function of energy. The linear dependence of multi-mode quantum communication on energy for lossless coding (see section 5.2) remains in this setting including losses during state transmission. The single-mode coding also still features a logarithmic growth as a function of energy similar to that of the one observed for lossless state transmission. Consequently, the multi-mode protocol achieves an *exponential* increase over single-mode coding even in the presence of loss, as long as a certain minimum amount of energy is used in the communication.

This effect is even more prominent when we consider optimal *flat* multi-mode EPR state distributions, as depicted in figure 16(a). It achieves higher quantum communication rates in comparison to the multi-mode coding on *common* squeezer distribution, while still featuring linear growth as a function of energy as present in the lossless coding discussed in section 5.2.2.

However, to achieve the optimal quantum channel capacity, the squeezing values of the individual EPR states in the communication protocol have to be adapted to the losses in the

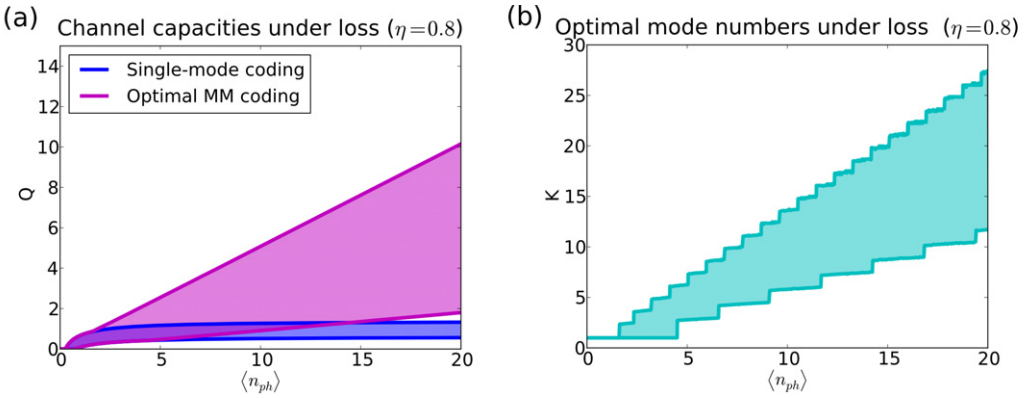

Figure 15. (a) Q_A and Q_G (measured in *q-nats*) for single-mode and optimal multi-mode coding given a *common* mode distribution as a function of energy for a constant loss rate of $\eta = 0.8$. (b) Effective mode number K required for optimal multi-mode coding. Even when considering losses multi-mode coding shows a linear increase with energy, which constitutes an exponential increase over the logarithmic growth of the single-mode protocol.

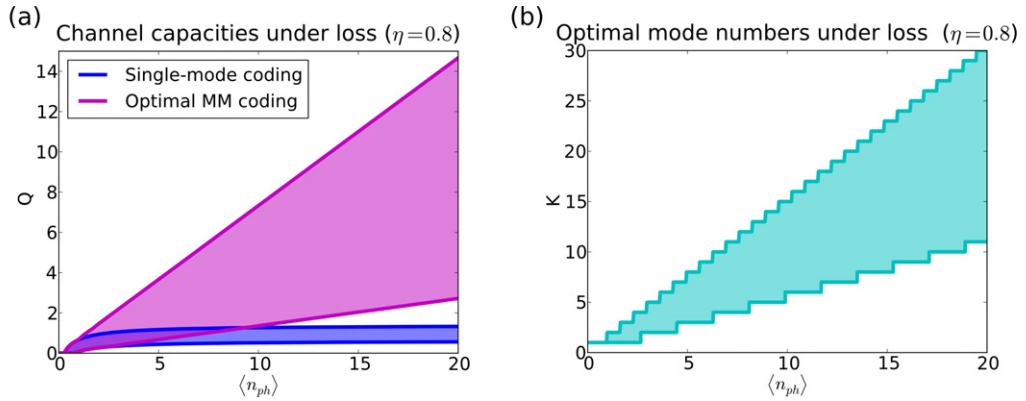

Figure 16. (a) Q_A and Q_G (measured in *q-nats*) for single-mode and optimal multi-mode coding given a *flat* mode distribution as a function of energy for a constant loss rate of $\eta = 0.8$. (b) Effective mode number K required for optimal multi-mode coding. Even when considering losses multi-mode coding shows a linear increase with energy, which constitutes an exponential increase over the logarithmic growth of the single-mode protocol.

channel. Starting from the aforementioned 4.96 dB and 7.33 dB discussed in section 5.2.2 for lossless communication, rising amounts of EPR squeezing are required for optimal coding. The exact values, as a function of the transmissivity η, are depicted in figure 17.

In summary, even in the presence of loss, multi-mode coding not only gives an *exponential* increase in the observed quantum communication rate in comparison to the single-mode coding as a function of energy, but also features enhanced loss resilience.

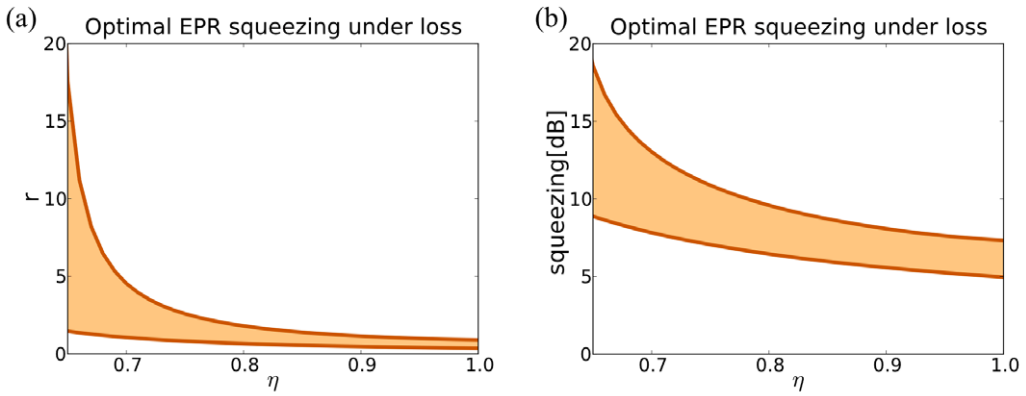

Figure 17. The optimal squeezing values, in r (a) and dB (b), for the individual EPR states in the multiplexed protocol adapted to the losses in the channel.

6. Conclusion

In conclusion, we expanded the theory of CV quantum teleportation into the multi-mode domain and presented a practical approach to implement the proposed multiplexing protocol. We calculated upper and lower bounds on the attainable quantum channel capacities by encoding information on multiple optical modes. Our analysis reveals that multiplexing not only features enhanced energy efficiency leading to an *exponential* increase in the achievable quantum communication rates in comparison to single-mode coding, but also gives improved loss resilience.

However, as reliable quantum information transfer is achieved only for squeezed modes above a certain threshold value, a careful optimization of the number of used coding modes is needed.

Our findings show that EPR states with squeezing values between 3.01 and 4.34 dB are required for having reliable quantum information transfer through the teleportation channel. Due to the energy constraints inside a quantum channel the optimum is reached when EPR states with squeezing values in the range from 4.96 up to 7.33 dB are employed. Creating squeezing above this bound is actually detrimental to the overall quantum communication rate. It is much more resourceful to invest the excess energy in creating EPR states in multiple optical modes.

Acknowledgments

The authors thank Benjamin Brecht for help with the PDC calculations. They also thank Stefano Mancini, Vittorio Giovannetti, Filippo Caruso and Stefano Pirandola, for useful comments. The research leading to these results has received funding from the European Commission's Seventh Framework Programme CORNER (FP7/2007-2013) under grant agreement no. 213681.

Appendix A. Calculation of the lower bound Q_G

For computing Q_G, we have to maximize the coherent information over the Gaussian states. In this case, we can assume without loss of generality that $|\psi\rangle_{\rho_G}$ is an EPR state with the squeezing

parameter s, shared between the subsystem A and the auxiliary subsystem C, described by the Wigner function,

$$W_{|\psi\rangle_{\rho_G}\langle\psi|}(q_A, p_A; q_C, p_C) = G_{(0,\gamma_s^{AC})}(q_A, p_A; q_C, p_C), \tag{A.1}$$

where

$$\gamma_s^{AC} = \frac{1}{2}\begin{pmatrix} \cosh 2s & 0 & \sinh 2s & 0 \\ 0 & \cosh 2s & 0 & -\sinh 2s \\ \sinh 2s & 0 & \cosh 2s & 0 \\ 0 & -\sinh 2s & 0 & \cosh 2s \end{pmatrix}. \tag{A.2}$$

The action of the channel transmitting the state of subsystem A from Alice to Bob, transforms this state to

$$W_{(\phi\otimes\mathcal{I})(|\psi\rangle_{\rho_G}\langle\psi|)}(q_B, p_B; q_C, p_C) = G_{(0,\gamma_s^{BC})}(q_B, p_B; q_C, p_C), \tag{A.3}$$

with

$$\gamma_s^{BC} = \frac{1}{2}\begin{pmatrix} 2N+\cosh 2s & 0 & \sinh 2s & 0 \\ 0 & 2N+\cosh 2s & 0 & -\sinh 2s \\ \sinh 2s & 0 & \cosh 2s & 0 \\ 0 & -\sinh 2s & 0 & \cosh 2s \end{pmatrix}. \tag{A.4}$$

which is known as the Choi–Jamiołkowski (CJ) state associated with the channel. After tracing out the C subsystem the reduced state of subsystem B takes on the form

$$W_{\phi(\rho)}(q_B, p_B) = G_{(0,\gamma_s^B)}(q_B, p_B), \tag{A.5}$$

with

$$\gamma_s^B = \frac{1}{2}\begin{pmatrix} 2N+\cosh 2s & 0 \\ 0 & 2N+\cosh 2s \end{pmatrix}. \tag{A.6}$$

In order to evaluate Q_G, we have to determine the von Neumann entropy of the two states in (A.3) and (A.5). In the case of Gaussian states this is a straightforward calculation, because the state is defined by its CM and the von Neumann entropy is determined by their symplectic eigenvalues [22, 42]. Then we have

$$S[\phi(\rho)] = g(\nu^B - 1/2), \tag{A.7}$$

where $g(w) := (w+1)\ln(w+1) - w\ln w$, and ν^B is the symplectic eigenvalue of the CM γ_s^B. The symplectic eigenvalue is calculated from the matrix $\Omega\gamma_s^B$, where $\Omega = \imath\sigma_2$ is the symplectic form, with

$$\imath\sigma_2 = \begin{pmatrix} 0 & -1 \\ 1 & 0 \end{pmatrix}. \tag{A.8}$$

In particular, the eigenvalues of $\Omega\gamma_s^B$ are $\pm\imath\nu^B$.

Similarly,

$$S[(\phi\otimes\mathcal{I})(|\psi\rangle_\rho\langle\psi|)] = g(\nu_+^{BC} - 1/2) + g(\nu_-^{BC} - 1/2), \tag{A.9}$$

where $\nu_\pm^{BC}$ are the symplectic eigenvalues of the CM γ_s^{BC}, where $\pm\imath\nu_+^{BC}$ and $\pm\imath\nu_-^{BC}$ are the eigenvalues of $(\Omega\oplus\Omega)\gamma_s^{BC}$.

The resulting coherent information is an increasing function of s:

$$\nu^B = N + \tfrac{1}{2}\cosh 2s, \tag{A.10}$$

$$\nu_{\pm}^{BC} = \tfrac{1}{2}\sqrt{1+2N^2+2N\cosh 2s \pm 2N\sqrt{1+N^2+2N\cosh 2s}}. \tag{A.11}$$

In the limit of an infinitely squeezed state ($s \to \infty$), we obtain

$$\nu^B \simeq N + \frac{1}{4}\mathrm{e}^{2s}, \tag{A.12}$$

and

$$\nu_{\pm}^{BC} \simeq \frac{\mathrm{e}^s\sqrt{N}}{2} \pm N. \tag{A.13}$$

Finally, after straightforward algebra, we obtain

$$\begin{aligned} Q_{\mathrm{G}} &= \max\left\{0, \lim_{s\to\infty} g(\nu^B - 1/2) - g(\nu_+^{BC} - 1/2) - g(\nu_-^{BC} - 1/2)\right\} \\ &= \max\{0, -1 - \ln N\}. \end{aligned} \tag{A.14}$$

Appendix B. Classical communication allowed

In the main part of the paper, we have considered a scenario in which Alice and Bob make use of error correction to convey quantum information through the noisy teleportation channel. Alternatively, if they are also allowed to exchange classical information in a two-way fashion, they can perform a protocol of entanglement purification to extract maximally entangled states up to a rate equal to the *two-way distillable entanglement* [43], denoted D_2, of the CJ state (A.3). Alice and Bob can then use the maximally entangled states to establish a perfect teleportation channel, allowing reliable quantum communication up to a rate $Q_2 = D_2$ [43]. The assistance of two-way classical communication can in general augment the quantum capacity[10], i.e. $Q_2 \geqslant Q$ [43].

We then compute the logarithmic negativity of the CJ state, denoted Q_E, which is an upper bound for D_2 [44]. To compute the logarithmic negativity, first we have to apply the operation of partial time reversal, denoted Γ, on the CJ state (A.3), which transforms the CM (A.4) to

$$\Gamma(\gamma_s^{BC}) = \frac{1}{2}\begin{pmatrix} 2N+\cosh 2s & 0 & \sinh 2s & 0 \\ 0 & 2N+\cosh 2s & 0 & \sinh 2s \\ \sinh 2s & 0 & \cosh 2s & 0 \\ 0 & \sinh 2s & 0 & \cosh 2s \end{pmatrix}.$$

Then, we compute its symplectic eigenvalues:

$$d_{\pm} = \frac{1}{2}\sqrt{2N^2+2N\cosh 2s+\cosh 4s \pm (N+\cosh 2s)\sqrt{4N^2-2+2\cosh 4s}}. \tag{B.1}$$

The logarithmic negativity of the CJ state equals $\max\{0, -\ln(2d_-)\}$. Taking the limit $s \to \infty$, after straightforward algebra, we obtain

$$Q_E = \max\{0, -\ln N\}. \tag{B.2}$$

[10] That does not hold true for one-way classical communication [43].

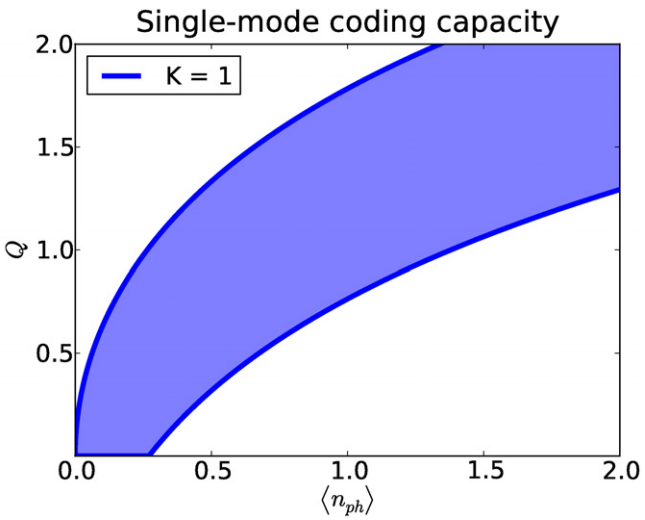

Figure B.1. Upper Q_E and lower Q_{G} bounds, in *q-nats*, for the quantum channel capacity of CV quantum teleportation using a single-mode EPR state when classical communication between Alice and Bob is allowed.

Finally, generalizing this expression to the multi-mode setting, and putting $N_k = \mathrm{e}^{-2r_k}$ we obtain

$$Q_E = 2\sum_{k=1}^{n} r_k. \tag{B.3}$$

Figure B.1 shows the bounds $Q_{\mathrm{G}} \leqslant Q_2 \leqslant Q_E$ as functions of $\langle n_{\mathrm{ph}}\rangle$. The analysis of subsections 5.1–5.3 can be repeated for the quantity Q_2 leading to similar results: the only qualitative difference relies on the fact that the upper bound Q_E is strictly non-zero for all non-vanishing values of the squeezing. In order to maximize this bound it is hence optimal to distribute the energy over as many modes as possible since there is no trade-off between the multi-mode structure and having zero quantum capacity [38].

Appendix C. Optimal squeezing distributions

Our aim is to optimize the squeezing distribution under energy constraint. Let us denote

$$Q := \sum_{k=1}^{K} q(r_k), \tag{C.1}$$

(K integer) the function to be optimized. We want to consider general distributions, including those with an infinite number of non-zero squeezers ($K \to \infty$). To fix the ideas, we consider the case of lossless teleportation (the extension to the lossy case is straightforward). Hence, the optimization of the lower and upper bounds on the lossless quantum teleportation capacity is recovered by identifying the function $q(r)$ with

$$q_{\mathrm{G}}(r) = \max\{0, 2r - 1\} \tag{C.2}$$

or

$$q_A(r) = \max\{0, 2r + \log(1 - \mathrm{e}^{-2r})\}. \tag{C.3}$$

These functions are zero if the value of r is below a certain threshold. It hence follows that it is sufficient to consider a finite number of squeezers corresponding to values of the squeezing parameters above the threshold; hence we can assume without loss of generality that $K < \infty$ in (C.1). That also allows us to substitute the functions q_{G}, q_A with

$$\tilde{q}_{\mathrm{G}}(r) := 2r - 1, \tag{C.4}$$

$$\tilde{q}_A(r) := 2r + \log\left(1 - \mathrm{e}^{-2r}\right). \tag{C.5}$$

In order to optimize the quantum capacity bounds under the constraint

$$\langle n_{\mathrm{ph}} \rangle = \sum_{k=1}^{K} \sinh^2 r_k, \tag{C.6}$$

we introduce the Lagrange function

$$F(r_1, r_2, \ldots, r_n, \lambda) = \sum_{k=1}^{K} \tilde{q}(r_k) - \lambda \sum_{k=1}^{K} \sinh^2 r_k, \tag{C.7}$$

with λ being the Lagrange multiplier, whose value is determined by $\langle n_{\mathrm{ph}} \rangle$, and $\tilde{q}$ stands for either $\tilde{q}_{\mathrm{G}}$ or $\tilde{q}_A$. Differentiating with respect to r_k, we get the Lagrange equations

$$\frac{\mathrm{d}\tilde{q}(r_k)}{\mathrm{d}r_k} = \lambda \sinh(2r_k), \tag{C.8}$$

which implies

$$\frac{1}{\sinh(2r_k)} \frac{\mathrm{d}\tilde{q}(r_k)}{\mathrm{d}r_k} = \lambda. \tag{C.9}$$

That means that the optimal distribution is that in which the function $\frac{1}{\sinh(2r_k)} \frac{\mathrm{d}\tilde{q}(r_k)}{\mathrm{d}r_k}$ is constant for all values of k. It hence follows that the flat distribution of the squeezing parameters is optimal. To check the uniqueness of the solution, we first note that

$$\frac{1}{\sinh(2r_k)} \frac{\mathrm{d}\tilde{q}(r_k)}{\mathrm{d}r_k} = \frac{\mathrm{d}\tilde{q}(r(n_k))}{\mathrm{d}n_k}, \tag{C.10}$$

where $r(n_k) = \operatorname{arcsinh}\sqrt{n_k}$. The Lagrange equations are then rewritten as follows:

$$\frac{\mathrm{d}\tilde{q}(r(n_k))}{\mathrm{d}n_k} = \lambda. \tag{C.11}$$

A sufficient condition for the uniqueness of the solution is that the function $\tilde{q}(r(n_k))$ has a given concavity as a function of n_k. The derivatives with respect to n_k,

$$\frac{\mathrm{d}\tilde{q}_{\mathrm{G}}(r(n_k))}{\mathrm{d}n_k} = \frac{1}{\sqrt{n_k(1+n_k)}}, \tag{C.12}$$

$$\frac{\mathrm{d}\tilde{q}_A(r(n_k))}{\mathrm{d}n_k} = \frac{\mathrm{e}^{2\operatorname{arcsinh}\sqrt{n_k}}}{\mathrm{e}^{2\operatorname{arcsinh}\sqrt{n_k}} - 1} \frac{1}{\sqrt{n_k(1+n_k)}}, \tag{C.13}$$

are both monotonically decreasing functions of n_k, which proves the concavity of $\tilde{q}_{\mathrm{G}}(r(n_k))$, and $\tilde{q}_A(r(n_k))$, as functions of n_k.

In conclusion, we have proven that, for any given integer K, the flat distribution is the unique optimal squeezing distribution over the modes, as long as all individual modes feature a positive quantum channel capacity. Then, the optimal mode number K can be evaluated for any given $\langle n_{\mathrm{ph}} \rangle$, yielding the expressions presented in (38).

References

[1] Bennett C and Brassard G 1984 IEEE. Quantum cryptography: public key distribution and coin tossing *Proc. IEEE Int. Conf. on Computers, Systems and Signal Processing* pp 175–9

[2] Ekert A K 1991 Quantum cryptography based on Bell's theorem *Phys. Rev. Lett.* **67** 661

[3] Bennett C H and Wiesner S J 1992 Communication via one- and two-particle operators on Einstein–Podolsky–Rosen states *Phys. Rev. Lett.* **69** 2881

[4] Kimble H J 2008 The quantum internet *Nature* **453** 1023–30

[5] Vaidman L 1994 Teleportation of quantum states *Phys. Rev.* A **49** 1473

[6] Braunstein S L and Kimble H J 1998 Teleportation of continuous quantum variables *Phys. Rev. Lett.* **80** 869

[7] Bennett C H, Brassard G, Crépeau C, Jozsa R, Peres A and Wootters W K 1993 Teleporting an unknown quantum state via dual classical and Einstein–Podolsky–Rosen channels *Phys. Rev. Lett.* **70** 1895

[8] Laurat J, Longchambon L, Fabre C and Coudreau T 2005 Experimental investigation of amplitude and phase quantum correlations in a type II optical parametric oscillator above threshold: from nondegenerate to degenerate operation *Opt. Lett.* **30** 1177–9

[9] Villar A S, Cruz L S, Cassemiro K N, Martinelli M and Nussenzveig P 2005 Generation of bright two-color continuous variable entanglement *Phys. Rev. Lett.* **95** 243603

[10] Laurat J, Keller G, Oliveira-Huguenin J A, Fabre C, Coudreau T, Serafini A, Adesso G and Illuminati F 2005 Entanglement of two-mode Gaussian states: characterization and experimental production and manipulation *J. Opt. B: Quantum Semiclass. Opt.* **7** S577–87

[11] Loudon R and Knight P L 1987 Squeezed light *J. Mod. Opt.* **34** 709–59

[12] Levenson M D, Shelby R M, Aspect A, Reid M and Walls D F 1985 Generation and detection of squeezed states of light by nondegenerate four-wave mixing in an optical fiber *Phys. Rev.* A **32** 1550

[13] Rarity J G, Tapster P R and Jakeman E 1987 Observation of sub-Poissonian light in parametric downconversion *Opt. Commun.* **62** 201–6

[14] Wasilewski W, Lvovsky A I, Banaszek K and Radzewicz C 2006 Pulsed squeezed light: simultaneous squeezing of multiple modes *Phys. Rev.* A **73** 063819

[15] Lvovsky A I, Wasilewski W and Banaszek K 2007 Decomposing a pulsed optical parametric amplifier into independent squeezers *J. Mod. Opt.* **54** 721

[16] Wenger J, Tualle-Brouri R and Grangier R 2004 Pulsed homodyne measurements of femtosecond squeezed pulses generated by single-pass parametric deamplification *Opt. Lett.* **29** 1267–9

[17] Anderson M E, McAlister D F, Raymer M G and Mool Gupta C 1997 Pulsed squeezed-light generation in χ^2 nonlinear waveguides *J. Opt. Soc. Am.* B **14** 3180

[18] Ban M, Sasaki M and Takeoka M 2002 Continuous variable teleportation as a generalized thermalizing quantum channel *J. Phys. A: Math. Gen.* **35** L401–5

[19] Bowen G and Bose S 2001 Teleportation as a depolarizing quantum channel, relative entropy, and classical capacity *Phys. Rev. Lett.* **87** 267901

[20] Devetak I 2005 The private classical capacity and quantum capacity of a quantum channel *Inf. Theory IEEE Trans.* **51** 44–55

[21] Lloyd S 1997 Capacity of the noisy quantum channel *Phys. Rev.* A **55** 1613

[22] Holevo A S and Werner R F 2001 Evaluating capacities of bosonic Gaussian channels *Phys. Rev.* A **63** 032312

[23] Wolf M M, Pérez-García D and Giedke G 2007 Quantum capacities of bosonic channels *Phys. Rev. Lett.* **98** 130501

[24] Smith G, Smolin J A and Yard J 2011 Quantum communication with Gaussian channels of zero quantum capacity *Nature Photonics* **5** 624–7

[25] Christ A, Laiho K, Eckstein A, Cassemiro K N and Silberhorn C 2011 Probing multimode squeezing with correlation functions *New J. Phys.* **13** 033027

[26] Eckstein A, Christ A, Mosley P J and Silberhorn C 2011 Highly efficient single-pass source of pulsed single-mode twin beams of light *Phys. Rev. Lett.* **106** 013603

[27] Botero A and Reznik B 2003 Modewise entanglement of Gaussian states *Phys. Rev.* A **67** 052311
[28] Giedke G, Eisert J, Cirac J I and Plenio M B 2003 Entanglement transformations of pure Gaussian states *Quantum Inf. Comput.* **3** 211–23
[29] U'Ren A B, Banaszek K and Walmsley I A 2003 Photon engineering for quantum information processing *Quantum Inf. Comput.* **3** 480–502
[30] Christ A, Lupo C and Silberhorn C 2012 unpublished
[31] Eckstein A, Brecht B and Silberhorn C 2011 A quantum pulse gate based on spectrally engineered sum frequency generation *Opt. Express* **19** 13770–8
[32] Brecht B, Eckstein A, Christ A, Suche H and Silberhorn C 2011 From quantum pulse gate to quantum pulse shaper-engineered frequency conversion in nonlinear optical waveguides *New J. Phys.* **13** 065029
[33] Raymer M G, van Enk S J, McKinstrie C J and McGuinness H J 2010 Interference of two photons of different color *Opt. Commun.* **283** 747–52
[34] McGuinness H J, Raymer M G, McKinstrie C J and Radic S 2010 Quantum frequency translation of single-photon states in a photonic crystal fiber *Phys. Rev. Lett.* **105** 093604
[35] Beck M, Dorrer C and Walmsley I A 2001 Joint quantum measurement using unbalanced array detection *Phys. Rev. Lett.* **87** 253601
[36] Armstrong S, Morizur J-F, Janousek J, Hage B, Treps N, Lam P K and Bachor H-A 2012 Programmable multimode quantum networks arXiv:1201.6024
[37] Eberly J H 2006 Schmidt analysis of pure-state entanglement *Laser Phys.* **16** 921–6
[38] van Enk S J and Hirota O 2005 Entangled states of light and their robustness against photon absorption *Phys. Rev.* A **71** 062322
[39] Pirandola S 2011 Quantum reading of a classical digital memory *Phys. Rev. Lett.* **106** 090504
[40] Pirandola S, Lupo C, Giovannetti V, Mancini S and Braunstein S L 2011 Quantum reading capacity *New J. Phys.* **13** 113012
[41] Kraus B and Cirac J I 2004 Discrete entanglement distribution with squeezed light *Phys. Rev. Lett.* **92** 013602
[42] Ferraro A, Olivares S and Paris M 2005 *Gaussian States in Quantum Information* (Naples: Bibliopolis)
[43] Bennett C H, DiVincenzo D P, Smolin J A and Wootters W K 1996 Mixed-state entanglement and quantum error correction *Phys. Rev.* A **54** 3824
[44] Vidal G and Werner R F 2002 Computable measure of entanglement *Phys. Rev.* A **65** 032314

The rest is silence.

(Hamlet)

11. Conclusion and Outlook

In this thesis we expanded the formalism of ultrafast waveguided parametric down-conversion to include the spatial, spectral and photon-number degree of freedom. Our rigorous theoretical description of PDC enabled us to build, develop and propose enhanced sources for quantum information processing: we explored the limits of PDC to serve as a source of single-photon Fock states, put forward a scheme to create single-mode PDC states independently of the applied material, presented a loss resilient method to effectively probe PDC states in the laboratory and, based on the multi-mode nature of PDC, developed a multiplexed quantum communication protocol featuring an exponentially enhanced quantum communication rate in comparison to the standard single-mode coding.

After a short introduction into the theory of PDC in Chap. 4 we included the spatial degree of freedom for waveguided PDC [1, 2] in Chap. 5. This enabled a complete description of the spatial-spectral interplay during the process of waveguided parametric down-conversion, which leads to the creation of hyperentangled quantum states [2], and is vital for the engineering of integrated PDC sources for quantum information processing. Currently our developed model serves not only as a tool to model waveguided PDC, but also forms the basis to engineer integrated two-photon quantum walks in waveguide arrays [35].

We further extended the current models of PDC, based on first-order perturbation approaches, to include higher-order contributions which, based on the solution of coupled integro-differential equations, enables a rigorous description of the ultrafast down-conversion process. Additionally we developed a simplified model that, at the expense of neglecting time-ordering effects, enables an analytic solution which accurately describes the down-conversion process in a broad parameter range. These models enable us to incorporate higher-order photon number effects into the theoretical descriptions of ultrafast PDC and consequently lead to an enhanced precision when evaluating their performance for quantum enhanced applications [3]. Furthermore our developed theoretical framework of PDC is also able to describe the process of frequency conversion, which enabled us to benchmark the performance of FC processes serving as quantum pulse gates.

The rigorous PDC description enabled us to derive the fundamental limits of parametric down-conversion to serve as a single-photon source. Our investigations reveal that an optimal PDC source in conjunction with a perfect photon number resolving detector is able to herald a pure single-photon state with 25% probability. For the creation of a *deterministic* ($\geq 99\%$) single-photon source consequently an array of 17 switched PDC sources is required [4].

To date, however, the creation of single-mode PDC states is difficult, since the applied

nonlinear crystal material has to feature very specific dispersion properties. In order to circumvent this problem we propose creating PDC states with counterpropagating signal and idler photons, which enables the creation of single-mode PDC states independent of the applied nonlinear material [5].

In order to characterize the developed PDC sources in the laboratory quantum state tomography is required. This, however, demands complex setups and long measurement times, due to the multi-mode structure of PDC. As an alternative we developed a new state characterization tool based on broadband, time-integrated correlation function measurements. It enables the robust, fast and most importantly *loss independent* characterization of down-conversion requiring only broadband time-integrated $g^{(2)}$ and $g^{(1,1)}$ measurements [6].

Finally we turned to the question of quantum communication using parametric down-conversion. Our knowledge of the spectral properties of PDC enabled us to propose parametric down-conversion as a fundamental building block of a multiplexed CV quantum communication protocol which features an *exponential* increase in the achievable quantum communication rate in comparison to the standard single-mode CV coding protocols [7].

Still the process of parametric down-conversion offers many interesting open questions for future research. Concerning our theoretical treatment of PDC and the spatial-spectral interplay in waveguides and waveguide arrays the created quantum states offer the possibility to create hyperentangled quantum states in the spatial *and* spectral domain. However, a detailed characterization and optimisation of this entanglement has yet to be performed.

Furthermore it would be very interesting to include the effects of intra-crystal losses during the state creation into our theoretical description of PDC. These intra crystal losses are one of *the* limiting factors for the creation of highly squeezed EPR states and their inclusion would give an enhanced precision in benchmarking the prospects of PDC in the framework of quantum information. While limited models of this issue already exist, merging the spectral degree of freedom and losses into a unified picture still poses an open research question.

Additionally parasitic processes, like fluorescence decrease the quality of the emitted PDC states. To date however only a few of these have been identified and their theoretical description is still under debate [137, 138]. Yet a theoretical investigation of these is necessary to effectively cope with this additional noise and to design sources which minimize their impact on the output states.

Concerning our discussion of frequency conversion and quantum pulse gates in Sec. 6.4 it is still unclear if adapted pump shapes and hypergrating structures are able to improve the performance of frequency conversion as a quantum pulse gate. Whether or not it is possible to remove the limitations imposed by the sinc structure and time-ordering effects is an open research question.

Finally, in our multiplexed quantum communication protocol, we currently describe the losses during the state distribution using the widespread approach of modelling them via a beam-splitter transformation with a varying transmissivity η. This however is only an approximation to an actual optical fiber which features frequency dependent loss

rates. An inclusion of these frequency dependent loss effects is currently under way.

12. List of Publications

12.1. Main publications

The following publications — sorted by date of publication — are the main publications for this thesis. All of them, except "Theory of quantum frequency conversion and parametric down-conversion in the high gain regime", which is currently under peer review, have been published in scientific journals.

- **Theory of quantum frequency conversion and parametric down-conversion in the high gain regime**
  Andreas Christ, Benjamin Brecht, Wolfgang Mauerer, Christine Silberhorn
  arXiv:1210.8342 (2012) (in peer review)

- **Exponentially enhanced quantum communication rate by multiplexing continuous-variable teleportation**
  Andreas Christ, Cosmo Lupo, Christine Silberhorn
  New J. Phys. 14 083007 (2012)

- **Limits on the deterministic creation of pure single-photon states using parametric down-conversion**
  Andreas Christ, Christine Silberhorn
  Phys. Rev. A 85, 023829 (2012)

- **Probing multimode squeezing with correlation functions**
  Andreas Christ, Kaisa Laiho, Andreas Eckstein, Katiúscia N. Cassemiro, Christine Silberhorn
  New J. Phys. 13 033027 (2011)

- **Direct Measurement of the Spatial-Spectral Structure of Waveguided Parametric Down-Conversion**
  Peter J. Mosley, Andreas Christ, Andreas Eckstein, Christine Silberhorn
  Phys. Rev. Lett. 103, 233901 (2009)

- **Spatial modes in waveguided parametric down-conversion**
  Andreas Christ, Kaisa Laiho, Andreas Eckstein, Thomas Lauckner, Peter J. Mosley, Christine Silberhorn
  Phys. Rev. A 80, 033829 (2009)

- **Pure single photon generation by type-I PDC with backward-wave amplification**
  Andreas Christ, Andreas Eckstein, Peter J. Mosley, Christine Silberhorn
  Opt. Express 17, 3441-3446 (2009)

12.2. Additional publications

The following publications — sorted by date of publications — are part of the research during my PhD, but are not in the main focus of this thesis. All of them are peer reviewed and published in scientific journals. They can be found in App. B:

- **From quantum pulse gate to quantum pulse shaper – engineered frequency conversion in nonlinear optical waveguides**
  Benjamin Brecht, Andreas Eckstein, Andreas Christ, Hubertus Suche, Christine Silberhorn
  New J. Phys. 13 065029 (2011)

- **Testing spectral filters as Gaussian quantum optical channels**
  Kaisa Laiho, Andreas Christ, Katiúscia N. Cassemiro, Christine Silberhorn
  Opt. Lett. 36, 1476-1478 (2011)

- **Highly Efficient Single-Pass Source of Pulsed Single-Mode Twin Beams of Light**
  Andreas Eckstein, Andreas Christ, Peter J. Mosley, Christine Silberhorn
  Phys. Rev. Lett. 106, 013603 (2011)

13. Author contributions

13.1. Main publications

- **Theory of quantum frequency conversion and parametric down-conversion in the high gain regime**
  Andreas Christ, Benjamin Brecht, Wolfgang Mauerer, Christine Silberhorn
  arXiv:1210.8342 (2012) (in peer review)

  Wolfgang Mauerer created the theoretical framework and developed the integration routine [77]. After he left the group the work was taken over by Andreas Christ, who refined and extended the calculations to the results depicted in the paper. Benjamin Brecht helped with the frequency conversion calculations. Christine Silberhorn supervised the work and took part in the scientific discussions.

  Andreas Christ wrote the manuscript with feedback from Benjamin Brecht, Wolfgang Mauerer and Christine Silberhorn, who helped refining the article.

- **Exponentially enhanced quantum communication rate by multiplexing continuous-variable teleportation**
  Andreas Christ, Cosmo Lupo, Christine Silberhorn
  New J. Phys. 14 083007 (2012)

  Andreas Christ performed the parametric down-conversion calculations and multimode state analysis. Cosmo Lupo performed the channel capacity calculations and derived the channel capacity formulas. Both jointly evaluated the optimal quantum communication bounds. Christine Silberhorn supervised the work and took part in the scientific discussions.
  Andreas Christ and Cosmo Lupo jointly wrote the manuscript. Christine Silberhorn gave feedback and helped refining the article.

- **Limits on the deterministic creation of pure single-photon states using parametric down-conversion**
  Andreas Christ, Christine Silberhorn
  Phys. Rev. A 85, 023829 (2012)

  Andreas Christ performed the calculations and theoretical analysis. Christine Silberhorn supervised the work and gave scientific feedback.

  Andreas Christ wrote the manuscript. Christine Silberhorn gave feedback and helped refining the article.

- **Probing multimode squeezing with correlation functions**
  Andreas Christ, Kaisa Laiho, Andreas Eckstein, Katiúscia N. Cassemiro, Christine Silberhorn
  New J. Phys. 13 033027 (2011)

  Andreas Christ formulated the theory supported by Kaisa Laiho, Andreas Eckstein and Katiúscia N. Cassemiro. Christine Silberhorn supervised the work and gave scientific feedback.

  Andreas Christ wrote the manuscript with contributions and suggestions from Kaisa Laiho, Andreas Eckstein and Katiúscia N. Cassemiro. Christine Silberhorn helped refining the article.

- **Direct Measurement of the Spatial-Spectral Structure of Waveguided Parametric Down-Conversion**
  Peter J. Mosley, Andreas Christ, Andreas Eckstein, Christine Silberhorn
  Phys. Rev. Lett. 103, 233901 (2009)

  Peter Mosley performed the experiments and the data analysis. Andreas Christ formulated the theory and adapted the theory to the experimental data. Andreas Eckstein took part in the scientific discussion. Christine Silberhorn supervised the work and gave scientific feedback.

  Andreas Christ and Peter J. Mosley jointly wrote the manuscript. Andreas Eckstein and Christine Silberhorn helped refining the article.

- **Spatial modes in waveguided parametric down-conversion**
  Andreas Christ, Kaisa Laiho, Andreas Eckstein, Thomas Lauckner, Peter J. Mosley, Christine Silberhorn
  Phys. Rev. A 80, 033829 (2009)

  Andreas Eckstein together with Thomas Lauckner started the work on the spatial mode theory. It was then taken over by Andreas Christ who refined the calculations and finalized the work, with the help of Kaisa Laiho and Peter J. Mosely to the results presented in the paper. Kaisa Laiho performed the experimental measurements. Andreas Christ analysed the data. Christine Silberhorn supervised the work and gave scientific feedback.

  Andreas Christ wrote the theory part of the manuscript, whereas Kaisa Laiho was responsible for the experimental section. Andreas Eckstein, Peter J. Mosley and Christine Silberhorn helped refining the article.

- **Pure single photon generation by type-I PDC with backward-wave amplification**
  Andreas Christ, Andreas Eckstein, Peter J. Mosley, Christine Silberhorn
  Opt. Express 17, 3441-3446 (2009)

Andreas Christ performed the theoretical calculations and analysis with help from Andreas Eckstein and Peter J. Mosley. Christine Silberhorn supervised the work and gave scientific feedback.

Andreas Christ wrote the manuscript with help from Andreas Eckstein and Peter J. Mosley. Christine Silberhorn gave feedback and took part in refining the article.

13.2. Additional publications

- **From quantum pulse gate to quantum pulse shaper – engineered frequency conversion in nonlinear optical waveguides**
  Benjamin Brecht, Andreas Eckstein, Andreas Christ, Hubertus Suche, Christine Silberhorn
  New J. Phys. 13 065029 (2011)

  Andreas Christ provided assistance for the frequency conversion calculations and took part in the scientific discussions. He helped refining the manuscript.

- **Testing spectral filters as Gaussian quantum optical channels**
  Kaisa Laiho, Andreas Christ, Katiúscia N. Cassemiro, Christine Silberhorn
  Opt. Lett. 36, 1476-1478 (2011)

  Andreas Christ provided assistance for the correlation function calculations and took part in the scientific discussions. He helped refining the manuscript.

- **Highly Efficient Single-Pass Source of Pulsed Single-Mode Twin Beams of Light**
  Andreas Eckstein, Andreas Christ, Peter J. Mosley, Christine Silberhorn
  Phys. Rev. Lett. 106, 013603 (2011)

  Andreas Christ was involved in the initial experiments and provided theoretical assistance in building the theory for the correlation function measurements. He took part in the scientific discussions and helped refining the manuscript.

14. Conference presentations

- **Poster award presentation: Multiplexed ultrafast quantum communication**
  Andreas Christ, Cosmo Lupo, Christine Silberhorn
  500. Wilhelm und Else Heraeus-Seminar: Highlights of Quantum Optics, Bad Honnef, Germany (2012)

- **Poster: Multiplexed ultrafast quantum communication**
  Andreas Christ, Cosmo Lupo, Christine Silberhorn
  500. Wilhelm und Else Heraeus-Seminar: Highlights of Quantum Optics, Bad Honnef, Germany (2012)

- **Talk: Probing Multimode Squeezing with Correlation Functions**
  Andreas Christ, Kaisa Laiho, Andreas Eckstein, Katiúscia N. Cassemiro, Christine Silberhorn
  OSA Topical Meeting: Quantum Information and Measurement, Berlin, Germany (2012)

- **Invited Talk: Ultrafast optical information coding: State generation, manipulation and distribution**
  Andreas Christ, Andreas Eckstein, Benjamin Brecht, Cosmo Lupo, Christine Silberhorn
  IEEE Summer Topicals 2011, Montreal, Canada (2011)

- **Talk: Multimode ultrafast information coding: State generation, transmission and loss evaluation**
  Andreas Christ, Cosmo Lupo, Christine Silberhorn
  4th International Conference on Quantum Information, Ottawa, Canada (2011)

- **Talk: Multimode ultrafast information coding: State generation, characterization and loss evaluation**
  Andreas Christ, Cosmo Lupo, Kaisa Laiho, Andreas Eckstein, Katiúscia N. Cassemiro, Christine Silberhorn
  The European Conference on Lasers and Electro-Optics and the XIIth European Quantum Electronics Conference, Munich, Germany (2011)

- **Talk: Probing multimode squeezing with correlation functions**
  Andreas Christ, Kaisa Laiho, Andreas Eckstein, Katiúscia N. Cassemiro, Christine Silberhorn
  DPG Spring Meeting, Dresden, Germany (2011)

- **Talk: Multi-mode quantum mechanical propagation equations for waveguided PDC**
  Andreas Christ, Wolfgang Mauerer, Christine Silberhorn
  DPG Spring Meeting, Hannover, Germany (2010)

- **Poster: Pure single photon generation by type-I PDC with backward-wave amplification**
  Andreas Christ, Andreas Eckstein, Peter J. Mosley, Christine Silberhorn
  European Conference on Lasers and XIth Electro-Optics and European Quantum Electronics Conference, Munich, Germany (2009)

- **Talk: Spatial to spectral mode mapping in waveguided PDC**
  Andreas Christ, Kaisa Laiho, Andreas Eckstein, Thomas Lauckner, Peter J. Mosley, Christine Silberhorn
  DPG Spring Meeting, Hamburg, Germany (2009)

- **Poster: Counterpropagating PDC photon source with PPLN waveguides**
  Andreas Christ, Andreas Eckstein, Thomas Lauckner, Christine Silberhorn
  DPG Spring Meeting, Darmstadt, Germany (2009)

So Long, and Thanks for All the Fish

(Douglas Adams)

15. Acknowledgements

Science is a team effort and none of the work presented in this thesis could have been performed without the invaluable help of all the people that guided and aided me along the way, all of whom I deeply thank for their support and assistance.

First and foremost I thank my advisor Prof. Dr. Christine Silberhorn for giving me the opportunity to be a part of her research group. I thank her for the continuous support and guidance during all these years. Our extensive discussions provided me with invaluable insights into the field of quantum optics, led me to interesting problems and always set me on the right track to solve the challenges at hand.

Further thanks goes to my second advisor Prof. Dr. Torsten Meier, and Dr. Matthias Reichelt, from our theory department, who always had on open ear for my questions concerning coding, math and bureaucracy.

Thanks to my brilliant collaborator Dr. Cosmo Lupo, who introduced me to the field of quantum communication and safely guided me over all the mathematical obstacles on the way. It was a pleasure working with you and I look forward to continuing to do so in the future.

Then there are my great colleagues of whom I was fortunate to have many. In all my years in the IQO group I enjoyed working with (in alphabetical order):

Vahid Ansari, Matthias Bechert, Agata M. Brańczyk, Benjamin Brecht, Katiúscia N. Cassemiro, Thomas Dirmeier, Andreas Eckstein, Christoph Eigner, Georg Harder, Harald Herrmann, Felix Just, Fabian Katschmann, Stephan Krapick, Kaisa Laiho, Sarah Leineweber, Kai Hong Lou, Wolfgang Mauerer, Peter J. Mosley, Thomas Nitsche, Rita Prevor, Viktor Quiring, Raimund Ricken, Peter Rohde, Helge Rütz, Andreas Schreiber, Christoph Söller, Hubertus Suche, Xu Yang, and Irmgard Zimmermann.

I thank you all for our scientific and unscientific discussions. For all the help with my research and for all the fun we had while procrastinating from research. It was a pleasure working with you and great fun distracting you from work.

Kudos to my friends — especially Alex, Simon, Kalle and Easy — who always managed to drag me back into the real world when I ventured too long and too deep into the realms of physics. Thanks for tolerating me missing many an event due to being stuck with research.

I further thank my family for their continued love, support and never asking when I am going to graduate.

Finally thanks to Regina who lovingly took care of me during my studies. Thank you for being there. Your importance to me vigorously exceeds that of Club-Mate in writing this thesis.

Bibliography

[1] Andreas Christ, Kaisa Laiho, Andreas Eckstein, Thomas Lauckner, Peter J. Mosley, and Christine Silberhorn. Spatial modes in waveguided parametric down-conversion. *Physical Review A*, 80(3):033829, 2009.

[2] Peter J. Mosley, Andreas Christ, Andreas Eckstein, and Christine Silberhorn. Direct measurement of the spatial-spectral structure of waveguided parametric down-conversion. *Physical Review Letters*, 103(23):233901, December 2009.

[3] Andreas Christ, Benjamin Brecht, Wolfgang Mauerer, and Christine Silberhorn. Theory of quantum frequency conversion and parametric down-conversion in the high gain regime. *arXiv:1210.8342*, October 2012.

[4] Andreas Christ and Christine Silberhorn. Limits on the deterministic creation of pure single-photon states using parametric down-conversion. *Physical Review A*, 85(2):023829, February 2012.

[5] A. Christ, A. Eckstein, P. J. Mosley, and C. Silberhorn. Pure single photon generation by type-i PDC with backward-wave amplification. *Optics Express*, 17(5):3441–3446, March 2009.

[6] Andreas Christ, Kaisa Laiho, Andreas Eckstein, Katiúscia N Cassemiro, and Christine Silberhorn. Probing multimode squeezing with correlation functions. *New Journal of Physics*, 13:033027, March 2011.

[7] Andreas Christ, Cosmo Lupo, and Christine Silberhorn. Exponentially enhanced quantum communication rate by multiplexing continuous-variable teleportation. *New Journal of Physics*, 14(8):083007, August 2012.

[8] Jagdish Mehra. *The Quantum Theory of Planck, Einstein, Bohr and Sommerfeld: Its Foundation and the Rise of Its Difficulties 1900-1925 1.* Springer, 1 edition, August 1982.

[9] Wikipedia contributors. Quantum mechanics, August 2012. Page Version ID: 505846328.

[10] H. J Kimble, M. Dagenais, and L. Mandel. Photon antibunching in resonance fluorescence. *Phys. Rev. Lett.*, 39(11):691–695, September 1977.

[11] W. E. Lamb. Anti-photon. *Applied Physics B Laser and Optics*, 60(2-3):77–84, 1995.

[12] W. H. Louisell, A. Yariv, and A. E. Siegman. Quantum fluctuations and noise in parametric processes. i. *Physical Review*, 124(6):1646–1654, December 1961.

[13] B. R. Mollow and R. J. Glauber. Quantum theory of parametric amplification. i. *Physical Review*, 160(5):1076–1096, August 1967.

[14] B. R. Mollow. Quantum statistics of coupled oscillator systems. *Physical Review*, 162(5):1256–1273, October 1967.

[15] D. A. Kleinman. Theory of optical parametric noise. *Physical Review*, 174(3):1027–1041, October 1968.

[16] John Tucker and Daniel F. Walls. Quantum theory of the traveling-wave frequency converter. *Physical Review*, 178(5):2036–2043, February 1969.

[17] B. R. Mollow. Photon correlations in the parametric frequency splitting of light. *Physical Review A*, 8(5):2684–2694, November 1973.

[18] A. N. Penin and A. V. Sergienko. Absolute standardless calibration of photodetectors based on quantum two-photon fields. *Applied Optics*, 30(25):3582–3588, September 1991.

[19] B. Ya Zel'Dovich and D. N. Klyshko. Field statistics in parametric luminescence. *ZhETF Pis ma Redaktsiiu*, 9:69, January 1969.

[20] David C. Burnham and Donald L. Weinberg. Observation of simultaneity in parametric production of optical photon pairs. *Physical Review Letters*, 25(2):84–87, July 1970.

[21] C. K. Hong, Z. Y. Ou, and L. Mandel. Measurement of subpicosecond time intervals between two photons by interference. *Physical Review Letters*, 59(18):2044, November 1987.

[22] E. Knill, R. Laflamme, and G. J. Milburn. A scheme for efficient quantum computation with linear optics. *Nature*, 409(6816):46–52, January 2001.

[23] Alfred B. U'Ren, Christine Silberhorn, Konrad Banaszek, and Ian A. Walmsley. Efficient conditional preparation of high-fidelity single photon states for fiber-optic quantum networks. *Physical Review Letters*, 93(9):093601, 2004.

[24] Peter J. Mosley, Jeff S. Lundeen, Brian J. Smith, Piotr Wasylczyk, Alfred B. U'Ren, Christine Silberhorn, and Ian A. Walmsley. Heralded generation of ultrafast single photons in pure quantum states. *Physical Review Letters*, 100(13):133601–4, April 2008.

[25] T.B. Pittman, B.C. Jacobs, and J.D. Franson. Heralding single photons from pulsed parametric down-conversion. *Optics Communications*, 246(4-6):545–550, February 2005.

[26] A. L. Migdall, D. Branning, and S. Castelletto. Tailoring single-photon and multiphoton probabilities of a single-photon on-demand source. *Physical Review A*, 66(5):053805, November 2002.

[27] M. D. Eisaman, J. Fan, A. Migdall, and S. V. Polyakov. Invited review article: Single-photon sources and detectors. *Review of Scientific Instruments*, 82(7):071101–071101–25, July 2011.

[28] Paul G. Kwiat, Klaus Mattle, Harald Weinfurter, Anton Zeilinger, Alexander V. Sergienko, and Yanhua Shih. New high-intensity source of polarization-entangled photon pairs. *Physical Review Letters*, 75(24):4337–4341, December 1995.

[29] Paul G. Kwiat, Edo Waks, Andrew G. White, Ian Appelbaum, and Philippe H. Eberhard. Ultrabright source of polarization-entangled photons. *Physical Review A*, 60(2):R773–R776, 1999.

[30] Christian Kurtsiefer, Markus Oberparleiter, and Harald Weinfurter. High-efficiency entangled photon pair collection in type-II parametric fluorescence. *Physical Review A*, 64(2):023802, July 2001.

[31] Matthew E. Anderson, D. F. McAlister, M. G. Raymer, and Mool C. Gupta. Pulsed squeezed-light generation in chi^(2) nonlinear waveguides. *Journal of the Optical Society of America B*, 14(11):3180, November 1997.

[32] D. K. Serkland, M. M. Fejer, R. L. Byer, and Y. Yamamoto. Squeezing in a quasi-phase-matched LiNbO3 waveguide. *Optics Letters*, 20(15):1649–1651, 1995.

[33] Stephen M. Barnett and Paul M. Radmore. *Methods in theoretical quantum optics*. Oxford University Press, January 2003.

[34] A. Einstein, B. Podolsky, and N. Rosen. Can quantum-mechanical description of physical reality be considered complete? *Physical Review*, 47(10):777–780, May 1935.

[35] Alexander S. Solntsev, Andrey A. Sukhorukov, Dragomir N. Neshev, and Yuri S. Kivshar. Spontaneous parametric down-conversion and quantum walks in arrays of quadratic nonlinear waveguides. *Physical Review Letters*, 108(2):023601, January 2012.

[36] Andreas Eckstein, Andreas Christ, Peter J. Mosley, and Christine Silberhorn. Highly efficient single-pass source of pulsed single-mode twin beams of light. *Physical Review Letters*, 106(1):013603, January 2011.

[37] W. P. Grice and I. A. Walmsley. Spectral information and distinguishability in type-II down-conversion with a broadband pump. *Physical Review A*, 56(2):1627, 1997.

[38] Marco Fiorentino, Sean M. Spillane, Raymond G. Beausoleil, Tony D. Roberts, Philip Battle, and Mark W. Munro. Spontaneous parametric down-conversion in periodically poled KTP waveguides and bulk crystals. *Optics Express*, 15(12):7479–7488, June 2007.

[39] Yu. M. Mikhailova, P. A. Volkov, and M. V. Fedorov. Biphoton wave packets in parametric down-conversion: Spectral and temporal structure and degree of entanglement. *Physical Review A (Atomic, Molecular, and Optical Physics)*, 78(6):062327–17, December 2008.

[40] Robert W. Boyd. *Nonlinear Optics Second Edition*. Academic Press, 2003.

[41] Jun Chen, Xiaoying Li, and Prem Kumar. Two-photon-state generation via four-wave mixing in optical fibers. *Physical Review A*, 72(3):033801, September 2005.

[42] Christoph Söller. *Optical fiber sources of pulsed single- and multi-photon states for quantum networks*. PhD thesis, Universität Erlangen-Nürnberg, Universitätsstraße. 4, 91054 Erlangen, 2011.

[43] Frits Zernike and John E. Midwinter. *Applied Nonlinear Optics*. Dover Pubn Inc, November 2006.

[44] I. S. Grant and W. R. Phillips. *Electromagnetism*. Wiley-Blackwell, 2nd edition edition, October 1990.

[45] K. J. Blow, Rodney Loudon, Simon J. D. Phoenix, and T. J. Shepherd. Continuum fields in quantum optics. *Physical Review A*, 42(7):4102, October 1990.

[46] Rodney Loudon. *The Quantum Theory of Light*. Oxford University Press, USA, 3 edition, November 2000.

[47] Toshiaki Suhara and Masatoshi Fujimura. *Waveguide Nonlinear-Optic Devices*. Springer, 1 edition, June 2003.

[48] Andreas Eckstein. *Mastering quantum light pulses with nonlinear waveguide interactions*. PhD thesis, Uni Erlangen-Nürnberg, 2012.

[49] Benjamin Brecht, Andreas Eckstein, Andreas Christ, Hubertus Suche, and Christine Silberhorn. From quantum pulse gate to quantum pulse shaper—engineered frequency conversion in nonlinear optical waveguides. *New Journal of Physics*, 13(6):065029, June 2011.

[50] J. J. Sakurai. *Modern Quantum Mechanics*. Prentice Hall, revised edition. edition, August 1993.

[51] Agata M Brańczyk. *Non-classical States of Light*. PhD thesis, University of Queensland, August 2010.

[52] Alfred B U'Ren, Christine Silberhorn, Reinhard Erdmann, Konrad Banaszek, Warren P Grice, Ian A Walmsley, and Michael G Raymer. Generation of pure-state single-photon wavepackets by conditional preparation based on spontaneous parametric downconversion. *arXiv:quant-ph/0611019*, November 2006. Las. Phys. 15 146 (2005).

[53] K. Laiho, K. N. Cassemiro, and Ch. Silberhorn. Producing high fidelity single photons with optimal brightness via waveguided parametric down-conversion. *Optics Express*, 17(25):22823–22837, December 2009.

[54] Michael A. Nielsen and Isaac L. Chuang. *Quantum Computation and Quantum Information*. Cambridge University Press, 1 edition, January 2004.

[55] C. K. Law, I. A. Walmsley, and J. H. Eberly. Continuous frequency entanglement: Effective finite hilbert space and entropy control. *Physical Review Letters*, 84(23):5304, June 2000.

[56] Peter P Rohde, Wolfgang Mauerer, and Christine Silberhorn. Spectral structure and decompositions of optical states, and their applications. *New Journal of Physics*, 9:91–91, April 2007.

[57] J. H. Eberly. Schmidt analysis of pure-state entanglement. *Laser Physics*, 16(6):921–926, June 2006.

[58] R Grobe, K Rzazewski, and J H Eberly. Measure of electron-electron correlation in atomic physics. *Journal of Physics B: Atomic, Molecular and Optical Physics*, 27(16):L503, 1994.

[59] J. A. Armstrong, N. Bloembergen, J. Ducuing, and P. S. Pershan. Interactions between light waves in a nonlinear dielectric. *Physical Review*, 127(6):1918–1939, September 1962.

[60] M.M. Fejer, G.A. Magel, D.H. Jundt, and R.L. Byer. Quasi-phase-matched second harmonic generation: tuning and tolerances. *IEEE Journal of Quantum Electronics*, 28(11):2631 –2654, November 1992.

[61] M. Yamada, N. Nada, M. Saitoh, and K. Watanabe. First-order quasi-phase matched LiNbO3 waveguide periodically poled by applying an external field for efficient blue second-harmonic generation. *Applied Physics Letters*, 62(5):435–436, February 1993.

[62] Matthew E. Anderson, M. Beck, M. G. Raymer, and J. D. Bierlein. Quadrature squeezing with ultrashort pulses in nonlinear-optical waveguides. *Optics Letters*, 20(6):620–622, March 1995.

[63] Jun Chen, Aaron J. Pearlman, Alexander Ling, Jingyun Fan, and Alan L. Migdall. A versatile waveguide source of photon pairs for chip-scale quantum information processing. *Optics Express*, 17(8):6727–6740, April 2009.

[64] S. Tanzilli, H. De Riedmatten, H. Tittel, H. Zbinden, P. Baldi, M. De Micheli, D.B. Ostrowsky, and N. Gisin. Highly efficient photon-pair source using periodically poled lithium niobate waveguide. *Electronics Letters*, 37(1):26–28, 2001.

[65] Tian Zhong, Franco N. Wong, Tony D. Roberts, and Philip Battle. High performance photon-pair source based on a fiber-coupled periodically poled KTiOPO4 waveguide. *Optics Express*, 17(14):12019–12030, July 2009.

[66] D. Marcuse. *Theory of dielectric optical waveguides*. Academic Press, 1974.

[67] T. B Koch, J. B Davies, and D. Wickramasinghe. Finite element/finite difference propagation algorithm for integrated optical device. *Electronics Letters*, 25(8):514–516, April 1989.

[68] D.F. Walls and G.J. Milburn. *Quantum Optics*. Springer, February 1995.

[69] Mikhail I. Kolobov. The spatial behavior of nonclassical light. *Reviews of Modern Physics*, 71(5):1539, October 1999.

[70] Andreas Eckstein, Benjamin Brecht, and Christine Silberhorn. A quantum pulse gate based on spectrally engineered sum frequency generation. *Optics Express*, 19(15):13770–13778, July 2011.

[71] H. J. McGuinness, M. G. Raymer, and C. J. McKinstrie. Theory of quantum frequency translation of light in optical fiber: application to interference of two photons of different color. *Optics Express*, 19(19):17876–17907, 2011.

[72] Leonard Mandel and Emil Wolf. *Optical Coherence and Quantum Optics*. Cambridge University Press, 1995.

[73] Samuel L. Braunstein. Squeezing as an irreducible resource. *Physical Review A*, 71(5):055801, May 2005.

[74] Artur K. Ekert and Peter L. Knight. Relationship between semiclassical and quantum-mechanical input-output theories of optical response. *Physical Review A*, 43(7):3934, April 1991.

[75] Agata M. Brańczyk, Thomas M. Stace, and T. C. Ralph. Time ordering in spontaneous parametric down-conversion. *AIP Conference Proceedings*, 1363(1):335–338, October 2011.

[76] E. Brambilla, A. Gatti, M. Bache, and L. A. Lugiato. Simultaneous near-field and far-field spatial quantum correlations in the high-gain regime of parametric down-conversion. *Physical Review A*, 69(2):023802, February 2004.

[77] Wolfgang Mauerer. *On Colours, Keys, and Correlations: Multimode Parametric Downconversion in the Photon Number Basis*. PhD thesis, Universität Erlangen-Nürnberg, Universitätsstraße. 4, 91054 Erlangen, 2008.

[78] Wojciech Wasilewski, A. I. Lvovsky, Konrad Banaszek, and Czeslaw Radzewicz. Pulsed squeezed light: Simultaneous squeezing of multiple modes. *Physical Review A (Atomic, Molecular, and Optical Physics)*, 73(6):063819–12, June 2006.

[79] A. I. Lvovsky, Wojciech Wasilewski, and Konrad Banaszek. Decomposing a pulsed optical parametric amplifier into independent squeezers. *Journal of Modern Optics*, 54(5):721, 2007.

[80] Agata M. Branczyk, Alessandro Fedrizzi, Thomas M. Stace, Tim C. Ralph, and Andrew G. White. Engineered optical nonlinearity for quantum light sources. *Optics Express*, 19(1):55–65, January 2011.

[81] Nicolas Gisin and Rob Thew. Quantum communication. *Nat Photon*, 1(3):165–171, March 2007.

[82] Vittorio Giovannetti, Seth Lloyd, and Lorenzo Maccone. Quantum-enhanced measurements: Beating the standard quantum limit. *Science*, 306(5700):1330 –1336, November 2004.

[83] Ian A. Walmsley and Michael G. Raymer. Toward quantum-information processing with photons. *Science*, 307(5716):1733 –1734, March 2005.

[84] P. Michler, A. Kiraz, C. Becher, W. V. Schoenfeld, P. M. Petroff, Lidong Zhang, E. Hu, and A. Imamoglu. A quantum dot single-photon turnstile device. *Science*, 290(5500):2282 –2285, December 2000.

[85] Charles Santori, David Fattal, Jelena Vuckovic, Glenn S. Solomon, and Yoshihisa Yamamoto. Indistinguishable photons from a single-photon device. *Nature*, 419(6907):594–597, October 2002.

[86] Axel Kuhn, Markus Hennrich, and Gerhard Rempe. Deterministic single-photon source for distributed quantum networking. *Physical Review Letters*, 89(6):067901, July 2002.

[87] J. Beugnon, M. P. A. Jones, J. Dingjan, B. Darquié, G. Messin, A. Browaeys, and P. Grangier. Quantum interference between two single photons emitted by independently trapped atoms. *Nature*, 440(7085):779–782, April 2006.

[88] P. Maunz, D. L. Moehring, S. Olmschenk, K. C. Younge, D. N. Matsukevich, and C. Monroe. Quantum interference of photon pairs from two remote trapped atomic ions. *Nat Phys*, 3(8):538–541, 2007.

[89] H G Barros, A Stute, T E Northup, C Russo, P O Schmidt, and R Blatt. Deterministic single-photon source from a single ion. *New Journal of Physics*, 11(10):103004, October 2009.

[90] J. Rarity, J. Fulconis, J. Duligall, W. Wadsworth, and P. Russell. Photonic crystal fiber source of correlated photon pairs. *Optics Express*, 13(2):534–544, January 2005.

[91] Jun Chen, Kim Fook Lee, Chuang Liang, and Prem Kumar. Fiber-based telecom-band degenerate-frequency source of entangled photon pairs. *Optics Letters*, 31(18):2798–2800, 2006.

[92] Jingyun Fan and Alan Migdall. A broadband high spectral brightness fiber-based two-photon source. *Optics Express*, 15(6):2915–2920, March 2007.

[93] Jérémie Fulconis, Olivier Alibart, Jeremy L. O'Brien, William J. Wadsworth, and John G. Rarity. Nonclassical interference and entanglement generation using a photonic crystal fiber pair photon source. *Physical Review Letters*, 99(12):120501, 2007.

[94] Brian J. Smith, P. Mahou, Offir Cohen, J. S. Lundeen, and I. A. Walmsley. Photon pair generation in birefringent optical fibers. *Optics Express*, 17(26):23589–23602, December 2009.

[95] Alexander Ling, Jun Chen, Jingyun Fan, and Alan Migdall. Mode expansion and bragg filtering for a high-fidelity fiber-based photon-pair source. *Optics Express*, 17(23):21302–21312, November 2009.

[96] Christoph Söller, Benjamin Brecht, P. J. Mosley, L. Y. Zang, A. Podlipensky, N. Y. Joly, P. St. J. Russell, and C. Silberhorn. Bridging visible and telecom wavelengths with a single-mode broadband photon pair source. *Physical Review A*, 81(3):031801, March 2010.

[97] Christoph Söller, Offir Cohen, Brian J. Smith, Ian A. Walmsley, and Christine Silberhorn. High-performance single-photon generation with commercial-grade optical fiber. *Physical Review A*, 83(3):031806, March 2011.

[98] S Castelletto, I P Degiovanni, V Schettini, and A Migdall. Optimizing single-photon-source heralding efficiency and detection efficiency metrology at 1550 nm using periodically poled lithium niobate. *Metrologia*, 43:S56–S60, April 2006.

[99] A. I. Lvovsky, H. Hansen, T. Aichele, O. Benson, J. Mlynek, and S. Schiller. Quantum state reconstruction of the single-photon fock state. *Physical Review Letters*, 87(5):050402, July 2001.

[100] Thomas Gerrits, Martin J. Stevens, Burm Baek, Brice Calkins, Adriana Lita, Scott Glancy, Emanuel Knill, Sae Woo Nam, Richard P. Mirin, Robert H. Hadfield, Ryan S. Bennink, Warren P. Grice, Sander Dorenbos, Tony Zijlstra, Teun Klapwijk, and Val Zwiller. Generation of degenerate, factorizable, pulsed squeezed light at telecom wavelengths. *Optics Express*, 19(24):24434–24447, November 2011.

[101] P. G. Evans, R. S. Bennink, W. P. Grice, T. S. Humble, and J. Schaake. Bright source of spectrally uncorrelated polarization-entangled photons with nearly single-mode emission. *Physical Review Letters*, 105(25):253601, December 2010.

[102] Hou Shun Poh, Jiaqing Lim, Ivan Marcikic, Antía Lamas-Linares, and Christian Kurtsiefer. Eliminating spectral distinguishability in ultrafast spontaneous parametric down-conversion. *Physical Review A*, 80(4):043815, October 2009.

[103] P. Sekatski, N. Sangouard, F. Bussieres, C. Clausen, N. Gisin, and H. Zbinden. Detector imperfections in photon-pair source characterization. *arXiv:1109.0194*, September 2011.

[104] Jianming Huang and Prem Kumar. Photon-counting statistics of multimode squeezed light. *Physical Review A*, 40(3):1670, 1989.

[105] Malcolm N. O'Sullivan, Kam Wai Clifford Chan, Vasudevan Lakshminarayanan, and Robert W. Boyd. Conditional preparation of states containing a definite number of photons. *Physical Review A*, 77(2):023804, February 2008.

[106] Peter P Rohde, James G Webb, Elanor H Huntington, and Timothy C Ralph. Photon number projection using non-number-resolving detectors. *New Journal of Physics*, 9(7):233–233, July 2007.

[107] Peter P Rohde. Improving the fidelity of single photon preparation from conditional down-conversion via asymmetric multiport detection. *quant-ph/0703238*, March 2007.

[108] Yu-Ping Huang, Joseph B. Altepeter, and Prem Kumar. Optimized heralding schemes for single photons. *Physical Review A*, 84(3):033844, 2011.

[109] Wojciech Wasilewski, Czesław Radzewicz, Robert Frankowski, and Konrad Banaszek. Statistics of multiphoton events in spontaneous parametric down-conversion. *Physical Review A*, 78(3):033831, 2008.

[110] Daryl Achilles, Christine Silberhorn, and Ian A. Walmsley. Direct, loss-tolerant characterization of nonclassical photon statistics. *Physical Review Letters*, 97(4):043602, July 2006.

[111] Wolfgang Mauerer, Malte Avenhaus, Wolfram Helwig, and Christine Silberhorn. How colors influence numbers: Photon statistics of parametric down-conversion. *Physical Review A*, 80(5):053815, November 2009.

[112] M. A. Broome, M. P. Almeida, A. Fedrizzi, and A. G. White. Reducing multi-photon rates in pulsed down-conversion by temporal multiplexing. *Optics Express*, 19(23):22698–22708, November 2011.

[113] Christine Silberhorn. Detecting quantum light. *Contemporary Physics*, 48(3):143, 2007.

[114] Pieter Kok, W. J. Munro, Kae Nemoto, T. C. Ralph, Jonathan P. Dowling, and G. J. Milburn. Linear optical quantum computing with photonic qubits. *Reviews of Modern Physics*, 79(1):135, January 2007.

[115] Jean-Loup Smirr, Matthieu Deconinck, Robert Frey, Imad Agha, Eleni Diamanti, and Isabelle Zaquine. Optimal photon-pair single mode coupling in narrow-band spontaneous parametric down-conversion with arbitrary pump profile. *arXiv:1108.5884*, August 2011.

[116] Agata M Brańczyk, T C Ralph, Wolfram Helwig, and Christine Silberhorn. Optimized generation of heralded fock states using parametric down-conversion. *New Journal of Physics*, 12(6):063001, June 2010.

[117] T. B. Pittman, B. C. Jacobs, and J. D. Franson. Single photons on pseudodemand from stored parametric down-conversion. *Physical Review A*, 66(4):042303, October 2002.

[118] Xiao-song Ma, Stefan Zotter, Johannes Kofler, Thomas Jennewein, and Anton Zeilinger. Experimental generation of single photons via active multiplexing. *Physical Review A*, 83(4):043814, April 2011.

[119] Thomas Jennewein, Marco Barbieri, and Andrew G. White. Single-photon device requirements for operating linear optics quantum computing outside the post-selection basis. *Journal of Modern Optics*, 58(3-4):276–287, February 2011.

[120] Jiri Svozilik, Martin Hendrych, Amr S. Helmy, and Juan P. Torres. Generation of paired photons in a quantum separable state in bragg reflection waveguides. *Optics Express*, 19(4):3115–3123, February 2011.

[121] S. E. Harris. PROPOSED BACKWARD WAVE OSCILLATION IN THE INFRARED. *Applied Physics Letters*, 9(3):114–116, 1966.

[122] Mark C. Booth, Mete Atatüre, Giovanni Di Giuseppe, Bahaa E. A. Saleh, Alexander V. Sergienko, and Malvin C. Teich. Counterpropagating entangled photons from a waveguide with periodic nonlinearity. *Physical Review A*, 66(2):023815, 2002.

[123] L. Lanco, S. Ducci, J.-P. Likforman, X. Marcadet, J. A. W. van Houwelingen, H. Zbinden, G. Leo, and V. Berger. Semiconductor waveguide source of counterpropagating twin photons. *Physical Review Letters*, 97(17):173901, October 2006.

[124] M. Ravaro, Y. Seurin, S. Ducci, G. Leo, V. Berger, A. De Rossi, and G. Assanto. Nonlinear AlGaAs waveguide for the generation of counterpropagating twin photons in the telecom range. *Journal of Applied Physics*, 98(6):063103, 2005.

[125] Carlota Canalias and Valdas Pasiskevicius. Mirrorless optical parametric oscillator. *Nat Photon*, 1(8):459–462, 2007.

[126] Roy J. Glauber. The quantum theory of optical coherence. *Physical Review*, 130(6):2529, June 1963.

[127] Werner Vogel and Dirk-Gunnar Welsch. *Quantum Optics*. Wiley-VCH, 3 edition, August 2006.

[128] M. Avenhaus, K. Laiho, M. V. Chekhova, and C. Silberhorn. Accessing higher order correlations in quantum optical states by time multiplexing. *Physical Review Letters*, 104(6):063602, February 2010.

[129] K. Laiho, A. Christ, K. N. Cassemiro, and C. Silberhorn. Testing spectral filters as gaussian quantum optical channels. *Optics Letters*, 36(8):1476–1478, April 2011.

[130] Lev Vaidman. Teleportation of quantum states. *Physical Review A*, 49(2):1473, February 1994.

[131] Samuel L. Braunstein and H. J. Kimble. Teleportation of continuous quantum variables. *Physical Review Letters*, 80(4):869, January 1998.

[132] Masashi Ban, Masahide Sasaki, and Masahiro Takeoka. Continuous variable teleportation as a generalized thermalizing quantum channel. *Journal of Physics A: Mathematical and General*, 35(28):L401–L405, July 2002.

[133] Seth Lloyd. Capacity of the noisy quantum channel. *Physical Review A*, 55(3):1613, March 1997.

[134] I. Devetak. The private classical capacity and quantum capacity of a quantum channel. *Information Theory, IEEE Transactions on*, 51(1):44–55, 2005.

[135] Michael M. Wolf, David Pérez-García, and Geza Giedke. Quantum capacities of bosonic channels. *Physical Review Letters*, 98(13):130501, March 2007.

[136] A. S. Holevo and R. F. Werner. Evaluating capacities of bosonic gaussian channels. *Physical Review A*, 63(3):032312, February 2001.

[137] A. Hordvik and H. Schlossberg. Luminescence from LiNbO3. *Applied Physics Letters*, 20(5):197–199, March 1972.

[138] Y. Zhang, L. Guilbert, and P. Bourson. Characterization of Ti?:?LiNbO 3 waveguides by micro-raman and luminescence spectroscopy. *Applied Physics B: Lasers and Optics*, 78(3-4):355–361, February 2004.

[139] A. B U'Ren, K. Banaszek, and I. A Walmsley. Photon engineering for quantum information processing. *Quantum Info. Comput.*, 3(7):480–502, October 2003. ACM ID: 2011567.

Somewhere, something incredible is waiting to be known.

(Carl Sagan)

A. The singular value decomposition

Throughout this thesis, especially in Chap. 4 and Chap. 6, we performed singular value decompositions (SVD) to decompose PDC processes in their amplitudes and corresponding mode functions. In its most general form the singular value decomposition of our joint-spectral amplitudes reads

$$f(\omega,\omega') = \sum_{k=0}^{\infty} \lambda_k \phi_k(\omega)\psi_k(\omega'), \tag{A.1}$$

where $\lambda_k \in \mathbb{R}$, $\lambda_k \geq 0$, and $\{\phi_k(\omega)\}$ and $\{\psi_k(\omega')\}$ each from an orthonormal basis. In the special case of two-dimensional Gaussian functions it is straightforward to evaluate the SVD since an analytic formula exists [139]:

$$\begin{aligned} &\exp\left[-\frac{1+\mu^2}{2(1-\mu^2)}(\alpha_1^2 x_1^2 + \alpha_2^2 x_2^2) + \frac{2\alpha_1\alpha_2\mu x_1 x_2}{1-\mu^2}\right] \\ &\qquad = \sqrt{1-\mu^2}\sum_{n=0}^{\infty} \mu^n u_n(\alpha_1 x_1) u_n(\alpha_2 x_2) \end{aligned} \tag{A.2}$$

Here $0 \leq \mu \leq 1$, $u_n(x) = (2^n n!)^{-\frac{1}{2}} H_n(x)\exp(-x^2/2)$ and $H_n(x)$ is the nth order Hermite polynomial.

Care however has to be taken to when performing these decompositions numerically. In this case we have to use a discretized versions of $f(\omega,\omega')$:

$$f(\omega,\omega') \to f_{\omega,\omega'} \tag{A.3}$$

Decomposing $f_{\omega,\omega'}$ we obtain three matrices

$$f_{\omega,\omega'} = \sum_k A_{\omega,k} D_{kk} B_{k,\omega'}, \tag{A.4}$$

where A and B are unitary matrices which store the normalized basis vectors in their rows and columns and the diagonal matrix D holds the singular values. However, despite the resemblance of Eq. A.1 to Eq. A.4, the result of the numerical SVD on a grid is *not* identical to an analytical SVD. The problem arises due to the fact that the norms work differently in the continuous and discrete space:

$$\int \mathrm{d}\omega\, |\phi_k(\omega)|^2 = 1 \qquad \text{vs.} \qquad \sum_{\omega} |A_{\omega,y}|^2 = 1 \tag{A.5}$$

While in the discrete regime the *sum* over all matrix elements absolute value squared in one row / column, depending on how the mode functions are stored, has to evaluate to one, in the continuous regime the *integral* over a mode function absolute values squared must yield one. Consequently the amplitudes of the basis functions, from the different regimes, differ by a factor of square root of the applied step size $\Delta\omega$ used during the discretization of $f(\omega, \omega')$. In order to obtain the correct continuous mode amplitudes from the matrices A and B we consequently have to multiply each matrix with $1/\sqrt{\Delta\omega}$ and, furthermore, we have to readjust the singular values in D via multiplication with $\Delta\omega$ to transform them into the continuous picture:

$$D_{kk}\Delta\omega = \lambda_k \tag{A.6}$$

In total, after having performed a numerical SVD on a grid with step size $\Delta\omega$, all parameters have to be readjusted via:

$$\begin{aligned} &A_{\omega,k}/\sqrt{\Delta\omega} \Rightarrow \phi_k(\omega) \\ &B_{k,\omega'}/\sqrt{\Delta\omega} \Rightarrow \psi_k(\omega') \\ &D_{kk}\Delta\omega \Rightarrow r_k \end{aligned} \tag{A.7}$$

The same normalization hast to be applied when working with the $U(\omega, \omega')$ and $V(\omega, \omega')$ matrices.

Additional publications

New Journal of Physics
The open-access journal for physics

From quantum pulse gate to quantum pulse shaper—engineered frequency conversion in nonlinear optical waveguides

Benjamin Brecht[1,3], Andreas Eckstein[1,2], Andreas Christ[1,2], Hubertus Suche[1] and Christine Silberhorn[1,2]

[1] Applied Physics, University of Paderborn, Warbuger Strasse 100, 33098 Paderborn, Germany
[2] Max Planck Institute for the Science of Light, Günther-Scharowsky-Strasse 1/Building 24, 91058 Erlangen, Germany
E-mail: benjamin.brecht@uni-paderborn.de

New Journal of Physics **13** (2011) 065029 (22pp)
Received 1 February 2011
Published 30 June 2011
Online at http://www.njp.org/
doi:10.1088/1367-2630/13/6/065029

Abstract. Full control over the spatiotemporal structure of quantum states of light is an important goal in quantum optics, to generate, for instance, single-mode quantum pulses or to encode information on multiple modes, enhancing channel capacities. Quantum light pulses feature an inherent, rich spectral broadband-mode structure. In recent years, exploring the use of integrated optics as well as source engineering has led to a deep understanding of the pulse-mode structure of guided quantum states of light. In addition, several groups have started to investigate the manipulation of quantum states by means of single-photon frequency conversion. In this paper, we explore new routes towards complete control of the inherent pulse-modes of ultrafast pulsed quantum states by employing specifically designed nonlinear waveguides with adapted dispersion properties. Starting from our recently proposed quantum pulse gate (QPG), we further generalize the concept of spatiospectral engineering for arbitrary $\chi^{(2)}$-based quantum processes. We analyse the sum-frequency generation-based QPG and introduce the difference-frequency generation-based quantum pulse shaper (QPS). Together, these versatile and robust integrated optical devices allow for arbitrary manipulations of the pulse-mode structure of ultrafast pulsed quantum states. The QPG can be utilized to select an

[3] Author to whom any correspondence should be addressed.

arbitrary pulse mode from a multimode input state, whereas the QPS enables the generation of specific pulse modes from an input wavepacket with a Gaussian-shaped spectrum.

Contents

1. Motivation

Ultrafast pulsed quantum states of light play an increasingly important role in quantum information and quantum communication as they allow for efficient network synchronization and high data transmission rates. In general, they feature a rich spectral mode structure, which is most naturally described on a broadband pulse-mode basis. This is not a new result in either classical or quantum optics [1]. For classical states, all basis sets are formally equivalent and no specific choice can be distinguished. In contrast, it has been shown that pulsed quantum states of light exhibit an inherent pulse-mode structure, which is solely determined by their generation process [2]. Different kinds of applications require specifically tailored pulsed quantum states, be it single-mode states for linear optical quantum computation [3] or multimode states for high-capacity quantum information encoding. Thus, a thorough understanding of the spatiospectral modal structure of ultrafast quantum states as well as the ability to exercise full control over that structure is an important goal in today's quantum optical research.

In this paper, we investigate the potential of engineered nonlinear waveguides for the manipulation of pulsed quantum states, which cannot be achieved within the framework of linear optics. Special emphasis is put on an accurate description of the $\chi^{(2)}$-process inside the guide, which takes into account rigorously the spatial and spectral degrees of freedom. Thus quantitative measures can be derived for the efficiency of practical quantum optical devices.

This paper is organized as follows. In section 2, we review the state-of-the-art methods for generating ultrafast pulsed quantum states and manipulating their inherent pulse-mode structure in bulk crystals and waveguides. We briefly discuss the latest developments and introduce new ideas by combining dispersion engineering techniques, which have become established by now for photon-pair preparation, with current methods of state manipulation utilizing $\chi^{(2)}$-nonlinearities. In this context, we analyse the experimental implementation of our recently proposed quantum pulse gates (QPG) [4] and extend the formalism further by presenting the concept of a quantum pulse shaper (QPS). In sections 3 and 4, we develop a theoretical framework for our devices. We start with the linear operator transformations for sum- and difference-frequency generation and derive the interaction Hamiltonian of these processes considering spatial and temporal degrees of freedom. Our analysis results in a completely quantitative model. Section 5 is dedicated to merging the derived theoretical framework with dispersion engineering methods known from state preparation, thus paving the way for real-world applications, the performance of which is investigated in section 6. Here, we introduce realistic experimental parameters for our waveguide devices and demonstrate the capability to fully control the pulse-mode structure of ultrafast pulsed quantum states of light. Finally, in section 7, we highlight the most important results of this work, and end with an outlook on the use of QPG and QPS in continuous variable quantum information processing.

2. Introduction

In recent years, different approaches have been introduced to prepare and manipulate ultrafast pulsed quantum states of light. One of the most common sources for the generation of photonics quantum states is parametric down-conversion (PDC) in nonlinear crystals. This is mainly due to the rather simple experimental implementation of PDC sources and their ability to achieve high photon-pair generation rates. When pumped by ultrafast pulses, PDC processes generate pulsed bi-photons with broad spectra. However, these states are usually highly correlated due to the constraints imposed by energy and momentum conservation [5, 6]. Hence, photon pairs are typically emitted into many inter- and intra-correlated spatial-spectral modes, the exact structure of which can be retrieved by applying a Schmidt decomposition to the biphoton amplitude distribution [7]. Upon the detection of one of the photons, the other one is projected onto a mixed state of all possible modes, rendering it ill-suited to linear optical quantum computation applications [8]. The common way of overcoming this limitation has been to use narrow-band spectral filtering to force the photons into one optical mode [9, 10]. However, this approach prohibitively lowers the photon generation rate as most of the generated signal is lost in the filtering process. It is thus not feasible in the case of large-scale quantum information applications [8]. In addition, only in the limit of infinitely narrow filtering one monochromatic, temporally de-localized mode is selected, and the photon's pulse characteristic is lost.

2.1. Preparation of ultrafast pulsed quantum states with waveguides

Recently, two new developments have made it possible to tackle the aforementioned problems. The use of integrated waveguide sources has a major impact on the structure of PDC photon pair states. In a bulk crystal, the generated photons are emitted at the natural phase-matching angles. This poses two problems. Firstly, the collection of photons pairs is experimentally challenging and typically inefficient. Secondly, the pump field always couples to an infinite

number of spectral–spatially correlated modes, and thus the probability of creating a photon pair in one distinct mode becomes very low. In contrast, the emission in nonlinear waveguides is restricted to a well-defined set of discrete spatial modes defined by the waveguide, ideally allowing only the propagation of one individual mode in a single-mode waveguide[4]. It turns out that the probability of generating a photon pair in a distinct spatial mode is enhanced by several orders of magnitude [11, 12], since the total number of allowed modes is dramatically reduced inside the waveguide. Moreover, it also leads to an effective decoupling of the spatial from the spectral degree of freedom, since any spatial–spectral correlation necessitates more than one spatial mode. Even if other spatial modes apart from the ground mode are guided in the waveguide, modal waveguide dispersion usually ensures that both photons in those modes are created at different frequencies. Thus they can readily be removed by applying broadband spectral filters on the output state [13].

The second step on the way to achieving complete control over the modal structure of the generated quantum states of light is spectral source engineering. It has been proposed that by choosing adapted dispersion properties, photon pair generation can be tailored such that the signal and the idler are emitted into a single spectral pulse mode each [8, 14]. Later this was experimentally demonstrated for bulk crystal sources [15–17] and photonic crystal fibre sources [18–20]. Only recently has this been realized in a waveguided PDC source in a $KTiOPO_4$ crystal [21]. In this setup, the use of a waveguiding structure has led to an unprecedented brightness for sources of separable photon-pair states. Note that narrow-band spectral filtering is not necessary with these sources as the generation process itself only allows a single spectral pulse mode. Thus, the generated photon pairs are genuine quantum pulses and are completely separable, spectrally as well as spatially.

2.2. Manipulation of the pulse-mode structure of ultrafast quantum states

Until now, research on the manipulation of pulsed quantum states has mostly focused on shifting their central frequency. It has been shown that the sum-frequency generation (SFG) of single photons, in combination with subsequent photodetection, surpasses the efficiency of direct detection of near-infrared single photons [22–25]. Additionally, SFG has been proven to conserve the quantum characteristics of the input photon [26–28] and has already been utilized to implement measurement schemes with very high timing resolution, which overcomes the long integration times of current single-photon detectors [16]. Only last year, SFG was demonstrated for single-photon Fock states [29]. Note that recently also four-wave mixing in photonic crystal fibres has also been employed to demonstrate coherent frequency translation of single photons [30]. This highlights the broad interest in and numerous application possibilities for these techniques. With more and more single-photon sources available in the visible range, difference-frequency generation (DFG) has now attracted increasing interest. Recent experiments employ DFG to implement wavelength interfaces for quantum networks [31–33], which equivalently to the SFG process preserve the quantum characteristics of the input state.

Despite this considerable progress, the generation of ultrafast pulsed quantum states with a specific pulse-mode structure, be it the number of excited modes or their shape, has not been

[4] Here we only consider guided modes, neglecting any contributions that could be present due to phase-matched substrate modes. This simplification is justified, because the continuous distribution of substrate modes can be easily filtered out by spectral or spatial filters.

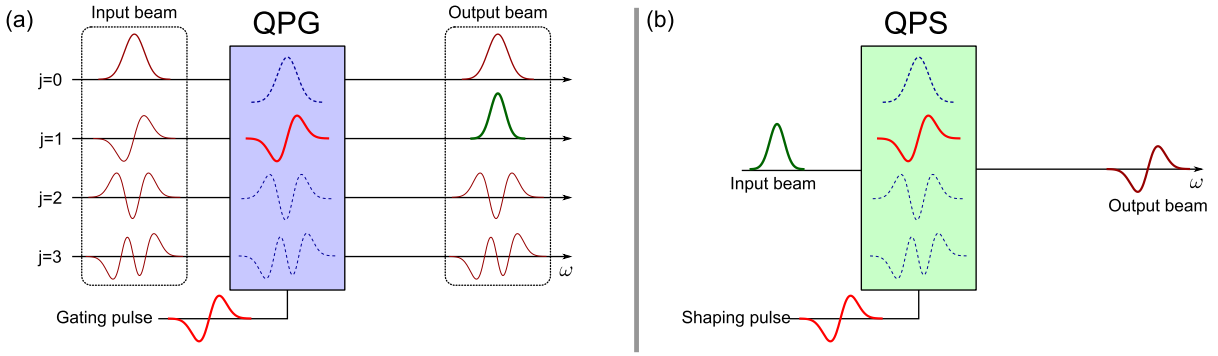

Figure 1. Schematic diagram of (a) a QPG and (b) a QPS. The QPG is based on an engineered ultrafast SFG in nonlinear optical waveguides. By shaping an ultrafast gating pulse, one specific pulse mode from a pulsed multimode input state is selected and shifted to another frequency. Then it can easily be split off while leaving the rest of the state untouched. The QPS is based on engineered ultrafast difference-frequency generation in nonlinear optical waveguides. An input pulse mode can be converted into an arbitrary output pulse mode by nonlinear interaction with an ultrafast shaping pulse. The output pulse mode's shape is given by the mode of the shaping pulse.

explored yet. Although the rich inherent mode structure of ultrafast optical quantum states is well known, before the QPG [4] there was no feasible way of controlling and manipulating the different modes separately.

2.3. Quantum pulse gate (QPG) and quantum pulse shaper (QPS)

We now combine findings from the field of quantum-state generation with techniques from state manipulation. Applying source engineering to frequency conversion reveals fascinating possibilities to achieve the desired goal of complete control over the pulse-mode structure of ultrafast quantum states. In [4], we have already proposed a QPG, a device based on engineered ultrafast SFG in nonlinear waveguides. This device enables us to address different inherent pulse modes of an ultrafast pulsed quantum state of light individually, as illustrated in figure 1(a). We would like to highlight that the QPG operation does not have any impact on the residual pulse-mode structure. This sets it apart from other experiments that focus on a direct manipulation of the spectral broadband-mode structure of ultrafast pulsed quantum states and that employ pulse shaping of photon-pair states [34–36]. This alternative approach also leads to highly interesting results for entanglement-based applications. Still, the manipulation is not pulse mode sensitive in the sense of accessing and separating out a single-mode quantum state with a specific temporal profile. In contrast, the QPG achieves mode selection by shaping an ultrafast, coherent gating pulse instead of the pulsed quantum state. The addressed mode is converted to the sum-frequency of the input pulse and gating pulse and is thus easily accessible. In addition, different orthogonal pulse modes can be interconverted into each other, rendering interference between them possible.

In this paper, we elaborate on the QPG concept and come up with another fundamental device, the QPS based on engineered ultrafast DFG. While the QPG addresses single pulse

modes, the QPS enables us to convert an input quantum state with a Gaussian-shaped spectrum into a single-mode quantum state with arbitrary shape (see figure 1(b)). Here, an arbitrarily chosen pulse form of the coherent shaping pulse defines the output pulse mode. We would like to mention that a similar idea of shaping quantum pulses by means of frequency conversion with dispersion matching has been proposed in [37]. In contrast to this earlier work, we put special emphasis on the engineering of the dispersion characteristics of the nonlinear medium used, such that single-mode operation can be ensured, avoiding the insertion of any unwanted vacuum contributions.

Using QPG and QPS, pulsed quantum states can be generated and selected with unit efficiency in arbitrary pulse forms, and the encoding of quantum information in broadband mode basis and the successive read-out become possible. Therefore QPG and QPS will enable the implementation of quantum communication protocols, which exploit the rich pulse-mode structure of ultrafast states.

3. Linear transformations for sum-frequency generation (SFG) and difference-frequency generation (DFG) in comparison with parametric down-conversion

In this section, we qualitatively discuss the nonlinear three-wave mixing processes SFG, DFG and PDC, highlighting their formal similarities as well as examining their differences. In such a three-wave mixing process, three electrical fields interact inside a nonlinear medium, and the interaction Hamiltonian in the rotating-wave approximation is of the form

$$\hat{H}_{\mathrm{int}} \propto \chi^{(2)} \int \mathrm{d}^3 r\, \hat{E}_{\mathrm{a}}^{(+)}(\vec{r},t)\hat{E}_{\mathrm{b}}^{(-)}(\vec{r},t)\hat{E}_{\mathrm{c}}^{(-)}(\vec{r},t) + \mathrm{h.c.} \tag{1}$$

The $\hat{E}_i^{(+)}(\vec{r},t)$ describe the positive frequency parts of the interacting electric fields and $\chi^{(2)}$ is the second-order nonlinearity of the medium. In PDC and single-photon SFG and DFG, two of the three fields are generally considered quantum mechanically. The remaining field is a bright, immutable pump field that can be treated classically. In this case, the interaction Hamiltonian becomes bilinear and Heisenberg's equation of motion yields linear input–output transformations for the creation and annihilation operators. Depending on which of the three fields is defined as a pump, one can distinguish between two flavours of processes that are characterized by different linear operator transformations.

This can be derived when considering a single-mode approximation to equation (1),

$$\hat{H}_{\mathrm{int}} \propto \hat{a}\hat{b}^{\dagger}\hat{c}^{\dagger} + \hat{a}^{\dagger}\hat{b}\hat{c}. \tag{2}$$

Firstly, we assume that the field $E_{\mathrm{a}}(\vec{r},t)$ is the classical coherent pump field. We insert its classical amplitude α into the above equation and find that

$$\hat{H}_{\mathrm{int}} \propto \alpha\, \hat{b}^{\dagger}\hat{c}^{\dagger} + \alpha^{*}\, \hat{b}\hat{c}. \tag{3}$$

The resulting operator formally corresponds to a two-mode squeezing operator (compare e.g. [38]), which means that this case describes PDC. Depending on the pump power of the bright field, either the photon pair characteristics (low-power regime) or the squeezer characteristics (high-power regime) dominate the PDC output state. The linear transformations between input and output operators evaluate to

$$\hat{b} \rightarrow \cosh(\zeta)\hat{b} - \sinh(\zeta)\hat{c}^{\dagger}, \tag{4}$$

$$\hat{c} \rightarrow -\sinh(\zeta)\hat{b}^{\dagger} + \cosh(\zeta)\hat{c}, \tag{5}$$

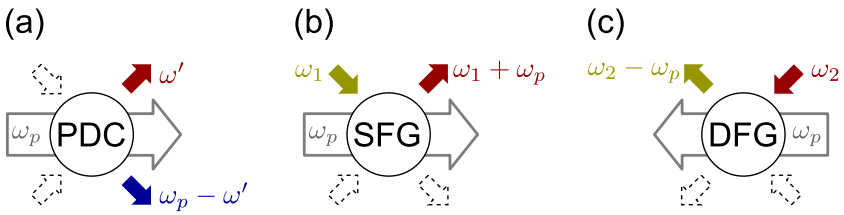

Figure 2. Schematic diagrams illustrating two different flavours of second-order nonlinear process. All processes are pumped by a classical undepleted field at a frequency ω_{p}, and the dashed arrows indicate vacuum modes. (a) In a PDC process, two photons are created and the evolution operator for this process is a two-mode squeezing operator. (b, c) In an SFG or DFG process, one incoming photon is annihilated and an outgoing photon at another frequency is created. Assuming that the frequencies involved in the two processes are equal, one can readily see that SFG and DFG are similar yet reversed processes, which is indicated in the schematics by the different directions that the arrows point to. The corresponding evolution operator for these processes is equivalent to a beamsplitter. For further details, see the text.

where the parameter ζ depends on the pump power and is related to the amount of squeezing in the generated pair state. This is discussed, for instance, in [39].

We find the other flavour of $\chi^{(2)}$ processes by assuming that the field $E_{\mathrm{b}}(\vec{r}, t)$ corresponds to the pump field. We substitute its classical amplitude β in (2) and obtain

$$\hat{H}_{\mathrm{int}} \propto \beta\, \hat{a}\hat{c}^{\dagger} + \beta^{*}\, \hat{a}^{\dagger}\hat{c}. \tag{6}$$

This expression is formally equivalent to an optical beamsplitter Hamiltonian and we can use the well-known beamsplitter input/output transformations for the operators $\hat{a}$ and $\hat{c}$,

$$\hat{a} \rightarrow \cos(\theta)\hat{a} - \mathrm{i}\sin(\theta)\hat{c}, \tag{7}$$

$$\hat{c} \rightarrow -\mathrm{i}\sin(\theta)\hat{a} + \cos(\theta)\hat{c}. \tag{8}$$

We identify θ with the beamsplitter angle, which depends on the pump power and the strength of the nonlinear interaction. This will be discussed later in great detail. We interpret this $\chi^{(2)}$-process as a beamsplitter that diverts optical beams into different frequency output ports depending on their initial frequency. Note that in single-photon quantum optics, this Hamiltonian describes SFG as well as DFG. In classical nonlinear optics, however, DFG is understood as a stimulated process. The bright pump field has the highest frequency and the process is seeded with a weak input field, which is enhanced through continuous conversion of pump photons. In that case, operator transformations similar to those for PDC are valid and the process could also be interpreted as seeded PDC. In contrast, we assume a single (or a few)-photon input state, which has the highest frequency and the 'seed' field is the bright field. By pinning the pump field to a fixed value in our process model, we exclude that stimulation can occur and the process becomes formally equivalent to SFG. Note that the usual no-pump-*depletion* approximation ($\partial E_{\mathrm{p}}/\partial z = 0$) needs to be interpreted as a no-pump-*enhancement* approximation in this case. These findings are shown schematically in figure 2.

We move on to the derivation of the interaction Hamiltonian for quantum mechanical frequency conversion inside an optical waveguide.

4. Quantitative derivation of the SFG and DFG interaction Hamiltonian

4.1. Spatial mode considerations in a monochromatic approach

The interaction Hamiltonian of a frequency conversion process can be expressed as

$$\hat{H}_{\text{int}} = -d_{\text{eff}}\varepsilon_0 \int \mathrm{d}^3 r\, E_{\text{p}}(\vec{r}, t)\hat{E}_{\text{i}}^{(+)}(\vec{r}, t)\hat{E}_{\text{o}}^{(-)}(\vec{r}, t) + \text{h.c.}, \tag{9}$$

where d_{eff} denotes the effective nonlinearity, E_{p} is the classical pump field, and $\hat{E}_{\text{i}}^{(+)}$ and $\hat{E}_{\text{o}}^{(-)}$ denote the operator expressions for the input signal and the converted output, respectively. As the interaction happens inside a nonlinear optical waveguide, the propagation of the fields is restricted to one direction, which is given by the waveguide axis and which we define as the z-direction. The ultrafast pump field then reads

$$E_{\text{p}}(\vec{r}, t) = A_{\text{p}} f_{\text{p}}(x, y) \int \mathrm{d}\omega_{\text{p}} \alpha(\omega_{\text{p}}) \mathrm{e}^{-\mathrm{i}\omega_{\text{p}} t + \mathrm{i}\beta_{\text{p}} z}. \tag{10}$$

Here, $\alpha(\omega_{\text{p}})$ is the normalized spectral amplitude of the pump. The function $f_{\text{p}}(x, y)$ describes the transverse spatial distribution of the pump field with $\int \mathrm{d}^2 r |f_{\text{p}}(x, y)|^2 = 1$ and β_{p} is the propagation constant of the corresponding transverse mode. By requiring that the area integration over the field intensity $I = \frac{1}{2} c\, n_{\text{p}} \varepsilon_0 |E|^2$, where n_{p} denotes the refractive index at the pump frequency, corresponds to a power, we find that the amplitude A_{p} is related to the average pump pulse peak power P_{p} by

$$A_{\text{p}} = \left(\frac{2P_{\text{p}}}{c\, \varepsilon_0 n_{\text{p}}(\omega_{\text{p}}) |\int \mathrm{d}\omega_{\text{p}} \alpha(\omega_{\text{p}})|^2} \right)^{1/2}. \tag{11}$$

We implicitly make use of the slowly varying envelope approximation in this calculation, which is valid as we consider only pulses with $\Delta\omega \ll \omega_0$. This also means that we can neglect the frequency dependence of the propagation constant β_{p} in (10).

To derive expressions for the quantized fields in a nonlinear waveguide, we start from the electric field operator for a propagating field in a dielectric with finite cross-section area $\mathcal{A}$, given in [40]. Note that we assume the wavevector components k_x and k_y of the quantum field to have fixed, finite values.

$$\hat{E}^{(+)}(x, y, z, t) = \mathrm{i} \int \mathrm{d}\omega \left(\frac{\hbar\omega}{4\pi\varepsilon_0 c\, n(\omega) \mathcal{A}} \right)^{1/2} \hat{a}(\omega) \mathrm{e}^{-\mathrm{i}\omega t + \mathrm{i}(k_x x + k_y y + k_z z)}. \tag{12}$$

In a nonlinear waveguide with field propagation along the z-direction, the solution of the Helmholtz equation yields a discrete spectrum of valid propagation constants $\beta_{mn} = k_z^{(mn)}$ and a set of allowed, localized transverse modes $\{f_{mn}(x, y)\}$, determined by the boundary conditions of the guiding geometry. The indices m and n denote the order of the transverse mode in the x- and y-directions. Each β_{mn} corresponds to exactly one mode and, in the case of a symmetric situation, the β_{mn} for the corresponding modes (e.g. β_{01} and β_{10}) become degenerate. For better readability, we only use one index m to describe the modes. The spatial localization of the fields implies continuous spectra of the individual wavevector components $k_x^{(m)}$ and $k_y^{(m)}$, given by $\tilde{f}_m(k_x, k_y) = \mathcal{FT}[f_m(x, y)]$.[5] The electric field inside a nonlinear waveguide is accordingly

[5] We deploy the symmetric definition of the Fourier transform, that is, $\tilde{f}(k) = \frac{1}{\sqrt{2\pi}} \int \mathrm{d}x\, f(x) \mathrm{e}^{-\mathrm{i}kx}$ and accordingly $f(x) = \frac{1}{\sqrt{2\pi}} \int \mathrm{d}k\, \tilde{f}(k) \mathrm{e}^{\mathrm{i}kx}$.

comprised of a superposition of quantum fields of the form given in (12), each corresponding to a single propagation direction. Summing over the transverse waveguide modes and integrating over $k_x^{(m)}$ and $k_y^{(m)}$, we find that

$$\hat{E}^{(+)}(x,y,z,t) = \mathrm{i}\sum_m \int \mathrm{d}\omega \left(\frac{\hbar\omega}{4\pi\varepsilon_0 c\, n_m(\omega)}\right)^{1/2} \hat{a}_m(\omega)\mathrm{e}^{-\mathrm{i}\omega t+\mathrm{i}\beta_m z} \times \int \mathrm{d}k_x^{(m)}\,\mathrm{d}k_y^{(m)}\,\tilde{f}_m(k_x,k_y)\mathrm{e}^{\mathrm{i}k_x^{(m)}x+\mathrm{i}k_y^{(m)}y}. \tag{13}$$

This can—due to the Fourier relationship between position and momentum—be written as

$$\hat{E}^{(+)}(x,y,z,t) = \mathrm{i}\sum_m 2\pi f_m(x,y)\int \mathrm{d}\omega \left(\frac{\hbar\omega}{4\pi\varepsilon_0 c\, n_m(\omega)}\right)^{1/2} \hat{a}_m(\omega)\mathrm{e}^{-\mathrm{i}\omega t+\mathrm{i}\beta_m z}. \tag{14}$$

We would like to point out that we account for the cross-sectional area by the spatial distributions $f_m(x,y)$, which are normalized such that $\int \mathrm{d}x\,\mathrm{d}y|f_m(x,y)|^2 = 1$ and which have units of inverse metres. Moreover, we assume that within the frequency range of the considered fields the variation in the spatial properties is negligible, due to the narrow-band approximation $\Delta\omega \ll \omega_0$. We substitute the electric field operators into (9) and rephrase the interaction Hamiltonian for single-photon frequency conversion as

$$\hat{H}_{\mathrm{int}} = \frac{d_{\mathrm{eff}}\hbar\pi}{c} A_{\mathrm{p}} \sum_{l,m}\sqrt{\frac{\omega_{\mathrm{i}}\omega_{\mathrm{o}}}{n_{\mathrm{i},l}n_{\mathrm{o},m}}}\int \mathrm{d}x\,\mathrm{d}y f_{\mathrm{p}}(x,y) f_{\mathrm{i},l}(x,y) f^*_{\mathrm{o},m}(x,y)\int \mathrm{d}z\,\mathrm{e}^{\mathrm{i}(\beta_{\mathrm{p}}\pm\beta_{\mathrm{i},l}\mp\beta_{\mathrm{o},m})z} \times \int \mathrm{d}\omega_{\mathrm{p}}\,\mathrm{d}\omega_{\mathrm{i}}\,\mathrm{d}\omega_{\mathrm{o}}\alpha(\omega_{\mathrm{p}})\mathrm{e}^{-\mathrm{i}(\omega_{\mathrm{p}}\pm\omega_{\mathrm{i}}\mp\omega_{\mathrm{o}})t}\hat{a}_l(\omega_{\mathrm{i}})\hat{c}^{\dagger}{}_m(\omega_{\mathrm{o}}) + \mathrm{h.c.}, \tag{15}$$

where we discriminate between SFG and DFG. Here, labels i and o denote input and output fields, whereas indices l and m describe the transverse spatial modes of input and output fields respectively.

Now we move on to the calculation of the time evolution of the input quantum state during the conversion process. Note that the interaction of the Hamilton operator of equation (15) is time dependent and thus the exact solution has to take into account time-ordering effects. Here we present an approximate solution that neglects time-ordering effects, in order to emphasize the conceptual structure and to illustrate the main idea. In the appendix, we validate this approach by comparing the approximate solution with rigorous calculations we performed. We find that the shape of the mode functions does not change significantly when taking into account time ordering, but the maximum conversion efficiency drops to 90%. Still, these findings confirm that the analytical solution leads to reasonable results and can safely be applied. Hence, we write the time evolution of the quantum state during the conversion process

$$|\psi\rangle_{\mathrm{out}} = \hat{U}(t)|\psi\rangle_0 = \exp\left(-\frac{\mathrm{i}}{\hbar}\int \mathrm{d}t\,\hat{H}_{\mathrm{int}}(t)\right)|\psi\rangle_0. \tag{16}$$

Thus, we need to perform a time integration of the interaction Hamiltonian given in (15). This is a well-known procedure discussed, for PDC, in great detail in [8]. We only present the result

here, as the calculation, including the waveguide aspects, is straightforward,

$$\int \mathrm{d}t\, \hat{H}_{\mathrm{int}}(t) = \frac{2d_{\mathrm{eff}}\hbar\pi^2}{c} A_{\mathrm{p}} L \sum_{l,m} \sqrt{\frac{\omega_{\mathrm{i}}\omega_{\mathrm{o}}}{n_{\mathrm{i},l} n_{\mathrm{o},m}}} \frac{1}{\sqrt{A^{(\mathrm{eff})}_{l,m}}} \int \mathrm{d}\omega_{\mathrm{i}}\, \mathrm{d}\omega_{\mathrm{o}} \alpha(\omega_{\mathrm{io}}) \phi_{l,m}(\omega_{\mathrm{i}}, \omega_{\mathrm{o}}) \hat{a}_l(\omega_{\mathrm{i}}) \hat{c}^{\dagger}{}_m(\omega_{\mathrm{o}}) + \mathrm{h.c.} \tag{17}$$

Here, L is the length of the nonlinear waveguide. The function $\alpha(\omega_{\mathrm{io}})$ is the spectral pump distribution defined as $\alpha(\omega_{\mathrm{o}} - \omega_{\mathrm{i}})$ for SFG and $\alpha(\omega_{\mathrm{i}} - \omega_{\mathrm{o}})$ for DFG, respectively, whereas the function $\phi_{l,m}(\omega_{\mathrm{i}}, \omega_{\mathrm{o}})$ characterizes the phase-matching and is given by

$$\phi_{l,m}(\omega_{\mathrm{i}}, \omega_{\mathrm{o}}) = \mathrm{sinc}\left(\frac{\Delta\beta_{l,m} L}{2}\right) \approx \exp\left[-0.193 \cdot \left(\frac{\Delta\beta_{l,m} L}{2}\right)^2\right]. \tag{18}$$

The expression $\Delta\beta_{l,m}$ describes the phase-mismatch of the propagation constants and evaluates to $\Delta\beta_{l,m} = \beta_{\mathrm{p}} + \beta_{\mathrm{i},l} - \beta_{\mathrm{o},m} - \frac{2\pi}{\Lambda}$ for SFG and $\Delta\beta_{l,m} = \beta_{\mathrm{p}} - \beta_{\mathrm{i},l} + \beta_{\mathrm{o},m} - \frac{2\pi}{\Lambda}$ for DFG, respectively. Finally, Λ is an optional poling period for quasi-phase-matching inside the waveguide. Following the usual conventions, we define an effective interaction area $A^{(\mathrm{eff})}_{l,m}$,

$$\frac{1}{A^{(\mathrm{eff})}_{l,m}} := \left[\int \mathrm{d}x\, \mathrm{d}y\, f_{\mathrm{p}}(x, y) f_{\mathrm{i},l}(x, y) f^{*}_{\mathrm{o},m}(x, y)\right]^2. \tag{19}$$

Note that this should not be mistaken as a geometric area defined, for instance, by the waveguide cross-section. Instead it describes the overlap of the transverse spatial modes of the three interacting fields inside the nonlinear waveguide. This result also implies that simply using a smaller waveguide—while not changing the modal overlap characteristics—will not alter $A^{(\mathrm{eff})}$ and will therefore not have any impact on the efficiencies of the processes. The product of pump distribution and phase-matching function is conveniently defined as the joint spectral distribution function,

$$G_{l,m}(\omega_{\mathrm{i}}, \omega_{\mathrm{o}}) = \frac{1}{N_{l,m}} \alpha(\omega_{\mathrm{io}}) \phi_{l,m}(\omega_{\mathrm{i}}, \omega_{\mathrm{o}}), \tag{20}$$

which describes the mapping between input and output frequencies for a specific pair of spatial modes l, m. The normalization factor $N_{l,m}$ reads $(\int \mathrm{d}\omega_{\mathrm{i}}\, \mathrm{d}\omega_{\mathrm{o}} |\alpha(_{\mathrm{io}}) \phi_{l,m}(\omega_{\mathrm{i}}, \omega_{\mathrm{o}})|^2)^{1/2}$.

4.2. Broadband pulse mode picture

The description derived so far has been in terms of monochromatic creation and annihilation operators. However, since we concentrate on $\chi^{(2)}$-interactions between ultrafast pulses, a much more natural approach is to consider broadband pulse modes. A suitable pulse-mode basis is found by applying a Schmidt decomposition to the joint spectral distribution function,

$$G_{l,m}(\omega_{\mathrm{i}}, \omega_{\mathrm{o}}) = \sum_j \kappa^{(l,m)}_j \varphi^{(l,m)}_j(\omega_{\mathrm{i}}) \psi^{(l,m)}_j(\omega_{\mathrm{o}}). \tag{21}$$

Equation (21) yields two correlated sets of orthonormal broadband pulse-mode functions $\{\varphi^{(l,m)}(\omega_{\mathrm{i}})\}$ and $\{\psi^{(l,m)}(\omega_{\mathrm{o}})\}$. The diagonal values $\kappa^{(l,m)}_j$ are the real and positive Schmidt coefficients and satisfy $\sum_j (\kappa^{(l,m)}_j)^2 = 1$. It is well known, for PDC, that the basis sets of the Schmidt decomposition, and thus the modal structure of the photons, are uniquely defined [2].

The same argument can also be applied here in the context of SFG and DFG. As for PDC, we define broadband creation and annihilation operators,

$$\hat{A}_{j,l,m} = \int \mathrm{d}\omega_\mathrm{i}\, \varphi_j^{(l,m)}(\omega_\mathrm{i})\hat{a}_l(\omega_\mathrm{i}), \tag{22}$$

$$\hat{C}_{j,l,m} = \int \mathrm{d}\omega_\mathrm{o}\, \psi_j^{(l,m)}(\omega_\mathrm{o})\hat{c}_m(\omega_\mathrm{o}). \tag{23}$$

Substituting those, we rewrite the expression for the time-integrated interaction Hamiltonian from (17), and arrive at the broadband pulse-mode picture,

$$\begin{aligned}\int \mathrm{d}t\, \hat{H}_\mathrm{int}(t) &= \frac{2d_\mathrm{eff}\hbar\pi^2}{c} A_\mathrm{p} L \sum_{l,m} \sqrt{\frac{\omega_\mathrm{i}\omega_\mathrm{o}}{n_{\mathrm{i},l} n_{\mathrm{o},m}}} \frac{N_{l,m}}{\sqrt{A_{l,m}^{(\mathrm{eff})}}} \sum_j (\kappa_j^{(l,m)} \hat{A}_{j,l,m}\hat{C}_{j,l,m}^\dagger + \mathrm{h.c.}) \\ &= \hbar \sum_{l,m}\sum_j \theta_{j,l,m}(\hat{A}_{j,l,m}\hat{C}_{j,l,m}^\dagger + \hat{A}_{j,l,m}^\dagger \hat{C}_{j,l,m}).\end{aligned} \tag{24}$$

By introducing the effective coupling constant $\theta_{j,l,m}$ into (24), we reveal the simple beamsplitter structure of the Hamiltonian [41], as already announced in (6). In contrast to a conventional beamsplitter, however, this Hamiltonian does not couple two k-modes (or beam paths), but rather two broadband pulse modes $\hat{A}_{j,l,m}$ and $\hat{C}_{j,l,m}$ at different frequencies! This is a unique feature of ultrafast frequency conversion processes and makes them ideal candidates for the implementation of the QPG and QPS.

5. Pushing towards applications

5.1. General non-engineered SFG and DFG

QPG and QPS are unique in their single-mode operation on broadband pulse modes. In this section, we discuss the implementation of genuine QPG or QPS in a feasible experimental setup. We restrict the analysis to only one pair of transverse spatial modes (l, m), which simplifies the notation but does not change the underlying physics. In the experimental setting, the selection of one spatial mode can be accomplished by broadband spectral filtering [13]. In this case, the time-integrated, effective SFG and DFG Hamiltonian from (24) reads

$$\int \mathrm{d}t\, \hat{H}_\mathrm{int}(t) = \hbar \sum_j \theta_j(\hat{A}_j\hat{C}_j^\dagger + \hat{A}_j^\dagger \hat{C}_j), \tag{25}$$

with the broadband operators defined as

$$\hat{A}_j = \int \mathrm{d}\omega_\mathrm{i}\, \varphi_j(\omega_\mathrm{i})\hat{a}(\omega_\mathrm{i}), \tag{26}$$

$$\hat{C}_j = \int \mathrm{d}\omega_\mathrm{o}\, \psi_j(\omega_\mathrm{o})\hat{c}(\omega_\mathrm{o}). \tag{27}$$

The complete, orthonormal function sets $\{\varphi_j(\omega_\mathrm{i})\}$ and $\{\psi_j(\omega_\mathrm{o})\}$ represent the intrinsic pulse-mode structure of the SFG or DFG processes, obtained from the Schmidt decomposition of the joint spectral distribution function $G(\omega_\mathrm{i}, \omega_\mathrm{o}) = \alpha(\omega_\mathrm{io})\phi(\omega_\mathrm{i}, \omega_\mathrm{o})$. On the one hand, these are determined by the pump pulse characteristics, but on the other hand they also depend

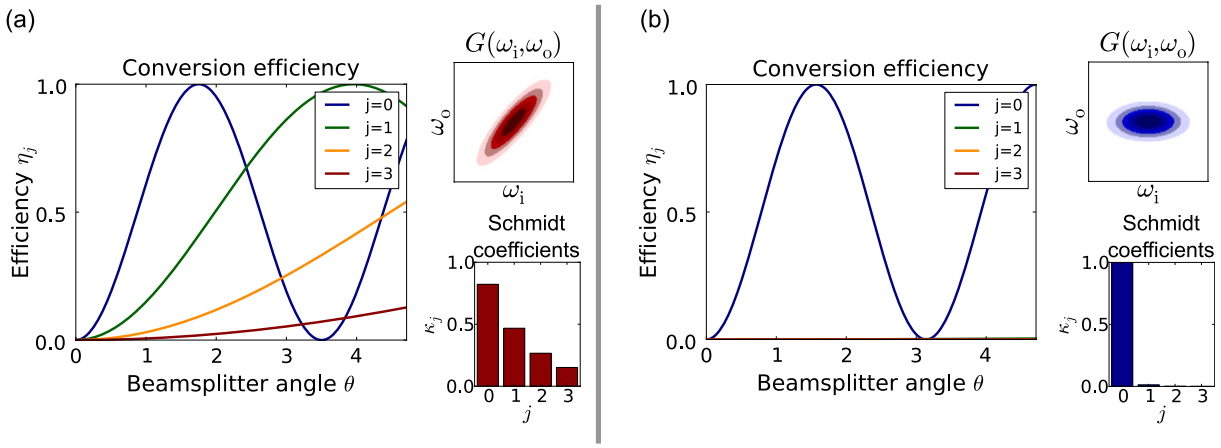

Figure 3. Conversion efficiencies η_j, joint spectral distribution functions $G(\omega_\mathrm{i}, \omega_\mathrm{o})$ and Schmidt coefficients κ_j for the first four pairs of pulse modes ($j = 0, \ldots, 3$). (a) Non-engineered process with several $\kappa_j \neq 0$. For a given overall beamsplitter angle θ, all modes are converted to a certain extent given by $\eta_j = \sin(\kappa_j \cdot \theta)^2$. However, an overall unit efficiency can generally not be accomplished. (b) Source-engineered process with one predominant $\kappa_j \approx 1$. By choosing an appropriate θ, pulse mode $\varphi(\omega_\mathrm{i})$ can be converted into pulse mode $\psi(\omega_\mathrm{o})$ with unit efficiency, allowing for QPG operation.

critically on the nonlinear waveguide's material and modal dispersion properties. We have already stressed the formal equivalence between the expression from (25) and a sum of optical beamsplitter Hamiltonians. Hence the linear transformation for the broadband operators can be readily written as

$$\hat{A}_j \to \cos(\theta_j)\hat{A}_j - \mathrm{i}\sin(\theta_j)\hat{C}_j, \tag{28}$$

corresponding to a pulse mode conversion between $\varphi_j(\omega_\mathrm{i})$ and $\psi_j(\omega_\mathrm{o})$ with efficiency $\eta_j = \sin^2(\theta_j)$. According to (24), the coupling constant θ_j is given by

$$\theta_j = \kappa_j \cdot \frac{2d_\mathrm{eff}\pi^2 LN}{c}\sqrt{\frac{2\omega_\mathrm{i}\omega_\mathrm{o}}{c\,\varepsilon_0 n_\mathrm{p} n_\mathrm{i} n_\mathrm{o}\left|\int \mathrm{d}\omega_\mathrm{p}\alpha(\omega_\mathrm{p})\right|^2}}\sqrt{\frac{P_\mathrm{p}}{A^{(\mathrm{eff})}}} = \kappa_j \cdot \theta. \tag{29}$$

Here, θ is an overall beamsplitter angle defined by the process parameters. Its impact on the different modes j is given by θ_j, where, for each mode, the overall beamsplitter angle is weighted with the corresponding Schmidt coefficient κ_j. In figure 3(a), we illustrate a general, non-engineered SFG. We show the joint spectral distribution function $G(\omega_\mathrm{i}, \omega_\mathrm{o})$ as well as the Schmidt coefficients κ_j for the first four pairs of pulse modes and plot the conversion efficiencies η_j versus the beamsplitter angle θ. It is obvious that for any given value of θ, all pulse modes with $\kappa_j \neq 0$ are converted to a certain extent. Yet, in general, single-mode operation is not achievable, nor can conversion with $\eta_j = 1$ for different pulse modes simultaneously be accomplished. We note an exception to this rule: under certain conditions (e.g. a cw pump), input and output modes are perfectly correlated. Then all κ_j share the same value and all modes are converted with the same efficiency. The process is then highly multimode but the overall efficiency can reach unity for high pump powers.

5.2. Source-engineered SFG and DFG: towards genuine QPG and QPS

We have shown that SFG and DFG in general are multimode processes. But for QPG and QPS we require single-mode operation in order to avoid the signal degradation introduced by vacuum contributions and to achieve unit efficiency. Reducing the intrinsic pulse-mode structure of a $\chi^{(2)}$-nonlinear process to only one pair of modes has been extensively studied in PDC, where source engineering led to the desired results [8, 15, 16]. Experimentally, this is accomplished by group-velocity matching inside the nonlinear medium. If the pump and either the signal or the idler share the same group velocity, the phase-matching function becomes parallel to one of the axes when plotted in an $(\omega_\mathrm{s}, \omega_\mathrm{i})$-diagram. Then, the Schmidt decomposition yields—given that the process is pumped by an ultrafast pump—only one pair of pulse modes that is excited with unit efficiency.

We transfer this insight to our analysis of SFG and DFG and employ it for spectral engineering of the conversion. The time-integrated Hamiltonian from (25) for our special case reduces to

$$\int \mathrm{d}t\, \hat{H}_\mathrm{int} = \hbar\theta(\hat{A}\hat{C}^\dagger + \hat{A}^\dagger\hat{C}) \tag{30}$$

and can be interpreted as a beamsplitter operating on only one pair of pulse modes $\varphi(\omega_\mathrm{i})$ and $\psi(\omega_\mathrm{o})$. As an example, we show an engineered case in figure 3(b), where pump and input signals are group-velocity matched. Note that, in contrast to the previous non-engineered case, the joint spectral distribution function now shows no spectral correlations between input and output frequencies; that is, it is oriented along the axes of the diagram. As in PDC, this is a direct consequence of the horizontally oriented phase-matching function and thus of the group-velocity matching. The distribution of κ_j reveals that only one coefficient, κ_0, differs significantly from zero. This is also reflected in the plot of the conversion efficiencies. Only a single pulse mode is addressed and, by choosing $\theta = \frac{\pi}{2}$, converted with unit efficiency, and no vacuum is coupled into the signal beam. Hence we find that by group-velocity matching the pump and either the input or the output, we can achieve genuine single-mode operation and therefore implement QPG and QPS. Note that the data in figure 3 have been calculated using our modelling and realistic experimental parameters, which are specified in section 6.

Knowing how to achieve single-mode operation of SFG and DFG, the next step is to investigate how we can exact complete control over the pulse modes $\varphi(\omega_\mathrm{i})$ and $\psi(\omega_\mathrm{o})$. A QPG selects a specific pulse mode from an input state and a QPS generates an arbitrary pulse mode from a Gaussian input mode. Hence, for QPG we require control over $\varphi(\omega_\mathrm{i})$, whereas for QPS we require the shaping of $\psi(\omega_\mathrm{o})$, respectively. In figures 4(a)–(c), we consider QPG. Shown are the phase-matching and pump functions as well as the resulting joint spectral distribution function. Note that the axes are given wavelength units rather than frequency for convenience. We find that the output mode $\psi(\omega_\mathrm{o})$ is defined solely by the phase-matching. We performed calculations for three different spectral shapes of the pump and it is obvious that the input mode $\varphi(\omega_\mathrm{i})$ has the form of the respective pump mode. Thus, in a QPG, spectrally shaping the bright gating pulse leads to the selection of an arbitrary pulse mode. In contrast, figures 4(d)–(f) illustrate the situation for QPS. Now, the pump and the output are group-velocity matched, causing a vertical phase-matching function. Again we calculated three different spectral pump distributions. We find that the spectral shape of the pump now defines the output mode $\psi(\omega_\mathrm{o})$ of the QPS and the input mode $\varphi(\omega_\mathrm{i})$ is fixed by the phase-matching. Summing up these findings,

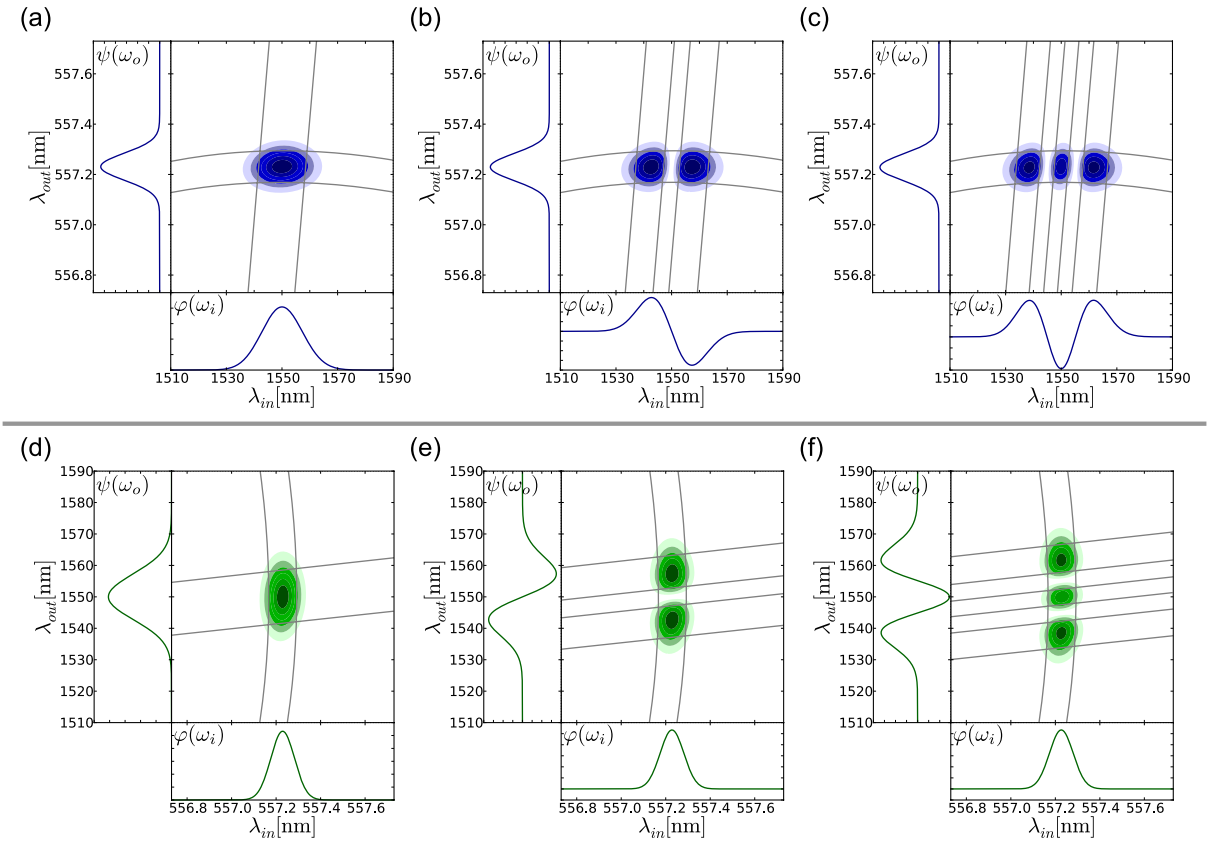

Figure 4. Joint spectral distribution, pump and phase-matching function as well as pulse modes $\varphi(\omega_\mathrm{i})$ and $\psi(\omega_\mathrm{o})$ for QPG (a–c) and QPS (d–f). Note that the functions are plotted against wavelengths for reasons of convenience. In a QPG, the intrinsic pulse mode $\varphi(\omega_\mathrm{i})$ can be manipulated by shaping the bright gating pulse, whereas the pulse mode $\psi(\omega_\mathrm{o})$ is fixed by the phase-matching function. Therefore, arbitrary input modes are mapped to the same output mode, allowing for interference of formerly orthogonal modes. In contrast, in a QPS, shaping the bright pulse defines the output pulse mode $\psi(\omega_\mathrm{o})$. The input pulse mode is now defined by the phase-matching function. Thus, an arbitrary mode can be generated from an input that is matched to $\varphi(\omega_\mathrm{i})$. The data presented here are calculated using realistic experimental parameters, as specified in section 6.

we end up with the following correspondences,

$$\alpha(\omega_\mathrm{p}) \to \varphi(\omega_\mathrm{i}), \quad \phi(\omega_\mathrm{i}, \omega_\mathrm{o}) \to \psi(\omega_\mathrm{o}) \quad \text{for QPG}, \tag{31}$$

$$\phi(\omega_\mathrm{i}, \omega_\mathrm{o}) \to \varphi(\omega_\mathrm{i}), \quad \alpha(\omega_\mathrm{p}) \to \psi(\omega_\mathrm{o}) \quad \text{for QPS}. \tag{32}$$

We have demonstrated that we can achieve complete control over the required pulse mode of the QPG or QPS by shaping the bright gating pulse or shaping pulse, respectively. Note, however, that we considered only the intrinsic modes of the QPG and QPS, which do not necessarily have to coincide with the pulse-mode structure of an input signal.

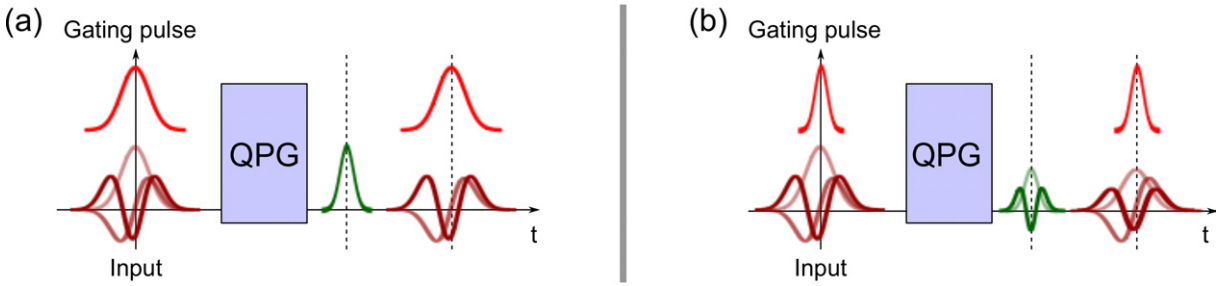

Figure 5. (a) Mode-matched QPG. The bright gating pulse has the same duration as the input signal, leading to matching of the input pulse-mode structure and $\varphi(\omega_i)$ of the QPG. Only a single pulse mode of the input—the one that overlaps with $\varphi(\omega_i)$—is selected and converted with unit efficiency. (b) Mode-mismatch in a QPG. The gating pulse and input signal have different durations, leading to an overlap of $\varphi(\omega_i)$ with all input signal modes with the same parity. Hence, all of those modes are selected and converted to a certain degree. QPG operation is then not possible.

5.3. Mode matching a QPG or a QPS

Given a specific QPG or QPS, the input signal's pulse-mode structure must coincide with the pulse modes $\{\varphi(\omega_i)\}$ accepted by the device, in order to guarantee mode selectivity and high conversion efficiency. We first discuss this for the QPG. We have shown that the QPG can be easily adapted to a wide range of input signals by spectrally shaping the coherent gating pulse. The output mode $\psi(\omega_o)$ is solely defined by the phase-matching function and is independent of the pump pulse shape. It can typically be approximated by a Gaussian spectrum [8]. Hence any selected mode from an input state is mapped to the same output mode.

In figure 5(a), we illustrate this situation. The input signal and gating pulse share the same duration and the QPG is mode-matched to the input. Only the desired mode from the input signal is selected and converted with unit efficiency. In contrast, figure 5(b) demonstrates the impact of a mode mismatch on the QPG operation. The gating pulse duration significantly differs from the input pulse duration and the intrinsic QPG pulse mode $\varphi(\omega_i)$ overlaps with all signal modes of the same parity. We end up with a case similar to multimode SFG, with the only difference being that the diverse conversion efficiencies for the modes are due to the different overlaps between $\varphi(\omega_i)$ and the corresponding signal-state modes. Because an overall efficiency of unity cannot be achieved here and the process is not mode-selective anymore, it becomes clear that careful mode-matching is vital for a successful QPG implementation.

The situation is different for QPS: the phase-matching function is vertical in the (ω_i, ω_o)-plane (compare figures 4(c)–(f)) and the input mode $\varphi(\omega_i)$ is now defined by the phase-matching function alone. The QPS accepts only Gaussian input modes that are matched to $\varphi(\omega_i)$. However, shaping the bright pulse allows for defining the output mode $\psi(\omega_o)$, rendering it possible to generate any pulse mode from an input pulse with a Gaussian spectrum. If the input state is not matched to $\varphi(\omega_i)$, this does not change the spectral form of the output pulse. The drawback is that it is not the complete input that gets converted and vacuum contributions are introduced.

We note that the same physical nonlinear waveguide device could be used as QPG or QPS, depending on whether SFG or DFG is implemented: this shows that QPG and QPG can be

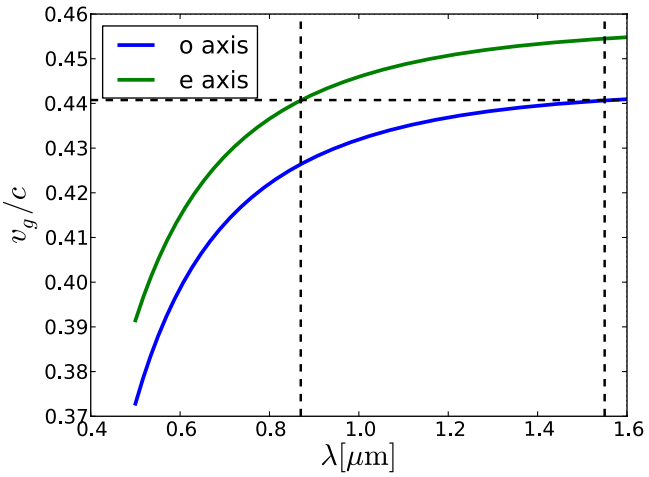

Figure 6. Group velocities of the fundamental waveguide modes in a Ti-indiffused PPLN waveguide. For a 1550 nm input oriented along the ordinary axis, an extraordinarily polarized pump pulse centred on 870 nm is group-velocity matched. For a QPG, this consequently leads to an output at 557 nm that has to be oriented along the ordinary axis. It becomes obvious that for a wide range of input signal wavelengths, group-velocity matched gating pulses can be found that still satisfy feasible experimental parameters.

seen as reverse operations of each other. The results illustrate that QPG and QPS are versatile tools that can be easily adapted to a large range of input and output states, making them highly flexible and appealing for many applications.

6. Performance of QPG and QPS considering realistic experimental parameters

We conclude our analysis demonstrating the experimental feasibility of a QPG and derive, with the help of the theoretical model outlined in sections 3–5, an expression for the pump power for maximally efficient operation. The results of the calculation apply to QPS as well, since both devices can be implemented in the same nonlinear waveguide. SFG phase-matching implies an existing DFG phase-matching; only the roles of input and output fields are interchanged. The coupling constant θ is the same for both processes. The bright pulse, used as a gating or shaping pulse depending on the application, will be called a pump in this paragraph for ease of reading. The input field is at 1550 nm and the third field is referred to as the output.

As a key point for the experimental setup, we require that it can be operated at 1550 nm. The constraint of group-velocity matching determines the pump wavelength as soon as the input wavelength gets fixed, which in turn then also defines the output wavelengths due to energy conservation. We assume that the conversion takes place in a Ti-indiffused PPLN waveguide with a length of $L = 10$ mm and at a temperature of $T = 190^{\circ}$C to prevent the impact of photorefraction. The effective Sellmeier equations for the three participating fields were obtained by calculating the effective refractive indices of ordinary and extraordinary polarized fields with a finite-element method described in [42]. The effective equations were then fitted against the calculated values. Note that the following calculations are based on these effective Sellmeier equations.

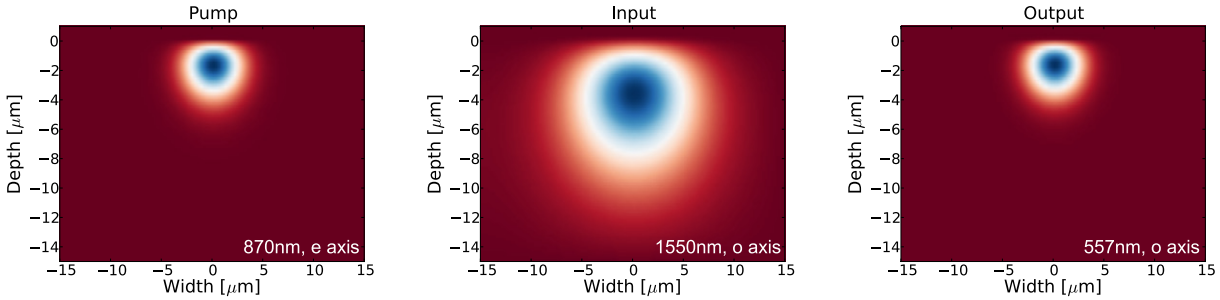

Figure 7. Transverse spatial mode profiles of the fundamental waveguide modes in a Ti-indiffused PPLN waveguide. The mode profiles were calculated using a finite elements method. The overlap between the pump and the output exceeds 99% because the guiding for ordinarily polarized fields is not as strongly pronounced as for extraordinarily polarized fields.

In figure 6, we plot the group velocities for the ordinary and extraordinary crystal axes and assume for our modelling that all fields propagate in the fundamental transverse waveguide mode. If the input light is ordinarily (TE-)polarized with a central wavelength of 1550 nm, we find that the group-velocity matched pump has to be extraordinarily (TM-) polarized and centred on 870 nm. The ordinarily polarized output is then at 557 nm. From figure 6, we can clearly recognize that a group-velocity matched pump can be found for any input, as long as the input is o-polarized. The effective refractive indices of the participating fields were calculated to be $n_\mathrm{p} = 2.18$, $n_\mathrm{i} = 2.21$ and $n_\mathrm{o} = 2.32$ and we derive a periodic poling period of $\Lambda \approx 4.28\,\mu$m required for quasi-phase-matching inside the waveguide.

In figure 7, we plot the transverse spatial distributions of the input, pump and output modes, also obtained with the finite-element method from [42]. From these we calculate the effective interaction area $A^{(\mathrm{eff})} \approx 64\,\mu\mathrm{m}^2$. The conversion efficiency for a single-mode operation is $\eta = \sin^2(\theta)$ and the condition for unit efficiency can be specified by

$$\theta \stackrel{!}{=} \frac{\pi}{2}, \tag{33}$$

$$P_\mathrm{p} \stackrel{!}{=} \left(\frac{c}{4\pi d_\mathrm{eff} L N}\right)^2 \frac{c\,\varepsilon_0 n_\mathrm{p} n_\mathrm{i} n_\mathrm{o} |\int \mathrm{d}\omega_\mathrm{p} \alpha(\omega_\mathrm{p})|^2 A^{(\mathrm{eff})}}{2\omega_\mathrm{i}\omega_\mathrm{o}}. \tag{34}$$

Assuming an input pulse duration of roughly 300 fs, we calculate a required pump peak power of $P_\mathrm{p} \approx 22$ W for optimal conversion efficiency. If a pump laser system with a repetition frequency of 76 MHz is used, we obtain an average pump power of $P_\mathrm{av} \approx 0.5$ mW inside the waveguide. This leads to required average pump powers of a few mW in front of the QPG or QPS, taking into account realistic waveguide coupling losses. These values are lower than formerly reported pump powers for similar experiments [22–24, 27, 29], owing to the careful source engineering that we applied to our process. This grants a significant advantage over experiments without spectrally engineered SFG, even though we employ a cross-polarized process with an effective nonlinearity that is lower by one order of magnitude than that of a process where all three fields are oriented along the extraordinary crystal axis.

7. Conclusion and outlook

In conclusion, we have presented a feasible way to achieve complete control over the pulse-mode structure of ultrafast pulsed quantum states of light. We combined findings from quantum state generation and techniques from state manipulation, by applying spectral-source engineering and integrated optics to frequency conversion of ultrafast single photons. We showed that single-mode ultrafast SFG and DFG in $\chi^{(2)}$-nonlinear materials are possible and analysed two highly flexible and versatile devices, namely QPG and QPS. The QPG is based on ultrafast SFG and offers the possibility of selecting arbitrary pulse modes from an ultrafast multimode input state. The selected mode gets converted with unit efficiency and is mapped onto a Gaussian output mode. The residual mode structure of the input is left intact, allowing for cascaded operation to convert multiple modes. As all input modes are mapped onto the same output mode, interference of formerly orthogonal states becomes possible. In contrast, the newly introduced QPS is based on DFG and implements the reverse operation of a QPG. It enables us to generate an arbitrary pulse form from a Gaussian input mode. The output mode is defined by a bright shaping pulse; thus highly flexible state preparation can be achieved. We have presented a quantitative analysis of QPG and QPS and derived feasible experimental parameters with which the proposed devices can be implemented, rendering them practical instead of merely conceptual.

As a final remark, we would like to point out that our analysis is in no way constrained to single-photon states. Although we consider single-photon input states, the introduced concepts can be generalized to classical and non-classical multi-photon states. In this framework, the use of QPG and QPS provides us with an attractive opportunity to successively select and spatially separate arbitrary pulse modes from a multimode input state while leaving the residual beam intact. Employing a series of QPGs operating on the same pulse mode in each arm of a multimode twin-beam squeezer source allows for a feasible implementation of non-Gaussian operations and thus constitutes an important step towards the realization of multimode continuous variable entanglement distillation. QPS, on the other hand, can be used to synthesize multimode continuous variable Gaussian states in a mode-by-mode fashion. The prepared states can then be transmitted as a bundle, since they do not interact with each other and since they all experience the same dispersion during transmission and therefore stay orthogonal. This paves the way for dense channel multiplexing in continuous variable quantum communication.

Acknowledgments

We thank Michael Raymer for invaluable discussions on this work. The research leading to these results received funding from the European Community's Seventh Framework Programme FP7/2001-2013 under grant agreement no. 248095 through the Integrated Project Q-ESSENCE.

Appendix. Impact of time ordering

Since the interaction of the Hamilton operator of equation (15) is time dependent, it might be assumed that time-ordering effects have a major impact on the intrinsic mode structure of the process, in particular if a perturbative solution is not sufficient. This case is associated with unit conversion efficiency, needed for perfect QPG and QPS operation. In our analysis, we have nevertheless deployed the approximate solution that neglects time ordering. The impact of time ordering on the process of ultrafast PDC has been thoroughly investigated in [43], with the result

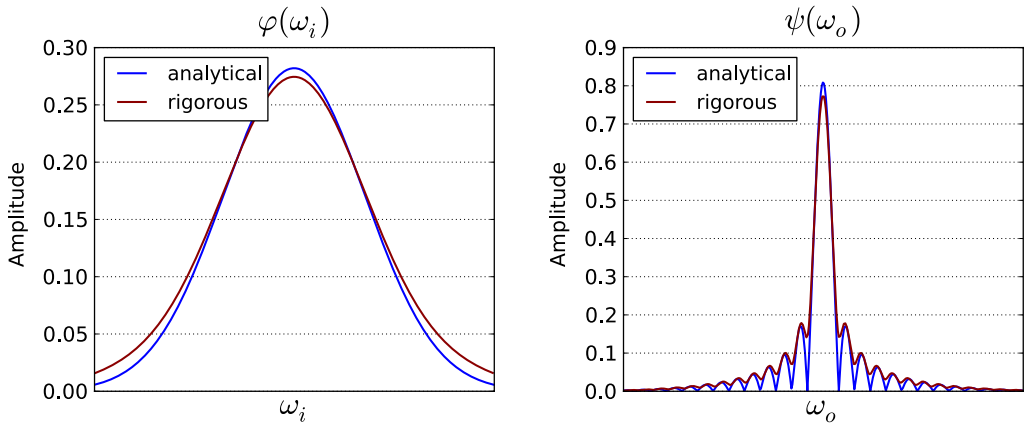

Figure A.1. Input modes $\varphi(\omega_i)$ as well as output modes $\psi(\omega_o)$ of the considered processes, obtained from the analytical solution (blue) and rigorous calculation (red), respectively. Obviously, time ordering has only a small impact on the actual mode shape. This can simply be corrected for in our schemes by adjusting the spectrum of the bright pump pulse. Note that the oscillations in the output modes originate from the sinc function that describes the phase matching.

that time ordering mostly affects the amplitudes but not the shapes of the intrinsic pulse modes. In [37], the authors actually study a three-wave mixing process and find in their numerical simulation no major discrepancy with their analytical solution. This already indicates that, at least for low conversion efficiencies where a perturbative solution is sufficient, time ordering can be neglected. However, since we aim at conversion efficiencies of unity and cannot conclude for sure that the above results remain valid in our case, we performed rigorous numerical simulations that take into account all time-ordering effects. Note that the results presented are all obtained for the case of maximum conversion efficiency. Additionally, the simulated processes are the ones discussed in this work. That is, the pump pulse and the input pulse are group-velocity matched and the processes have decorrelated joint spectral distribution functions, as is the case in figure 3(b).

Figure A.1 depicts the analytical as well as the rigorous input modes $\varphi_{\mathrm{ana}}(\omega_i)$ and $\varphi_{\mathrm{rig}}(\omega_i)$ and the corresponding output modes $\psi_{\mathrm{ana}}(\omega_o)$ and $\psi_{\mathrm{rig}}(\omega_o)$, respectively. It nicely illustrates that time ordering has only a slight impact on the shape of the modes, as expected from [43]. The change in the modes can easily be compensated for, in our proposed scheme, by adjusting the spectrum of the bright gating pulse. Note that the oscillations in the output modes originate from the sinc function that describes the phase-matching. These also cause the slight multi-modeness that can be seen in the Schmidt coefficients in figure A.2, where the first higher-order mode is also excited with a certain probability. Comparing again analytical and rigorous solutions, we find that time ordering slightly shifts the weights between the different modes. However, we want to note that no new modes occur in the process due to time ordering. The main difference is found when considering the maximum conversion efficiency. It turns out that this value drops in the rigorous solution to 90%, instead of the unit efficiency obtained with the analytical approach.

This behaviour will be thoroughly analysed in [44]. We want to stress here that all characteristics introduced by the side lobes of the sinc function can be washed out through careful design of the nonlinearity inside the waveguide, as shown in [45]. Therefore the device

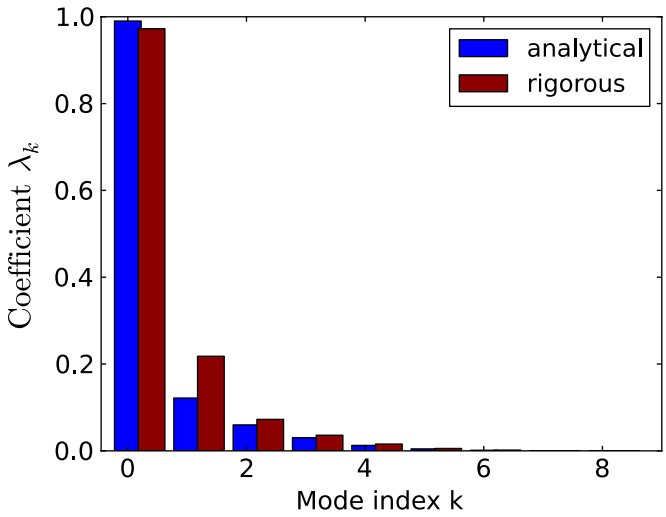

Figure A.2. Schmidt coefficients λ_k obtained from the analytical as well as the rigorous solution. Time ordering causes a slight shift in the excitation of the different modes. In addition, it leads to a drop in the maximum conversion efficiency to 90%, as compared with the unit conversion efficiency reached in the analytical solution.

performance calculated here only represents a lower bound and might be increased in the future, for instance by implementing a Gaussian-shaped phase-matching function.

In conclusion, we find by comparing analytical and numerical solutions that the assumption that time ordering can be neglected is, in fact, a rather good approximation, even for the cases of high conversion efficiencies analysed in this work.

References

[1] Titulaer U M and Glauber R J 1966 Density operators for coherent fields *Phys. Rev.* **145** 1041–50
[2] Martinelli M, Treps N, Ducci S, Gigan S, Maître A and Fabre C 2003 Experimental study of the spatial distribution of quantum correlations in a confocal optical parametric oscillator *Phys. Rev.* A **67** 023808
[3] Knill E, Laflamme R and Milburn G J A 2001 Scheme for efficient quantum computation with linear optics *Nature* **409** 46–52
[4] Eckstein A, Brecht B and Silberhorn C 2010 A quantum pulse gate based on spectrally engineered sum frequency generation arXiv:1007.3215
[5] Keller T E and Rubin M H 1997 Theory of two-photon entanglement for spontaneous parametric down-conversion driven by a narrow pump pulse *Phys. Rev.* A **56** 1534–41
[6] Grice W P, U'Ren A B and Walmsley I A 2001 Eliminating frequency and space-time correlations in multiphoton states *Phys. Rev.* A **64** 063815
[7] Law C K, Walmsley I A and Eberly J H 2000 Continuous frequency entanglement: effective finite hilbert space and entropy control *Phys. Rev. Lett.* **84** 5304–7
[8] U'Ren A B, Silberhorn C, Banaszek K, Walmsley I A, Erdmann R, Grice W P and Raymer M G 2005 Generation of pure-state single-photon wavepackets by conditional preparation based on spontaneous parametric downconversion *Laser Phys.* **15** 146–61
[9] de Riedmatten H, Marcikic I, Tittel W, Zbinden H and Gisin N 2003 Quantum interference with photon pairs created in spatially separated sources *Phys. Rev.* A **67** 022301

[10] Kaltenbaek R, Blauensteiner B, Zukowski M, Aspelmeyer M and Zeilinger A 2006 Experimental interference of independent photons *Phys. Rev. Lett.* **96** 240502
[11] Tanzilli S, de Riedmatten H, Tittel W, Zbinden H, Baldi P, de Micheli M, Ostrowsky D B and Gisin N 2001 Highly efficient photon-pair source using periodically poled lithium niobate waveguide *Electron. Lett.* **37** 26–8
[12] Fiorentino M, Spillane S M, Beausoleil R G, Roberts T D, Battle P and Munro M W 2007 Spontaneous parametric down-conversion in periodically poled KTP waveguides and bulk crystals *Opt. Express* **15** 7479–88
[13] Mosley P J, Christ A, Eckstein A and Silberhorn C 2009 Direct measurement of the spatial-spectral structure of waveguided parametric downconversion *Phys. Rev. Lett.* **103** 233901
[14] Garay-Palmett K, Rangel-Rojo R and U'Ren A B 2009 Tailored photon pair preparation relying on full group velocity matching in fibre-based spontaneous four-wave mixing *J. Mod. Opt.* **56** 946
[15] Mosley P J, Lundeen J S, Smith B J, Wasylczyk P, U'Ren A B, Silberhorn C and Walmsley I A 2008 Heralded generation of ultrafast single photons in pure quantum states *Phys. Rev. Lett.* **100** 133601
[16] Kuzucu O, Wong F N C, Kurimura S and Tovstonog S 2008 Joint temporal density measurements for two-photon state chracterization *Phys. Rev. Lett.* **101** 153602
[17] Shi X, Valencia A, Hendrych M and Torres J 2008 Generation of indistinguishable and pure heralded single photons with tunable bandwidth *Opt. Lett.* **33** 875–7
[18] Cohen O, Lundeen J S, Smith B J, Puentes G, Mosley P J and Walmsley I A 2009 Tailored photon-pair generation in optical fibers *Phys. Rev. Lett.* **102** 123603
[19] Halder M, Fulconis J, Cemlyn B, Clark A, Xiong C, Wadsworth W J and Rarity J G 2009 Nonclassical 2-photon interference with separate intrinsically narrowband fibre sources. *Opt. Express* **17** 4670–6
[20] Söller C, Brecht B, Mosley P J, Zang L, Podlipensky A, Joly N Y, Russell P, St J and Silberhorn C 2010 Bridging visible and telecom wavelengths with a single-mode broadband photon pair source *Phys. Rev.* A **81** 031801
[21] Eckstein A, Christ A, Mosley P J and Silberhorn C 2011 Highly efficient single-pass source of pulsed single-mode twin beams of light *Phys. Rev. Lett.* **106** 013603
[22] Roussev R V, Langrock C, Kurz J R and Fejer M M 2004 Periodically poled lithium niobate waveguide sum-frequency generator for efficient single-photon detection at communication wavelengths *Opt. Lett.* **29** 1518–20
[23] VanDevender A P and Kwiat P G 2004 High efficiency single photon detection via frequency up-conversion *J. Mod. Opt.* **51** 1433–45
[24] Langrock C, Diamanti E, Roussev R V, Yamamoto Y, Fejer M M and Takesue H 2005 Highly efficient single-photon detection at communication wavelengths by use of upconversion in reverse-proton-exchangend periodically poled $LiNbO_3$ waveguides *Opt. Lett.* **30** 1725–7
[25] Albota M A and Robinson B S 2010 Photon-counting 1.55 μm optical communications with pulse-position modulation and a multimode upconversion single-photon receiver *Opt. Lett.* **35** 2627–9
[26] Huang J and Kumar P 1992 Observation of quantum frequency conversion *Phys. Rev. Lett.* **68** 2153–6
[27] Tanzilli S, Tittel W, Halder M, Alibart O, Baldi P, Gisin N and Zbinden H 2005 A photonic quantum information interface *Nature* **437** 116–20
[28] Van Denvender A P and Kwiat P G 2007 Quantum transduction via frequency upconversion (invited) *J. Opt. Soc. Am.* B **24** 295–9
[29] Rakher M T, Ma L, Slattery O, Tang X and Srinivasan K 2010 Quantum transduction of telecommunications-band single photons from a quantum dot by frequency upconversion *Nat. Photonics* **4** 786–91
[30] McGuinness H J, Raymer M G, McKinstrie C J and Radic S 2010 Quantum frequency translation of single-photon states in a photonic crystal fibre *Phys. Rev. Lett.* **105** 093604
[31] Koshino K 2009 Down-conversion of a single photon with unit efficiency. *Phys. Rev.* A **79** 013804
[32] Ding Y and Ou Z Y 2010 Frequency downconversion for a quantum network *Opt. Lett.* **35** 2591–3
[33] Takesue H 2010 Single-photon frequency down-conversion experiment *Phys. Rev.* A **82** 013833

[34] Dayan B, Pe'er A, Friesem A A and Silberberg Y 2004 Two photon absorption and coherent control with broadband down-converted light *Phys. Rev. Lett.* **93** 023005
[35] Pe'er A, Dayan B, Friesem A A and Silberberg Y 2005 Temporal shaping of entangled photons *Phys. Rev. Lett.* **94** 073601
[36] Dayan B, Bromberg Y, Afek I and Silberberg Y 2007 Spectral polarization and spectral phase control of time-energy entangled photons *Phys. Rev.* A **75** 043804
[37] Kielpinski D, Corney J F and Wiseman H M 2011 Quantum optical waveform conversion *Phys. Rev. Lett.* **106** 130501
[38] Barnett S M and Radmore P M 1997 *Methods in Theoretical Quantum Optics* (Oxford: Oxford Science)
[39] Loudon R 2000 *The Quantum Theory of Light* 3rd edn (Oxford: Oxford Science)
[40] Blow K J, Loudon R and Phoenix S J D 1990 Continuum fields in quantum optics *Phys. Rev.* A **42** 4102–14
[41] Raymer M G, van Enk S J, McKinstrie C J and McGuinness H J 2010 Interference of two photons of different color *Opt. Commun.* **283** 747–52
[42] Strake E, Bava G P and Montrosset I 1988 Guided modes of Ti:$LiNbO_3$ channel waveguides: a novel quasi-analytical technique in comparison with the scalar finite-element method *J. Lightwave Technol.* **6** 1126–35
[43] Wasilewski W, Lvovsky A I, Banaszek K and Radzewicz C 2006 Pulsed squeezed light: simultaneous squeezing of multiple modes *Phys. Rev.* A **73** 063819
[44] Christ A *et al* unpublished work
[45] Branczyk A M, Fedrizzi A, Stace T M, Ralph T C and White A G 2011 Engineered optical nonlinearity for quantum light sources *Opt. Express* **19** 55–65

Testing spectral filters as Gaussian quantum optical channels

K. Laiho,[1,*] A. Christ,[1,2] K. N. Cassemiro,[1] and C. Silberhorn[1,2]

[1]*Max Planck Institute for the Science of Light, Günther-Scharowsky-Straße 1/Bldg. 24, D-91058 Erlangen, Germany*

[2]*Applied Physics, University of Paderborn, Warburgerstraße 100, D-33098 Paderborn, Germany*

**Corresponding author: kaisa.laiho@mpl.mpg.de*

Received December 14, 2010; revised March 15, 2011; accepted March 15, 2011;
posted March 16, 2011 (Doc. ID 139699); published April 15, 2011

We experimentally investigate the mode characteristics of multimode radiation fields propagating through frequency-dependent Gaussian channels. After manipulating the twin beams emitted from a conventional parametric downconversion source via spectral filtering, we study the changes in their mode characteristics, utilizing the joint normalized correlation functions. While filtering reduces the number of spectral modes, it also leads to an apparent mode mismatch, which destroys the perfect photon-number correlation between the twin beams, and influences the mode properties of heralded states. © 2011 Optical Society of America

OCIS codes: 270.5290, 270.6570, 190.4975.

Quantum channels are basic building blocks of many quantum optical applications, in particular of quantum communication protocols. Often, these communication channels, such as optical fibers, are Gaussian channels, which introduce losses and thus lead to decoherence, limiting the channel performance [1]. This becomes a more prominent problem if channel multiplexing is taken into account, especially for pulsed light exhibiting a broad spectrum. Therefore, efficient and robust methods for characterizing quantum optical multimode (MM) light fields gain importance in future quantum communication systems. In the past, loss-tolerant photon counters have been used for exploring the mode structure of quantum light [2–6]. Nonetheless, determining the mode number from photon statistics without *a priori* knowledge of the mode distribution is a challenging task.

In this Letter we experimentally investigate the normalized correlation functions (nCFs) [7], which provide *loss-independent* techniques for characterizing the effective numbers of the excited modes. The nCFs are closely related to the factorial moments of the photon number and can also disclose the spatiotemporal mode properties of the quantum states [8–10]. The measurement of nCFs is typically realized by splitting the light field in a beam splitter network, followed by coincidence photon counting [7]. This technique probes the complete photon-number content of the state. Thus, it has a distinct advantage over two-photon quantum interference experiments that normally explore only the single-photon components of the interfering states and regard the higher photon-number contributions as undesired background [6,11,12]. The nCFs have successfully been employed to study the photon-number content of quantum states [7,13,14], to investigate the single-mode (SM) properties of nonclassical light fields [8,15–17], and to demonstrate the temporal photon-number correlation between photon pairs [18,19].

Twin beams, produced in parametric downconversion (PDC), exhibit strict photon-number correlation but are conventionally also highly correlated in the spectral degree of freedom; in other words, they possess spectral entanglement [20]. This might be especially appealing for channel multiplexing, since a set of squeezed states is generated in orthogonal modes that can be transmitted simultaneously [21]. However, if MM radiation is used without care in the standard quantum-key-distribution protocols, they can introduce a severe security risk [22]: the mode characteristics can be manipulated in the channel, e.g., by spectral filtering. Contrariwise, regarding the preparation of heralded nonclassical states of light, such as photon-number Fock states [23,24], decorrelation of the used twin beams is essential. Therefore, spectral and spatial filtering are often involved in the state generation to ensure the SM characteristics.

Spectral filtering can be rigorously described as a frequency-dependent beam splitter, which destroys the perfect photon-number correlation between the twin beams [25]. Moreover, filtering disrupts the orthogonality of the previously independent modes, and it is not trivial to predict the remaining number of modes. Here, we determine the mode properties of spectrally correlated twin beams by measuring their joint, low-order nCFs in a time-integrated form. After modifying the mode structure by spectral filtering, we record different effective mode numbers for the twin beams. This indicates that any model that regards the filtered twin-beam state simply as a product of pure two-mode squeezers with a reduced number of modes incorrectly assumes equal mode numbers for the conjugate beams. Additionally, we investigate the mode characteristics of heralded quantum states of light.

The spectral structure of unfiltered twin beams, denoted as signal (s) and idler (i), is described by the joint correlation function $f(\nu_s, \nu_i)$ in terms of the frequencies ν_μ ($\mu = s, i$). The properties of $f(\nu_s, \nu_i)$ are defined by the energy and momentum conservation laws [20]. The former is determined by the spectral shape of the pump field, and the latter by the dispersion of the nonlinear medium, resulting in the so-called phase-matching function. According to our earlier studies [6], the employed source—a 1.45 mm long periodically poled type-II KTP waveguide (WG)—produces highly spectrally anticorrelated twin beams. Because of the type-II process, the signal and idler marginals also exhibit different spectral widths, and thus filtering has different impacts on them.

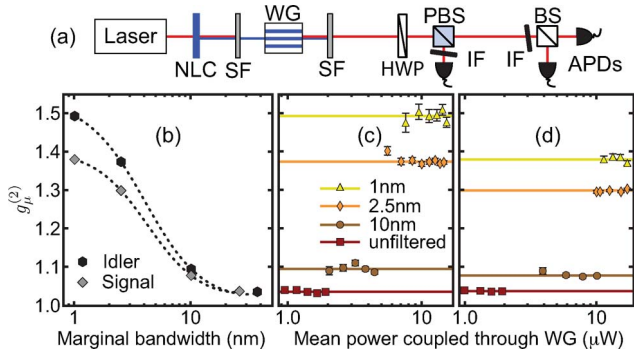

Fig. 1. (Color online) (a) Experimental setup, (b) $g_{\mu}^{(2)}$ versus the filtered marginal bandwidth, (c) $g_{i}^{(2)}$ versus the pump power, (d) $g_{s}^{(2)}$ versus the pump power. Symbols are measured values, solid lines fits, and dotted curves guides for the eye.

The broadband mode structure of pure twin-beam states is accessible by means of a singular-value decomposition, $f(\nu_s,\nu_i)=\sum_k \lambda_k \phi_k(\nu_s)\psi_k(\nu_i)$, where $\{\phi_k(\nu_s)\}$ and $\{\psi_k(\nu_i)\}$ each form a set of orthonormal functions [26]. The normalization is chosen such that $\sum_k \lambda_k^2 = 1$. This decomposition is unique, and it guarantees a perfect mode correlation between signal and idler. The number of excited modes can be determined with the K parameter $K = 1/\sum_k \lambda_k^4$, which indicates the effective number of uniformly occupied modes [27]. We gain information of this mode structure by exploring the joint nCFs [7]. In our time-integrated measurements, they probe a superposition of all modes and provide information of the complete mode structure [10]:

$$g^{(n,m)} = \frac{\langle :(\sum_k \hat{A}_k^\dagger \hat{A}_k)^n (\sum_{k'} \hat{B}_{k'}^\dagger \hat{B}_{k'})^m : \rangle}{\langle \sum_k \hat{A}_k^\dagger \hat{A}_k \rangle^n \langle \sum_{k'} \hat{B}_{k'}^\dagger \hat{B}_{k'} \rangle^m}.$$

The operators $\hat{A}_k^\dagger(\hat{A}_k)$ and $\hat{B}_k^\dagger(\hat{B}_k)$ describe the creation (annihilation) of a photon in the kth broadband signal and idler modes.

In the experiment, illustrated in Fig. 1(a), Ti:sapphire laser pulses (796 nm, 10 nm bandwidth, 4 MHz repetition rate) were frequency doubled in a nonlinear crystal (NLC) and employed as a pump for the PDC process. The residual pump fields were blocked with spectral filters (SFs), and signal and idler were separated in a polarizing beam splitter (PBS). One of the twin beams, selected by the setting of a half-wave plate (HWP), was directed to a 1 nm broad interference filter (IF) and then detected with an avalanche photodiode (APD). The other one was optionally filtered to a desired bandwidth of 1, 2.5, or 10 nm with exchangeable spectral filters and then split by a symmetric beam splitter (BS) and launched to two APD detection arms. The spatial SM characteristics of the twin beams were ensured by utilizing SM fibers. We recorded the coincidence and single counts for the evaluation of the nCFs from the measured raw counts according to [7]. Furthermore, nanosecond time gatings were used in all the detection channels to suppress background and dark count events.

First, we evaluate the second order moments $g^{(2,0)}$ and $g^{(0,2)}$, shortly $g_{\mu}^{(2)}$. They obey $1 < g_{\mu}^{(2)} \le 2$, with the boundaries indicating the MM (*Poissonian*) and SM (*thermal*) behavior of the marginal beams [4]. The measured values are shown in Fig. 1(b) with respect to the bandwidths of the marginal beams, estimated by the filter bandwidths or the spectral widths of the unfiltered marginal distributions. Assuming a loss-free PDC generation process, we can extract the effective mode number in each twin beam without *a priori* information of the weights of the mode distribution [10]: in the low-power regime $g_{\mu}^{(2)}$ is *independent* of the pump power and related to the corresponding K parameter by $g_{\mu}^{(2)} = 1 + 1/K_{\mu}$. By repeating the measurement at different pump powers, we confirm that the value of $g_{\mu}^{(2)}$ is unchanged, as shown in Figs. 1(c) and 1(d). The K parameters extracted from the measurements are shown in Table 1 with an accuracy given by the statistical fluctuations of $g_{\mu}^{(2)}$. As expected, the unfiltered marginal beams exhibit a large number of modes. Moreover, the mode numbers of the unfiltered twin beams coincide due to the perfect photon-number correlation of pure two-mode squeezed states. Spectral filtering leads to different effective mode numbers in signal and idler, which can only be explained by the fact that the perfect photon-number correlation between them is destroyed. Overall, $g_{\mu}^{(2)}$ provides a sensitive measure of the mode number mismatch and directly indicates that the filtered state is not perfectly two-mode squeezed anymore.

Table 1. The K Parameters of the Signal (K_s) and the Idler (K_i) for the Different Filter Bandwidths

Bandwidth (nm)	1	2.5	10	∞
K_s	2.63(3)	3.33(2)	12.7(4)	26(2)
K_i	2.03(3)	2.67(2)	10.4(4)	27.3(8)

Next, we examine the joint, low-order nCFs $g^{(1,2)}$ and $g^{(1,1)}$. For a pure twin-beam state, the SM and MM characteristics are predicted by $g_{\mathrm{SM}}^{(1,2)} = 4g^{(1,1)} - 2$ and $g_{\mathrm{MM}}^{(1,2)} = 2g^{(1,1)} - 1$. Our results, illustrated in Fig. 2(a), lie in between these boundaries. Furthermore, one clearly recognizes the linear behavior of the curves, whose slope is ideally governed by $2g_{\mu}^{(2)}$. The linear fits are in good agreement with the measured values of $g_{i}^{(2)}$. At higher gains several modes can be excited simultaneously,

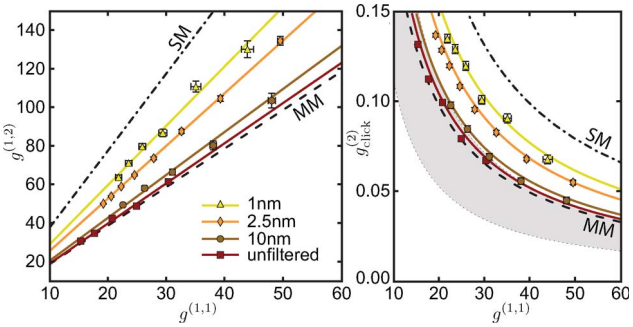

Fig. 2. (Color online) (a) $g^{(1,2)}$ versus $g^{(1,1)}$. Solid lines are linear fits. (b) $g_{\mathrm{click}}^{(2)}$ versus $g^{(1,1)}$. Solid curves are predicted by the fits in (a). Symbols indicate measured values, and dashed (dash-dotted) lines/curves illustrate the MM (SM) boundaries. The shaded area shows the boundaries for lossless detection.

and tight spectral filtering employed in only one of the twin beams is not sufficient to ensure the SM behavior of the joint state [Fig. 2(a), squares]. The mode structure is modified if filtering in both arms is introduced [Fig. 2(a), triangles]. Intriguingly, these results of the filtered twin-beam states are similar to those expected for photon-number correlated twin-beam states. Therefore, the loss-independent nCFs are partly insensitive to the disappearance of the strict photon-number correlation.

Regarding the preparation of heralded single photons, we investigate the conditional second order moment $g^{(2)}_{\mathrm{click}}$ of the idler, triggered by a click in signal. In Fig. 2(b) we present $g^{(2)}_{\mathrm{click}}$ with respect to $g^{(1,1)}$. A decrease in the pump power increases $g^{(1,1)}$, which indicates a high photon-number correlation between signal and idler, a desirable feature for heralding [10]. Nevertheless, the complete suppression of the higher photon-number contributions in the heralded state is experimentally challenging and happens at the cost of the source brightness. Unlike the joint nCFs, $g^{(2)}_{\mathrm{click}}$ depends on the efficiency in the trigger arm. According to our earlier studies [6], the second conditional moment is expressed in the low-efficiency regime as $g^{(2)}_{\mathrm{click}} = g^{(1,2)}/[g^{(1,1)}]^2$ for photon-number correlated twin beams. We predict the behavior of $g^{(2)}_{\mathrm{click}}$ with the help of the linear fits in Fig. 2(a) and find good agreement with the measurement. This indicates that the MM structure is still visible in the higher photon-number contributions of the heralded state. Moreover, the values of $g^{(2)}_{\mathrm{click}}$, as illustrated in Fig. 2(b), are significantly larger than expected for a lossless detection in the trigger arm.

We studied the changes in the mode structure of twin beams by investigating their joint nCFs. We quantified the effective mode number in the twin beams with the K parameter after modifying their spectral properties in frequency-dependent Gaussian channels. Our results show that the perfect photon-number correlation between signal and idler is lost. Furthermore, we gain a deeper insight into the spectral mode structure of the studied states, although the nCFs cannot resolve the weights of the individual modes. Our results can have a significant impact on controlling the mode properties by spectral filtering and will become important for quantum communication protocols implemented in optical fibers.

We thank M. Avenhaus and A. Schreiber for helpful discussions and useful comments. This work was supported by the European Commission under the grant agreement CORNER (FP7-ICT-213681). K. N. Cassemiro acknowledges financial support from the Alexander von Humboldt Foundation.

References

1. F. A. S. Barbosa, A. S. Coelho, A. J. de Faria, K. N. Cassemiro, A. S. Villar, P. Nussenzveig, and M. Martinelli, Nat. Photon. **4**, 858 (2010).
2. F. Paleari, A. Andreoni, G. Zambra, and M. Bondani, Opt. Express **12**, 2816 (2004).
3. W. Wasilevski, C. Radzewicz, R. Frankowsky, and K. Banaszek, Phys. Rev. A **78**, 033831 (2008).
4. M. Avenhaus, H. B. Coldenstrodt-Ronge, K. Laiho, W. Mauerer, I. A. Wamsley, and C. Silberhorn, Phys. Rev. Lett. **101**, 053601 (2008).
5. W. Mauerer, M. Avenhaus, W. Helwig, and C. Silberhorn, Phys. Rev. A **80**, 053815 (2009).
6. K. Laiho, K. N. Cassemiro, and C. Silberhorn, Opt. Express **17**, 22823 (2009).
7. M. Avenhaus, K. Laiho, M. V. Chekhova, and C. Silberhorn, Phys. Rev. Lett. **104**, 063602 (2010) and the references therein.
8. P. R. Tapster and J. G. Rarity, J. Mod. Opt. **45**, 595 (1998).
9. H. de Riedmatten, V. Scarani, I. Marcikic, A. Acin, W. Tittel, H. Zbinden, and N. Gisin, J. Mod. Opt. **51**, 1637 (2004).
10. A. Christ, K. Laiho, A. Eckstein, K. N. Cassemiro, and C. Silberhorn, New J. Phys. **13**, 033027 (2011).
11. P. J. Mosley, J. S. Lundeen, B. J. Smith, and I. A. Walmsley, New J. Phys. **10**, 093011 (2008).
12. K. N. Cassemiro, K. Laiho, and C. Silberhorn, New J. Phys. **12**, 113052 (2010).
13. H. J. Kimble, M. Dagenais, and L. Mandel, Phys. Rev. Lett. **39**, 691 (1977).
14. F. Bussieres, J. A. Slater, N. Godbout, and W. Tittel, Opt. Express **16**, 17060 (2008).
15. X. Li, L. Yang, L. Cui, Z.-Y. Ou, and D. Yu, Opt. Lett. **33**, 593 (2008).
16. B. Blauensteiner, I. Herbauts, S. Betelli, A. Poppe, and H. Hübel, Phys. Rev. A **79**, 063846 (2009).
17. A. Eckstein, A. Christ, P. J. Mosley, and C. Silberhorn, Phys. Rev. Lett. **106**, 013603 (2011).
18. E. Bocquillon, C. Couteau, M. Razavi, R. Laflamme, and G. Weihs, Phys. Rev. A **79**, 035801 (2009).
19. M. Scholz, L. Koch, and O. Benson, Phys. Rev. Lett. **102**, 063603 (2009).
20. W. P. Grice and I. A. Walmsley, Phys. Rev. A **56**, 1627 (1997).
21. W. Wasilewski, A. I. Lvovsky, K. Banaszek, and C. Radzewicz, Phys. Rev. A **73**, 063819 (2006).
22. W. Helwig, W. Mauerer, and C. Silberhorn, Phys. Rev. A **80**, 052326 (2009).
23. A. I. Lvovsky, H. Hansen, T. Aichele, O. Benson, J. Mlynek, and S. Schiller, Phys. Rev. Lett. **87**, 050402 (2001).
24. A. Ourjoumtsev, R. Tualle-Brouri, and P. Grangier, Phys. Rev. Lett. **96**, 213601 (2006).
25. A. M. Branczyk, T. C. Ralph, W. Helwig, and C. Silberhorn, New J. Phys. **12**, 063001 (2010).
26. C. K. Law, I. A. Walmsley, and J. H. Eberly, Phys. Rev. Lett. **84**, 5304 (2000).
27. J. H. Eberly, Laser Phys. **16**, 921 (2006).

Highly Efficient Single-Pass Source of Pulsed Single-Mode Twin Beams of Light

Andreas Eckstein,[1,*] Andreas Christ,[1,2] Peter J. Mosley,[1] and Christine Silberhorn[2,1]

[1]*Max Planck Institute for the Science of Light, Günther-Scharowsky-Strasse 1, 91054 Erlangen, Germany*

[2]*Applied Physics, University of Paderborn, Warburgerstrasse 100, 33098 Paderborn, Germany*

(Received 15 October 2010; published 7 January 2011)

We report the realization of a bright ultrafast type II parametric down-conversion source of twin beams free of any spatiotemporal correlations in a periodically poled $KTiOPO_4$ (PP-KTP) waveguide. From a robust, single-pass setup it emits pulsed two-mode squeezed vacuum states: photon-number entangled pairs of single-mode pulses or, in terms of continuous variables quantum optics, pulsed Einstein-Podolsky-Rosen states in the telecom wavelength regime. We verify the single-mode character of our source by measuring Glauber correlation functions $g^{(2)}$ and demonstrate with a pump energy as low as 75 pJ per pump pulse a mean photon number of 2.5.

DOI: 10.1103/PhysRevLett.106.013603 PACS numbers: 42.50.Dv, 03.67.Bg, 42.50.Gy, 42.65.Lm

The main obstacle to the real-world deployment of wide area quantum communication networks is the limited distance of guaranteed security between communication partners. In order overcome it, quantum repeaters [1] are needed to counter the security-degrading effects of transmission losses. For continuous variable (CV) quantum communication, these protocols heavily rely on the concatenation of non-Gaussian states and squeezed Gaussian states [2], namely, EPR states produced by parametric down-conversion (PDC) combined with photon counting [3]. In general though, PDC does not produce single-mode (SM) but multimode (MM) EPR states, requiring additional post-processing for optimal fidelity. Their MM structure is intrinsic to their generation process [4], and only direct manipulation of that process allows for the production of SM states.

For the generation of photon pairs, PDC sources have become an established standard: Inside a $\chi^{(2)}$-nonlinear medium, a pump photon decays into one signal and one idler photon. Recent works have shown that PDC source engineering [5,6] is capable of producing spectrally separable two-photon states $|1\rangle_s \otimes |1\rangle_i$, allowing for the preparation pure heralded single photons [7]. Going beyond the single photon pair approximation, PDC in general can be understood as a source of squeezed states of light [8,9]. First observed by Slusher *et al.* [10] in 1985, squeezed states originally garnered interest for the noise reduction in their quadrature observables $\hat{X}$, $\hat{Y}$ below the classical shot noise level, applicable in quantum-enhanced interferometry [11]. With the availability of mode locked lasers, MM pulsed squeezed states [12] became accessible [13]. Measuring with detectors incapable of resolving this MM structure, such as avalanche photo diodes (APD) implementing non-Gaussian operations [14], introduces mixedness which degrades the quantum features of the state [15]. Spectral engineering [5–7,16] made it possible to generate ultrafast photon pairs without spectral correlations in one spectral broadband mode [17]. Until now, PDC experiments relied on spatial [7] or narrow spectral [18] filtering of MM [9,12] squeezers to approximate SM biphotonic states, with severe loss of source brightness. In recent years, waveguide PDC sources [19] have become more and more popular as a means of achieving higher brightness [20] in a single-pass configuration, as well as for their easy integrability into miniaturized quantum optical experiments.

In this Letter, we demonstrate a waveguided single-pass type II PDC source of ultrafast SM EPR states of unprecedenced brightness in the telecom wavelength regime. For low pump powers ($\langle n\rangle \ll 1$), it doubles as a source of pure heralded single photons. By utilizing a SM PP-KTP waveguide, the output states can be used without narrow spatial filtering, and spectral engineering lets us avoid narrow spectral filtering, boosting source brightness considerably. The ultrafast, broadband nature of the pump beam makes spectral broadband modes a natural choice to describe our system. Our source emits pairs of spectrally broadband SM pulses. This we corroborated by a measurement of spectral separability, a $g^{(2)}$ measurement of one of the output arms to ensure the expected photon statistics, and a $\sinh^2$ gain in mean photon number. In contrast to MM PDC sources, the generated photons are not scattered over a number of broadband modes but concentrated in one mode. The resulting squeezing of several broadband modes cannot be trivially combined into one mode, as this would amount to entanglement distillation, which has been shown to be impossible using Gaussian operations [2]. But spectral engineering and a SM waveguide allow us to efficiently emit all output light into one spatiospectral mode, thus leading to a mean photon number $\langle n\rangle = 2.5$ per mode when pumping with picosecond pulses of only 75 pJ.

It has been shown early on in the experimental exploration of squeezing that PDC produces squeezed vacuum states of light [8]. In photon number representation, a two-mode squeezed vacuum state or SM EPR state has the form

$$|\psi\rangle = \hat{S}_{a,b}|0\rangle = e^{\imath\hat{H}_{a,b}}|0\rangle = \sqrt{1-|\lambda|^2}\sum_n \lambda^n |n,n\rangle, \quad (1)$$

where a and b are two orthogonal modes, $\hat{S}_{a,b}$ is the two-mode squeezing operator, and $\hat{H}_{a,b} = \zeta\hat{a}^\dagger\hat{b}^\dagger + \text{H.c.}$ is its effective Hamiltonian. It is a coherent superposition of strictly photon number correlated Fock states, and exhibits thermal photon statistics in both modes a and b. Its mean photon number $\langle n\rangle$ in each output beam is a measure of how much two-mode squeezing is generated $s = \frac{20}{\ln(10)}\, a \sinh(\sqrt{\langle n\rangle})$. The photon number correlation between both modes allows for heralding pure single photons with binary detectors. However, the underlying bilinear effective Hamiltonian $\hat{H}_{a,b}$ describes only a special case of PDC.

In general, the effective PDC Hamiltonian has a richer spatiospectral structure, and emits a continuum of momentum modes. Waveguided PDC, due to the boundary conditions of the guiding structure, exhibits a discrete spatial mode spectrum. In principle, any combination of pump, signal and idler waveguide modes will contribute to the overall PDC process. Their coupling strength is determined by their "overlap" integral [21], and multiple nonzero coupling coefficients between existing modes will result in a complex spectral structure of the output state. But using a SM waveguide allows us to restrict our analysis to one spatial mode for each beam, and we find

$$\hat{H}_{\text{PDC}} = \zeta \int d\omega_1 \int d\omega_2 f(\omega_1,\omega_2)\hat{a}^\dagger(\omega_1)\hat{b}^\dagger(\omega_2) + \text{H.c.}, \quad (2)$$

which generates a generalized version of the two-mode squeezed vacuum in Eq. (1) with spectrally correlated output beams. The coupling constant ζ determines the strength of this interaction, while spectral correlations between photons of the pairs produced are governed by the normalized joint spectral amplitude $f(\omega_1,\omega_2)$.

By applying a Schmidt decomposition to the joint amplitude $f(\omega_1,\omega_2) = \sum_k c_k \varphi_k(\omega_1)\psi_k(\omega_2)$, we obtain two orthonormal basis sets of spectral amplitude functions $\{\varphi_k(\omega_1)\}$ and $\{\psi_k(\omega_2)\}$ and a set of weighting coefficients $\{c_k\}$ with $\sum_k |c_k|^2 = 1$. For ultrafast pumped type II PDC, the φ_k, ψ_k are in good approximation to the Hermite functions [5,17]. Now the PDC Hamiltonian can be expressed in terms of broadband modes

$$\hat{H}_{\text{PDC}} = \sum_k \hat{H}_k = \zeta\sum_k c_k(\hat{A}_k^\dagger\hat{B}_k^\dagger + \hat{A}_k\hat{B}_k). \quad (3)$$

Each broadband mode operator $\hat{A}_k$, $\hat{B}_k$ describes a temporal pulse mode, or equivalently, an ultrafast spectral mode. It is defined as superposition of monochromatic creation/annihilation operators $\hat{a}(\omega)$, $\hat{b}(\omega)$ operators weighted with a function from the Schmidt basis: $\hat{A}_k^\dagger := \int d\omega\, \varphi_k(\omega)\hat{a}^\dagger(\omega)$ and $\hat{B}_k^\dagger := \int d\omega\, \psi_k(\omega)\hat{b}^\dagger(\omega)$. The effective Hamiltonians $\hat{H}_k$ do not interact with each other (since $[\hat{H}_k, \hat{H}_l] = 0$), and thus the PDC squeezing operator represents in fact an ensemble of independent two-mode squeezing operators $\hat{S}_{a,b} = e^{\imath\hat{H}_{\text{PDC}}} = \hat{S}_{A_0,B_0}\otimes\hat{S}_{A_1,B_1}\otimes\ldots$ where the coefficients c_k determine the relative strength of all squeezers as well as spectral correlation between signal and idler beams. This correlation is characterized by the source's effective mode number $K = \frac{1}{\sum_k |c_k|^4}$ [6,22]. We note that as the overall mean photon number n is shared between all modes, the amount of two-mode-squeezing has to be considered for each mode separately. For $c_0 = 1$ and all other $c_k = 0$, K assumes its minimum value of 1, and the PDC process can be described as a two-mode squeezer according to Eq. (1), and also optimal squeezing performance can be expected.

In our waveguided source pumped by an ultrafast pulsed laser beam we can manipulate spectral correlations of the photon pair joint spectra, thus the coefficients c_k, and as a result minimize K by simply adjusting the spectral width of the pump pulses [5,6,22].

We verified this by measuring the joint spectral intensity (JSI) of generated photon pairs at different spectral pump widths, to show the dependence of bi-photon frequency correlations on the pump width. The setup in Fig. 1(a) illustrates the PDC source: Ultrafast pump pulses at 768 nm are prepared with a Ti:sapphire mode locked laser system, spectrally filtered with a variable bandpass filter $4f$ setup, and then used to pump a type II PDC process within the PP-KTP waveguide with a poling period of 104 μm and 4 μm $\times$ 6 μm size. Its length is 10 mm but an effective length of 8 mm is used to correctly predict the measurement results in Figs. 2 and 3, since manufacturing imperfections in poling period and waveguide diameter lead to a widened phasematching distribution $\Phi(\omega_1,\omega_2)$ as if from a shorter waveguide. The generated photon pairs

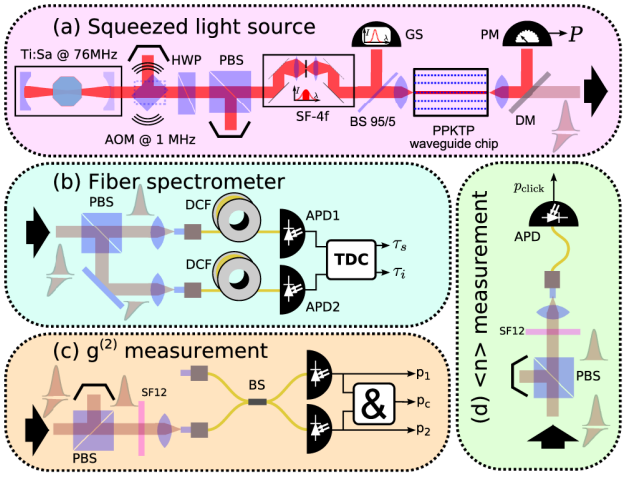

FIG. 1 (color online). Experimental setup: (a) PP-KTP waveguide source of two-mode squeezed vacuum states. (b) Fiber spectrometer for JSI measurement. (c) $g^{(2)}$ measurement setup. (d) Mean photon number $\langle n\rangle$ measurement.

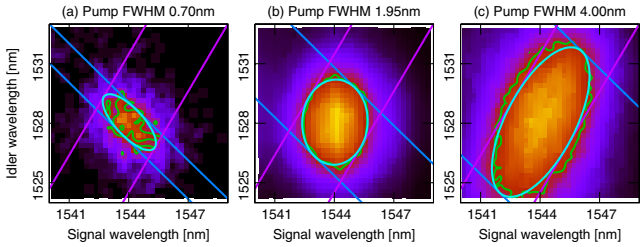

FIG. 2 (color online). Two-photon spectral intensities from the setup 1(b) with pump width below, equal to and above photon pair separability width at 1.95 nm FWHM. Green: 50% intensity. Violet: phase matching width. Blue: pump width. Bright blue: theoretical 50% intensity.

are analyzed in a fiber spectrometer [23] [Fig. 1(b)]: After separating signal and idler photons by polarization, they independently travel through long dispersive fibers, and are detected by a pair of idQuantique id201 avalanche photo diodes (APDs). Because of the chromatic dispersion of the fibers, the photons' group velocity and arrival time at the APDs depend on their wavelength. Thus we are able to determine the spectral intensity distribution of a stream of single photons from its arrival time spread. For a spectral pump FWHM of 0.70, 1.95, and 4.0 nm, we observe in Fig. 2 negative spectral correlations, an uncorrelated spectrum, and positive spectral correlations between signal and idler photons, respectively. For a fully uncorrelated state with just one contributing Schmidt mode pair φ_0, ψ_0 the marginal spectra of the biphoton amplitude are given by $|\varphi_0|^2$, $|\psi_0|^2$. In Fig. 3 (left), their shapes according to Fig. 2 (middle) are in good agreement with the Gaussian marginal distributions of their theory curve, indicating that the dominant Schmidt functions of the generated state are, up to phase, Gaussians as well. We have demonstrated control over spectral entanglement between signal and idler by filtering the pump spectrum, and found minimal spectral correlations of photon pairs around 1.95 nm pump FWHM.

To prove the genuine two-mode squeezer character of our source, an uncorrelated JSI is necessary but not sufficient. It is proportional to the modulus square of the complex joint amplitude $|f(\omega_1, \omega_2)|^2$ of the photon pair, so all phase information is lost in an intensity measurement. In order to detect phase entanglement between signal and idler, we need to measure an additional quantity sensitive to the source's mode number K, which is unity only in the absence of entanglement on the photon pair level, and larger otherwise.

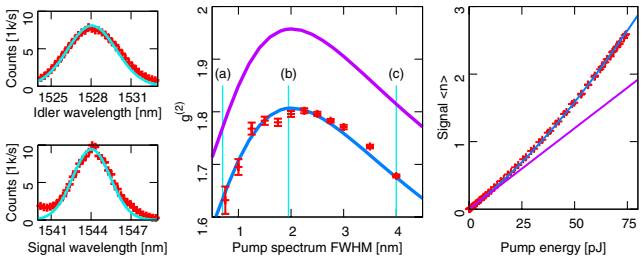

FIG. 3 (color online). Left: Marginal spectra of signal, idler beams from Fig. 2(b). Middle: $g^{(2)}$ values from setup 1(c) (red) with theory curve (blue) and background corrected theory curve (violet); (a), (b) and (c) mark pump FWHM of the JSI from Fig. 2. Right: Mean photon number from setup 1(d) (red) with the theoretical gain of a two-mode squeezer (blue) and the linear gain of a highly MM squeezer (violet).

The second order correlation function $g^{(2)}$ can be used to discriminate between beams with thermal ($g^{(2)} = 2$) and Poissonian photon statistics ($g^{(2)} = 1$) from a PDC source [18]. As has been noted above, type II PDC can in general be understood as an ensemble of two-mode squeezers, each of them emitting two beams with thermal photon statistics. In our waveguided type II setup, all broadband modes, A_k or B_k, share one polarization mode, a and b or, respectively. A detector with a spectral response function much wider than the characteristic width of the broadband modes cannot resolve them. It "sees" a convolution of the thermal photon statistics of all broadband modes, and in the limit of a large number of modes, this is a Poissonian distribution [24]. But if there is only one mode per polarization to begin with (which is only true for a two-mode squeezer), the detector receives a thermal distribution of photon numbers. Therefore, with the assumption that PDC emits a pure state, we can infer from $g^{(2)} = 2$ measured in either output beam a two-mode squeezer source. Indeed, for low pump power and thus low coupling strength ζ, we can find a simple connection between the $g^{(2)}$ correlation function on the one hand, and the broadband mode structure of our source and the effective mode number K on the other: $g^{(2)} = 1 + \sum |c_k|^4 = 1 + \frac{1}{K}$.

Figure 1(c) illustrates the $g^{(2)}$ measurement: Idler is discarded, and the signal beam is split by a 50/50 beamsplitter. Its output modes are fed into APDs, single (p_1, p_2) and coincidence (p_c) click probabilities for different spectral pump widths are recorded. When using binary detectors far from saturation, rather than intensity measurements, one finds $g^{(2)} = \frac{\langle \hat{a}^\dagger \hat{a}^\dagger \hat{a}\, \hat{a} \rangle}{\langle \hat{a}^\dagger \hat{a} \rangle^2} \approx \frac{p_c}{p_1 p_2}$ As has been demonstrated, frequency correlations between signal and idler beam and thus squeezer mode number K can be controlled by manipulation of the pump width. In Fig. 3 (middle) measurement results show a maximum $g^{(2)}$ value at 1.95 nm pump FWHM, in accordance with Fig. 2. When departing from the optimum pump width, $g^{(2)}$ decreases as predicted. Because of uncorrelated, residual background events from waveguide material fluorescence and detector dark counts that make up 5% of the total single event counts, we obtain a maximum of $g^{(2)} = 1.8$, and $g^{(2)} = 1.95$ after background correction. This highlights the next-to-perfect SM EPR states our source emits, and the degree of control we exact over the mode number and photon statistics of the system. Note that the two-mode character is shown with respect to frequency as well as

spatial degrees of freedom. Owing to the waveguide nature of our source, signal and idler beam occupy a single waveguide mode.

Nonlinear waveguides allow for dramatically higher source brightness when compared to bulk sources [20]: Instead of coupling to a continuum of spatial modes, inside a waveguide structure the generated waves couple to a discrete spectrum, and ideally to just one mode, boosting self-seeding of the PDC process and greatly simplifying collection of the output light. Adjusting our setup with a CW laser beam shows collection efficiency of the waveguide output mode into SM fibers up to 80%, indicating in good approximation a Gaussian mode profile. At mean photon numbers of $\langle n \rangle \approx 1$ per mode we will be able to observe the superlinear gain of a two-mode squeezer $\sinh^2(r)$ caused by self-seeding of signal and idler along the waveguide length, further corroborating our source's SM character. With a pump FWHM of 1.95 nm producing separable photon pairs, we measured the mean photon number $\langle n \rangle \approx \frac{p_{\text{click}}}{\eta}$ of the signal beam [Fig. 1(d)] by recording the power dependent APD click probability p_{click}. For binary detectors far from saturation, this is proportional to $\langle n \rangle$, with an overall quantum efficiency η of the setup. The source gain in Fig. 3 (right) exhibits with increasing pump power the departure from the linear gain profile that would be expected for a highly MM squeezer, while it is in very good agreement with the theoretical prediction for a two-mode squeezer gain. Mean photon numbers of up to 2.5 were achieved. Assuming ideal photon collection and detectors, this is equivalent to 11 dB of two-mode squeezing, in a pulsed, single-pass setting, demonstrating the potential of our source for future CV experiments. For an optimized setup we observed an overall detection efficiency of 15%. For a specified APD quantum efficiency of 25% at 1550 nm, this makes a photon collection efficiency into SM fiber of 60%, with our waveguide output facet not antireflection coated.

In conclusion, we have applied spectral engineering to a waveguided PDC source to create a bright, genuinely ultrafast pulsed two-mode squeezer in the telecom wavelength regime with mean photon number as high as 2.5, with only 75 pJ pump pulse energy. In future experiments, this value can be easily scaled up to harvest even higher photon numbers. It features near thermal photon statistics with $g^{(2)} = 1.95$ after background correction, or an effective mode number of $K = 1.05$. A collection efficiency of 60% into SM fibers demonstrates the high spatial mode quality of our waveguide device and shows its potential for inclusion into integrated optical networks. Because of its true two-mode character and brightness, we expect widespread adoption of our source in continuous variable quantum communication, where high squeezing values, purity and low-loss fiber transmission are prerequisite for efficient quantum cryptography [25], teleportation [26,27], and ultimately entanglement distillation [3,14] to overcome transmission losses in wide area quantum communication networks, a vital building block of quantum repeaters [1].

This work was supported by the EC under the grant agreement CORNER (FP7-ICT-213681).

*andreas.eckstein@mpl.mpg.de

[1] H.-J. Briegel, W. Dür, J. I. Cirac, and P. Zoller, Phys. Rev. Lett. **81**, 5932 (1998).
[2] J. Eisert, S. Scheel, and M. B. Plenio, Phys. Rev. Lett. **89**, 137903 (2002); G. Giedke and J. I. Cirac, Phys. Rev. A **66**, 032316 (2002).
[3] T. Opatrný, G. Kurizki, and D.-G. Welsch, Phys. Rev. A **61**, 032302 (2000).
[4] M. Martinelli *et al.*, Phys. Rev. A **67**, 023808 (2003).
[5] W. P. Grice, A. B. U'Ren, and I. A. Walmsley, Phys. Rev. A **64**, 063815 (2001).
[6] A. B. U'Ren *et al.*, Laser Phys. **15**, No. 1, 146 (2005).
[7] P. J. Mosley *et al.*, Phys. Rev. Lett. **100**, 133601 (2008).
[8] L. A. Wu, H. J. Kimble, J. L. Hall, and H. Wu, Phys. Rev. Lett. **57**, 2520 (1986).
[9] W. Wasilewski, A. I. Lvovsky, K. Banaszek, and C. Radzewicz, Phys. Rev. A **73**, 063819 (2006).
[10] R. E. Slusher, L. W. Hollberg, B. Yurke, J. C. Mertz, and J. F. Valley, Phys. Rev. Lett. **55**, 2409 (1985).
[11] C. M. Caves, Phys. Rev. D **23**, 1693 (1981).
[12] T. Opatrný, N. Korolkova, and G. Leuchs, Phys. Rev. A **66**, 053813 (2002).
[13] R. E. Slusher *et al.*, Phys. Rev. Lett. **59**, 2566 (1987).
[14] D. E. Browne, J. Eisert, S. Scheel, and M. B. Plenio, Phys. Rev. A **67**, 062320 (2003).
[15] P. P. Rohde, W. Mauerer, and C. Silberhorn, New J. Phys. **9**, 91 (2007).
[16] O. Kuzucu, F. N. C. Wong, S. Kurimura, and S. Tovstonog, Phys. Rev. Lett. **101**, 153602 (2008).
[17] C. K. Law, I. A. Walmsley, and J. H. Eberly, Phys. Rev. Lett. **84**, 5304 (2000).
[18] P. R. Tapster and J. G. Rarity, J. Mod. Opt. **45**, 595 (1998).
[19] M. E. Anderson, Opt. Lett. **20**, 620 (1995); S. Tanzilli *et al.*, Eur. Phys. J. D **18**, 155 (2002); G. Kanter *et al.*, Opt. Express **10**, 177 (2002); G. Fujii *et al.*, *ibid.* **15**, 12769 (2007); A. Politi *et al.*, Science **320**, 646 (2008).
[20] M. Fiorentino *et al.*, Opt. Express **15**, 7479 (2007).
[21] A. Christ *et al.*, Phys. Rev. A **80**, 033829 (2009).
[22] Y. M. Mikhailova, P. A. Volkov, and M. V. Fedorov, Phys. Rev. A **78**, 062327 (2008).
[23] M. Avenhaus, A. Eckstein, P. J. Mosley, and C. Silberhorn, Opt. Lett. **34**, 2873 (2009).
[24] M. Avenhaus, H. B. Coldenstrodt-Ronge, K. Laiho, W. Mauerer, I. A. Walmsley, and C. Silberhorn, Phys. Rev. Lett. **101**, 053601 (2008).
[25] D. Gottesman and J. Preskill, Phys. Rev. A **63**, 022309 (2001).
[26] A. Furusawa *et al.*, Science **282**, 706 (1998).
[27] W. P. Bowen *et al.*, Phys. Rev. A **67**, 032302 (2003).